

A Finite Volume Framework for Accurate Modeling of Fault Reactivation in Poroelastic Rocks

Novikov, A.

DOI

[10.4233/uuid:1f4731b3-cbdd-4317-98f7-8520b7446684](https://doi.org/10.4233/uuid:1f4731b3-cbdd-4317-98f7-8520b7446684)

Publication date

2024

Document Version

Final published version

Citation (APA)

Novikov, A. (2024). *A Finite Volume Framework for Accurate Modeling of Fault Reactivation in Poroelastic Rocks*. [Dissertation (TU Delft), Delft University of Technology]. <https://doi.org/10.4233/uuid:1f4731b3-cbdd-4317-98f7-8520b7446684>

Important note

To cite this publication, please use the final published version (if applicable). Please check the document version above.

Copyright

Other than for strictly personal use, it is not permitted to download, forward or distribute the text or part of it, without the consent of the author(s) and/or copyright holder(s), unless the work is under an open content license such as Creative Commons.

Takedown policy

Please contact us and provide details if you believe this document breaches copyrights. We will remove access to the work immediately and investigate your claim.

**A Finite Volume Framework for
Accurate Modeling of Fault
Reactivation in Poroelastic Rocks**

A Finite Volume Framework for Accurate Modeling of Fault Reactivation in Poroelastic Rocks

Proefschrift

ter verkrijging van de graad van doctor
aan de Technische Universiteit Delft,
op gezag van de Rector Magnificus prof. dr. ir. T.H.J.J. van der Hagen,
voorzitter van het College voor Promoties,
in het openbaar te verdedigen op
woensdag, 22 Mei 2024 om 10:00 uur

door

Aleksei Novikov

Master of Applied Mathematics and Physics,
Moscow Institute of Physics and Technology, Dolgoprudny, Rusland,
geboren te Saransk, Rusland.

Dit proefschrift is goedgekeurd door de promotoren.

Samenstelling promotiecommissie:

Rector Magnificus	voorzitter
Dr. D. V. Voskov	Technische Universiteit Delft, promotor
Prof. dr. ir. J.D. Jansen	Technische Universiteit Delft, promotor
Prof. dr. H. Hajibeygi	Technische Universiteit Delft, promotor

Onafhankelijke leden:

Prof. dr. M. Ferronato	University of Padova
Prof. dr. I. Berre	University of Bergen
Prof. dr. ir. L.J. Sluys	Technische Universiteit Delft
Dr. ir. A.C. Dieudonne	Technische Universiteit Delft
Prof. dr. S. Geiger	Technische Universiteit Delft, reservelid

This thesis is part of the project "Science4Steer: a scientific basis for production and reinjection strategies to minimize induced seismicity in Dutch gas fields" (with project number DEEP.NL.2018.046) of the research program "DeepNL" which is financed by the Dutch Research Council (NWO).



Keywords: Finite Volume Method, Multi-Point Approximation, Discrete Fracture Model, Fault Reactivation, Frictional Contact, Slip-Weakening, DARTS, Geomechanics, Contact Mechanics, Induced seismicity, Numerical simulation

Printed by: Gildeprint

Copyright © 2024 by A. Novikov

ISBN 978-94-6496-125-6

An electronic version of this dissertation is available at

<https://repository.tudelft.nl/>.

Contents

Summary	ix
Samenvatting	xi
Nomenclature	xiii
Operators	xiii
Roman Letters	xiii
Greek Letters	xiv
1. Introduction	1
1.1. Induced Seismicity	2
1.2. Societal Relevance	3
1.3. Numerical Modeling	4
1.4. Thesis Objectives	7
1.5. Outline of the Thesis	8
2. Mechanics of Faulted Saturated Porous Media	11
2.1. Main Definitions	12
2.2. Conservation Laws	13
2.3. Contact Mechanics	15
2.4. Constitutive Relationships	16
2.4.1. Infinitesimal Deformations	16
2.4.2. A Linear Saturated Thermoporoelastic Medium with Viscous Interaction Between Components	17
2.4.3. Sliding Criterion and Friction Laws	18
2.5. Governing Equations for This Thesis Study	19
3. Finite Volume Framework for Modeling of Induced Fault Slip	23
3.1. Finite Volume Method	24
3.2. Finite Volume Method for Poroelasticity	25
3.3. Approximation of Fluxes	27
3.3.1. Approximations at Interior Continuous Interface	27
3.3.2. Diffusive and Advective Terms	30
3.3.3. Approximations at Interior Contact Interface	31
3.3.4. Approximations at Boundary Interface	35
3.4. Stabilized Approximation	37
3.5. Reconstruction of Stresses	39
3.6. Nonlinear Finite Volume Method for Pure Elasticity Problem	40

3.7.	Contact Constraints	42
3.7.1.	Penalty Method with Return-Mapping Algorithm	42
3.8.	Linear Solution Strategies	43
3.8.1.	Fixed-Stress Split Preconditioner	44
3.8.2.	System Algebraic Multigrid (SAMG)	44
3.8.3.	Incomplete LU Factorization for Fully Dynamic Modeling	45
3.9.	Implementation Details	46
3.9.1.	Discretization	46
3.9.2.	Matrix Assembly	48
3.9.3.	Linear Solution	49
3.9.4.	User Interfaces	50
4.	Benchmarking Numerical Solution	51
4.1.	Linearity-Preserving Test	52
4.2.	Convergence Tests	53
4.3.	Terzaghi's Problem	55
4.4.	Mandel's Problem	56
4.5.	Two-Layer Terzaghi's Problem	59
4.6.	Inf-Sup Instability	61
4.7.	SPE10 with Mechanical Extension	63
4.8.	Comparison Against Other Simulators	66
4.8.1.	GEOS	66
4.8.2.	PorePy	74
4.9.	Displaced Fault Model	75
4.9.1.	Model Setup	77
4.9.2.	Initial State	79
4.9.3.	Vertical Frictionless Fault	82
4.9.4.	Inclined Fault with Static Friction	82
4.9.5.	Inclined Fault with Linear Slip-Weakening friction	85
4.10.	Benchmarking the Nonlinear Finite Volume Method	85
4.10.1.	Convergence Study	85
4.10.2.	Compression and Shear	89
4.11.	Conclusion	90
5.	Modeling of Experiments	93
5.1.	Core Injection Experiments	94
5.2.	Large-Scale Triaxial Loading Experiment	98
5.2.1.	Model Setup	98
5.2.2.	In-Plane Stress Distribution	100
5.2.3.	Sensitivity Study	102
5.2.4.	Loading Path	106
5.3.	Conclusion	107
6.	Beyond the Quasi-Static Modeling of Induced Seismicity	109
6.1.	Quasi-Dynamic Approach	110
6.2.	Fully-Dynamic Approach	110

6.3. Combined Quasi-Dynamic and Fully Dynamic Strategy	111
6.4. Validation	111
6.4.1. One-Dimensional Elastic Wave Propagation	111
6.5. Case Study: Displaced Fault	112
6.5.1. Uniform Depletion	113
6.5.2. Depletion from a Remote Production Well	118
6.6. Conclusion	124
7. Conclusion	125
7.1. Recapitulation and Key Learning Points	125
7.2. Future Perspectives	127
A. Finite Volume Method for Thermoporoelastic Media	129
A.1. Approximation of Fluxes at Interior Interfaces	129
A.2. Approximation of Fluxes at Boundary Interfaces	132
A.3. Uniaxial thermoporoelastic consolidation	132
Data availability statement	135
References	137
Acknowledgements	153
Curriculum Vitæ	157
Education	157
Professional Experience	158
List of Publications	159

Summary

Safe and sustainable exploitation of geo-energy resources requires not only a comprehensive evaluation of the performance and economics of the corresponding projects but also the assessments of the associated risks, including the risk of induced seismicity. Indeed, seismic events may arise from the reactivation of natural faults and fractures due to subsurface engineering activities. Numerous anthropogenic activities including geothermal energy production and CO₂ geological storage have been identified as potential triggers of these seismic events. The risks associated with induced seismicity stem from the potential for surface movement, structural damage, and negative impacts on both the environment and human health.

The corresponding risk assessments highly rely on geomechanical modeling which is progressively being integrated into the reservoir modeling workflows. This integration demands high levels of integrability, flexibility and performance from the computational engines employed. These requirements, along with the complexities of the underlying physical, numerical and implementation aspects severely constrain the availability of suitable computational capabilities. Increasing societal concerns about induced seismicity amplify the demand for such capabilities, highlighting a lack of efficient and comprehensive solutions in both academia and industry.

This thesis contributes to bridging this gap through the development of an innovative modeling framework. Leveraging the ubiquity of Finite Volume Methods (FVM) in traditional reservoir simulations, the newly proposed FVM schemes for coupled fluid mass and momentum balance equations present an opportunity for seamless integration of geomechanical modeling into existing reservoir modeling frameworks. As a result, the proposed approach satisfies the aforementioned requirements and presents an accurate and efficient framework for the investigation of induced seismicity in geo-energy applications.

The core innovation of the thesis is represented by fully implicit schemes of FVM for the coupled modeling of faulted poroelastic media implemented in the open-source Delft Advanced Research Terra Simulator (DARTS). The schemes are based on coupled multi-point flux and multi-point stress approximations derived from the local conservation of fluid mass and forces. They support arbitrary material heterogeneity, anisotropy, boundary conditions, fluid properties, and friction laws. To further improve the performance of coupled modeling, block-partitioned preconditioning strategy has been implemented. Besides, first-of-its-kind nonlinear scheme of FVM for the pure elasticity problem has been proposed and implemented in DARTS.

An accurate representation of faults has been developed with the mixed-dimensional conformal discrete fault model (DFM) which assumes the use of equidimensional

DFM in the integration of fluid mass fluxes and a lower-dimensional DFM for the integration of momentum balance. The incorporation of the stress approximations at the cell interfaces into this model enables convenient integration of contact mechanics at those interfaces. The penalty method and a return-mapping algorithm have been employed to enforce contact inequality constraints.

The proposed schemes of FVM and the numerical strategy for the resolving of frictional contact have been thoroughly validated in a number of benchmarks, including convergence studies, comparisons against analytical and semi-analytical solutions, and comparisons against numerical solutions obtained by other numerical frameworks. The efficiency of the employed solution strategy has been also assessed.

Laboratory experiments provide valuable insights into the material properties and frictional response of porous rocks. For convenient interpretation of these insights and further examination of the capabilities of numerical solvers, the modeling of two experimental setups has been conducted. This concerns the modeling of injection-induced slip in core cross-cuts and the modeling of a large-scale setup with displaced a fault configuration.

Even though the proposed framework demonstrated extended capabilities, the modeling under the quasi-static (QS) assumption restricts the characterization of seismicity. To overcome this limitation, fully dynamic (FD) modeling has been implemented in the framework. As a result, we demonstrate the combined QS and FD modeling of fault reactivation that allows aseismic slip, nucleation, rupture propagation and arrest to be resolved in one simulation run.

Samenvatting

Het veilig en duurzaam exploiteren van geo-energiebronnen vereist niet alleen een uitgebreide evaluatie van de prestaties en economische aspecten van de bijbehorende projecten, maar ook het beoordelen van de daarmee samenhangende risico's, inclusief het risico op geïnduceerde seismische activiteit. Seismische gebeurtenissen kunnen ontstaan door de heractivatie van natuurlijke breuken als gevolg van ondergrondse engineering activiteiten. Talrijke antropogene activiteiten, waaronder de productie van geothermische energie en de geologische opslag van CO₂, zijn geïdentificeerd als potentiële veroorzakers van deze seismische gebeurtenissen. De risico's verbonden aan geïnduceerde seismische activiteit komen voort uit de potentie voor oppervlakte beweging, schade aan constructies en negatieve gevolgen voor zowel het milieu als de menselijke gezondheid.

De bijbehorende risicobeoordelingen zijn sterk afhankelijk van geomechanische modellering, die steeds meer geïntegreerd wordt in de workflows van reservoirmodellering. Deze integratie vereist een hoog niveau van integreerbaarheid, flexibiliteit en rekenkundige mogelijkheden van de gebruikte rekenmodellen. Deze vereisten, samen met de complexiteit van de onderliggende fysische, numerieke en implementatieaspecten beperken de beschikbaarheid van geschikte berekenings capaciteiten. Toenemende maatschappelijke zorgen over geïnduceerde seismiciteit hebben de vraag naar dergelijke berekenings capaciteiten versterkt, waarbij een gebrek aan efficiënte en uitgebreide oplossingen in zowel de academische wereld als de industrie aan het licht komt.

Dit proefschrift draagt bij aan het overbruggen van deze kloof door de ontwikkeling van een innovatief modelleerkader. Door gebruik te maken van de alomtegenwoordigheid van Finite Volume Methoden (FVM) in traditionele reservoirsimulaties, bieden de nieuw voorgestelde FVM-schema's voor gekoppelde vloeistofmassa- en impulsvergelijkingen een kans voor een naadloze integratie van geomechanische modellering in bestaande reservoirmodelleringkaders. Als gevolg hiervan voldoet de voorgestelde aanpak aan de bovengenoemde rekenkundige vereisten en presenteert het een nauwkeurig en efficiënt kader voor het onderzoek van geïnduceerde seismische activiteit in geo-energietoepassingen.

De kerninnovatie van dit proefschrift worden gevormd door volledig impliciete FVM-schema's voor een gekoppelde modellering van poroelastische media met breuken, geïmplementeerd in de open-source Delft Advanced Research Terra Simulator (DARTS). De schema's zijn gebaseerd op gekoppelde meerpunts flux- en meerpunts spanning benaderingen, afgeleid van het lokaal behoud van vloeistofmassa en krachten. Ze ondersteunen willekeurige materiaal heterogeniteit, anisotropie, randvoorwaarden, vloeistofeigenschappen en wrijvingswetten. Om de prestaties van gekoppelde modellering verder te verbeteren, is een blokpartitioneer-

de preconditioneringsstrategie geïmplementeerd. Bovendien is het het eerste niet-lineaire FVM-schema voor het zuivere elasticiteitsprobleem dat is voorgesteld en geïmplementeerd in DARTS.

Een nauwkeurige weergave van breuken is ontwikkeld met het gemengd-dimensionale conforme discrete breukmodel (DFM), dat het zelfde dimensionale DFM gebruikt bij de integratie van vloeistofmassafluxen en een lager-dimensionale DFM voor de integratie van de krachten. De incorporatie van de spanningsbenaderingen op de celoppervlakken in dit model maakt een gemakkelijke integratie van contactmechanica op die celoppervlakken mogelijk. De penalty methode en een return-mapping-algoritme zijn gebruikt om contactongelijkheidsbeperkingen af te dwingen.

De voorgestelde schema's van FVM en de numerieke strategie voor de oplossing van wrijvingscontact zijn grondig gevalideerd in een aantal referentieonderzoeken, namelijk convergentieonderzoek, vergelijking met analytische en semi-analytische oplossingen, en vergelijking met numerieke oplossingen verkregen met andere numerieke methoden. De efficiëntie van de gebruikte preconditioneringsstrategie is ook beoordeeld.

Laboratoriumexperimenten bieden waardevolle inzichten in de materiaaleigenschappen en het wrijvingsgedrag van poreuze gesteente. Om deze inzichten gemakkelijk te kunnen interpreteren en de mogelijkheden van numerieke oplossingsmethoden verder te onderzoeken, zijn twee experimentele opstellingen gemodelleerd. Dit betreft de modellering van injectie-geïnduceerde verschuiving in een doorsneden kern, en de modellering van een grootschalige opstelling met verplaatste breukconfiguratie.

Hoewel het voorgestelde modellerings kader aanzienlijke capaciteiten heeft aangetoond, beperkt de modellering onder de quasi-statische (QS) aanname de karakterisering van seismische activiteit. Om deze beperking te heffen, is een volledig dynamische (FD) modellering geïmplementeerd in het kader. Als voorbeeld demonstreren we de gecombineerde QS en FD modellering van breukreactivatie die aseismische verschuiving, nucleatie, breukverspreiding en stilstand in één simulatie run mogelijk maakt.

Nomenclature

Vectors, rank-two tensors and matrices, and the tensors of rank higher than two are denoted with bold lowercase letters, bold capital letters, and script font respectively. The pore fluid and rock matrix are specified with f and s subscripts correspondingly.

Operators

symbol	description
\cdot	inner (dot) product
$:$	double inner (dot) product
\otimes	Kronecker product

Roman Letters

symbol	units	description
A	Pa K^{-1}	rank-two tensor of thermal dilation coefficients
B	1	rank-two tensor of Biot coefficients
b	1	Biot coefficient
C	Pa	rank-four drained stiffness tensor
C	Pa	6×6 stiffness matrix in Voigt notation
c	Pa	contact cohesion
D_c	m	critical slip distance
d	m	distance
E	1	Almansi strain tensor
E	Pa	Young's modulus
G	Pa	shear modulus
g	m s^{-2}	gravitational acceleration
g	m	gap vector
h	J	enthalpy
f	Pa	traction vector
f'	Pa	effective (Biot) traction vector
f''	Pa	effective (Terzaghi) traction vector
f_N, f_T	Pa	normal and tangential components of traction vector
I	1	identity matrix
K	m^2	rank-two tensor of permeability

symbol	units	description
K	Pa	bulk modulus
k	D	scalar permeability
M	Pa	Biot modulus
\mathbf{n}	1	unit normal to interface
p	Pa	pore pressure
t	s	time
q_f	m s^{-1}	fluid flux
r	$\text{kg m}^{-3} \text{s}^{-1}$	the source of fluid mass
U	J	internal energy
\mathbf{u}	m	vector of displacements
V	m^3	volume
\mathbf{v}	m s^{-1}	vector of velocities
v^*	m s^{-1}	reference velocity in rate-dependent friction laws
\mathbf{w}	m s^{-1}	vector of Darcy velocities
\mathbf{x}_i	m	i th cell center
\mathbf{x}_δ	m	center of the interface δ
\mathbf{y}_i	m	projection of the i th cell center on interface
z	m	depth

Greek Letters

symbol	units	description
α_ϕ	K^{-1}	volumetric thermal dilation coefficient related to porosity
Δt	s	time step
δ	m^2	surface area
η	$\text{J K}^{-1} \text{kg}^{-1}$	specific (mass) entropy
θ	K	temperature
ξ^p, ξ_τ^p	Pa m^{-1}	normal and 3×1 tangential components of pressure gradients
ξ^u, ξ_τ^u	1	3×1 normal and 9×1 tangential components of displacement gradients
Λ	$\text{W m}^{-1} \text{K}^{-1}$	thermal conductivity tensor
μ	1	friction coefficient
μ_f	Pa s	fluid dynamic viscosity
ν	1	Poisson's ratio
ρ	kg m^{-3}	mass density
Σ	Pa	Cauchy stress tensor
Σ'	Pa	effective (Biot) Cauchy stress tensor
Σ''	Pa	effective (Terzaghi) Cauchy stress tensor
σ	Pa	Cauchy stress tensor in Voigt notation
σ'	Pa	effective (Biot) Cauchy stress tensor in Voigt notation
σ''	Pa	effective (Terzaghi) Cauchy stress tensor in Voigt notation
Φ	Pa	sliding surface
ϕ	1	porosity
ψ	1	one-third of the trace of tensor \mathbf{B}

1

Introduction

1.1. Induced Seismicity

Seismicity, or the occurrence and behavior of earthquakes, is among the widely studied areas in geoscience. Earthquakes occur when strain energy stored in the Earth's crust is released with a sudden movement of rocks typically along faults or boundaries of tectonic plates. These events can range in magnitude from very small tremors ($M_w < 2$) to massive earthquakes ($M_w > 6$) that cause widespread damage and loss of life. Seismicity can be broadly classified into two categories: tectonic or natural and induced or anthropogenic. Tectonic earthquakes result from the movement of tectonic plates, while induced earthquakes are caused by human activities.

The study of tectonic seismicity remains an active research field for a long period of time, and much progress has been made in recent years. The development of new monitoring technologies, such as GPS and satellite imagery, has enabled researchers to understand better the dynamics of tectonic plates and the mechanisms that drive earthquakes (Scholz 2019). Additionally, advances in computational modeling have allowed researchers to simulate the behavior of faults and better predict the likelihood of earthquakes (Aagaard *et al.* 2010).

Induced seismicity has received increasing attention in recent years. An abrupt rise in the rate of induced earthquakes has been observed since 2008 (Keranen *et al.* 2018). Induced earthquakes have been recorded in many parts of the world, including the United States, Europe, and Asia (Ellsworth 2013; Foulger *et al.* 2018; Grigoli *et al.* 2017; Keranen *et al.* 2018; Muntendam-Bos *et al.* 2022; Shapiro 2015). These induced earthquakes are typically of smaller magnitudes than natural earthquakes but can still cause damage to infrastructure and lead to public safety concerns (McGarr *et al.* 2002; van der Voort *et al.* 2015).

Various kinds of anthropogenic activity have been proven to be potential causes of induced seismicity. The impoundment of reservoirs (Carder 1945; Gupta 2002; Simpson 1976), fluid withdrawal (Pratt *et al.* 1926; Segall 1989; Van Thienen-Visser *et al.* 2015), fluid injection (Davis *et al.* 1989; Healy *et al.* 1968; Kim 2013), hydraulic fracturing (Atkinson *et al.* 2016; Schultz *et al.* 2017), mining (McGarr 1984; Riemer *et al.* 2012), geothermal energy production (Buijze *et al.* 2020; Ellsworth *et al.* 2019; Majer *et al.* 2007) and CO₂ geological storage (Cheng *et al.* 2023) can cause seismicity. A growing number of induced earthquakes has inspired the development of dedicated global databases (Chen *et al.* 2023; Wilson *et al.* 2017).

The development of geo-energy resources in the subsurface motivated special attention to the seismicity induced by pore pressure and temperature variations. Poroelastic effect can play a significant role in the mechanics of induced earthquakes. Pore pressure redistribution caused by a major earthquake was observed by water level change in wells (Jónsson *et al.* 2003) and may lead to delayed aftershocks (Nur *et al.* 1972; Segall *et al.* 1995). On the other hand, pore pressure may stabilize a weakening fault zone leading to precursory creep (Rice *et al.* 1979; Rudnicki 2001; Veltmeijer *et al.* 2022).

Another essential feature of induced seismicity is the localization of events in space. In this case, a microseismic monitoring network can be installed for gaining a deeper comprehension of the physical processes that control induced seis-

mic activity. To assess the hazard of induced seismicity companies involved in resource extraction are obligated by governments to establish suitable infrastructure for microseismic monitoring in Italy, Netherlands, and Switzerland (Dost *et al.* 2012). Well-designed microseismic monitoring networks allow seismic events to be evaluated in terms of their magnitude and location, identifying even weak events ($M_w < 0$) in the presence of noise contamination (Grigoli *et al.* 2017).

A bulk of knowledge about induced seismicity is obtained from laboratory experiments. The design of these experiments allows the relationship between the state of stress and observed rupture response to be investigated in a controlled setting. In particular, friction experiments showed that the rate-and-state (Dieterich 1979; Ruina 1983) and more sophisticated friction laws (Chen *et al.* 2022; Chen *et al.* 2016; Niemeijer *et al.* 2007) are essential for descriptive modeling of induced seismicity. The parameters of these laws control the areas of contact prone to frictional instabilities (Hunfeld *et al.* 2017). Core loading experiments show the significant role of inelastic deformation observed in seismically active formations (Pijenburg *et al.* 2019), the effect of loading rate (Naderloo *et al.* 2023) and time-dependent deformation on estimated subsidence (Shinohara *et al.* 2022). Core injection experiments demonstrate how frictional response varies under different injection strategies (Hutka *et al.* 2023; Ji *et al.* 2022; Wang *et al.* 2020a). The use of passive and active acoustic monitoring in a laboratory environment can be especially gainful, so it provides insights on earthquake precursors that may improve the prediction of seismicity (Bolton *et al.* 2020).

Although field and laboratory studies contribute to reservoir characterization and understanding of the underlying mechanisms of seismic events, they, by themselves, are not capable to develop a specific operational strategy for the mitigation of induced seismicity or safe field management. In addition to field and laboratory studies, numerical modeling based on reservoir geomechanics and contact mechanics can achieve this. A numerical model constrained to the accumulated field and laboratory data represents a digital twin of the reservoir that can resolve physical processes relevant to the triggering of seismic events.

1.2. Societal Relevance

The increasing attention towards induced seismicity requires a deeper understanding of the mechanisms governing these events, and the potential risks and benefits they entail. Numerical modeling of induced seismicity has become an essential research area, with significant social relevance, primarily due to the need for accurate predictions, early warning systems, and risk assessments associated with human activities in the subsurface.

The risks associated with induced seismicity stem from the potential for surface movement, structural damage, and adverse effects on the environment and human health. These concerns have been documented in several studies that highlight the importance of risk assessment and management for subsurface activities (McGarr *et al.* 2002; van der Voort *et al.* 2015). Induced seismic events, while typically smaller in magnitude than natural earthquakes, can still cause considerable damage

to infrastructure, particularly in densely populated areas or regions with vulnerable structures. Furthermore, induced seismicity can lead to public safety concerns and anxiety, as well as economic losses due to property damage, compensation claims, and reduced property values (van der Voort *et al.* 2015).

These concerns are increased by the growing demand for energy and commodities (International Energy Agency 2022), which has led to increased human activity in the subsurface. The extraction of natural gas, oil, and geothermal energy can offer economic growth, job creation, and increased energy security. However, these benefits must be carefully weighted against the risks posed by the associated induced seismic events.

The role of subsurface energy resources in the green transition further emphasizes the importance of research in the numerical modeling of induced seismicity. Geothermal energy, for example, offers a clean, reliable, and renewable energy source, which can contribute to the global effort to reduce greenhouse gas emissions and mitigate climate change. Additionally, carbon capture and storage technology can help reduce the carbon footprint of fossil fuel-based energy production, thereby complementing the green transition.

To ensure the safe and sustainable utilization of subsurface resources, it is crucial to develop and implement robust regulatory frameworks, best practices, and technological innovations that mitigate the risks of induced seismicity. Numerical modeling of induced seismicity plays a pivotal role in this process, enabling scientists and policymakers to better understand, predict, and manage the risks associated with subsurface activities. Accurate numerical models can help guide the development of effective monitoring networks, as well as inform the design of laboratory experiments that investigate the relationships between stress states, pore pressure variations, and rupture responses in controlled settings.

One prominent example of induced seismicity is the case of the Groningen gas field in the Netherlands (Dost *et al.* 2017). The extraction of natural gas from the field has led to a series of induced earthquakes, causing significant damage to buildings, infrastructure, and the environment. These events have raised public concern and prompted the need for a more stringent management approach to minimize the adverse impacts of induced seismicity (Perlaviciute *et al.* 2017; van der Voort *et al.* 2015). Numerical modeling of induced seismicity in Groningen can provide valuable insights into the relationship between gas extraction activities and seismic events, enabling the development of more effective monitoring and mitigation strategies. Furthermore, this case illustrates the importance of interdisciplinary research and collaboration among geoscientists, engineers, policymakers, and local communities to ensure the safe and sustainable management of subsurface resources.

1.3. Numerical Modeling

The success in reservoir characterization and monitoring of seismic events set the stage for the development of geomechanical models of various complexities (Jansen *et al.* 2022; Novikov *et al.* 2022b; Pampillón *et al.* 2018; Ruan *et al.* 2023; Shokrollahzadeh Behbahani *et al.* 2022b; Van Wees *et al.* 2017; Van Wees

et al. 2019) capable to reproduce the conditions at which seismicity occurs. Numerical modeling, e.g. geostatistical and flow modeling, constrained to field measurements, has been successfully developed and used in reservoir management for decades (Jansen *et al.* 2009; K. Aziz 1979; Michael J. Pyrcz 2014). At the same time, geomechanical modeling, extensively applied in geotechnics and civil engineering, also has been employed in reservoir engineering for the planning of fracking and drilling operations, and wellbore stability analysis (Zoback 2007). Land subsidence, induced seismicity, and the stability of underground storage have attracted additional attention to geomechanical and coupled poromechanical modeling in recent years.

Several studies have been developed in the literature for simulation of geomechanics and induced seismicity. More precisely, Biot's consolidation model has been simulated with a finite difference method using staggered 1D (Gaspar *et al.* 2003) and 2D (Gaspar *et al.* 2006) grids. Galerkin Finite Element Methods (FEM) have been also employed by many researchers to investigate induced seismicity in different geoscience applications (Garipov *et al.* 2019; Garipov *et al.* 2016; Jha *et al.* 2014). Mixed FEM was also extensively developed to allow for more accurate treatment of geomechanics (Arbogast *et al.* 1997; Phillips *et al.* 2007). To enhance convergence properties of the underlying linear systems, weakly-imposed symmetry of the stress tensor in the mixed FEM has been also suggested (Arnold *et al.* 2007) and employed in combination with a multi-point stress approximation (Ambartsumyan *et al.* 2020). Recently, the extended FEM method has been utilized for the fully dynamic modeling of induced rupture propagation (Han *et al.* 2023).

A number of research and community-driven geodynamic codes have been introduced to address the modeling of earthquakes. The finite difference method for the staggered spatially adaptive rectilinear grids has been implemented in GARNET (Pranger 2020). PyLith (Aagaard *et al.* 2022), an open-source FEM code for the quasi-static and fully-dynamic modeling of crustal deformation, earthquakes and volcanoes has recently been extended to poroelastic media (Walker *et al.* 2023). Despite the higher computational cost, Discontinuous Galerkin (DG) methods have become an increasingly popular choice for accurate modeling of both wave propagation and earthquake rupture simulations as they combine the advantages of Finite Volume Methods (FVM) and FEM: flux-based formulation which allows nonlinear interface conditions to be naturally incorporated (Tago *et al.* 2012), provide arbitrary order of accuracy in space and time (Dumbser *et al.* 2006; Wolf *et al.* 2022), support unstructured curvilinear meshes of different topologies (Uphoff *et al.* 2023), and demonstrate low numerical dispersion. The examples of DG-based high-performance codes are SeisSol (Uphoff *et al.* n.d.), Tandem (Uphoff *et al.* 2023), and ExaHyPE (Reinartz *et al.* 2020). The appearance of multiple simulation codes with different underlying numerical schemes has caused the development of community benchmarks including the SCEC/USGS Spontaneous Rupture Code Verification Project (Day *et al.* 2005; Harris *et al.* 2009), and the Sequences of Earthquakes and Aseismic Slip (SEAS) comparison study (Erickson *et al.* 2023; Jiang *et al.* 2022). Realistic earthquake modeling workflows require these computational engines to be optimized for high-performance systems, including the emerging exascale systems

(Folch *et al.* 2023).

Recently, FVM has gained considerable interest in the computational geomechanics community. This is despite the fact that a locally conservative stress field for geomechanics does not seem to be as crucial as the locally conservative mass flux typically required in multiphase flow simulations. Nonetheless, the schemes of FVM are still attractive choices because they respect the balance of fluxes on both local and global scales, admit a seamless integration with the FVM-based fluid dynamics solvers widely used in reservoir engineering, can easily incorporate nonlinearity, and support a wide range of cell topologies. Overshadowed by the success of FEM in structural and soil mechanics, FVM has been developed only over the past three decades (Cardiff *et al.* 2021). Recent literature includes the development of the FVM for geomechanical simulations with both staggered (Deb *et al.* 2017a; Sokolova *et al.* 2019) and collocated grids (Berge *et al.* 2020; Keilegavlen *et al.* 2017a; Nordbotten 2014; Terekhov 2020a; Terekhov *et al.* 2020). In this study, we employ the existing collocated cell-centered FVM for continuous poroelastic media (Terekhov 2020a; Terekhov *et al.* 2020) and extend it to faulted poroelastic media (Novikov *et al.* 2022a; Novikov *et al.* 2022b).

Most of the of FVM-based schemes rely on various flux approximations that determine the consistency, accuracy and stability of the method. In reservoir engineering applications, Two-Point Flux Approximation (TPFA) has been widely recognized as a reasonable trade-off that ensures numerical stability with an acceptable level of accuracy. Even though TPFA loses consistency on non-K-orthogonal grids (Wu *et al.* 2009), the more accurate and consistent alternative, i.e., Multi-Point Flux Approximation (MPFA) (Aavatsmark *et al.* 1996; Edwards *et al.* 1998) introduces numerical stability issues (Aavatsmark *et al.* 2008; Kershaw 1981; Nordbotten *et al.* 2007). A similar form of discretization technique, namely Multi-Point Stress Approximation (MPSA), has been also developed to solve the linear elasticity problem with FVM (Keilegavlen *et al.* 2017b; Martin 2014; Terekhov *et al.* 2020; Tuković *et al.* 2013). Its extension to the coupled poroelasticity problem with a collocated arrangement of unknowns often suffers from the violation of the inf-sup condition and requires additional stabilization (Honório *et al.* 2018; Nordbotten 2016; Terekhov 2021a). One of the possible ways to enhance the numerical stability of FVM is the use of nonlinear schemes which satisfy monotonicity (Nikitin *et al.* 2013; Schneider *et al.* 2018a) or discrete maximum principle (Terekhov *et al.* 2017) at every nonlinear iteration. In this thesis, a novel nonlinear MPFA scheme for the elasticity problem is introduced.

Different numerical approaches have been developed to address the approximation of fluid flow in faults. The Discrete Fracture Model (DFM) (Karimi-Fard *et al.* 2004) allows faults to be resolved explicitly at the interfaces of the grid cells. It respects fault geometry and material contrasts in the vicinity of the fault even on coarse meshes (de Hoop *et al.* 2022). In contrast to DFM, the Embedded Discrete Fracture Model (EDFM) (Li *et al.* 2008) and projection-based EDFM (Tene *et al.* 2017) do not require conformal meshing of faults, hence, independent grids for faults and rock matrix can be employed. A comprehensive review and benchmarking study of these approaches have been conducted (Berre *et al.* 2021).

Both concepts have been successfully applied for mechanics and poromechanics modeling (Berge *et al.* 2020; Deb *et al.* 2017b; Garipov *et al.* 2019; Garipov *et al.* 2016; Terekhov 2020b; Xu *et al.* 2021). In the embedded models, special discontinuity basis functions are used to resolve contact mechanics (Deb *et al.* 2017b; Xu *et al.* 2021) whereas the use of staggered grids (Garipov *et al.* 2019; Garipov *et al.* 2016) allows for natural treatment of the discontinuities within a DFM unstructured mesh. The present study follows the latter approach, where we employ the mixed-dimensional DFM within a cell-centered collocated FVM (Boon *et al.* 2023; Boon *et al.* 2021; Keilegavlen *et al.* 2021). This approach implies the equidimensional DFM to be utilized for the integration of fluid mass fluxes in faults, including the fluxes between fault cells, while the lower-dimensional DFM resolves the momentum fluxes at the contact interfaces at faults.

The simulation of realistic models imposes strict requirements on the performance of numerical frameworks. Some authors (Deb *et al.* 2017b; Garipov *et al.* 2018) use fixed-stress splitting algorithms (Kim *et al.* 2011; Settari *et al.* 1998) to decouple mechanics and flow equations. These are a form of sequential implicit (SI) solution schemes and often lead to more efficient simulations than fully implicit (FI) simulations. However, sequential schemes introduce certain restrictions on time step sizes. On the other hand, FI schemes (Berge *et al.* 2020; Garipov *et al.* 2019; Garipov *et al.* 2016; Garipov *et al.* 2018; Sokolova *et al.* 2019) are unconditionally stable and are often more robust and convenient approaches for the investigation of complex multiphysics problems. FI is often found to outperform the SI approach for coupled thermo-compositional-mechanical simulation (Garipov *et al.* 2018).

Although the FI approach theoretically does not imply restrictions on time step size, practically it requires efficient nonlinear and linear solution strategies for high-resolution models. A preconditioner based on the fixed-stress splitting concept has been developed (White *et al.* 2016). It utilizes a sparse approximation of the Schur complement to obtain a block-preconditioned solution strategy. Later this approach was combined with a constrained pressure residual (CPR) preconditioner to construct a robust and effective solution strategy for coupled multiphase flow and mechanics (White *et al.* 2019). Recently, block-partitioned preconditioners based on the pseudo-Schur complement have been developed for the contact mechanics problem solved with Lagrange multipliers (Ferronato *et al.* 2019; Franceschini *et al.* 2022a; Franceschini *et al.* 2022b). To enhance the performance of the proposed FVM framework, in this work we implement a block-partitioned preconditioner based on a sparse approximation of the Schur complement (White *et al.* 2016).

1.4. Thesis Objectives

In this thesis, we present a FVM-based computational framework for the modeling of fault reactivation. Regarding this topic, the goals of this thesis include

- The development of a fully implicit numerical method for the modeling of fluid mass and momentum balances in faulted porous media. This numerical scheme should be capable of handling arbitrary boundary conditions, heterogeneity, anisotropy, and fluid properties.

- The implementation of an iterative linear solution strategy for the acceleration solution of linear systems stemming from the fully implicit discretization of poroelastic equations.
- The incorporation of a mixed-dimensional conformal DFM into the developed numerical method for the coupled treatment of fluid mass and contact mechanics at faults. The use of the penalty method or the Lagrange method for enforcing the contact mechanics constraints at faults.
- The benchmarking of developed modeling capabilities in a number of tests, including the convergence study, benchmarks against existing analytical and semi-analytical solutions, other modeling frameworks, and laboratory experimental data.
- The validation of the framework against the experiment with injection-induced slip in core crosscuts. The modeling of a large-scale experimental setup with a displaced fault configuration. The evaluation of the possible loading path for the experiment.
- The development of a first-of-its-kind nonlinear stress approximation scheme for elasticity problem. The investigation of its accuracy and the convergence of nonlinear iterations.
- The extension of the framework to the fully dynamic (FD) modeling of rupture propagation. The investigation of nucleation, propagation, and arrest stages of the rupture induced in the displaced fault configuration under slip-weakening friction law.

1.5. Outline of the Thesis

The thesis presents a consecutive description of the theory of fluid mass and momentum transfer in porous faulted rocks, the proposed FVM, their validation in multiple benchmarks, the modeling of experimental frictional setups and the fully dynamic modeling of rupture propagation.

Sec. 2 describes the mathematical representation of faulted porous rocks and the theory of fluid mass and momentum transfer in those rocks. The key constitutive relationships defining the hydromechanical response of poroelastic media are considered. Besides, the contact mechanics including contact constraints are introduced together with friction laws most relevant to porous rocks.

Sec. 3 considers the discrete approximations of the continuous governing equations presented in Sec. 2. First, the FVM with derived multi-point approximations at continuous, contact, and boundary interfaces is described. Second, the inf-sup stabilization for the presented FVM is considered. Third, the derivation of the proposed nonlinear FVM for elasticity problem is presented. Subsequently, the discrete iterative process satisfying contact constraints is described in detail. In the final part of the section, we present the linear solution strategies and the details of implementation.

Sec. 4 includes several benchmarks for the developed FVM with incorporated contact mechanics. We start with the basic testing of FVM in continuous media (Terekhov 2020a; Terekhov *et al.* 2022) revealing its unstable behavior in the limit of undrained conditions. Next, we consider a larger heterogeneous example in the form of SPE10 model where we also check the performance of the implemented linear solution strategy. We compare the results of simulation against two other numerical frameworks for both continuous and faulted media. Then, we provide a detailed consideration of the displaced fault problem with an extensive comparison of the numerical simulation against those of a semi-analytical approach (Jansen *et al.* 2019; Jansen *et al.* 2022). Finally, we perform a few tests of the proposed nonlinear scheme.

Sec. 5 presents the modeling of two laboratory setups: injection-induced slip in a core cross-cut, and a large-scale experimental setup with displaced fault configuration. We perform modeling of the first setup with multiple friction laws and successfully reproduce the measured data. In the second case, we investigate the distribution of fault plane stresses and their sensitivity. As a result, we propose the loading path for the experiment that facilitates the investigation of the initiation and propagation of slippage in a laboratory-scale displaced fault configuration.

Sec. 6 considers the FD approach to the modeling of rupture propagation in order to overcome nonlinear convergence issues. For the displaced fault configuration, we perform the modeling of rupture propagation induced by a remote well and perform a sensitivity study.

Sec. 7 recapitulates the key takeaways from the thesis. It initiates a discussion about the suitability of the developed FVM for the modeling of induced seismicity and considers possible future directions of research.

2

Mechanics of Faulted Saturated Porous Media

Summary

This chapter presents the fundamentals of the mechanics of faulted saturated poroelastic media including the conservation laws and relevant constitutive relationships. Moreover, we present the basics of contact mechanics and the friction laws modeling the frictional response of faults in subsurface. Finally, the system of partial differential equations (PDEs), defining the behavior of quasi-static poroelastic media is presented.

2.1. Main Definitions

A saturated porous medium consists of a solid deformable porous *matrix* and a fluid. It is assumed that the pore space in matrix is connected in a way the fluid can flow through it. The *fluid* represents a mixture of liquids and vapours. In general, the fluid can be multicomponent and multiphase. We define *component* as a chemical substance that comprises a matrix or a fluid. A *phase* is a thermodynamically stable state of a substance distinct from other states of the same substance. For simplicity, we limit our consideration to a single-phase single-component fluid. The macroscale description of such dispersed media relies on *the hypothesis of superimposition of continuous media* (Coussy 2004; Nigmatulin 1978) which implies the existence of all constituents (matrix and fluid phases), each characterized by an independent state of motion, at the same point in space (de Boer 2005). A *representative elementary volume* (REV) or a *material point* is a volume of continuous medium negligibly small for the spatial scale of a problem but sufficiently large compared to the maximum pore size. Macroscale heterogeneities impose an even lower upper bound to REV. Every material point is characterized by its coordinates in three-dimensional space and by time. The way how they are assigned is called *coordinate system*.

Let us denote κ_α a volume of space occupied by medium $\alpha = \{s, f\}$ at time $t = t_0$. We call κ_α an *initial configuration*. The volume of space $\chi(t)$ occupied by all media at time $t > t_0$ is called a *current configuration*. The mapping of material points $\kappa_\alpha \rightarrow \chi(t)$ is called a *deformation* which, under certain assumptions, can be written in the form of *motion law* as (Kondaurov 2007)

$$\mathbf{X}_\alpha = \mathbf{X}_\alpha(\mathbf{x}, t), \quad \mathbf{X}_\alpha \in \kappa_\alpha, \quad \mathbf{x} \in \chi(t), \quad \alpha = \{s, f\}, \quad t > t_0. \quad (2.1)$$

The behaviour of medium α characterized by its properties as the functions of \mathbf{X}_α and time is called a *Lagrangian approach*. In the case these properties are considered to be functions of \mathbf{x} and time it is called *Eulerian approach*.

Note that in most literature (Coussy 2004; Truesdell 1991) the inverse motion law $\mathbf{x} = \mathbf{x}(\mathbf{X}_\alpha, t)$ is used which represents the deformation $\kappa_\alpha \rightarrow \chi(t)$. Although both laws lead to equivalent formulations, the law written in Eq. (2.1) leads us to Eulerian formulation of mechanics that can be more convenient in fluid dynamics and related applications.

If the motion law in Eq. (2.1) is differentiable then we can introduce a *distortion* as

$$\mathbf{G}_\alpha = \nabla \mathbf{X}_\alpha, \quad \alpha = \{s, f\}. \quad (2.2)$$

The velocity \mathbf{v}_α of material point \mathbf{X}_α and the particle change velocity \mathbf{m}_α at point \mathbf{x} are defined as

$$\mathbf{v}_\alpha = \left. \frac{\partial \mathbf{x}(\mathbf{X}_\alpha, t)}{\partial t} \right|_{\mathbf{X}_\alpha}, \quad \mathbf{m}_\alpha = \left. \frac{\partial \mathbf{X}_\alpha(\mathbf{x}, t)}{\partial t} \right|_{\mathbf{x}} = -\mathbf{G}_\alpha \mathbf{v}_\alpha, \quad \alpha = \{s, f\}. \quad (2.3)$$

Polar decomposition applied to the distortion gives

$$\mathbf{G}_\alpha = \mathbf{R}_\alpha \mathbf{U}_\alpha = \mathbf{V}_\alpha \mathbf{R}_\alpha, \quad \alpha = \{s, f\} \quad (2.4)$$

where \mathbf{R}_α is an orthogonal matrix, \mathbf{U}_α and \mathbf{V}_α are symmetric positive-definite matrices. The decomposition in Eq. (2.4) is a mathematical representation of the fact that the deformation can be decomposed into the combination of pure stretch and rotation where \mathbf{U}_α and \mathbf{V}_α characterize stretch, \mathbf{R}_α characterizes rotation.

In the applications, the matrices $\mathbf{C}_\alpha = (\mathbf{G}_\alpha^{-1})^T \mathbf{G}_\alpha^{-1}$ and $\mathbf{B}_\alpha = \mathbf{G}_\alpha^T \mathbf{G}_\alpha$ are used to introduce *Green-Lagrange* \mathbf{A}_α and *Euler-Almansi* \mathbf{E}_α strain tensors (Germain 1973)

$$\mathbf{A}_\alpha = (\mathbf{C}_\alpha - \mathbf{I})/2 = (\mathbf{V}_\alpha^{-2} - \mathbf{I})/2, \quad \alpha = \{s, f\}, \quad (2.5)$$

$$\mathbf{E}_\alpha = (\mathbf{I} - \mathbf{B}_\alpha)/2 = (\mathbf{I} - \mathbf{U}_\alpha^2)/2, \quad \alpha = \{s, f\}, \quad (2.6)$$

where superscript T denotes a transposed matrix. The tensors in Eqs. (2.5) and (2.6) define the measure of deformation.

Let us introduce the *vector of displacements* $\mathbf{u}_\alpha = \mathbf{x} - \mathbf{X}_\alpha$. Then, we have $\mathbf{G}_\alpha = \mathbf{I} - \nabla \mathbf{u}_\alpha$ and the strain tensors defined in Eqs. (2.5) and (2.6) can be rewritten as

$$\mathbf{A}_\alpha = (\nabla_{X_\alpha} \mathbf{u}_\alpha + (\nabla_{X_\alpha} \mathbf{u}_\alpha)^T + \nabla_{X_\alpha} \mathbf{u}_\alpha (\nabla_{X_\alpha} \mathbf{u}_\alpha)^T)/2, \quad \alpha = \{s, f\}, \quad (2.7)$$

$$\mathbf{E}_\alpha = (\nabla \mathbf{u}_\alpha + (\nabla \mathbf{u}_\alpha)^T + \nabla \mathbf{u}_\alpha (\nabla \mathbf{u}_\alpha)^T)/2, \quad \alpha = \{s, f\}, \quad (2.8)$$

where ∇ and ∇_{X_α} denote gradient operator with respect to \mathbf{x} and \mathbf{X}_α respectively. The distortion tensor determines the relation $\nabla = \mathbf{G}_\alpha^T \nabla_{X_\alpha}$ between them.

The quantities \mathbf{G}_α and \mathbf{m}_α are the first derivatives of motion law in Eq. (2.1) with respect to space and time, correspondingly. The assumption of piecewise twice continuous differentiability of Eq. (2.1) requires the *equation of compatibility of deformations and velocities* to be satisfied as

$$\frac{\partial \mathbf{G}_\alpha^T}{\partial t} + \nabla \cdot (\mathbf{G}_\alpha \mathbf{v}_\alpha) = \mathbf{0}, \quad \alpha = \{s, f\}. \quad (2.9)$$

The volume fraction of medium α is defined as a ratio of volume V_α occupied by medium α within volume V of three-dimensional space where all volumes are taken in the current configuration. The volume fraction of fluid $\phi = V_f/V$ is called *porosity*.

The elementary volume dV_{κ_α} transforms to dV_α with deformation $\kappa_\alpha \rightarrow \chi(t)$ as follows

$$dV_\alpha = J_\alpha^{-1} dV_{\kappa_\alpha}, \quad J_\alpha = |\det \mathbf{G}_\alpha|, \quad \alpha = \{s, f\}. \quad (2.10)$$

The *material derivative* with respect to particle \mathbf{X}_α is defined as

$$\frac{d_\alpha}{dt} = \frac{\partial}{\partial t} + \mathbf{v}_\alpha \cdot \nabla. \quad (2.11)$$

2.2. Conservation Laws

Using Eq. (2.10) the conservation of mass of medium α in Lagrange form can be written as

$$\int_{V_\alpha} \rho_{\kappa_\alpha} dV_{\kappa_\alpha} = \int_V \rho_\alpha dV_\alpha + j_\alpha, \quad \alpha = \{s, f\}, \quad (2.12)$$

where ρ_{κ_α} and ρ_α are densities of medium α in the initial and current configurations, respectively, and j_α stands for the sources and sinks of mass and the exchange of mass with other media. The material derivative of Eq. (2.12) gives us the conservation of mass balance in Euler form, i.e.,

$$\int_V \left(\frac{\partial}{\partial t} (\phi_\alpha \rho_\alpha) + \nabla \cdot \phi_\alpha \rho_\alpha \mathbf{v}_\alpha - r_\alpha \right) dV = 0, \quad \alpha = \{s, f\}, \quad (2.13)$$

where r_α is the intensity of the influx of mass in medium α .

In the same manner, one can achieve the conservation of linear momentum for medium α in Euler form

$$\int_V \left(\frac{\partial}{\partial t} (\phi_\alpha \rho_\alpha \mathbf{v}_\alpha) + \nabla \cdot (\phi_\alpha \rho_\alpha \mathbf{v}_\alpha \mathbf{v}_\alpha^T - \phi_\alpha \boldsymbol{\Sigma}_\alpha^T) - \phi_\alpha \rho_\alpha g \nabla z - \mathbf{f}_\alpha^{\text{int}} \right) dV = 0, \quad \alpha = \{s, f\}, \quad (2.14)$$

where $\boldsymbol{\Sigma}_\alpha$ is a Cauchy partial stress tensor of medium α , g is gravitational acceleration, $\mathbf{f}_\alpha^{\text{int}}$ is an interaction force to medium α exerted by other media such that $\mathbf{f}_s^{\text{int}} + \mathbf{f}_f^{\text{int}} = 0$.

The porosity, the partial Cauchy stress tensor and the interaction force can be represented as a sum of two terms (Kondaurov 2007; Nigmatulin 1978; Nikolaevskiy 1996)

$$\phi_\alpha = \phi_\alpha^0 + \phi_\alpha^{\text{dis}}, \quad \mathbf{f}_\alpha^{\text{int}} = \mathbf{f}_\alpha^0 + \mathbf{f}_\alpha^{\text{dis}}, \quad \boldsymbol{\Sigma}_\alpha = \boldsymbol{\Sigma}_\alpha^0 + \boldsymbol{\Sigma}_\alpha^{\text{dis}}, \quad \alpha = \{s, f\}, \quad (2.15)$$

where superscript "0" denotes properties taken in equilibrium, "dis" indicates the dissipative contribution. From Eq. (2.14) one can find that $\mathbf{f}_\alpha^0 = -\boldsymbol{\Sigma}_\alpha^0 \cdot \nabla \phi_\alpha^0$.

The sum of momentum balances in Eq. (2.14) for both media can be written as

$$\int_V \left(\frac{\partial}{\partial t} (\rho \mathbf{v}) + \nabla \cdot (\rho \mathbf{v} \mathbf{v}^T - \boldsymbol{\Sigma}^T) - \rho g \nabla z \right) dV = 0, \quad (2.16)$$

where $\rho \mathbf{v} = \sum_\alpha \phi_\alpha \rho_\alpha \mathbf{v}_\alpha$ is the total momentum, $\rho \mathbf{v} \mathbf{v}^T = \sum_\alpha \phi_\alpha \rho_\alpha \mathbf{v}_\alpha \mathbf{v}_\alpha^T$ represents the total velocity convection, $\boldsymbol{\Sigma} = \sum_\alpha \phi_\alpha \boldsymbol{\Sigma}_\alpha$ is the total Cauchy stress tensor, $\rho = \sum_\alpha \phi_\alpha \rho_\alpha$ is the total mass density.

The conservation of angular momentum is equivalent to the requirement of symmetry of the Cauchy stress tensor (Coussy 2004)

$$\boldsymbol{\Sigma}_\alpha = \boldsymbol{\Sigma}_\alpha^T, \quad \alpha = \{s, f\}, \quad (2.17)$$

The conservation of energy that represents the first law of thermodynamics reads as

$$\int_V \sum_{\alpha=\{s,f\}} \left(\frac{\partial}{\partial t} (\phi_\alpha \rho_\alpha e_\alpha) + \nabla \cdot (\phi_\alpha (\rho_\alpha e_\alpha \mathbf{v}_\alpha - \boldsymbol{\Sigma}_\alpha \mathbf{v}_\alpha)) - \phi_\alpha \rho_\alpha g \nabla z \cdot \mathbf{v}_\alpha \right) dV = 0, \quad (2.18)$$

where the $e_\alpha = U_\alpha + \mathbf{v}_\alpha^T \mathbf{v}_\alpha / 2$ is the specific total energy of medium α , U_α is the specific internal energy of medium α .

2.3. Contact Mechanics

Geologic formations in subsurface may contain *faults* and *fractures*. They introduce discontinuities into a continuous porous medium which require special treatment. For simplicity, below we call these discontinuities faults meaning that they may represent fractures as well.

The formulation of contact mechanics requires stresses and forces attributed to an interface to be defined. The projection of stress tensor Σ to an interface with unit normal vector \mathbf{n} is called *total traction vector* or *traction vector* and defined as

$$\mathbf{f} = -\Sigma\mathbf{n}, \quad (2.19)$$

where the negative sign is motivated by the sign of the corresponding term in the momentum balance. Traction vector can be decomposed into normal f_N and tangential components \mathbf{f}_T as

$$\mathbf{f} = f_N\mathbf{n} + \mathbf{f}_T, \quad f_N = -\mathbf{n}^T\Sigma\mathbf{n}, \quad \mathbf{f}_T = (\mathbf{I} - \mathbf{nn}^T)\mathbf{f}, \quad (2.20)$$

where we call $-f_N$ and $|\mathbf{f}_T|$ as *normal* and *shear* stresses, respectively, \mathbf{I} denotes identity matrix.

Along with total stress tensor, we consider the *effective Terzaghi* Σ' and *effective Biot* Σ'' stress tensors defined as

$$\Sigma' = \Sigma + p\mathbf{I}, \quad \Sigma'' = \Sigma + p\mathbf{B}, \quad (2.21)$$

where p is pore pressure, \mathbf{B} is the rank-two tensor of Biot's coefficients that will be defined in Sec. 2.4.2. Subsequently, *effective Terzaghi* \mathbf{f}' and *effective Biot* \mathbf{f}'' traction vectors can be defined as

$$\mathbf{f}' = -\Sigma'\mathbf{n}, \quad \mathbf{f}'' = -\Sigma''\mathbf{n}. \quad (2.22)$$

At the fault interfaces, we also consider a gap vector \mathbf{g} that is equal to the jump of matrix displacements over the contact as

$$\mathbf{g} = \mathbf{u}_s^+ - \mathbf{u}_s^- \quad (2.23)$$

where superscripts $+$ and $-$ denote different sides of the fault with respect to a reference plane. As for the traction vector, we consider the decomposition of the gap vector into normal g_N and tangential \mathbf{g}_T components as

$$\mathbf{g} = g_N\mathbf{n} + \mathbf{g}_T, \quad g_N = \mathbf{n}^T\mathbf{g}, \quad \mathbf{g}_T = (\mathbf{I} - \mathbf{nn}^T)\mathbf{g}, \quad (2.24)$$

where the absolute value of normal component $|g_N|$ is called *aperture* and the absolute value of tangential component $|\mathbf{g}_T|$ is called *slip*.

Fault segments can be in three different states: *stick*, *slip* and *open* which are defined as follows

$$\begin{cases} f'_N > 0, \\ \Phi < 0, \end{cases} \quad (\text{stick}), \quad (2.25)$$

$$\begin{cases} f'_N > 0, \\ \Phi = 0, \end{cases} \quad (\text{slip}), \quad (2.26)$$

$$f'_N = 0, \quad (\text{open}), \quad (2.27)$$

where Φ denotes a sliding surface (in analogy to yield surface) that defines sliding criterion $\Phi = 0$ (Yastrebov *et al.* 2013). Generally, a sliding surface could depend not only on stresses but also on other parameters, e.g., stress rate, slip, slip rate, and time. The particular form of sliding surface will be introduced in Sec. 2.4.3.

The formulation of contact mechanics includes inequality constraints that could be written separately for normal and tangential projections. Normal constraints are formulated in the form of Hertz-Signorini-Moreau (Seitz *et al.* 2019; Wriggers 2006) conditions as

$$\mathbf{g}_N - \mathbf{g}_N^0 \leq 0, \quad \mathbf{f}_N \geq 0, \quad \mathbf{f}_N (\mathbf{g}_N - \mathbf{g}_N^0) = 0, \quad (2.28)$$

where \mathbf{g}_N^0 represents the initial fault aperture. The tangential constraints can be written in the form of Karush-Kuhn-Tucker conditions (Simo *et al.* 1992; Wriggers 2006) as

$$\Phi \leq 0, \quad \dot{\mathbf{g}}_T = -v \frac{\partial \Phi}{\partial \mathbf{f}_T}, \quad v \geq 0, \quad v\Phi = 0, \quad (2.29)$$

where $\dot{\mathbf{g}}_T$ denotes time derivative of \mathbf{g}_T , v is a non-negative parameter. Eqs. (2.28) represent impenetrability condition, the condition that prohibits tension stress, and complementary conditions respectively. Eqs. (2.29) include a sliding (or slipping) criterion, the condition that defines the direction of sliding, and a complementary condition, respectively. The physical meaning of the complementary condition $v\Phi = 0$ is that it allows a fault segment to be either in slip state $\Phi = 0$ or in stick state $v = 0$.

2.4. Constitutive Relationships

Conservation laws and contact constraints presented above are not sufficient for even a qualitative representation of physical processes as many of their parameters remain undefined. For example, the relationship between stress and strains should be defined based on the rheology of the particular medium which is different for rocks, liquids and vapors (Germain 1973; Sedov 1997; Truesdell 1991). Another example is the interaction force between the constituents of a dispersive medium capable to move past each other. It is also different for gas bubbles in a liquid fluid (Nigmatulin 1978) and for a fluid flowing through porous rocks (de Boer 2005).

2.4.1. Infinitesimal Deformations

The assumption of infinitesimal deformations $|\mathbf{u}_\alpha| \ll 1$, on the one hand, is common and acceptable in many geo-energy-related applications and, on the other hand, it allows constitutive relationships and, as a result, governing equations to be remarkably simplified. Under this assumption, the gradients taken in two configurations become equal $\nabla = \nabla_{X_\alpha}$ and elementary volume transforms by a factor of $J_\alpha = |\det \mathbf{G}_\alpha| = 1 + \nabla \cdot \mathbf{u}_\alpha$. Moreover, in this case \mathbf{B}_α is linearized with respect to $\nabla \mathbf{u}_\alpha$ and the Euler-Almansi strain tensor reduces to the *infinitesimal strain tensor*

$$\mathbf{E}_\alpha = \frac{\nabla \mathbf{u}_\alpha + (\nabla \mathbf{u}_\alpha)^T}{2}. \quad (2.30)$$

We proceed with derivations below under the assumption of infinitesimal deformations.

2.4.2. A Linear Saturated Thermoporoelastic Medium with Viscous Interaction Between Components

An anisotropic linear saturated thermoporoelastic medium is defined by its total stress tensor Σ , porosity ϕ and specific matrix entropy η_s as (Biot 1977; Biot 1941; Cheng 1997; Coussy 2004; Kondaurov 2007)

$$\Sigma - \Sigma^0 = \mathbb{C} : (\mathbf{E}_s - \mathbf{E}_s^0) - (\theta - \theta^0)\mathbf{A} - (p - p^0)\mathbf{B}, \quad (2.31)$$

$$\phi - \phi^0 = \mathbf{B} : (\mathbf{E}_s - \mathbf{E}_s^0) + \alpha_\phi(\theta - \theta^0) + \frac{\psi - \phi^0}{K_s}(p - p^0), \quad (2.32)$$

$$\rho_s^0(\eta_s - \eta_s^0) = \mathbf{A} : (\mathbf{E}_s - \mathbf{E}_s^0) - \frac{\alpha_\phi}{\rho_s^0}(p - p^0) + \frac{c_s \rho_s^0}{\theta^0}(\theta - \theta^0), \quad (2.33)$$

and by dissipative part of the interaction force $\mathbf{f}_\alpha^{\text{dis}}$ and heat conduction vector \mathbf{q}_θ

$$\frac{\mathbf{K}\mathbf{f}_\alpha^{\text{dis}}}{\phi\mu_f} = -\mathbf{w}, \quad (2.34)$$

$$\mathbf{q}_\theta = -\Lambda\nabla\theta, \quad (2.35)$$

where \mathbb{C} is the rank-four stiffness tensor of drained rock, θ is temperature equal for both media, p is pore pressure, \mathbf{A} is the rank-two rock thermal dilation tensor (Coussy 2004), \mathbf{B} is the rank-two Biot's tensor, α_ϕ is the volumetric thermal dilation coefficient related to the porosity (Coussy 2004), $\psi = \text{tr}(\mathbf{B})/3$ denotes the one-third of the trace of \mathbf{B} , K_s is the bulk modulus of rock matrix, c_s is the specific heat capacity of rock matrix, \mathbf{K} is the rank-two permeability tensor, μ_f is the fluid viscosity, $\mathbf{w} = \mathbf{v}_f - \mathbf{v}_s$ is the relative fluid velocity with respect to matrix or *Darcy velocity*, Λ is the rank-two heat conductivity tensor.

Eqs. (2.31)-(2.33) define the response of saturated thermoporoelastic medium to thermomechanical perturbations and the coefficients in Eqs. (2.31)-(2.33) can be defined through the partial derivatives of the thermodynamic potential of the medium around its initial state $(\mathbf{E}_s^0, p^0, \theta^0)$. Eq. (2.34) leads to the Darcy law whereas Eq. (2.35) represents Fourier's law. Both relationships in Eqs. (2.34), (2.35) define fluid and thermal energy dissipation respectively. Tensors \mathbf{K} and Λ can be derived as the second partial derivatives of energy dissipation (Coussy 2004; Kondaurov 2007).

Following the same approach and expanding the free potential energy of fluid around the initial state (ρ_f^0, θ^0) one may derive the constitutive relationships for *slightly compressible fluid*

$$p - p^0 = K_f(\varepsilon_V - \varepsilon_V^0) + \alpha_f(\theta - \theta^0), \quad \eta_f - \eta_f^0 = -\frac{\alpha_f}{\rho_f^0}(\varepsilon_V - \varepsilon_V^0) - \frac{c_f}{\theta^0}(\theta - \theta^0), \quad (2.36)$$

and for *ideal gas* with constant heat capacity c_f

$$p = \frac{\rho_f}{M_f} R \theta, \quad \eta_f - \eta_f^0 = c_f \ln \frac{\theta}{\theta^0} + R \ln \frac{V_f}{V_f^0}, \quad (2.37)$$

where K_f is the fluid bulk modulus, ε_V is the fluid volumetric strain, α_f is the fluid thermal dilation (expansion) coefficient, M_f is the fluid molar mass, R is the universal gas constant, V_f is the volume that fluid occupies.

2.4.3. Sliding Criterion and Friction Laws

The Mohr-Coulomb potential represents a widely accepted failure criterion that provides accurate predictions in a variety of applications, and, especially, in rock and soil mechanics (Labuz *et al.* 2012; Wang 2017). We use the Mohr-Coulomb failure potential for a sliding surface as

$$\Phi = |\mathbf{f}_T| - \mu f_N - c, \quad (2.38)$$

where μ is friction coefficient, c is contact cohesion. These macroscale parameters characterize contact roughness, size and a number of asperities and can be obtained from frictional experiments under rock faults. For many types of rock materials cohesion can be taken equal to zero. In contrast, the friction coefficient may significantly vary for different materials and stress states. In the latter case, the dependence of friction coefficient on the stress state is called *friction law*.

The simplest form of friction law is expressed by a *static friction law* as

$$\mu = \mu_s, \quad (2.39)$$

where μ_s denotes a static friction coefficient (or factor) that may vary over the fault but remains fixed over time.

It was found that the friction coefficient may depend on the accumulated slip. In this case, the linear slip-dependent model can be written as

$$\mu = \begin{cases} \mu_s + \frac{\mu_d - \mu_s}{D_c} |\mathbf{g}_T|, & |\mathbf{g}_T| < D_c, \\ \mu_d, & |\mathbf{g}_T| \geq D_c, \end{cases} \quad (2.40)$$

where μ_d is a dynamic friction coefficient (or factor). If $\mu_d - \mu_s > 0$ then the friction mechanism is *slip-strengthening*. In the case of $\mu_d - \mu_s < 0$ the sliding demonstrates *slip-weakening* behavior. The latter can potentially cause seismicity.

The friction coefficient can exhibit the relation to slip rate $|\dot{\mathbf{g}}_T|$ which can be accounted by the following equation

$$\mu = \mu^* + (a - b) \ln \left(\frac{|\dot{\mathbf{g}}_T|}{v^*} \right), \quad (2.41)$$

where μ^* is a reference friction coefficient, v^* is a reference slip velocity, a and b are empirical constants.

Both slip and slip rate effect on friction coefficient are combined in *rate-and-state friction (RSF) law* (Dieterich 1979; Ruina 1983) that can be written as

$$\mu = \mu^* + a \ln \frac{|\dot{\mathbf{g}}_T|}{v^*} + b \ln \frac{v^* \theta}{D_c}, \quad (2.42)$$

where θ is a state parameter governed by either of the following laws

$$\frac{d\theta}{dt} = 1 - \frac{|\dot{\mathbf{g}}_T| \theta}{D_c}, \quad (\text{ageing law}), \quad (2.43)$$

$$\frac{d\theta}{dt} = -\frac{|\dot{\mathbf{g}}_T| \theta}{D_c} \ln \frac{|\dot{\mathbf{g}}_T| \theta}{D_c}, \quad |\dot{\mathbf{g}}_T| \neq 0 \quad (\text{slip law}), \quad (2.44)$$

where (2.44) turns into (2.43) when $|\dot{\mathbf{g}}_T| \approx v^*$. When the state parameter becomes constant over time $\theta \approx D_c/v^*$, Eq. (2.42) reduces to Eq. (2.41). Thus, Eq. (2.41) is sometimes called *steady-state RSF law*.

RSF model in Eq. (2.42) becomes inconsistent in the limit of $|\dot{\mathbf{g}}_T| \rightarrow 0$. The version of Dieterich-Ruina RSF law stabilized in this limit can be written in the following form (Lapusta et al. 2000; Rice et al. 2001)

$$\mu = a \sinh^{-1} \left(\frac{|\dot{\mathbf{g}}_T|}{2v^*} \exp \left(\frac{\mu^* + b \log(v^* \theta / D_c)}{a} \right) \right). \quad (2.45)$$

2.5. Governing Equations for This Thesis Study

Conservation laws in Eqs. (2.13), (2.14), (2.17), (2.18) and contact constraints in Eqs. (2.25)-(2.29) represent the thermomechanical response of a wide range of materials. In contrast, constitutive relationships determine the behavior of specific material for a specific range of states. In particular, Eqs. (2.30), (2.31)-(2.37) and Eqs. (2.38)-(2.45) define the behavior of a thermoporoelastic material saturated by a single-phase liquid or gaseous fluid and friction contact with a Coulomb sliding criterion. This formulation of mechanics has been found efficient since it is flexible with respect to the change of constitutive relationships.

At the same time, the governing equation for a particular application can be significantly simplified. For example, the typical value of relative fluid velocity with respect to matrix ($w < 10^{-4} \text{ m s}^{-1}$) is remarkably smaller than the speed of elastic waves ($v_s \sim 10^3 \text{ m s}^{-1}$). In many applications, it allows either fluid mass balance or matrix mass balance to be excluded from consideration. Due to the same reason the term proportional to $\mathbf{v}_f \mathbf{v}_f^T$ in the momentum balance for fluid is also omitted in many reservoir engineering applications. This difference between the velocities leads to two classes of models working in the limits of short and long timescales.

Fully dynamic models are working in a short timescale that is suitable to resolve the initiation and propagation of elastic waves. In this case, only the sum of momentum balances in Eq. (2.16) can be considered. Mass and energy balances are usually excluded from consideration as poroelastic and thermoporoelastic effects

may have a negligible influence on momentum balance at this timescale. These kinds of models are extensively used for seismic interpretation, the investigation of rupture propagation, and the monitoring of induced seismicity.

The focus of this work is *quasi-static models* that are working in a long timescale. In this case, the inertia and velocity convection (first two terms) can be omitted in Eq. (2.16) which reduces the equation to stationary momentum balance. As mentioned above, only fluid mass balance can be taken into account which is usually formulated with the help of the Darcy velocity \mathbf{w} leaving the matrix velocity term out of consideration in this timescale. Besides, in this work, we consider an *isothermal processes* that let us disregard the energy balance in Eq. (2.18) and the influence of temperature on hydromechanical response in Eqs. (2.31), (2.32). Accumulating all aforementioned simplifications the conservation laws can be rewritten as

$$\int_V \left(\frac{\partial}{\partial t} (\phi \rho_f) + \nabla \cdot \rho_f \mathbf{w} - r_f \right) dV = 0, \quad (2.46)$$

$$- \int_V (\nabla \cdot \boldsymbol{\Sigma} + \rho g \nabla z) dV = 0, \quad (2.47)$$

subjected to the following constraints

$$\boldsymbol{\Sigma} - \boldsymbol{\Sigma}^0 = \mathbb{C} : (\mathbf{E} - \mathbf{E}^0) - (p - p^0) \mathbf{B}, \quad (2.48)$$

$$\phi - \phi^0 = \mathbf{B} : (\mathbf{E} - \mathbf{E}^0) + \frac{\psi - \phi^0}{K_s} (p - p^0), \quad (2.49)$$

$$\mathbf{E} = \frac{\nabla \mathbf{u} + (\nabla \mathbf{u})^T}{2}, \quad (2.50)$$

$$\mathbf{w} = -\frac{\mathbf{K}}{\mu_f} (\nabla p - \rho_f g \nabla z), \quad (2.51)$$

$$\rho_f = \rho_f(p), \quad \mu_f = \mu_f(p), \quad (2.52)$$

$$\rho = \phi \rho_f + (1 - \phi) \rho_s, \quad (2.53)$$

where $\mathbf{E} = \mathbf{E}_s$ represents a matrix strain tensor according to Eq. (2.50), Darcy velocity \mathbf{w} is derived from Eq. (2.34) and stationary fluid momentum balance, Eq. (2.52) represents an arbitrary relation suitable for both liquid and gaseous fluids, Eq. (2.53) defines the total density of saturated porous medium. Furthermore, in isotropic media we define a stiffness tensor \mathbb{C} by either Young's modulus E and Poisson's ratio ν or Lamé's parameters λ and G as

$$\mathbb{C} = \lambda \mathbf{I} \otimes_{\text{outer}} \mathbf{I} + 2G \mathbf{1}, \quad \lambda = \frac{E\nu}{(1+\nu)(1-2\nu)}, \quad G = \frac{E}{2(1+\nu)}, \quad (2.54)$$

where \otimes_{outer} denotes outer product, $\mathbf{1}$ stands for the symmetric part of the rank-four identity tensor, which transforms rank-two tensors as $\mathbf{1} : \mathbf{E} = (\mathbf{E} + \mathbf{E}^T)/2$.

Boundary conditions for the system of Eqs. (2.46)-(2.53) can be written as

$$\begin{cases} \mathbf{n}^T (a_n \mathbf{u}_b - b_n \mathbf{f}'_b) = r_n, \\ (\mathbf{I} - \mathbf{n}\mathbf{n}^T) (a_t \mathbf{u}_b - b_t \mathbf{f}'_b) = \mathbf{r}_t, \\ a_p p_b - b_p \mathbf{n}^T \mathbf{w} = r_p, \end{cases} \quad (2.55)$$

where \mathbf{f}'_b , \mathbf{u}_b , and p_b are effective traction, matrix displacement, and pore pressure at the boundary, respectively. In addition, $a_n, b_n, a_t, b_t, a_p, b_p$ are coefficients that determine the magnitude of their corresponding boundary conditions, while r_n, \mathbf{r}_t, r_p are the corresponding condition values. All these constants are allowed to be time-dependent.

Eqs. (2.46)-(2.53) represent the system of equations with respect to unknown displacement vector and pressure. Therefore, the following initial conditions can be applied

$$\mathbf{u} = \mathbf{u}^0(x, y, z), \quad p = p^0(x, y, z). \quad (2.56)$$

3

Finite Volume Framework for Modeling of Induced Fault Slip

Summary

The mathematical models of faulted saturated poroelastic media discussed in the previous chapter require numerical consideration. In this chapter, we present recently proposed numerical schemes of Finite Volume Method (FVM) for the integration of those models. We extend those schemes for the support of discontinuities exhibited at faults and fractures. A mixed-dimensional fault representation is employed for the incorporation of fluid mass and momentum transfer in faults. Contact constraints are satisfied with the use of the penalty method and the return-mapping algorithm. The efficient solution of linear systems is enabled by the implementation of a block-partitioned preconditioning strategy. Moreover, we propose a novel nonlinear FVM scheme for the solving pure elasticity problems. Finally, the details of implementation are presented.

3.1. Finite Volume Method

Let us consider the system of partial differential equations (PDEs) of the following conservative form

$$\frac{\partial \mathbf{a}}{\partial t} + \nabla \cdot \mathfrak{F} = \mathbf{r}, \quad (3.1)$$

where \mathbf{a} , \mathbf{r} are vectors, \mathfrak{F} is a matrix. In the case of

$$\mathbf{a} = [\phi \rho_f], \quad \mathfrak{F} = [\rho_f \mathbf{w}], \quad (3.2)$$

Eq. (3.1) represents the conservation of fluid mass in a porous medium, and ϕ is porosity, ρ_f is fluid density, \mathbf{w} is fluid velocity with respect to the porous matrix. In the case of

$$\mathbf{a} = [\phi \rho_f U_f + (1 - \phi) \rho_s U_s], \quad \mathfrak{F} = [\rho_f h_f \mathbf{w} - \Lambda \nabla \theta], \quad (3.3)$$

Eq. (3.1) represents the conservation of energy in a saturated porous medium, and ρ_s is rock density, U_f and U_r are fluid and rock internal energies respectively, h_f is fluid enthalpy, Λ is the heat conductivity tensor, and θ is temperature. In the case of

$$\mathbf{a} = \rho \frac{\partial \mathbf{u}}{\partial t}, \quad \mathfrak{F} = -\Sigma, \quad (3.4)$$

Eq. (3.1) represents the fully dynamic momentum balance, where ρ is total density, \mathbf{u} is displacement, Σ is the Cauchy stress tensor. In the case of $\mathbf{a} = \mathbf{0}$, Eq. (3.4) simplifies to a stationary momentum balance.

The conservation laws represented by Eq. (3.1) can be written in integral form and discretized with the FVM (Kloforn *et al.* 2020; LeVeque 2002; Vassilevski *et al.* 2020). This implies the representation of integrals of divergence term $\nabla \cdot \mathfrak{F}$ as the fluxes $\mathbf{q} = \mathfrak{F} \mathbf{n}$ over cell interfaces with the help of Gauss formula as

$$\int_{V_i} \left(\frac{\partial \mathbf{a}}{\partial t} + \nabla \cdot \mathfrak{F} \right) dV = \int_{V_i} \frac{\partial \mathbf{a}}{\partial t} dV + \sum_{\beta \in \partial V_i} \int_{\beta} \mathbf{q} dS \approx \frac{\mathbf{a}_i^{n+1} - \mathbf{a}_i^n}{\Delta t} V_i + \sum_{\beta \in \partial V_i} \delta_{\beta} \mathbf{q}_{ij} = \mathbf{r} V_i, \quad (3.5)$$

where subscript i denotes the values defined at cell i and subscript ij means that the value is evaluated at the interface between cells i and j , superscripts n and $n + 1$ define variables taken at a previous and current time step respectively, Δt is a time step, V_i is a cell volume and δ_j is an area of the interface between neighboring cells. The backward Euler scheme is used here for time integration.

It is worth to be mentioned that the assumption of $\mathbf{a} = \mathbf{0}$ in Eqs. (3.2), (3.4) leads to elliptic PDEs with respect to the unknown pressure p and the vector of displacements \mathbf{u} , correspondingly. Eq. (3.3) includes both convective and conductive heat transport so that in the case $\mathbf{a} = \mathbf{0}$ it is close to an elliptic PDE for Peclet numbers (ratio between advective and conductive transport rates) close to zero.

Eqs. (3.2)-(3.4) and their extension to compositional fluid flow, transport and coupled poromechanics are extensively used in reservoir modelling (Chen 2007; K. Aziz 1979; Zoback 2007). Robust solution of these equations requires reliable numerical schemes capable to handle severe heterogeneity, arbitrary material anisotropy and advanced gridding techniques. Moreover, consistent numerical

schemes must preserve local conservation of fluid mass to guarantee the proper solution of transport problems (Rivière 2008). FVM schemes can fit these requirements. They are both locally and globally conservative and can be used to resolve highly heterogeneous anisotropic media with arbitrary star-shaped polyhedral meshes (Vassilevski *et al.* 2020).

3.2. Finite Volume Method for Poroelasticity

The fluid mass and momentum balance in Eqs. (2.46) and (2.49) govern the hydromechanical behavior of poroelastic media. Let us start by rewriting Eq. (3.5) for a single-phase fluid mass balance in a poroelastic media as

$$\begin{aligned}
0 &= \int_{V_i} \left(\frac{\partial}{\partial t} (\phi \rho_f) + \nabla \cdot \rho_f \mathbf{w} - r_f \right) dV = \\
&= \int_{V_i} \left(\frac{\partial}{\partial t} (\tilde{\phi} \rho_f) - r_f \right) dV + \int_{V_i} \left[\nabla \cdot \rho_f \mathbf{w} + \frac{\partial}{\partial t} (\rho_f \nabla \cdot \mathbf{B} (\mathbf{u} - \mathbf{u}^0) - \rho_f (\mathbf{u} - \mathbf{u}^0) \cdot (\nabla \cdot \mathbf{B})) \right] dV \approx \\
&\quad \approx \int_{V_i} \left(\frac{\partial}{\partial t} (\tilde{\phi} \rho_f) - r_f \right) dV + \\
&\quad + \int_{\partial V_i} \rho_f \mathbf{w}^T \mathbf{n} dS + \frac{\partial}{\partial t} \left(\rho_{f,i} \left[\int_{\partial V_i} (\mathbf{u} - \mathbf{u}^0)^T \mathbf{B} \mathbf{n} dS - (\mathbf{u}_i - \mathbf{u}^0)^T \int_{\partial V_i} \mathbf{B} \mathbf{n} dS \right] \right) \approx \\
&\quad \approx V_i \left(\frac{(\tilde{\phi} \rho_f)_i^{n+1} - (\tilde{\phi} \rho_f)_i^n}{\Delta t_n} - r_{f,i}^{n+1} \right) + \\
&\quad + \sum_{\beta \in \partial V_i} \delta_\beta \left[(\rho_f \mathbf{w}^T \mathbf{n})_\beta^{n+1} + \frac{\rho_{f,i}^{n+1} (\mathbf{u}_\beta - \mathbf{u}_i)^{n+1} - \rho_{f,i}^n (\mathbf{u}_\beta - \mathbf{u}_i)^n}{\Delta t_n} \cdot (\mathbf{B} \mathbf{n})_\beta \right] \quad (3.6)
\end{aligned}$$

where porosity was decomposed as

$$\phi = \tilde{\phi} + \mathbf{B} : (\mathbf{E} - \mathbf{E}^0) = \tilde{\phi} + \mathbf{B} : \nabla (\mathbf{u} - \mathbf{u}^0) = \tilde{\phi} + \nabla \cdot \mathbf{B} (\mathbf{u} - \mathbf{u}^0) - (\mathbf{u} - \mathbf{u}^0) \cdot \nabla \cdot \mathbf{B}, \quad (3.7)$$

$$\tilde{\phi} = \phi^0 + \frac{\psi - \phi^0}{K_s}, \quad (3.8)$$

with implied symmetry of the Biot tensor \mathbf{B} . Besides, the following approximations of integrals are used

$$\rho_{f,i} = \rho_f(p_i), \quad p_i = \frac{1}{V_i} \int_{V_i} p dV, \quad \mathbf{u}_i = \frac{1}{V_i} \int_{V_i} \mathbf{u} dV, \quad (3.9)$$

$$(\rho_f \mathbf{w}^T \mathbf{n})_\beta = \frac{1}{\delta_\beta} \int_\beta \rho_f \mathbf{w}^T \mathbf{n} dS, \quad \mathbf{u}_\beta^T (\mathbf{Bn})_\beta = \frac{1}{\delta_\beta} \int_\beta \mathbf{u}^T \mathbf{Bn} dS, \quad (\mathbf{Bn})_\beta = \frac{1}{\delta_\beta} \int_\beta \mathbf{Bn} dS. \quad (3.10)$$

Let us introduce the following notations:

$$q_{i,\beta} = (\mathbf{w}^T \mathbf{n})_\beta, \quad \tilde{q}_\beta = (\mathbf{u}_\beta - \mathbf{u}_i) \cdot (\mathbf{Bn})_\beta, \quad (3.11)$$

where q_i denotes the *Darcy flux*. Using Eq. (3.11) we can define the residual $H_{f,i}^{n+1}$ of Eq. (3.6) as

$$H_{f,i}^{n+1} = V_i \left(\frac{(\tilde{\phi} \rho_f)_i^{n+1} - (\tilde{\phi} \rho_f)_i^n}{\Delta t_n} - r_{i,i}^{n+1} \right) + \sum_{\beta \in \partial V_i} \delta_\beta \left[(\rho_f q_f)_\beta^{n+1} + \frac{\rho_{f,i}^{n+1} \tilde{q}_\beta^{n+1} - \rho_{f,i}^n \tilde{q}_\beta^n}{\Delta t_n} \right], \quad (3.12)$$

We obtain a discrete fluid mass balance in Eq. (3.12) that consists of two terms. The first term, called the *accumulation* term, represents the change of fluid mass in cell V_i due to pressure changes and sources (sinks). We use the backward Euler method for time integration of this term so that its discrete approximation is provided. The second term in Eq. (3.12), called the *flux term*, is responsible for the exchange of fluid mass with other cells that can be caused by a pressure gradient, gravity, or matrix movement. The conservation of fluid mass during this exchange is governed by the approximation of the flux term that will be considered in the next section.

The FVM can be applied to the stationary momentum balance in Eq. (2.47) subject to Eq. (2.48). The associated residual vector $\mathbf{H}_{s,i}^{n+1}$ can be written as

$$\mathbf{H}_{s,i}^{n+1} = -\rho_i^{n+1} V_i g \nabla z + \sum_{\beta \in \partial V_i} \delta_\beta \mathbf{f}_\beta^{n+1}, \quad (3.13)$$

where the total traction vector is to be found at the interface β as

$$\mathbf{f}_\beta = - \left(\mathbb{C} : \frac{\nabla \mathbf{u} + (\nabla \mathbf{u})^T}{2} - p \mathbf{B} \right)_\beta \cdot \mathbf{n}_\beta, \quad (3.14)$$

and the approximation of porosity is derived from Eqs. (3.7) as

$$\phi_i = \tilde{\phi}_i + \frac{1}{V_i} \sum_{\beta \in \partial V_i} \delta_\beta (\tilde{q}_\beta - \tilde{q}_\beta^0), \quad (3.15)$$

where the approximations from Eq. (3.10) are used.

The gravity force constitutes the accumulation term in the discrete momentum balance in Eq. (3.13) while its flux term is represented by the traction vector. Both terms require accurate approximations at all interfaces in a computational grid.

3.3. Approximation of Fluxes

The complete discrete formulation of the conservation laws in Eqs. (3.12) and (3.13) necessitates the approximation of q_f , \tilde{q} , \mathbf{f} at every interface of the computational grid. Below we derive the approximations of these terms provided for interior interfaces without contact, interior contact interfaces and boundary interfaces from the corresponding balance laws imposed locally. The goal of this section is to present the extension of coupled multi-point flux and multi-point stress approximations (Terekhov 2020a) to the interior contact interfaces.

3.3.1. Approximations at Interior Continuous Interface

The conservation laws in Eqs. (3.12) and (3.13) are formulated with respect to the vector of unknowns $\mathbf{d} = [\mathbf{u}^T p]^T$. By imposing the continuity of the unknowns and the continuity of fluid fluxes defined in Eq. (3.11) and the tractions defined in Eq. (3.14) between neighboring cells 1 and 2 (Terekhov et al. 2020), one obtains a *local problem* as

$$\mathbf{d}_{\beta 1} = \mathbf{d}_1 + [\mathbf{I} \otimes (\mathbf{x}_\beta - \mathbf{x}_1)^T] (\nabla \otimes \mathbf{d}_1) = \mathbf{d}_2 + [\mathbf{I} \otimes (\mathbf{x}_\beta - \mathbf{x}_2)^T] (\nabla \otimes \mathbf{d}_2) = \mathbf{d}_{\beta 2} \quad (3.16)$$

$$- [\mathbf{I} \otimes \mathbf{n}^T] \mathbf{S}_1 (\nabla \otimes \mathbf{u}_1) + p_{\beta 1} \mathbf{B}_1 \mathbf{n} = - [\mathbf{I} \otimes \mathbf{n}^T] \mathbf{S}_2 (\nabla \otimes \mathbf{u}_2) + p_{\beta 2} \mathbf{B}_2 \mathbf{n}, \quad (3.17)$$

$$- (\nabla p_1 - \rho_i g \nabla z) \cdot \mathbf{K}_1 \mathbf{n} = - (\nabla p_2 - \rho_i g \nabla z) \cdot \mathbf{K}_2 \mathbf{n}, \quad (3.18)$$

where \mathbf{d}_1 and \mathbf{d}_2 are unknowns at the cell centers, \mathbf{x}_1 and \mathbf{x}_2 are the positions of the cell centers, \otimes denotes the Kronecker product, \mathbf{x}_β denotes the center of the interface, $\mathbf{I} \otimes (\mathbf{x}_\beta - \mathbf{x}_1)^T$ and $\mathbf{I} \otimes (\mathbf{x}_\beta - \mathbf{x}_2)^T$ represent 4×12 matrices constructed as

$$\mathbf{I} \otimes (\mathbf{x}_\beta - \mathbf{x}_i)^T = \begin{pmatrix} (\mathbf{x}_\beta - \mathbf{x}_i)^T & & & \\ & (\mathbf{x}_\beta - \mathbf{x}_i)^T & & \\ & & (\mathbf{x}_\beta - \mathbf{x}_i)^T & \\ & & & (\mathbf{x}_\beta - \mathbf{x}_i)^T \end{pmatrix}, \quad i = 1, 2,$$

$\mathbf{I} \otimes \mathbf{n}^T$ stands for 3×9 matrix constructed in a similar way, $\nabla \otimes \mathbf{d}_1$, $\nabla \otimes \mathbf{d}_2$ and $\nabla \otimes \mathbf{u}_1$, $\nabla \otimes \mathbf{u}_2$ are 12×1 and 9×1 vectors respectively, constructed as

$$\nabla \otimes \mathbf{d}_i = \begin{pmatrix} \nabla \otimes \mathbf{u}_i \\ \nabla p_i \end{pmatrix} = \begin{pmatrix} \nabla u_{ix} \\ \nabla u_{iy} \\ \nabla u_{iz} \\ \nabla p_i \end{pmatrix}, \quad i = 1, 2, \quad (3.19)$$

where $[u_{ix} u_{iy} u_{iz}]^T$ are the components of displacement vector \mathbf{u}_i , $\mathbf{S}_1 = \mathbf{Y} \mathbf{C}_1 \mathbf{Y}^T$, $\mathbf{S}_2 = \mathbf{Y} \mathbf{C}_2 \mathbf{Y}^T$ are 9×9 matrices where \mathbf{C} denotes a 6×6 symmetric stiffness matrix in

Voigt notation and where

$$\mathbf{Y}^T = \begin{bmatrix} 1 & 0 & 0 & 0 & 0 & 0 & 0 & 0 & 0 \\ 0 & 0 & 0 & 0 & 1 & 0 & 0 & 0 & 0 \\ 0 & 0 & 0 & 0 & 0 & 0 & 0 & 0 & 1 \\ 0 & 0 & 0 & 0 & 0 & 1 & 0 & 1 & 0 \\ 0 & 0 & 1 & 0 & 0 & 0 & 1 & 0 & 0 \\ 0 & 1 & 0 & 1 & 0 & 0 & 0 & 0 & 0 \end{bmatrix}.$$

Flux balances in Eqs. (3.17) and (3.18) stem from the flux terms of the discrete conservation laws in Eqs. (3.12) and (3.13), respectively. In Eq. (3.18), we neglect the fluid mass flux caused by matrix movement.

The following decompositions

$$\nabla \otimes \mathbf{d}_i = [\mathbf{I} \otimes \mathbf{n}] \xi_i + \xi_{\tau i}, \quad \xi_i = [\mathbf{I} \otimes \mathbf{n}^T] [\nabla \otimes \mathbf{d}_i], \quad \xi_{\tau i} = [\mathbf{I} \otimes (\mathbf{I} - \mathbf{nn}^T)] [\nabla \otimes \mathbf{d}_i], \quad (3.20)$$

$$[\mathbf{I} \otimes \mathbf{n}^T] \mathbf{S}_i = \mathbf{T}_i [\mathbf{I} \otimes \mathbf{n}^T] + \Gamma_i, \quad \mathbf{T}_i = [\mathbf{I} \otimes \mathbf{n}^T] \mathbf{S}_i [\mathbf{I} \otimes \mathbf{n}], \quad \Gamma_i = [\mathbf{I} \otimes \mathbf{n}^T] \mathbf{S}_i [\mathbf{I} \otimes (\mathbf{I} - \mathbf{nn}^T)], \quad (3.21)$$

$$\mathbf{K}_i \mathbf{n} = \kappa_i \mathbf{n} + \boldsymbol{\kappa}_i, \quad \kappa_i = \mathbf{n}^T \mathbf{K}_i \mathbf{n}, \quad \boldsymbol{\kappa}_i = (\mathbf{I} - \mathbf{nn}^T) \mathbf{K}_i \mathbf{n}, \quad (3.22)$$

$$\begin{aligned} \mathbf{x}_\beta - \mathbf{x}_1 &= d_1 \mathbf{n} + (\mathbf{x}_\beta - \mathbf{y}_1), & d_1 &= \mathbf{n} \cdot (\mathbf{x}_\beta - \mathbf{x}_1) > 0, & \mathbf{y}_1 &= \mathbf{x}_1 + d_1 \mathbf{n}, \\ \mathbf{x}_2 - \mathbf{x}_\beta &= d_2 \mathbf{n} + (\mathbf{y}_2 - \mathbf{x}_\beta), & d_2 &= \mathbf{n} \cdot (\mathbf{x}_2 - \mathbf{x}_\beta) > 0, & \mathbf{y}_2 &= \mathbf{x}_2 - d_2 \mathbf{n}, \end{aligned} \quad (3.23)$$

are used, where the subscripts $i = 1, 2$ refer to the cells neighboring an interface, d_1 and d_2 are distances between the cell centers and the interface, \mathbf{y}_1 and \mathbf{y}_2 are projections of the cell centers on the interface, \mathbf{T}_1 and \mathbf{T}_2 are 3×3 matrices, Γ_1 and Γ_2 are 3×9 matrices, while scalars κ_1 and κ_2 and vectors $\boldsymbol{\kappa}_1$ and $\boldsymbol{\kappa}_2$ provide co-normal decompositions of \mathbf{K}_1 and \mathbf{K}_2 . The 4×1 vectors ξ_1 and ξ_2 , and the 12×1 vectors $\xi_{\tau 1}$ and $\xi_{\tau 2}$ represent normal and tangential projections respectively of the gradients of the unknowns. The decomposition of distances in Eq. (3.23) is shown in Fig. 3.1.

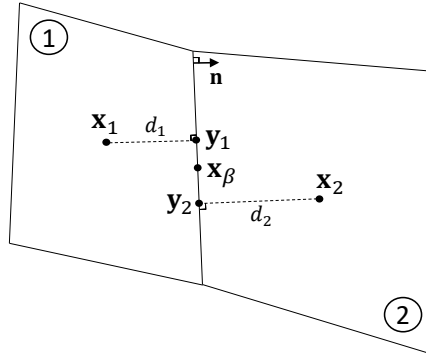


Figure 3.1.: Normal decomposition of distances between the centers of cells 1, 2 and the center of interface β .

Using the notation introduced above, the continuity of fluxes, represented in Eqs. (3.17) and (3.18), can be written in the coupled form of

$$\mathbf{A}_1 \mathbf{d}_1 + \mathbf{Q}_1 \xi_1 + \boldsymbol{\theta}_1 \xi_{\tau 1} + \zeta_1 = \mathbf{A}_2 \mathbf{d}_2 + \mathbf{Q}_2 \xi_2 + \boldsymbol{\theta}_2 \xi_{\tau 2} + \zeta_2, \quad (3.24)$$

where

$$\mathbf{A}_i = \begin{bmatrix} \mathbf{0} & \mathbf{B}_i \mathbf{n} \\ \mathbf{0} & \mathbf{0} \end{bmatrix}, \quad \mathbf{Q}_i = \begin{bmatrix} -\mathbf{T}_i & \\ & -\kappa_i \end{bmatrix} \pm d_i \mathbf{A}_i, \quad (3.25)$$

$$\boldsymbol{\theta}_i = \begin{bmatrix} -\Gamma_i & \\ & -\boldsymbol{\kappa}_i^T \end{bmatrix} + \mathbf{A}_i \otimes (\mathbf{x}_\beta - \mathbf{y}_i)^T, \quad \boldsymbol{\zeta} = \begin{bmatrix} \mathbf{0} \\ \rho_f g \nabla z \cdot \mathbf{K}_i \mathbf{n} \end{bmatrix}, \quad (3.26)$$

Here \mathbf{A}_i and \mathbf{Q}_i are 4×4 matrices, $\boldsymbol{\theta}_i$ is a 4×12 matrix and $\boldsymbol{\zeta}_i$ is a 4×1 vector and “ \pm ” in \mathbf{Q}_i corresponds to $i = 1, 2$ respectively.

According to Eq. (3.16) the tangential projections of the gradients are $\xi_{\tau 1} = \xi_{\tau 2} = \xi_\tau$. Deriving ξ_2 from Eq. (3.16) and substituting the result into Eq. (3.24) we obtain the following expression for ξ_1 :

$$\begin{aligned} & (d_1 \mathbf{Q}_2 + d_2 \mathbf{Q}_1) \xi_1 = \\ & = (d_2 \mathbf{A}_2 + \mathbf{Q}_2) \mathbf{d}_2 - (d_2 \mathbf{A}_1 + \mathbf{Q}_2) \mathbf{d}_1 + (\mathbf{Q}_2 \otimes (\mathbf{y}_1 - \mathbf{y}_2)^T + d_2 (\boldsymbol{\theta}_2 - \boldsymbol{\theta}_1)) \xi_\tau + d_2 (\boldsymbol{\zeta}_2 - \boldsymbol{\zeta}_1). \end{aligned} \quad (3.27)$$

Substituting Eq. (3.27) into the left-hand side of Eq. (3.24), one obtains the multi-point approximation for the Darcy flux $q_{f,\beta}$ defined in Eq. (3.11) and the traction \mathbf{f}_β , as given in Eq. (3.14), as

$$\begin{aligned} \begin{bmatrix} \mathbf{f} \\ \mu_f q_{f,\beta} \end{bmatrix} & = \mathbf{Q}_1 (d_1 \mathbf{Q}_2 + d_2 \mathbf{Q}_1)^{-1} \mathbf{Q}_2 (\mathbf{d}_2 - \mathbf{d}_1 + [\mathbf{I} \otimes (\mathbf{y}_1 - \mathbf{y}_2)^T] \xi_\tau) + \\ & + d_1 \mathbf{Q}_2 (d_1 \mathbf{Q}_2 + d_2 \mathbf{Q}_1)^{-1} (\mathbf{A}_1 \mathbf{d}_1 + \boldsymbol{\theta}_1 \xi_\tau + \boldsymbol{\zeta}_1) + d_2 \mathbf{Q}_1 (d_1 \mathbf{Q}_2 + d_2 \mathbf{Q}_1)^{-1} (\mathbf{A}_2 \mathbf{d}_2 + \boldsymbol{\theta}_2 \xi_\tau + \boldsymbol{\zeta}_2). \end{aligned} \quad (3.28)$$

The coupled multi-point approximation Eq. (3.28) was presented in (Terekhov *et al.* 2020). The gravity term $\rho_f g \nabla z \cdot \mathbf{K} \mathbf{n}$ in the Darcy flux q_f includes fluid density ρ_f which requires manual treatment as it participates in the discretization according to Eq. (3.18) while the density depends on the unknown pressure. Before assembly, this term is multiplied by the fluid density evaluated at the interface as the linear interpolation between cells $\rho_{f,\beta} = (d_1 \rho_{f,2} + d_2 \rho_{f,1}) / (d_1 + d_2)$.

The approximation in Eq. (3.28) requires the tangential projection of the gradients of the unknowns to be reconstructed. One can derive ξ_2 from Eq. (3.24) and substitute it into Eq. (3.16) to obtain the interpolation equation as

$$\begin{aligned} & (\mathbf{Q}_2 \otimes (\mathbf{x}_2 - \mathbf{x}_1)^T + d_2 (\mathbf{Q}_1 - \mathbf{Q}_2) \otimes \mathbf{n}^T + d_2 (\boldsymbol{\theta}_1 - \boldsymbol{\theta}_2)) (\nabla \otimes \mathbf{d}_1) = \\ & = (\mathbf{Q}_2 + d_2 \mathbf{A}_2) \mathbf{d}_2 - (\mathbf{Q}_2 + d_2 \mathbf{A}_1) \mathbf{d}_1 + d_2 (\boldsymbol{\zeta}_2 - \boldsymbol{\zeta}_1). \end{aligned} \quad (3.29)$$

It is necessary to consider at least 3 interfaces (in 3D) of the first cell to enclose the system with respect to the 12 components of $\nabla \otimes \mathbf{d}_1$.

Bringing together the results of Eq. (3.29) for N considered interfaces of the i -th cell, we build up the system

$$\mathbf{M}_i (\nabla \otimes \mathbf{d}_i) = \mathbf{D}_i \boldsymbol{\psi}_i, \quad (3.30)$$

where \mathbf{M}_i is a $4N \times 12$ matrix and \mathbf{D}_i is a $4N \times 4(N+1)$ matrix of coefficients $\mathbf{Q}_2 + d_2 \mathbf{A}_2$, $-(\mathbf{Q}_2 + d_2 \mathbf{A}_1)$ in front of the corresponding unknowns at the right-hand

side of Eq. (3.29), while $\boldsymbol{\psi}_i$ is a $4(N + 1) \times 1$ vector of $N + 1$ unknowns (or free terms in the right-hand side of boundary conditions). The solution of Eq. (3.30) can be obtained in a least-squares sense as

$$\nabla \otimes \mathbf{d}_i = (\mathbf{M}_i^T \mathbf{M}_i)^{-1} \mathbf{M}_i^T \mathbf{D}_i \boldsymbol{\psi}_i. \quad (3.31)$$

For the approximation of $\boldsymbol{\xi}_\tau$ in Eq. (3.28) the following combination of gradients

$$\boldsymbol{\xi}_\tau = \frac{\boldsymbol{\xi}_{\tau 1} + \boldsymbol{\xi}_{\tau 2}}{2}, \quad (3.32)$$

is used. A set of cells that contribute to the approximation Eq. (3.32) for each interface of some cell i is illustrated in Fig. 3.2.

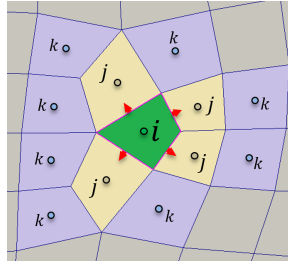


Figure 3.2.: Cells that contribute to the approximation of fluxes over the interfaces of cell i . Index j denotes the nearest neighbours of cell i . Index k denotes farther neighbours that contribute to the gradients reconstructed in cells j .

It is worth to be mentioned that the least squares solution in Eq. (3.31) allows computing the gradients of unknowns locally and independently for every cell. Note, however, that it does not guarantee the local conservation property for the scheme. In order to maintain it, individual gradients for every interface that respects the corresponding flux balance should be employed.

3.3.2. Diffusive and Advective Terms

The momentum and fluid mass fluxes used in Eqs. (3.12) and (3.13) can be represented through the diffusive (d) and advective (a) terms

$$\begin{bmatrix} \mathbf{f} \\ q \end{bmatrix}_\beta^{(d)} = \begin{bmatrix} \mathbf{f}' \\ \mu_\tau q_\tau \end{bmatrix}_\beta, \quad \begin{bmatrix} \mathbf{f} \\ q \end{bmatrix}_\beta^{(a)} = \begin{bmatrix} p \mathbf{B} \mathbf{n} \\ \tilde{q} \end{bmatrix}_\beta, \quad (3.33)$$

where the effective Biot traction \mathbf{f}'_β is defined in Eq. (2.22), the fluid fluxes q_τ, \tilde{q} are defined in Eq. (3.11). Both diffusive and advective terms are to be approximated at the interface β , but the diffusive term depends on the gradient of unknowns while the advective terms are linear with respect to unknowns. The total traction \mathbf{f}

and the total fluid mass flux q admit the following representation with the diffusive and advective terms

$$\begin{aligned} \begin{bmatrix} \mathbf{f} \\ q \end{bmatrix}_\beta &= \begin{bmatrix} \mathbf{f}'_\beta + (p\mathbf{B}\mathbf{n})_\beta \\ (\rho_f q_f)_\beta + \frac{\rho_{i,i}^{n+1} \bar{q}_\beta^{n+1} - \rho_{i,i}^n \bar{q}_\beta^n}{\Delta t_n} \end{bmatrix} = \\ &= \begin{bmatrix} \mathbf{I} \\ (\rho_f \mu_f^{-1})_u \end{bmatrix} \begin{bmatrix} \mathbf{f} \\ q \end{bmatrix}_\beta^{(d)} + \begin{bmatrix} \mathbf{I} \\ \rho_{i,i}^{n+1} \Delta t_n^{-1} \end{bmatrix} \begin{bmatrix} \mathbf{f} \\ q \end{bmatrix}_\beta^{(a)} - \begin{bmatrix} \mathbf{0} \\ \rho_{i,i}^n \Delta t_n^{-1} \end{bmatrix} \begin{bmatrix} \mathbf{f} \\ q \end{bmatrix}_\beta^{(a)} \end{aligned} \quad (3.34)$$

where subscript u denotes the property taken from the upwind direction defined by the sign of $q_{i,\beta}^n$: $q_{i,\beta}^n \geq 0 \Rightarrow u = i$ and $q_{i,\beta}^n < 0 \Rightarrow u = j$. Note that $q_{i,\beta}^n$ is calculated under the convention about the outward direction of normal vector $(\mathbf{x}_j - \mathbf{x}_i) \cdot \mathbf{n}_\beta > 0$. We denote time steps with $n, n+1$ superscripts only in the term representing the time derivative while the rest of the terms are taken implicitly, i.e., at the $n+1$ th time step.

The approximation derived in Eq. (3.28) can be easily rewritten only for diffusive term as

$$\begin{bmatrix} \mathbf{f} \\ q \end{bmatrix}_\beta^{(d)} = (\mathbf{Q}_1 - d_1 \mathbf{A}_1) \boldsymbol{\xi}_1 + (\boldsymbol{\Theta}_1 - \mathbf{A}_1 \otimes (\mathbf{x}_\beta - \mathbf{y}_1)^T) \boldsymbol{\xi}_\tau + \boldsymbol{\zeta}_1, \quad (3.35)$$

where $\boldsymbol{\xi}_1$ is defined in Eq. (3.27) and $\boldsymbol{\xi}_\tau$ is defined in Eqs. (3.31), (3.32). The advective term requires the approximation of the vector of unknowns \mathbf{d} at the center of the interface. Multiple approximations can be provided: a single-side interpolations $\mathbf{d}_{\beta 1}, \mathbf{d}_{\beta 2}$ defined in Eq. (3.16) or a two-side interpolation derived from the local problem (Terekhov *et al.* 2020; Vassilevski *et al.* 2020). Substituting Eq. (3.27) into the left-hand side of Eq. (3.16) one can obtain

$$\begin{aligned} \mathbf{d}_\beta &= (d_1 \mathbf{Q}_2 + d_2 \mathbf{Q}_1)^{-1} [d_2 \mathbf{Q}_1 \mathbf{d}_1 + d_1 \mathbf{Q}_2 \mathbf{d}_2 + \\ &\quad + d_1 d_2 ((\mathbf{A}_2 \mathbf{d}_2 + \boldsymbol{\Theta}_2 \boldsymbol{\xi}_\tau + \boldsymbol{\zeta}_2) - (\mathbf{A}_1 \mathbf{d}_1 + \boldsymbol{\Theta}_1 \boldsymbol{\xi}_\tau + \boldsymbol{\zeta}_1)) + \\ &\quad + (d_2 \mathbf{Q}_1 \otimes (\mathbf{x}_\beta - \mathbf{y}_1)^T + d_1 \mathbf{Q}_2 \otimes (\mathbf{x}_\beta - \mathbf{y}_2)^T) \boldsymbol{\xi}_\tau]. \end{aligned} \quad (3.36)$$

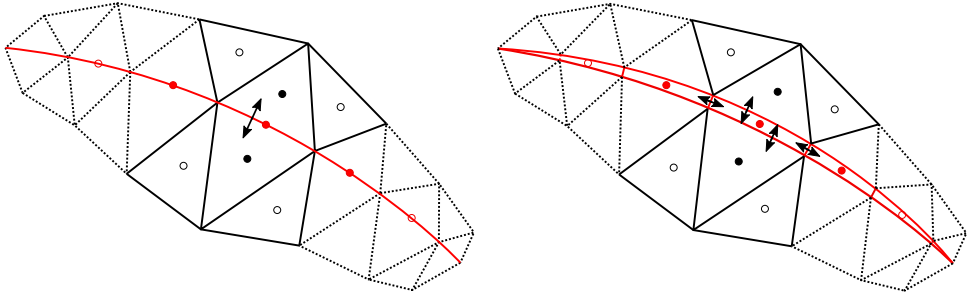
This second-order accurate interpolation can lead to inf-sup instability, i.e. spurious oscillations appearing in the solution of a coupled displacement-pressure system under undrained conditions or close to them (Gaspar *et al.* 2008). The substitution of Eq. (3.36) in Eq. (3.33) provides the approximation of the advective term.

3.3.3. Approximations at Interior Contact Interface

Faults introduce breaches in porous media which, on the one hand, can be highly conductive flow pathways, and, on the other hand, can represent frictional contacts between two edges. The transfer of fluid mass along the fault requires the equidimensional fault representation in a numerical model as longitudinal fluxes are proportional to the fault aperture. A number of these models have been proposed to resolve fluid flow in fractured porous media (Berre *et al.* 2021; Karimi-Fard *et al.*

2004; Li *et al.* 2008; Tene *et al.* 2017). In contrast to high hydraulic conductivity, the conductivity of momentum fluxes (stiffness) of saturated space in breaches is negligible compared to the one in the matrix. Moreover, momentum fluxes between equidimensional fault segments are eliminated by miniature fault apertures. Neglecting inter-fault momentum fluxes allows a lower-dimensional fault model to be used in the momentum balance. Furthermore, the equidimensional fault model may significantly complicate the solution of the momentum balance due to nonsmooth geometry.

In this work, we use a mixed-dimensional fault model that includes the equidimensional Discrete Fracture Model for fluid mass balance and a lower-dimensional fault model for momentum balance (Boon *et al.* 2023). Fault representations are shown in Fig. 3.3. The fault partitioning is conformal with the computational grid.



(a) Fault representation for momentum fluxes

(b) Fault representation for fluid fluxes

Figure 3.3.: Fault representations in the approximation of momentum fluxes (a) and the approximation of fluid mass fluxes (b).

The mixed-dimensional fault model described above implies a continuous pressure as fault cell has the same dimension as cells in the matrix. In contrast, the model allows matrix displacements to be discontinuous. We consider the gap vector defined in Eq. (2.23) and pressure as primary unknowns assigned to the centers of fault cells. In regard of that, we have the following continuity of unknowns and fluxes over the contact between matrix cells 1, 2 and fault cell 3 in between

$$\mathbf{u}_1 \pm \mathbf{g}_3 + [\mathbf{I} \otimes (\mathbf{x}_3 - \mathbf{x}_1)^T] (\nabla \otimes \mathbf{u}_1) = \mathbf{u}_2 + [\mathbf{I} \otimes (\mathbf{x}_3 - \mathbf{x}_2)^T] (\nabla \otimes \mathbf{u}_2), \quad (3.37)$$

$$p_1 + (\mathbf{x}_{\beta_1} - \mathbf{x}_1)^T \cdot \nabla p_1 = p_3 + (\mathbf{x}_{\beta_1} - \mathbf{x}_3)^T \cdot \nabla p_3, \quad (3.38)$$

$$p_3 \mathbf{B}_1 \mathbf{n} - [\mathbf{I} \otimes \mathbf{n}^T] \mathbf{S}_1 (\nabla \otimes \mathbf{u}_1) = p_3 \mathbf{B}_2 \mathbf{n} - [\mathbf{I} \otimes \mathbf{n}^T] \mathbf{S}_2 (\nabla \otimes \mathbf{u}_2), \quad (3.39)$$

$$-(\nabla p_1 - \rho_f g \nabla z) \cdot \mathbf{K}_1 \mathbf{n} = -(\nabla p_3 - \rho_f g \nabla z) \cdot \mathbf{K}_3 \mathbf{n}, \quad (3.40)$$

where \pm is positive when cells 1 and 2 are located at negative and positive sides of the fault, respectively. Also $\mathbf{x}_1, \mathbf{x}_2$, and \mathbf{x}_3 are the centers of matrix cells 1, 2 and fault cell 3, respectively. Furthermore, \mathbf{x}_{β_1} and \mathbf{x}_{β_2} are the centers of the fault interfaces β_1 and β_2 in the equidimensional fault representation respectively. It is worth to be noted that we do not approximate pressure in Eq. (3.39). Instead, we use an unknown pressure p_3 assigned to a fault cell.

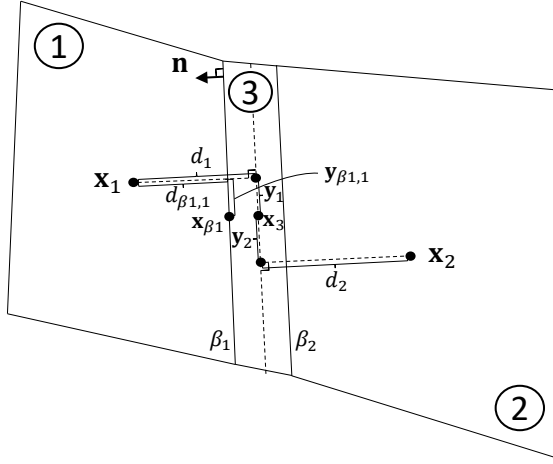


Figure 3.4.: Normal decomposition of distances between the centers of cells 1, 2 and the center of interface β .

Below we will use the following co-normal decompositions

$$\begin{aligned}
 \mathbf{x}_3 - \mathbf{x}_1 &= d_1 \mathbf{n} + (\mathbf{x}_3 - \mathbf{y}_1), & d_1 &= \mathbf{n} \cdot (\mathbf{x}_3 - \mathbf{x}_1) > 0, & \mathbf{y}_1 &= \mathbf{x}_1 + d_1 \mathbf{n}, \\
 \mathbf{x}_2 - \mathbf{x}_3 &= d_2 \mathbf{n} + (\mathbf{y}_2 - \mathbf{x}_3), & d_2 &= \mathbf{n} \cdot (\mathbf{x}_2 - \mathbf{x}_3) > 0, & \mathbf{y}_2 &= \mathbf{x}_2 - d_2 \mathbf{n}, \\
 \mathbf{x}_{\beta_1} - \mathbf{x}_1 &= d_{\beta_1,1} \mathbf{n} + (\mathbf{x}_{\beta_1} - \mathbf{y}_{\beta_1,1}), & d_{\beta_1,1} &= \mathbf{n} \cdot (\mathbf{x}_{\beta_1} - \mathbf{x}_1) > 0, & \mathbf{y}_{\beta_1,1} &= \mathbf{x}_1 + d_{\beta_1,1} \mathbf{n}, \\
 \mathbf{x}_3 - \mathbf{x}_{\beta_1} &= d_{\beta_1,3} \mathbf{n}, & d_{\beta_1,3} &= \mathbf{n} \cdot (\mathbf{x}_3 - \mathbf{x}_{\beta_1}) > 0, & &
 \end{aligned} \tag{3.41}$$

where we assume that $\mathbf{x}_3 - \mathbf{x}_{\beta_1} = d_{\beta_1,3} \mathbf{n}$ which means that the center of the interface between matrix cell 1 and fault cell 3 is shifted by $d_{\beta_1,3}$ along the direction normal to the fault. The aforementioned geometrical properties are shown in Fig. 3.4. It is worth to be noted that $d_{\beta_1,3}$ is a half-aperture and it is to be equal to $|\mathbf{g}_3^T \mathbf{n}|/2$. However, the treatment of this distance as an unknown makes the discretization nonlinear. It means that the conservative discretization may require taking into account this nonlinearity and resolving it at every nonlinear iteration. Fault opening is out of the scope of this work which allows us to treat this distance as a constant.

A co-normal split of Eqs. (3.37)-(3.40) reads as

$$\mathbf{u}_1 \pm \mathbf{g}_3 + d_1 \xi_1^u + \mathbf{I} \otimes (\mathbf{x}_\beta - \mathbf{y}_1)^T \xi_{\tau 1}^u = \mathbf{u}_2 - d_2 \xi_2^u + \mathbf{I} \otimes (\mathbf{x}_\beta - \mathbf{y}_2)^T \xi_{\tau 2}^u, \tag{3.42}$$

$$p_1 + d_{\beta_1,1} \xi_1^p + (\mathbf{x}_{\beta_1} - \mathbf{y}_{\beta_1,1})^T \xi_\tau^p = p_3 - d_{\beta_1,3} \xi_3^p, \tag{3.43}$$

$$p_3 \mathbf{B}_1 \mathbf{n} - \mathbf{T}_1 \xi_1^u - \Gamma_1 \xi_{\tau 1}^u = p_3 \mathbf{B}_2 \mathbf{n} - \mathbf{T}_2 \xi_2^u - \Gamma_2 \xi_{\tau 2}^u, \tag{3.44}$$

$$-\kappa_1 \xi_1^p - \kappa_1 \xi_\tau^p + \rho_i g \nabla z \cdot \mathbf{K}_1 \mathbf{n} = -\kappa_3 \xi_3^p - \kappa_3 \xi_\tau^p + \rho_i g \nabla z \cdot \mathbf{K}_3 \mathbf{n}, \tag{3.45}$$

where ξ_i^u, ξ_i^p are normal projections of displacement and pressure gradients in cell i while $\xi_{\tau i}^u$ denote tangential projections of displacement gradients in cell $i = 1, 2$.

In contrast to displacements, pressure remains continuous in the equidimensional fault representation and Eq. (3.32) defines the tangential projection of the pressure gradient ξ_τ^p .

Following the same way as we derived the approximation at a continuous interface, we derive the approximations at a contact interface. Taking ξ_2^u, ξ_3^p from Eqs. (3.42) and (3.43) and substituting them to Eqs. (3.44) and (3.45) results in

$$(d_1 \mathbf{T}_2 + d_2 \mathbf{T}_1) \xi_1^u = \mathbf{T}_2 (\mathbf{u}_2 - \mathbf{u}_1 \mp \mathbf{g}_3) + d_2 (\mathbf{B}_1 - \mathbf{B}_2) \mathbf{n} p_3 + (\mathbf{T}_2 \otimes (\mathbf{x}_\beta - \mathbf{y}_2))^T + d_2 \Gamma_2) \xi_{\tau 2}^u - (\mathbf{T}_2 \otimes (\mathbf{x}_\beta - \mathbf{y}_1))^T + d_2 \Gamma_1) \xi_{\tau 1}^u, \quad (3.46)$$

$$(d_{\beta 1,3} \kappa_1 + d_{\beta 1,1} \kappa_3) \xi_1^p = \kappa_3 (p_3 - p_1) - (\kappa_3 (\mathbf{x}_{\beta 1} - \mathbf{y}_{\beta 1,1}))^T + d_{\beta 1,3} (\kappa_1 - \kappa_3)^T) \xi_\tau^p + d_{\beta 1,3} \rho_f g \nabla z \cdot (\mathbf{K}_1 - \mathbf{K}_3) \mathbf{n}, \quad (3.47)$$

which, once substituted to Eqs. (3.39) and (3.40), provide the following approximations

$$\mathbf{f}_\beta^{(d)} = \mathbf{T} (\mathbf{u}_1 \pm \mathbf{g}_3 - \mathbf{u}_2 - \mathbf{I} \otimes (\mathbf{x}_\beta - \mathbf{y}_2))^T \xi_{\tau 2}^u + \mathbf{I} \otimes (\mathbf{x}_\beta - \mathbf{y}_1))^T \xi_{\tau 1}^u - d_1 \mathbf{T}_2 (d_2 \mathbf{T}_1 + d_1 \mathbf{T}_2)^{-1} \Gamma_1 \xi_{\tau 1}^u - d_2 \mathbf{T}_1 (d_2 \mathbf{T}_1 + d_1 \mathbf{T}_2)^{-1} (\Gamma_2 \xi_{\tau 2}^u + (\mathbf{B}_1 - \mathbf{B}_2) \mathbf{n} p_3), \quad (3.48)$$

$$\mathbf{f}_\beta^{(a)} = p_3 \mathbf{B}_1 \mathbf{n}, \quad (3.49)$$

$$q_{\beta 1}^{(d)} = \kappa (p_1 - p_3 - (\mathbf{x}_{\beta 1} - \mathbf{y}_{\beta 1,1})^T \xi_\tau^p) + d_{\beta 1,3} \kappa_1 (d_{\beta 1,3} \kappa_1 + d_{\beta 1,1} \kappa_3)^{-1} (\kappa_1 - \kappa_2)^T \xi_\tau^p - d_{\beta 1,1} \kappa_3 (d_{\beta 1,3} \kappa_1 + d_{\beta 1,1} \kappa_3)^{-1} \rho g \nabla z \cdot \mathbf{K}_1 \mathbf{n} - d_{\beta 1,3} \kappa_1 (d_{\beta 1,3} \kappa_1 + d_{\beta 1,1} \kappa_3)^{-1} \rho g \nabla z \cdot \mathbf{K}_3 \mathbf{n}, \quad (3.50)$$

$$(3.51)$$

where $\mathbf{T} = \mathbf{T}_1 (d_1 \mathbf{T}_2 + d_2 \mathbf{T}_1)^{-1} \mathbf{T}_2$, $\kappa = \kappa_1 (d_{\beta 1,3} \kappa_1 + d_{\beta 1,1} \kappa_3)^{-1} \kappa_3$ while the tangential gradients of displacements relate to each other as $\xi_{\tau 1}^u \pm \nabla \otimes \mathbf{g}_3 = \xi_{\tau 2}^u$.

The final approximation of the traction vector $\mathbf{f}_\beta = \mathbf{f}_\beta^{(d)} + \mathbf{f}_\beta^{(a)}$ is obtained as the arithmetic mean of the approximations defined in Eqs. (3.48) and (3.49) written for both sides $\beta 1$ and $\beta 2$ of the fault cell, i.e.,

$$\mathbf{f}_\beta = \frac{\mathbf{f}_{\beta 1}^{(d)} + \mathbf{f}_{\beta 2}^{(a)} - \mathbf{f}_{\beta 2}^{(d)} - \mathbf{f}_{\beta 1}^{(a)}}{2}, \quad (3.52)$$

where “-” takes into account the fact that the approximations $\mathbf{f}_{\beta 1}^{(d)}, \mathbf{f}_{\beta 2}^{(d)}$ are defined in Eqs. (3.48) and (3.49) for opposite orientations of the normal vector.

Eqs. (3.46) and (3.47) can be substituted to Eqs. (3.37) and (3.38) and we obtain the approximation of unknowns at corresponding interfaces.

$$\mathbf{u}_\beta = (d_1 \mathbf{T}_2 + d_2 \mathbf{T}_1)^{-1} [d_2 \mathbf{T}_1 (\mathbf{u}_1 \pm \mathbf{g}_3) + d_1 \mathbf{T}_2 \mathbf{u}_2 + d_1 d_2 (\mathbf{B}_1 - \mathbf{B}_2) \mathbf{n} p_3 + (d_2 \mathbf{T}_1 \otimes (\mathbf{x}_\beta - \mathbf{y}_1))^T - d_1 d_2 \Gamma_1) \xi_{\tau 1}^u + (d_1 \mathbf{T}_2 \otimes (\mathbf{x}_\beta - \mathbf{y}_2))^T + d_1 d_2 \Gamma_2) \xi_{\tau 2}^u] \quad (3.53)$$

$$p_{\beta 1} = (d_{\beta 1,1} \kappa_3 + d_{\beta 1,3} \kappa_1)^{-1} [d_{\beta 1,1} \kappa_3 + d_{\beta 1,3} \kappa_1 + (d_{\beta 1,3} \kappa_1 (\mathbf{x}_{\beta 1} - \mathbf{y}_{\beta 1,1}))^T + d_{\beta 1,1} d_{\beta 1,3} (\kappa_3 - \kappa_1)^T) \xi_\tau^p + d_{\beta 1,1} d_{\beta 1,3} \rho_f g \nabla z \cdot (\mathbf{K}_1 - \mathbf{K}_3) \mathbf{n}]. \quad (3.54)$$

We approximate the advective term for fluid flux as

$$q_{\beta 1}^{(a)} = \tilde{q}_{\beta 1} = (\mathbf{B}_1 \mathbf{n})^T \otimes (\mathbf{x}_{\beta 1} - \mathbf{x}_1)^T (\nabla \otimes \mathbf{u}_1), \quad (3.55)$$

where $(\mathbf{B}_i \mathbf{n})^T \otimes (\mathbf{x}_{\beta 1} - \mathbf{x}_i)^T$ is a 1×9 row vector.

We use a DFM for simulation of the mass balance equation which implies having discrete equations for fracture segments of non-zero volumes. We assume continuous pressure at the boundary between fault cells. The following two-point approximation of Darcy flux is used for these connections

$$q_{f, \beta 1} = \frac{\kappa_1 \kappa_2}{d_1 \kappa_2 + d_2 \kappa_1} (p_1 - p_2) + \rho_{f, 12} g \nabla z \cdot \mathbf{n}, \quad (3.56)$$

where $\rho_{f, 12} = (d_1 \rho_{f, 2} + d_2 \rho_{f, 1}) / (d_1 + d_2)$ is linearly interpolated between cells.

The approximations in Eqs. (3.48)-(3.55) require the gradients of the unknowns to be reconstructed. We follow the same approach as in the expressions for gradient reconstruction derived for interior interfaces, but the particular condition in Eq. (3.29) should be modified for a contact interface. One can derive ξ_2^u and ξ_3^p from Eqs. (3.44) and (3.45) and substitute them into Eqs. (3.42) and (3.43) to obtain the interpolation equation as

$$\begin{aligned} & (\mathbf{T}_2 \otimes (\mathbf{x}_2 - \mathbf{x}_1)^T + d_{23} (\mathbf{T}_1 - \mathbf{T}_2) \otimes \mathbf{n}^T + d_{23} (\mathbf{\Gamma}_1 - \mathbf{\Gamma}_2)) [\nabla \otimes \mathbf{u}_1] = \\ & = \mathbf{T}_2 (\mathbf{u}_2 - \mathbf{u}_1 \mp \mathbf{g}_3) \mp (\mathbf{T}_2 \otimes (\mathbf{y}_{23} - \mathbf{x}_3)^T - d_{23} \mathbf{\Gamma}_2) \nabla \otimes \mathbf{g}_3, \end{aligned} \quad (3.57)$$

$$(\kappa_3 (\mathbf{x}_3 - \mathbf{x}_1) + d_{3\delta} (\mathbf{K}_1 - \mathbf{K}_3) \mathbf{n}) \cdot \nabla p_1 = \kappa_3 (p_3 - p_1) + d_{3\delta} \rho_{f, \beta 1} g \nabla z (\mathbf{K}_1 - \mathbf{K}_2) \mathbf{n}. \quad (3.58)$$

Eq. (3.58) is used as a condition for pressure gradient reconstruction not only between matrix and fault cells but also between fault cells.

Gap gradients are reconstructed by using the following relation for the connections between fault cells

$$[\mathbf{I} \otimes (\mathbf{x}_2 - \mathbf{x}_1)^T] \nabla \otimes \mathbf{g}_1 = \mathbf{g}_2 - \mathbf{g}_1. \quad (3.59)$$

In the connection between a fault cell and an open boundary interface, we have

$$[\mathbf{I} \otimes (\mathbf{x}_2 - \mathbf{x}_1)^T] \nabla \otimes \mathbf{g}_1 = \mathbf{0}, \quad (3.60)$$

whereas for a closed boundary (fault tip) we have

$$[\mathbf{I} \otimes (\mathbf{x}_2 - \mathbf{x}_1)^T] \nabla \otimes \mathbf{g}_1 = -\mathbf{g}_1. \quad (3.61)$$

Note, that Eqs. (3.59)-(3.61) do not take into account material contrasts.

3.3.4. Approximations at Boundary Interface

The approximations of fluxes at boundary interfaces must satisfy corresponding boundary conditions defined in Eq. (2.55). Using the single-side approximation of

normal pressure gradient ξ_1^p one can derive pressure p_b and Darcy flux $q_{t,b}$ at the boundary interface as

$$p_b = \left(a_p + \frac{b_p \kappa_1}{\mu_f d_1} \right)^{-1} \left(r_p + \frac{b_p \kappa_1}{\mu_f d_1} p_1 - \frac{b_p}{\mu_f} \left(\frac{\kappa_1}{d_1} (\mathbf{y}_1 - \mathbf{x}_b) + \boldsymbol{\kappa}_1 \right) \cdot \boldsymbol{\xi}_\tau^p + \frac{b_p}{\mu_f} \rho_f g \nabla z \cdot \mathbf{K}_1 \mathbf{n} \right), \quad (3.62)$$

$$q_{t,b} = -\frac{1}{\mu_f} \left(a_p + \frac{b_p \kappa_1}{\mu_f d_1} \right)^{-1} \left(\frac{\kappa_1}{d_1} r_p - a_p \frac{\kappa_1}{d_1} p_1 + a_p \left(\frac{\kappa_1}{d_1} (\mathbf{y}_1 - \mathbf{x}_b) + \boldsymbol{\kappa}_1 \right) \cdot \boldsymbol{\xi}_\tau^p - a_p \rho_f g \nabla z \cdot \mathbf{K}_1 \mathbf{n} \right), \quad (3.63)$$

where \mathbf{x}_b denotes the center of boundary interface (Terekhov 2020a).

In the same manner, one can substitute the single-side approximation of displacement gradients ξ_1^u to boundary conditions in Eq. (2.55) and derive \mathbf{u}_b and the total traction vector at the boundary interface as

$$\begin{aligned} \mathbf{u}_b = & \left(a_t \mathbf{I} + \frac{b_t}{d_1} \mathbf{T}_1 \right)^{-1} \left(l r_n \mathbf{n} + (\mathbf{I} - l \mathbf{nn}^T \mathbf{L}) r_t \right) + \\ & + \left(a_t \mathbf{I} + \frac{b_t}{d_1} \mathbf{T}_1 \right)^{-1} \left(b_t \mathbf{I} + l \mathbf{nn}^T (b_n \mathbf{I} - b_t \mathbf{L}) \right) \cdot \\ & \cdot \left(\frac{1}{d_1} \mathbf{T}_1 \mathbf{u}_1 - \left(\frac{1}{d_1} \mathbf{T}_1 [\mathbf{I} \otimes (\mathbf{y}_1 - \mathbf{x}_b)^T] + \Gamma_1 \right) \boldsymbol{\xi}_\tau^u + p_b \mathbf{B}_1 \mathbf{n} \right), \end{aligned} \quad (3.64)$$

$$\begin{aligned} \mathbf{f}_b = & -\frac{1}{d_1} \mathbf{T}_1 \left(a_t \mathbf{I} + \frac{b_t}{d_1} \mathbf{T}_1 \right)^{-1} \left(l r_n \mathbf{n} + (\mathbf{I} - l \mathbf{nn}^T \mathbf{L}) r_t \right) - \\ & \frac{1}{d_1} \mathbf{T}_1 \left(a_t \mathbf{I} + \frac{b_t}{d_1} \mathbf{T}_1 \right)^{-1} \left(l \mathbf{nn}^T (b_n \mathbf{I} - b_t \mathbf{L}) - a_t d_1 \mathbf{T}_1^{-1} \right) \cdot \\ & \cdot \left(\frac{1}{d_1} \mathbf{T}_1 \mathbf{u}_1 - \left(\frac{1}{d_1} \mathbf{T}_1 [\mathbf{I} \otimes (\mathbf{y}_1 - \mathbf{x}_b)] + \Gamma_1 \right) \boldsymbol{\xi}_\tau^u + p_b \mathbf{B}_1 \mathbf{n} \right), \end{aligned} \quad (3.65)$$

where $\mathbf{L} = \left(a_n \mathbf{I} + \frac{b_n}{d_1} \mathbf{T}_1 \right) \left(a_t \mathbf{I} + \frac{b_t}{d_1} \mathbf{T}_1 \right)^{-1}$ is a 3×3 matrix and $l = (\mathbf{n}^T \mathbf{L} \mathbf{n})^{-1}$ is a scalar. The approximation of \tilde{q}_β in Eq. (3.11) can be achieved from Eq. (3.64).

Eqs. (3.62) and (3.64) can be rewritten for the reconstruction of gradients in the cells with boundary interfaces as

$$\begin{aligned} & \left(a_p (\mathbf{x}_b - \mathbf{x}_1) + \frac{b_p}{\mu_f} \mathbf{K}_1 \mathbf{n} \right) \cdot \nabla p_1 = r_p + \frac{b_p}{\mu_f} \rho_f g \nabla z \cdot \mathbf{K}_1 \mathbf{n} - a_p p_1, \quad (3.66) \\ & \left(a_t [\mathbf{I} \otimes (\mathbf{x}_b - \mathbf{x}_1)^T] + b_t [\mathbf{I} \otimes \mathbf{n}^T] \mathbf{S}_1 + \right. \\ & \quad \left. + l \mathbf{nn}^T (b_n \mathbf{I} - b_t \mathbf{L}) \left(\Gamma_1 + \frac{1}{d_1} \mathbf{T}_1 [\mathbf{I} \otimes (\mathbf{y}_1 - \mathbf{x}_b)^T] \right) \right) [\nabla \otimes \mathbf{u}_1] = \\ & = l r_n \mathbf{n} + (\mathbf{I} - l \mathbf{nn}^T \mathbf{L}) r_t + \left(l \mathbf{nn}^T (b_n \mathbf{I} - b_t \mathbf{L}) \frac{1}{d_1} \mathbf{T}_1 - a_t \mathbf{I} \right) \mathbf{u}_1 + (b_t \mathbf{I} + l \mathbf{nn}^T (b_n \mathbf{I} - b_t \mathbf{L})) \mathbf{B}_1 \mathbf{n} p_b. \end{aligned} \quad (3.67)$$

3.4. Stabilized Approximation

The displacement-pressure system is a known example of a saddle-point problem. Many numerical schemes approximating the system violate the Ladyzhenskaya-Babuska-Brezzi (LBB or inf-sup) condition (Franco Brezzi 1991; Ladyzhenskaya 1969) which introduces unphysical oscillations to numerical solution in the limit of undrained conditions (Gaspar *et al.* 2008; Murad *et al.* 1994; Preisig *et al.* 2011). The collocated FVM based on the multi-point approximations presented above is not an exception (Nordbotten 2016; Terekhov 2020a; Terekhov *et al.* 2022). Therefore, it requires appropriate treatment of this instability.

Numerous techniques have been proposed to stabilize these kind of systems. Most of the techniques introduce a specially-designed perturbation that suppresses the instability maintaining the accurate discretization of original equations including Brezzi-Pitkaranta scheme (Brezzi *et al.* 1984), the Galerkin least-squares method (Hughes *et al.* 1986), Polynomial Pressure Projection (Dohrmann *et al.* 2004), Physical Influence Scheme for the Element-based FVM for poroelasticity (Honório *et al.* 2018), penalization of pressure jump across macroelements (Hughes *et al.* 1987) and related Local Pressure Jump stabilization (Silvester *et al.* 1990) applied to the multiphase poroelastic systems (Aronson *et al.* 2023; Camargo *et al.* 2021). The use of a staggered grid for fluid mass and momentum balance may help to avoid stability issues (Gaspar *et al.* 2006; Shokrollahzadeh Behbahani *et al.* 2022a; Wheeler *et al.* 2014), but it imposes additional limitations to admissible grids, complicates the satisfaction of conservation principles (Morinishi *et al.* 1998; Perot 2000) and amplifies the technical challenges related to building efficient solvers.

Flux vector splitting (FVS) has been widely utilized for the approximation of advection terms in computational fluid dynamics (Toro 2009). Recently, FVS has been successfully extended to the schemes of FVM applied to saddle-point problems (Terekhov 2021a), including the mixed formulation of the Darcy problem (Terekhov *et al.* 2019), Navier-Stokes equations (Terekhov 2021b) and a coupled poroelastic problem (Terekhov 2020b; Terekhov *et al.* 2022). In the following, the latter approach is briefly introduced.

We can write the single-side approximation of the vector \mathbf{q} of momentum and fluid mass fluxes as

$$\mathbf{q}_i = \Lambda_i [\nabla \otimes \mathbf{d}_i] + \mathbf{M}_i \mathbf{d}_\delta + \zeta_i, \quad (3.68)$$

where the first term is a diffusion term, the second term is an advection term and last term is a free term, $\mathbf{d}_\delta = [\mathbf{u}^T p]$ is a vector of unknowns at the center of the interface and the following notations are used

$$\Lambda_i = [\mathbf{I} \otimes \mathbf{n}^T] \begin{pmatrix} -\mathbf{S}_i & \\ & -\Delta t \mu^{-1} \mathbf{K}_i \end{pmatrix}, \quad \mathbf{M}_i = \begin{pmatrix} & \mathbf{B}_1 \mathbf{n} \\ (\mathbf{B}_1 \mathbf{n})^T & \end{pmatrix}, \quad \zeta_i = \begin{bmatrix} \mathbf{0} \\ \rho_i g \nabla z \cdot \mathbf{K}_i \mathbf{n} \end{bmatrix}. \quad (3.69)$$

Let us consider the following decomposition of gradient vector of unknowns into normal and transversal parts

$$\begin{aligned} \nabla \otimes \mathbf{d}_1 &= [\mathbf{I} \otimes \mathbf{n}] \xi_1 + \xi_\tau = d_1^{-1} [\mathbf{I} \otimes \mathbf{n}] (\mathbf{d}(\mathbf{y}_1) - \mathbf{d}_1) + \xi_\tau = \\ &= d_1^{-1} [\mathbf{I} \otimes \mathbf{n}] (\mathbf{d}_\delta - \mathbf{d}_1) + (\mathbf{I} - d_1^{-1} \mathbf{I} \otimes \mathbf{n}(\mathbf{x}_\delta - \mathbf{y}_1)^T) \xi_\tau, \end{aligned} \quad (3.70)$$

where $\xi_1 = [\mathbf{I} \otimes \mathbf{n}^T][\nabla \otimes \mathbf{d}_1]$, $\xi_\tau = [\mathbf{I} \otimes (\mathbf{I} - \mathbf{n}\mathbf{n}^T)][\nabla \otimes \mathbf{d}_1]$ are normal and transversal components of $\nabla \otimes \mathbf{d}_1$. Substituting the last definition into Eq. (3.70) and decomposing $\nabla \otimes \mathbf{d}_2$ in the following manner one may come to the following form

$$\nabla \otimes \mathbf{d}_1 = d_1^{-1}[\mathbf{I} \otimes \mathbf{n}](\mathbf{d}_\delta - \mathbf{d}_1) + (\mathbf{I} - d_1^{-1}\mathbf{I} \otimes \mathbf{n}(\mathbf{x}_\delta - \mathbf{x}_1)^T)[\nabla \otimes \mathbf{d}_1], \quad (3.71)$$

$$\nabla \otimes \mathbf{d}_2 = d_2^{-1}[\mathbf{I} \otimes \mathbf{n}](\mathbf{d}_2 - \mathbf{d}_\delta) + (\mathbf{I} - d_2^{-1}\mathbf{I} \otimes \mathbf{n}(\mathbf{x}_2 - \mathbf{x}_\delta)^T)[\nabla \otimes \mathbf{d}_2], \quad (3.72)$$

Using co-normal decomposition $\Lambda_i = d_i \mathbf{Q}_i[\mathbf{I} \otimes \mathbf{n}^T] + \boldsymbol{\theta}_i$, $\mathbf{Q}_i = d_i^{-1}\Lambda_i[\mathbf{I} \otimes \mathbf{n}]$ and substituting Eq. (3.70) into Eq. (3.68) we will have the following representation of fluxes

$$\mathbf{q}_1 = -\mathbf{Q}_1 \mathbf{d}_1 + (\mathbf{M}_1 + \mathbf{Q}_1)\mathbf{d}_\delta + (\Lambda_1 - \mathbf{Q}_1 \otimes (\mathbf{x}_\delta - \mathbf{x}_1)^T)[\nabla \otimes \mathbf{d}_1] + \zeta_1, \quad (3.73)$$

$$\mathbf{q}_2 = \mathbf{Q}_2 \mathbf{d}_2 + (\mathbf{M}_2 - \mathbf{Q}_2)\mathbf{d}_\delta + (\Lambda_2 - \mathbf{Q}_2 \otimes (\mathbf{x}_2 - \mathbf{x}_\delta)^T)[\nabla \otimes \mathbf{d}_2] + \zeta_2, \quad (3.74)$$

where the terms $(\mathbf{M}_1 + \mathbf{Q}_1)\mathbf{d}_\delta$, $(\mathbf{M}_2 - \mathbf{Q}_2)\mathbf{d}_\delta$ can cause numerical instability. To avoid it one can add the following terms to the fluxes

$$\mathbf{R}_1(\mathbf{d}_1 - \mathbf{d}_\delta) + \mathbf{R}_1 \otimes (\mathbf{x}_\delta - \mathbf{x}_1)^T[\nabla \otimes \mathbf{d}_1] = 0, \quad (3.75)$$

$$\mathbf{S}_2(\mathbf{d}_\delta - \mathbf{d}_2) + \mathbf{R}_2 \otimes (\mathbf{x}_2 - \mathbf{x}_\delta)^T[\nabla \otimes \mathbf{d}_2] = 0, \quad (3.76)$$

which are equal to zero because of linearity of \mathbf{d} within each cell, $\mathbf{R}_1, \mathbf{R}_2$ are 4×4 matrices defined as

$$\mathbf{R}_i = \alpha_i \begin{pmatrix} b_i^{-1} \mathbf{M}_i \mathbf{n} \mathbf{n}^T \mathbf{M}_i & \\ & b_i \end{pmatrix}, \quad \alpha_i \geq \frac{\sqrt{(k_i - c_i)^2 + 4b_i^2 \tau} - (k_i + c_i)}{2b_i} \quad (3.77)$$

$$b_i = \sqrt{\mathbf{n}^T \mathbf{B}_i^2 \mathbf{n}}, \quad c_i = \frac{1}{d_i b_i^2} (\mathbf{n}^T \mathbf{B}_i \otimes \mathbf{n}^T) \mathbf{Q}_i (\mathbf{n} \otimes \mathbf{B}_i \mathbf{n}), \quad k_i = (d_i \mu_f)^{-1} \kappa_i, \quad (3.78)$$

Adding Eqs. (3.75) and (3.76) to Eqs. (3.73) and (3.74) we have the following flux approximations

$$\mathbf{q}_1 = (\mathbf{R}_1 - \mathbf{Q}_1) \mathbf{u}_1 - (\mathbf{R}_1 - \mathbf{M}_1 - \mathbf{Q}_1)\mathbf{d}_\delta + (\Lambda_1 - (\mathbf{Q}_1 - \mathbf{R}_1) \otimes (\mathbf{x}_\delta - \mathbf{x}_1)^T)[\nabla \otimes \mathbf{d}_1] + \zeta_1, \quad (3.79)$$

$$\mathbf{q}_2 = (\mathbf{R}_2 + \mathbf{M}_2 - \mathbf{Q}_2)\mathbf{d}_\delta - (\mathbf{R}_2 - \mathbf{Q}_2)\mathbf{d}_2 + (\Lambda_2 - (\mathbf{Q}_2 - \mathbf{R}_2) \otimes (\mathbf{x}_2 - \mathbf{x}_\delta)^T)[\nabla \otimes \mathbf{d}_2] + \zeta_2. \quad (3.80)$$

The continuity of fluxes \mathbf{q}_1 and \mathbf{q}_2 can provide the approximation of the vector of unknowns at the interface between \mathbf{d}_δ

$$\mathbf{d}_\delta = (\mathbf{Q}_1 + \mathbf{Q}_2 + \mathbf{M}_1 - \mathbf{M}_2 - \mathbf{R}_1 - \mathbf{R}_2)^{-1} ((\mathbf{Q}_1 - \mathbf{R}_1)\mathbf{d}_1 + (\mathbf{Q}_2 - \mathbf{R}_2)\mathbf{d}_2 + (\Lambda_2 - (\mathbf{Q}_2 - \mathbf{R}_2) \otimes (\mathbf{x}_2 - \mathbf{x}_\delta)^T)[\nabla \otimes \mathbf{d}_2] - (\Lambda_1 - (\mathbf{Q}_1 - \mathbf{R}_1) \otimes (\mathbf{x}_\delta - \mathbf{x}_1)^T)[\nabla \otimes \mathbf{d}_1] + \zeta_2 - \zeta_1), \quad (3.81)$$

which once substituted back to Eq. (3.79) can provide a final approximation as

$$\begin{aligned} \mathbf{q} = & \mathbf{G}_2(\mathbf{G}_1 + \mathbf{G}_2)^{-1}(\mathbf{R}_1 - \mathbf{Q}_1)\mathbf{d}_1 - \mathbf{G}_1(\mathbf{G}_1 + \mathbf{G}_2)^{-1}(\mathbf{R}_2 - \mathbf{Q}_2)\mathbf{d}_2 + \\ & + \mathbf{G}_2(\mathbf{G}_1 + \mathbf{G}_2)^{-1}(\mathbf{A}_1 - (\mathbf{Q}_1 - \mathbf{R}_1) \otimes (\mathbf{x}_\delta - \mathbf{x}_1)^T) [\nabla \otimes \mathbf{d}_1] + \mathbf{G}_2(\mathbf{G}_1 + \mathbf{G}_2)^{-1}\zeta_1 + \\ & + \mathbf{G}_1(\mathbf{G}_1 + \mathbf{G}_2)^{-1}(\mathbf{A}_2 - (\mathbf{Q}_2 - \mathbf{R}_2) \otimes (\mathbf{x}_2 - \mathbf{x}_\delta)^T) [\nabla \otimes \mathbf{d}_2] + \mathbf{G}_1(\mathbf{G}_1 + \mathbf{G}_2)^{-1}\zeta_2, \end{aligned} \quad (3.82)$$

where $\mathbf{G}_1 = \mathbf{R}_1 - \mathbf{M}_1 - \mathbf{Q}_1$, $\mathbf{G}_2 = \mathbf{R}_2 + \mathbf{M}_2 - \mathbf{Q}_2$. The separate approximation of advective part $\mathbf{q}^{(a)}$ of flux can be derived from Eq. (3.79) as

$$\mathbf{q}^{(a)} = (\mathbf{R}_1 - \mathbf{Q}_1)\mathbf{d}_1 - (\mathbf{R}_1 - \mathbf{M}_1 - \mathbf{Q}_1)\mathbf{d}_\delta - (\mathbf{Q}_1 - \mathbf{R}_1) \otimes (\mathbf{x}_\delta - \mathbf{x}_1)^T [\nabla \otimes \mathbf{d}_1], \quad (3.83)$$

where the approximation of \mathbf{d}_δ is provided in Eq. (3.81).

The approximation from Eq. (3.82) can be used as a standalone approximation or the approximation of the advective part from Eq. (3.83) can be supplemented by the approximation of the diffusive term from Eq. (3.35). The latter approach is utilized in here. The boundary fluxes are not subjected to any stabilization procedure.

3.5. Reconstruction of Stresses

Solving the system of discrete mass and momentum balance in every cell provides the vector of unknowns in the cell centers. To reconstruct effective stresses at the same locations we use the algorithm from Terekhov 2020a.

For the j th interface of the cell let us construct the matrices

$$\mathbf{N}_j = \begin{pmatrix} n_x & 0 & 0 & 0 & n_z & n_y \\ 0 & n_y & 0 & n_z & 0 & n_x \\ 0 & 0 & n_z & n_y & n_x & 0 \end{pmatrix}, \quad \mathbf{T}_j = \begin{pmatrix} x_j - x_V & 0 & 0 & 0 & \frac{z_j - z_V}{2} & \frac{y_j - y_V}{2} \\ 0 & y_j - y_V & 0 & \frac{z_j - z_V}{2} & 0 & \frac{x_j - x_V}{2} \\ 0 & 0 & z_j - z_V & \frac{y_j - y_V}{2} & \frac{x_j - x_V}{2} & 0 \end{pmatrix}, \quad (3.84)$$

where n_x , n_y and n_z are components of the unit normal to the j th interface; x_j , y_j and z_j are components of the j th interface center position; and x_V , y_V and z_V are components of the cell center position.

Collecting these matrices for N interfaces of the cell we obtain the following $3N \times 6$ and $3N \times 6$ matrices, and $3N \times 1$ vector

$$\mathbf{N} = \begin{pmatrix} \delta_1 \mathbf{N}_1 \\ \dots \\ \delta_N \mathbf{N}_N \end{pmatrix}, \quad \mathbf{T} = \begin{pmatrix} \mathbf{T}_1 \\ \dots \\ \mathbf{T}_N \end{pmatrix}, \quad \mathbf{f}'' = \begin{pmatrix} \delta_1 (\mathbf{f}_1 + \mathbf{b}p_{\beta 1}) \\ \dots \\ \delta_N (\mathbf{f}_N + \mathbf{b}p_{\beta N}) \end{pmatrix}, \quad (3.85)$$

where vector \mathbf{b} represents the Biot tensor \mathbf{B} in Voigt notation. The stresses at the cell center can then be reconstructed using the least squares solution

$$\boldsymbol{\sigma}'' = (\mathbf{T}^T \mathbf{N})^{-1} \mathbf{T}^T \mathbf{f}'', \quad (3.86)$$

where the Biot effective stress tensor $\boldsymbol{\sigma}'' = [\sigma''_{xx}, \sigma''_{yy}, \sigma''_{zz}, \sigma''_{yz}, \sigma''_{xz}, \sigma''_{xy}]^T$ is written in Voigt notation.

3.6. Nonlinear Finite Volume Method for Pure Elasticity Problem

The approximation of the traction vector derived in Eq. (3.28) can be repeated with $\mathbf{A}_1 = \mathbf{A}_2 = \mathbf{0}$ which corresponds to pure elasticity. Under this assumption, the approximation in Eq. (3.28) can be represented as a sum of *harmonic* $\mathbf{T}(\mathbf{u}_1 - \mathbf{u}_2)$ and *transversal* \mathbf{f}_τ terms (Terekhov *et al.* 2020) as

$$\mathbf{f} = \mathbf{T}(\mathbf{u}_1 - \mathbf{u}_2) + \mathbf{f}_\tau, \quad (3.87)$$

$$\mathbf{f}_\tau = -\Gamma \xi_\tau^u, \quad \mathbf{T} = \mathbf{T}_1(d_1 \mathbf{T}_2 + d_2 \mathbf{T}_1)^{-1} \mathbf{T}_2, \quad (3.88)$$

$$\Gamma = d_2 \mathbf{T}_1(d_1 \mathbf{T}_2 + d_2 \mathbf{T}_1)^{-1} \Gamma_2 + d_1 \mathbf{T}_2(d_1 \mathbf{T}_2 + d_2 \mathbf{T}_1)^{-1} \Gamma_1 + \mathbf{T}[\mathbf{I} \otimes (\mathbf{y}_1 - \mathbf{y}_2)^T], \quad (3.89)$$

where ξ_τ^u represents 9×1 vector of tangential gradients of displacements, the other notations are defined in Eqs. (3.20)-(3.23).

The weighting scheme applied to this approximation of the traction vector in Eq. (3.87) can be written as follows

$$\mathbf{f} = \mathbf{T}(\mathbf{u}_1 - \mathbf{u}_2) + \mathbf{M}_1 \mathbf{f}_{\tau 1} + \mathbf{M}_2 \mathbf{f}_{\tau 2}, \quad (3.90)$$

where $\mathbf{f}_{\tau 1}$ and $\mathbf{f}_{\tau 2}$ are the single-side approximations of traction vector, $\mathbf{f}_{\tau 1}$ and $\mathbf{f}_{\tau 2}$ are single-side approximations of the transversal term defined in Eq. (3.88). Furthermore, \mathbf{M}_1 and \mathbf{M} are 3×3 positive semidefinite matrices of the coefficients of convex combination such that $\mathbf{M}_1 + \mathbf{M}_2 = \mathbf{I}$. Taking $\mathbf{M}_1 = \mathbf{M}_2 = \mathbf{I}/2$ as defined in Eq. (3.32) results in the Average MPSA scheme (Terekhov *et al.* 2020) called according to the analogy of Average MPFA scheme (Schneider *et al.* 2018b).

The following general representation of single-side tractions $\mathbf{f}_{\tau 1}$ and $\mathbf{f}_{\tau 2}$ can be used once the gradient reconstruction described in the previous sections has been performed

$$\mathbf{f}_{\tau 1} = \mathbf{R}_2(\mathbf{u}_1 - \mathbf{u}_2) + \sum_{k \in \omega_1 \setminus \{2\}} \mathbf{R}_k(\mathbf{u}_1 - \mathbf{u}_k) + \sum_{k \in \tilde{\omega}_1} \mathbf{R}_k(\mathbf{u}_1 - \mathbf{r}_k) + \mathbf{h}_1, \quad (3.91)$$

$$\mathbf{f}_{\tau 2} = \mathbf{S}_1(\mathbf{u}_1 - \mathbf{u}_2) + \sum_{k \in \omega_2 \setminus \{1\}} \mathbf{S}_k(\mathbf{u}_k - \mathbf{u}_2) + \sum_{k \in \tilde{\omega}_2} \mathbf{S}_k(\mathbf{r}_k - \mathbf{u}_2) + \mathbf{h}_2, \quad (3.92)$$

where ω_1 and ω_2 denote the sets of cells participated in the approximation of $\mathbf{f}_{\tau 1}$ and $\mathbf{f}_{\tau 2}$ respectively, $\tilde{\omega}_1$ and $\tilde{\omega}_2$ denote the sets of boundary conditions defined in Eq. (2.55) and contributed to $\mathbf{f}_{\tau 1}$ and $\mathbf{f}_{\tau 2}$. Moreover, \mathbf{R}_k and \mathbf{S}_k are 3×3 matrices that represent the single-side approximations of $\mathbf{f}_{\tau 1}$ and $\mathbf{f}_{\tau 2}$, respectively. They are obtained from the reconstruction of displacement gradients in cells 1 and 2 being substituted to either Eq. (2.19) or to Eq. (3.87). Also, $\mathbf{r}_k = \mathbf{r}_{t,k} + r_{n,k} \mathbf{n}$ represents the right-hand side of boundary condition in Eq. (2.55) contributed to the single-side approximations, $\mathbf{h}_1, \mathbf{h}_2$ denotes the sum of Neumann boundary conditions contributed to the approximation of $\mathbf{f}_{\tau 1}$ and $\mathbf{f}_{\tau 2}$, respectively.

Substituting Eqs. (3.91) and (3.92) in Eq. (3.90) and rearranging the terms we can come up with the following equation

$$\mathbf{f} = \mathbf{D}_1 \mathbf{u}_1 - \mathbf{D}_2 \mathbf{u}_2 - (\mathbf{M}_1 \mathbf{a}_1 - \mathbf{M}_2 \mathbf{a}_2), \quad (3.93)$$

where the following notations are used

$$\mathbf{D}_1 = \mathbf{M}_1 \sum_{k \in \omega_1 \cup \tilde{\omega}_1} \mathbf{R}_k + \mathbf{M}_2 \mathbf{S}_1, \quad \mathbf{D}_2 = \mathbf{M}_1 \mathbf{R}_2 + \mathbf{M}_2 \sum_{k \in \omega_2 \cup \tilde{\omega}_2} \mathbf{S}_k, \quad (3.94)$$

$$\mathbf{a}_1 = \sum_{k \in \omega_1 \setminus \{2\}} \mathbf{R}_k \mathbf{u}_k + \sum_{k \in \tilde{\omega}_1} \mathbf{R}_k \mathbf{r}_k - \mathbf{h}_1, \quad \mathbf{a}_2 = \sum_{k \in \omega_2 \setminus \{1\}} \mathbf{S}_k \mathbf{u}_k + \sum_{k \in \tilde{\omega}_2} \mathbf{S}_k \mathbf{r}_k + \mathbf{h}_2. \quad (3.95)$$

We can construct a two-point nonlinear scheme in the same way as it was done for the flux approximation, by eliminating all the terms in Eq. (3.93) except those that are proportional to $\mathbf{u}_1, \mathbf{u}_2$. Assuming that the matrices of weights $\mathbf{M}_1, \mathbf{M}_2$ are diagonal, the following linear system of equations completely defines them

$$\mathbf{M}_1 \mathbf{a}_1 - \mathbf{M}_2 \mathbf{a}_2 = 0, \quad (3.96)$$

$$\mathbf{M}_1 + \mathbf{M}_2 = \mathbf{I}, \quad (3.97)$$

which solution is

$$\mathbf{M}_1 = \text{diag} \left\{ \frac{\mathbf{a}_2^{(i)} + \varepsilon}{\mathbf{a}_1^{(i)} + \mathbf{a}_2^{(i)} + 2\varepsilon} \right\}, \quad \mathbf{M}_2 = \text{diag} \left\{ \frac{\mathbf{a}_1^{(i)} + \varepsilon}{\mathbf{a}_1^{(i)} + \mathbf{a}_2^{(i)} + 2\varepsilon} \right\}, \quad i = 1, 2, 3, \quad (3.98)$$

where $\mathbf{a}_1^{(i)}, \mathbf{a}_2^{(i)}$ represent the components of $\mathbf{a}_1, \mathbf{a}_2$ vectors, and ε stands for a small regularization parameter (Terekhov *et al.* 2017).

The weights $\mathbf{M}_1, \mathbf{M}_2$ defined in Eq. (3.98) introduce nonlinearity to the scheme as they depend on unknown displacements through $\mathbf{a}_1, \mathbf{a}_2$. It leads to nonlinear discrete equations even for the linear continuous problem. This artificial complexity allows the numerical properties of the scheme to be adjusted. Here we reduce the stencil of the scheme to a two-point version as it results to a monotone convergent scheme for a scalar diffusion operator (Terekhov *et al.* 2017). However, the constraint in Eq. (3.96) can be chosen in a different way. For example, keeping only the terms with a single displacement component in each row in Eq. (3.93) it is possible to split nine coupled scalar diffusion operators in Eq. (2.19) into three decoupled operators. If a two-point stencil is also preserved within this constraint then it can be seen that the full matrix will be an M-matrix (Berman *et al.* 1979). Here we impose the constraint in Eq. (3.96) that produces a two-point approximation, but each semi-flux in Eqs. (3.91), (3.92) may include contributions from all displacement components.

The positivity of the solution is required for the purpose of nonlinear convergence (Terekhov *et al.* 2017). For those setups where negative values of any displacement component may be exhibited, we add a large constant to the corresponding displacement component as an initial guess. Dirichlet boundary conditions were modified accordingly.

3.7. Contact Constraints

The solution of a momentum balance at the contact under the constraints formulated in Eqs. (2.25)-(2.29) is challenging. From the mathematical standpoint, the existence and uniqueness of the solution of a contact problem have been proved only for small deformation frictionless contact (Kikuchi *et al.* 1995). The lack of existence theory in the case of Coulomb friction motivated the introduction of possible simplifications (known contact pressure or tangential stress, regularized Coulomb friction) that allow the existence and uniqueness of the solution to be proved (Yastrebov *et al.* 2013). Furthermore, the computational aspects of a frictional contact problem are complicated by the non-smooth energy functional associated with Coulomb friction (Kikuchi *et al.* 1995).

Several numerical techniques have been proposed to satisfy the contact constraints within FEM frameworks. The Lagrange multiplier method proposes the introduction of extra degrees of freedom called Lagrange multipliers that allow the constrained minimization problem to be converted to an unconstrained saddle-point problem. The necessity to update contact status requires the incorporation of the active-set strategy (Luenberger *et al.* 2008) into a nonlinear convergence loop. The penalty method imposes the contact constraints as numerical barriers defined by a penalty parameter which has to be infinite to fulfill the constraints precisely. In practice, it has been found that penalty parameter equal to one magnitude higher than Young's modulus represents a good balance between the fulfillment of the constraints and the ill-conditioning of the numerical problem for higher values. The augmented Lagrangian method represents a sort of Lagrange multiplier method regularized by a penalty term (Simo *et al.* 1992). Consequently, it yields a smooth energy functional for a fully unconstrained problem, satisfying the contact constraints with a finite value of the penalty parameter. Further developments in computational contact mechanics include the treatment of contact between non-conforming meshes, mortar and Nitsche's methods, finite deformations and contact detection (Chouly *et al.* 2022; Laursen 2010; Wriggers 2006; Yastrebov *et al.* 2013).

3.7.1. Penalty Method with Return-Mapping Algorithm

We employ the penalty method (Gallyamov *et al.* 2018; Garipov *et al.* 2016; Simo *et al.* 1992; Wriggers 2006; Yastrebov *et al.* 2013) to enforce contact constraints written in Eqs. (2.28) and (2.29). The penalty method leads to the return-mapping algorithm that can be formulated separately for normal and contact constraints as

$$\mathbf{f}'_N{}^{n+1} - \varepsilon_N \langle \mathbf{g}_N^{n+1} \rangle = 0, \quad (3.99)$$

$$\tilde{\mathbf{f}}_T = \mathbf{f}'_T{}^n + \varepsilon_T (\mathbf{g}_T^{n+1} - \mathbf{g}_T^n), \quad \tilde{\Phi} = |\tilde{\mathbf{f}}_T| - \mu^{n+1} \mathbf{f}'_N{}^{n+1}, \quad (3.100)$$

$$\mathbf{f}'_T{}^{n+1} - \tilde{\mathbf{f}}_T + \langle \tilde{\Phi} \rangle \frac{\tilde{\mathbf{f}}_T}{|\tilde{\mathbf{f}}_T|} = \mathbf{0}, \quad (3.101)$$

where $\tilde{\mathbf{f}}_T$ denotes trial traction, which represents the penalized effective tangential traction (Simo *et al.* 1992). Penalty parameters $\varepsilon_N, \varepsilon_T \gg 1$ are calculated as $\varepsilon_N =$

$f_{\text{scale}}E\delta/V, \varepsilon_T = f_{\text{scale}}G\delta/V$ where f_{scale} is an empirical scaling factor, δ denotes the area of the contact interface, V stands for the mean volume of two neighboring matrix cells, while E and G denote the mean Young's and shear moduli of two contacting matrix cells (Cardiff *et al.* 2017). Moreover, the Coulomb friction function Φ used as a slipping criterion is evaluated at the trial state $\tilde{\Phi} = \Phi(\tilde{\mathbf{r}})$ that accounts for the change of slip \mathbf{g}_r over the time step. Macaulay brackets $\langle a \rangle$ are equal to a if $a \geq 0$ and otherwise equal to zero. Thus, in the slip state $\tilde{\Phi} = 0$ Eq. (3.101) requires contact to remain at the slipping surface defined by $\Phi = 0$ where the direction of forces is defined by the trial traction. Contact reaches the stick state once the slip increment in Eq. (3.100) becomes negligible compared to the previous traction ($\mathbf{g}_r = \mathbf{0}$). In this case, Eq. (3.101) claims the traction to be equal to the trial one.

Although Eqs. (3.99)-(3.101) might be treated as boundary conditions with no extra degrees of freedom (Terekhov 2020b), it might be convenient to treat the gap vector \mathbf{g} as an unknown assigned to particular fault cells, especially in induced seismicity applications. Moreover, it allows for maintaining the block structure of the Jacobian.

The influence of mechanical stresses on the conductivity of hydraulically active faults can be of high interest in the modeling of hydraulic fracturing. Although we do not consider fault opening, this effect was addressed by other researchers using FEM with penalty regularization (Garipov *et al.* 2016), Nitsche's method (Garipov *et al.* 2019) or Lagrange multipliers (Franceschini *et al.* 2022b); and in the FVM framework with using Lagrange multipliers (Berge *et al.* 2020). The latter development within FVM also demonstrates the applicability of our developed method to modeling of hydraulically active faults.

3.8. Linear Solution Strategies

The efficient treatment of the systems of linear equations produced by coupled quasi-static poro- and contact mechanics remains challenging. Algebraic Multi-grid (AMG) methods have proved their efficiency in the solution of diffusion, linear elasticity, and other elliptic problems (Baker *et al.* 2010; Griebel *et al.* 2003), and they have become a part of preconditioning strategies for multi-physics problems (Ferronato *et al.* 2019; Nardean *et al.* 2022). A fixed-stress split concept can be exploited to construct a block-partitioned preconditioner for a coupled poromechanics (White *et al.* 2016), and extended to coupled multiphase flow and poromechanics (White *et al.* 2019). Alternatively, System-AMG (McCormick 1987) can handle the entire linear system which has been successfully applied for the solution of coupled multiphase flow and geomechanics (Gries *et al.* 2019). A physics-based partitioning of unknown displacements and Lagrange multipliers is utilized to construct a block-partitioned preconditioner for coupled elasticity and contact mechanics (Ferronato *et al.* 2019; Franceschini *et al.* 2022a; Franceschini *et al.* 2022b).

3.8.1. Fixed-Stress Split Preconditioner

In this section, we describe the fixed-stress split concept (Kim *et al.* 2011) for the construction of an efficient preconditioner for poromechanics (White *et al.* 2016). The idea of the method is to consider the block-partitioned linear system

$$\begin{aligned} \mathbf{L}^{-1} \mathbf{J} \delta \mathbf{d} &= \begin{pmatrix} \mathbf{I} & \mathbf{0} \\ -\mathbf{J}_{pu} \mathbf{J}_{uu}^{-1} & \mathbf{I} \end{pmatrix} \begin{pmatrix} \mathbf{J}_{uu} & \mathbf{J}_{up} \\ \mathbf{J}_{pu} & \mathbf{J}_{pp} \end{pmatrix} \begin{pmatrix} \delta \mathbf{u} \\ \delta \mathbf{p} \end{pmatrix} = \\ &= \begin{pmatrix} \mathbf{J}_{uu} & \mathbf{J}_{up} \\ \mathbf{0} & \mathbf{S}_{pp} \end{pmatrix} \begin{pmatrix} \delta \mathbf{u} \\ \delta \mathbf{p} \end{pmatrix} = - \begin{pmatrix} \mathbf{H}_s \\ \mathbf{H}_f - \mathbf{J}_{pu} \mathbf{J}_{uu}^{-1} \mathbf{H}_s \end{pmatrix}, \end{aligned} \quad (3.102)$$

where \mathbf{J} , \mathbf{H}_s and \mathbf{H}_f are the Jacobian and the residuals for momentum and mass balance equations produced by the numerical scheme, $\delta \mathbf{u}$ and $\delta \mathbf{p}$ are unknown increments of the vector of displacements and pressure, \mathbf{J}_{uu} , \mathbf{J}_{up} , \mathbf{J}_{pu} , \mathbf{J}_{pp} are contributions to the momentum balance and mass balance equations from displacement and pressure unknowns, \mathbf{L} is the lower-triangular term in an LDU decomposition of the Jacobian, and $\mathbf{S}_{pp} = \mathbf{J}_{pp} - \mathbf{J}_{pu} \mathbf{J}_{uu}^{-1} \mathbf{J}_{up}$ represents the Schur complement of block \mathbf{J}_{uu} in the Jacobian.

The concept of fixed-stress splitting is used here to provide the sparse approximation of \mathbf{S}_{pp} as

$$\tilde{\mathbf{S}}_{pp} = \mathbf{J}_{pp} - \text{diag}(\mathbf{J}_{pu} \mathbf{P}_u^{-1} \mathbf{J}_{up} \cdot \mathbf{e}), \quad (3.103)$$

where $\mathbf{e} = [1, 1, \dots, 1]^T$ is a probing vector, and \mathbf{P}_u^{-1} is a preconditioner used for the elasticity system.

This preconditioner is applied as follows:

1. At the beginning of every nonlinear (Newton) iteration, $\tilde{\mathbf{S}}_{pp}$ is evaluated. A single V-cycle of an algebraic multi-grid (AMG) solver is typically used for \mathbf{P}_u^{-1} .
2. At every iteration of the linear solver (GMRES) we employ the approximation $\tilde{\mathbf{S}}_{pp}$ to solve the upper triangular system in Eq. (3.102) as follows:
 - a) Solve the second equation in upper triangular system in Eq. (3.102): $\tilde{\mathbf{S}}_{pp} \tilde{\delta \mathbf{p}} = -\mathbf{H}_f$.
 - b) Use the known value of $\tilde{\delta \mathbf{p}}$ to solve the first equation in Eq. (3.102): $\mathbf{J}_{uu} \tilde{\delta \mathbf{u}} = -\mathbf{H}_s - \mathbf{J}_{up} \tilde{\delta \mathbf{p}}$.
3. Provide the linear solver with the approximate solution $\{\tilde{\delta \mathbf{u}}, \tilde{\delta \mathbf{p}}\}$ as initial guess.

The system for the pressure unknowns is preconditioned using a single V-cycle as well. The generalized minimal residual (GMRES) method is used as an outer solver.

3.8.2. System Algebraic Multigrid (SAMG)

The discovery of the multigrid principle was a breakthrough for solving large systems of elliptic partial differential equations. This principle constitutes the use of

a hierarchical algorithm that works not only with a given discretization of differential operators but operates on a hierarchy of grids ensuring a rapid reduction of both high- and low-frequency error components. In particular, smoothing steps applied to a hierarchy of coarsened grids steadily eliminate various components of the Fourier transform of the error vector starting from the higher-frequency down to lower-frequency components. A wide range of possible applications dictated the increasing interest in algebraic multigrid (AMG) methods that construct a reasonable hierarchy automatically from the information contained in the provided Jacobian matrix rather than considering a hierarchy of discretizations (Brandt 1986; Ruge *et al.* 1987).

One of the implementations of AMG solvers, called System AMG or SAMG, further continues the line of the black-box solvers that require minimal extra knowledge about the used grid. Moreover, it extends the AMG method to the coupled linear systems with different physical unknowns involved (Clees 2005; Ruge *et al.* 1987). SAMG considers two approaches to handle the coupled linear system: unknown-wise and point-wise. An unknown-wise approach applies the scalar AMG independently to every unknown in the diagonalized matrix while the coupling terms are taken into account on the coarser levels. A point-wise approach utilizes the same coarse/fine splitting for every unknown constructed from the point connectivity identified from the matrix entries.

In this work, we attempt to utilize the SAMG library for the solving of linear systems stemming from the coupled formulation of poroelasticity and contact mechanics. The use of gap vectors as fault unknowns allows all mechanical unknowns to be treated in the same manner. As additional information, SAMG requires the tagging of the kind of unknowns (pressure, displacement, or saturation), the same physical unknowns and the equations written at the same point in space. Unfortunately, the linear systems obtained from the proposed FVM scheme coupled with penalty method for contact mechanics demonstrate neither symmetry nor positive-definiteness properties that are important for an effective work of AMG-based preconditioners. Additionally, in some cases the successful application of SAMG for these systems is limited by poor-conditioning which can be barely alleviated by suitable dimensionalization.

3.8.3. Incomplete LU Factorization for Fully Dynamic Modeling

The introduction of the inertia term into the momentum balance equation changes the kind of equations, making them hyperbolic-like. Incomplete LU (ILU) factorization has demonstrated its efficacy as a preconditioner, especially for the elimination of high-frequency errors in geo-energy applications (Cao *et al.* 2005; Forsyth Jr. *et al.* 1986; Wallis *et al.* 1985). We utilize the ILU(0) preconditioner with GMRES iterations for the implicit solution of a fully dynamic problem.

3.9. Implementation Details

The presented schemes of FVM, the penalty method for contact constraints and linear solution strategy described in the previous sections have been implemented in an open-source Delft Advanced Research Terra Simulator called DARTS (Voskov *et al.* 2023). It is a scalable parallel simulation framework, which has been successfully applied for geo-energy applications including modeling of hydrocarbon (Khait *et al.* 2018a; Lyu *et al.* 2021a), geothermal (Khait *et al.* 2018b; Wang *et al.* 2020b) and CO₂ sequestration (Kala *et al.* 2020; Lyu *et al.* 2021b).

One of the main advantages of DARTS as a simulation framework is its flexibility. It is achieved by the following a hybrid code structure. The computationally demanding interfaces are implemented and optimized in C++ and, subsequently, exposed to Python. On the Python side, those interfaces are combined into user-friendly routines that enable easy model setup with arbitrary user-defined properties, running high-performance simulations, and the post-processing of obtained results.

The flexibility in regard to fluid mixture properties is reinforced by the Operator-Based Linearization (OBL) technique incorporated into DARTS (Khait *et al.* 2018b; Voskov 2017). The idea behind this technique is the parametrization of operators participating in the discrete equations rather than deriving the analytical expressions for them. This parametrization is performed in a state space that is single for all cells sharing the same fluid physics. Interpolation techniques allow operator values and their derivatives with respect to the state dimensions to be evaluated. As a result, OBL can easily incorporate arbitrary user-defined fluid properties. In coupled poroelastic modeling, OBL is utilized in the assembly of operators participating in fluid mass balance equations.

The incorporation of the new functionality into the structure of DARTS can be done in a few following stages.

3.9.1. Discretization

The implementation of the FVM described above starts with the evaluation of the approximations of the vector of fluxes over all interfaces in a computational grid. In the presented version the discretization can be performed once at the pre-processing stage before simulation. The discretization includes the following steps:

1. **Geometry processing:** For a given mesh (vertices and cells) we evaluate an adjacency matrix of the cells comprising the computational grid. Besides, we prepare the necessary geometrical data: cell and face centroids, face normals and their areas, and cell volumes.
2. **Gradient reconstruction:** For a given mesh with specified material properties, boundary conditions, and contacts we calculate the approximation of the cell-wise gradients of unknown pressure and displacements. For every cell we assemble the linear system of Eqs. (3.29), (3.57)-(3.61), (3.66) and (3.67) (an equation per cell's interface, depending on the type of interface: matrix, contact, boundary, contact boundary). The least-square solution of the

assembled system from Eq. (3.31) provides the approximation of gradients.

3. **The approximation of fluxes:** We evaluate the approximation of fluid fluxes and tractions at every interface of the computational grid according to Eqs. (3.28), (3.35), (3.36), (3.48), (3.49), (3.52), (3.55), (3.56), (3.63), (3.65), (3.82) and (3.83). The approximations are assembled for diffusive and advective terms separately and provided as flattened arrays of coefficients with the associated stencil. For convenient Jacobian assembly, the approximations for every, either matrix or contact, interface are provided twice, for each of two neighboring cells.

The particular implementation of the described discretization procedures has been done in C++. For convenient and readable realization, a class for small matrices with support of BLAS operations and slicing has been added. Next, the structure that describes approximation has been developed with supported merge and scalar multiplication operations. This structure consists of an array of coefficients, an array of cell (or boundary condition) indices defining the stencil and the free terms. This structure has been utilized only during discretization: in gradient reconstruction and in the assembly of approximations. The final approximations are provided in the form of flattened arrays.

The other important implementation feature is that the contribution of boundary conditions to the approximations has been implemented in a way unified with the contributions of matrix or contact cells. Although, the boundary conditions do not represent unknowns they participate in the assembly of fluxes, not giving direct contributions to the Jacobian matrix. Therefore, during the discretization and matrix assembly stages, they have an enumeration shared with cells.

It is worth to be noted that the proper incorporation of the gravity term with pressure-dependent fluid density from Darcy's law to the coupled discretization is possible due to the fact that the approximations of both gradients and fluxes are linear with respect to this term.

Gradient Reconstruction

In our experience, special attention should be paid to the gradient reconstruction of unknowns and, in particular, to the matrix inversion in Eq. (3.31), as its quality may significantly affect the accuracy of the subsequent simulation.

First, we should clarify the reconstruction of gap gradients over the 2D surfaces representing faults. This reconstruction is based on the assembly of Eqs. (3.59)-(3.61) that represent interpolation conditions within these 2D surfaces. Note that even though we use the term 2D surface, they can represent curvilinear surfaces in 3D space which admit parametrization with only two variables. It is important as these in-surface conditions do not allow us to reconstruct full gradients. Instead, we use the Moore-Penrose matrix pseudoinverse based on the Singular Value Decomposition to evaluate the approximation of in-surface gradients in Eq. (3.31). Although an equidimensional fault representation is used in the calculation of fluid mass balance in faults, and fault-matrix (off-surface) connections also participate in

the reconstruction, we found that the use of pseudoinversion for the reconstruction of pressure gradients in fault cells is more robust than normal inversion in some cases.

Second, the reconstruction of gradients in matrix cells can be problematic. A particular combination of boundary conditions adjacent to matrix cell or heterogeneity pattern may dramatically increase the condition number of the matrix $\mathbf{M}_i^T \mathbf{M}_i$ in Eq. (3.31) making its inversion with standard LU-decomposition incorrect. In some cases, the use of a small regularization parameter $\xi \mathbf{I}$, which can be added to the matrix, can already help to restore the matrix conditionality (Terekhov 2021b). However, sometimes, this technique may not provide enough reduction in the condition number. We use dimensionality reduction to balance equations in \mathbf{M} either coming from different connections or between displacement and pressure conditions within a single connection.

The gradient reconstruction in the presence of the Neumann boundary condition for the momentum balance can sometimes introduce issues. We discovered that incorporating Neumann boundary condition in Eq. (3.67) into the gradient reconstruction can make $\mathbf{M}_i^T \mathbf{M}_i$ not-invertible or drastically change the final solution. Excluding the Neumann boundary conditions from the reconstruction of displacement gradients in adjacent cells has helped to overcome this issue. This approach applies only to the reconstruction of displacement gradients in cells adjacent to Neumann boundaries, while the boundary condition still receives the consistent approximation according to Sec. (3.3.4).

3.9.2. Matrix Assembly

In DARTS, an instance of the class called “engine” assembles the Jacobian matrix in block compressed sparse row format (BCSR) and the vector of residuals. For the new functionality of coupled poroelasticity and contact mechanics, a new engine class has been implemented. The following structure briefly outlines the assembly stage:

1. Iterate over matrix, fault and well cells.

- a) Assembly of *flux term*: Iterate over connections of a given matrix cell.
 - i. Iterate over cells within the stencil of approximation of fluxes at a given connection. Add corresponding contributions to the vector of fluxes, cell's volumetric strain, and to the Jacobian matrix.
 - ii. Iterate over the boundary conditions within the stencil of approximation of fluxes at a given connection. Add corresponding contributions to the vector of fluxes and the cell's volumetric strain.
 - iii. Add free terms to the vector of fluxes, and the cell's volumetric strain.
 - iv. Add an assembled vector of fluxes to the residual.
- b) Assembly of *accumulation term*: Add the time derivative term to the Jacobian matrix and the vector of residuals.

2. Iterate over faults and fault cells (contact mechanics).

- a) Assemble effective stresses used in sliding criterion
- b) Transform stresses and gaps to the local basis associated with a contact interface.
- c) For a given friction law, assemble a trial slipping criterion according to Eq. (3.100) and update the state.
- d) Assemble contact Eqs. (3.99) and (3.101) in the local basis. Apply appropriate dimensionality scaling if needed.
- e) Transform contact equations from unknowns written in the local basis to the Cartesian (global) unknowns. Add corresponding contributions to Jacobian matrix and the vector of residuals.

3. **Iterate over wells:** Apply well controls to the cells assigned to well heads. No momentum balance is considered in wellbores; assign an identity matrix to the corresponding Jacobian block to keep block structure. Add the contributions from fluid mass balance to Jacobian matrix and the vector of residuals.

The first round of iterations over all the cells does not cover the contact constraints which are assembled in the following loop over faults and associated fault cells. The assembly of the momentum and fluid mass fluxes constitutes the major part of the assembly procedure described above. It is important to store these fluxes as the reconstruction of cell-centered stresses described in Sec. (3.5) requires them. A similar reconstruction can be used to estimation of fluid velocities necessary for the evaluation of streamlines and associated analyses (Datta-Gupta *et al.* 2007).

3.9.3. Linear Solution

Usually, the solution of linear systems makes up the largest part of simulation time. In order to accelerate the numerical solution for fluid dynamics applications, a set of linear solvers for large sparse systems has been implemented and integrated into DARTS. They include the CPU and GPU implementations of a Constrained Pressure Residual preconditioning strategy with Algebraic Multigrid (AMG) and incomplete LU (ILU) factorization as preconditioners for elliptic (or parabolic) and hyperbolic subsystems. The preconditioners have been incorporated in the iterations of the generalized minimal residual method (GMRES) (Wang *et al.* 2020b).

For fully implicit poroelastic systems, the fixed-stress split preconditioner described in Sec. 3.8.1 has been implemented for CPU backend. Its program implementation basically follows the algorithm described in Sec. 3.8.1. The BoomerAMG solver (Henson *et al.* 2002) performs preconditioning \mathbf{P}_u^{-1} for an elastic subsystem while the local proprietary version of AMG has been utilized as the preconditioner \mathbf{P}_p^{-1} for a fluid flow subsystem. A local implementation of the ILU preconditioner is used for the fully dynamic simulation. All preconditioners are incorporated into the existing GMRES solver.

For the systems appearing in the fully implicit and coupled discretization of poroelasticity and contact mechanics, mainly, the direct solver from SuperLU library (Demmel *et al.* 1999; Li *et al.* 1999) has been employed. Apart from the direct solver, we

incorporated the interfaces to System Algebraic Multigrid solver (Gries *et al.* 2019; McCormick 1987) into DARTS.

3.9.4. User Interfaces

The Python side of DARTS provides users with shortcuts to many model setups. A model setup usually incorporates mesh import, specification of fluid physics and reservoir properties, well controls, initial and time-dependent boundary conditions. To facilitate the structured implementation of all these routines, the model class is utilized.

The poroelastic formulation substantially complicates the specification of reservoir properties compared to fluid dynamics. This motivated us to introduce a separate reservoir class that structures the setup of reservoir properties, including faults with frictional contacts. Once the model setup with reservoir properties is initialized, the simulation can be launched.

A main script for the running poroelastic simulation in DARTS usually includes two functions that are responsible for managing time steps and non-linear (Newton) iterations within a time step respectively. The one more function runs the whole script starting from the model setup, initialization and subsequent time stepping, and post-processing.

In some simulations, it is useful to turn off the poroelastic mode and perform a purely mechanical simulation with a predefined pressure distribution. Moreover, for modeling realistic subsurface reservoirs, a special initialization step is often required. For example, this step allows the initial volumetric strains associated with initial porosity to be estimated. These functionalities are supported with a special flag passed to the matrix assembly that prevents adding extra terms to the Jacobian matrix.

4

Benchmarking Numerical Solution

Summary

This chapter presents a number of benchmarks that the proposed Finite Volume framework has undergone. These include numerical convergence tests, as well as comparisons with existing analytical and semi-analytical solutions for continuous and faulted poroelastic media. Additionally, the framework's results are juxtaposed against numerical solutions obtained from other numerical frameworks, further demonstrating its efficacy and accuracy. The solution behavior in the presence of the inf-sup instability is investigated in multiple tests. Finally, the performance of the implemented linear solution strategy is assessed in the mechanical extension of the SPE10 model.

4.1. Linearity-Preserving Test

A numerical scheme is called *linearity-preserving* when its derivation is exact whenever the solution is piecewise linear and the permeability (or diffusion) tensor remains piecewise constant within each cell. As a result, a linearity-preserving scheme must demonstrate the accuracy of the magnitude of numerical precision for linear solutions. Linearity-preserving property is a desirable feature of numerical schemes as these schemes are found to be accurate on highly skewed meshes (Luo *et al.* 2017).

Consider a cubic domain $\Omega = [0, 1]^3$ [m] of a poroelastic body with the following constant stiffness matrix \mathbf{C} , Biot tensor \mathbf{B} and permeability tensor \mathbf{K} (Terekhov 2020a):

$$\mathbf{C} = \begin{bmatrix} 93 & 46 & 22 & 13 & 72 & 35 \\ 46 & 95 & 41 & 62 & 56 & 24 \\ 22 & 41 & 89 & 25 & 33 & 21 \\ 13 & 62 & 25 & 87 & 13 & 25 \\ 72 & 56 & 33 & 13 & 99 & 57 \\ 35 & 24 & 21 & 25 & 57 & 78 \end{bmatrix} \text{bar},$$

$$\mathbf{B} = \begin{bmatrix} 1 & 6 & 5 \\ 6 & 67 & 27 \\ 5 & 27 & 76 \end{bmatrix}, \quad \mathbf{K} = \begin{bmatrix} 25 & 2 & 39 \\ 2 & 42 & 7 \\ 39 & 7 & 100 \end{bmatrix} \text{mD}, \quad (4.1)$$

with the following linear reference solution

$$\begin{bmatrix} u \\ v \\ w \\ p \end{bmatrix} = \begin{bmatrix} 1 & 2 & 3 & 4 \\ 6 & 7 & 8 & 9 \\ 11 & 12 & 13 & 14 \\ 16 & 17 & 18 & 19 \end{bmatrix} \begin{bmatrix} x \\ y \\ z \\ t \end{bmatrix} + \begin{bmatrix} 5 \\ 10 \\ 15 \\ 20 \end{bmatrix}, \quad (4.2)$$

which satisfies the system of Eqs. (2.46), (2.47) and (2.55). Note, that in this example we employ a full Biot tensor \mathbf{B} . Although such a matrix is of no physical significance for practical applications, it serves to test the computational aspects of the algorithm. We assume that densities and viscosity in Eqs. (2.52) and (2.53) remain constant. Substituting material properties from Eq. (4.1) and reference solution from Eq. (4.2) into balance laws from Eqs. (2.46) and (2.47), we can analytically derive the magnitude of left-hand side of the equations. Substituting these values as a right-hand side and specifying initial and boundary (Dirichlet) conditions according to Eq. (4.2), we expect that the numerical solution will match the reference one from Eq. (4.2) up to machine precision. The parameters used for calculation are listed in Table 4.1.

The results are summarized in Table 4.2. The calculations were performed using structured grids composed of cubes and wedges, and an unstructured tetrahedral grid up to time $t = 1$ day. The linear solution was observed for every time step and for each type of grid. Absolute errors at $t = 1$ day with respect to the reference solution in Eq. (4.2) are almost at the level of machine double floating-point precision.

Table 4.1.: Parameters used for calculations in linearity preservation test case.

μ_f , cP	g , bar m ² kg ⁻¹	$1/M$, bar ⁻¹	ρ_f , kg m ⁻³
9.81E-2	9.81E-2	1.45E-06	978

Table 4.2.: Absolute errors of solutions calculated on different mesh types for Test Case 1.

Cell geometry	Nr. of cells	$\ \mathbf{u} - \mathbf{u}_h\ _{L_2}$	$\ p - p_h\ _{L_2}$
Cubic	64	3.0E-12	7.99E-11
Cubic	8000	3.38E-12	7.29E-10
Wedge	16000	7.14E-14	2.53E-11
Tetrahedron	16030	1.82E-11	4.55E-12

4.2. Convergence Tests

For the same $\Omega = [0, 1]^3$ m cubic domain let us consider the following constant stiffness matrix \mathbf{C} , Biot tensor \mathbf{B} and permeability tensor \mathbf{K}

$$\mathbf{C} = \begin{bmatrix} 1.323 & 0.0726 & 0.263 & 0.108 & -0.08 & -0.239 \\ 0.0726 & 1.276 & -0.318 & 0.383 & 0.108 & 0.501 \\ 0.263 & -0.318 & 0.943 & -0.183 & 0.146 & 0.182 \\ 0.108 & 0.383 & -0.183 & 1.517 & -0.0127 & -0.304 \\ -0.08 & 0.108 & 0.146 & -0.0127 & 1.209 & -0.326 \\ -0.239 & 0.501 & 0.182 & -0.304 & -0.326 & 1.373 \end{bmatrix} [\text{bar}], \quad (4.3)$$

$$\mathbf{B} = \begin{bmatrix} 1.5 & 0.1 & 0.5 \\ 0.1 & 1.5 & 0.15 \\ 0.5 & 0.15 & 1.5 \end{bmatrix}, \quad \mathbf{K} = \begin{bmatrix} 1.5 & 0.5 & 0.35 \\ 0.5 & 1.5 & 0.45 \\ 0.35 & 0.45 & 1.5 \end{bmatrix} [\text{mD}], \quad (4.4)$$

and the reference solution (Terekhov 2020a) as

$$\begin{aligned} u(x, y, z, t) &= [(x - 0.5)^2 - y - z](1 + t^2) \\ v(x, y, z, t) &= [(y - 0.5)^2 - x - z](1 + t^2) \\ w(x, y, z, t) &= [(z - 0.5)^2 - x - y](1 + t^2) \\ p(x, y, z, t) &= \frac{1}{2 \sin(1)} \sin((1 - x)(1 - y)(1 - z)) + 0.5(1 - x)^3(1 - y)^2(1 - z)(1 + t^2). \end{aligned} \quad (4.5)$$

Following the same procedure we explained in the previous test case, we substitute Eqs. (4.3) and (4.4) to Eqs. (2.46) and (2.47) and calculate the right-hand side sufficient for them to be satisfied. We use automatic differentiation for the calculation of derivatives. Dirichlet boundary and initial conditions are also aligned with Eq. (4.5). We assume that densities and viscosity in Eq. (2.52) and (2.53) remain constant. All relevant parameters used in the calculations are listed in Table 4.3.

L2 norms of differences between reference and calculated solutions are depicted in Fig. 4.1. The calculations were done for a few cubic meshes of different resolutions and using different time step sizes. They demonstrate superlinear convergence for the vector of displacements and nearly linear convergence for the pressure. The fact that the order of convergence is below the second order can be explained by the Backward-Euler scheme used for the time integration (Terekhov 2020a).

4

Table 4.3.: Parameters used for calculations in convergence test case.

μ_f , cP	g , bar m ² kg ⁻¹	$1/M$, bar ⁻¹	ρ_f , kg m ⁻³	ρ_s , kg m ⁻³
9.81E-2	9.81E-2	1.45E-06	978	2500

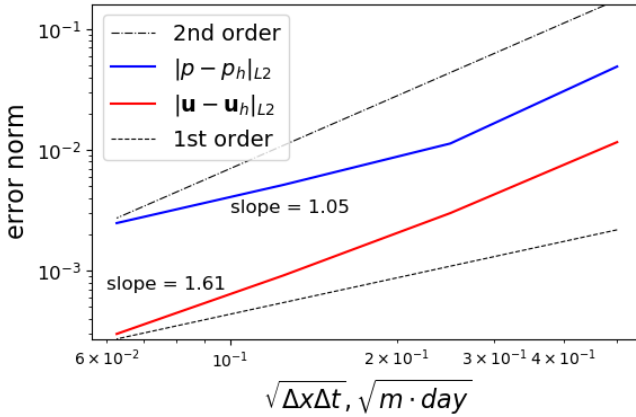


Figure 4.1.: Error norms of pressure and displacements calculated using cubic meshes of various resolutions.

4.3. Terzaghi's Problem

We further validate the numerical scheme against the analytical solution for the one-dimensional consolidation problem, also known as Terzaghi's problem. In this problem, an instant uniaxial compression is applied to the poroelastic domain depicted in Fig. 4.2. A horizontal compressive force $F = 10 \text{ MPa}$ and constant initial pressure $p_0 = 0 \text{ Pa}$ are applied at $t = 0$ to the right side of the domain of $h = 100 \text{ m}$ horizontal extent. All other sides of the domain are impermeable to fluid and subjected to the roller boundary conditions (normal displacement and tangential tractions are equal to zero). The domain's permeability $\mathbf{K} = k\mathbf{I}$ and Biot's tensor $\mathbf{B} = b\mathbf{I}$ are defined by scalar values $k = 1 \text{ mD}$, $b = 0.9$, while the domain's stiffness is determined by Young's modulus $E = 1 \text{ GPa}$ and Poisson's ratio $\nu = 0.25$. The domain of porosity $\phi = 0.375$, fluid compressibility $c_f = 10^{-5} \text{ bar}^{-1}$, fluid viscosity $\mu_f = 1 \text{ cP}$.

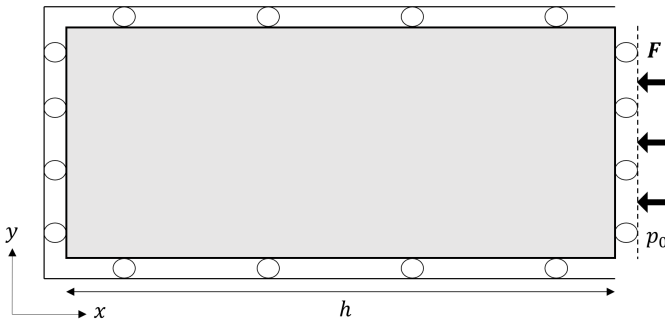


Figure 4.2.: Terzaghi setup.

The analytical solution for the Terzaghi problem can be written as follows (Verruijt 2016)

$$u_x(x, t) = -\frac{Fx(1-2\nu)}{2G(1-\nu)} - \frac{4Fh(\nu_u - \nu)}{\pi^2 G(1-\nu)(1-\nu_u)} \sum_{m=0}^{\infty} \frac{\exp\left(- (2m+1)^2 \frac{\pi^2 ct}{4h^2}\right)}{(2m+1)^2} \cos\left((2m+1) \frac{\pi(x+h)}{2h}\right), \quad (4.6)$$

$$p(x, t) = \frac{FB(1+\nu_u)}{3(1-\nu_u)} - \frac{FB(1+\nu_u)}{3(1-\nu_u)} \sum_{m=0}^{\infty} (-1)^m \left(\operatorname{erfc} \frac{(2m+1)h+x}{\sqrt{4ct}} + \operatorname{erfc} \frac{(2m+1)h-x}{\sqrt{4ct}} \right), \quad (4.7)$$

where G is shear modulus, and M is Biot modulus. The consolidation coefficient c , the undrained Poisson's ratio ν_u and Skempton's coefficient B are defined as follows

$$c = \frac{2kG(1-\nu)(\nu_u - \nu)}{\mu_f b^2 (1-\nu_u)(1-2\nu)^2}, \quad \nu_u = \frac{3\nu + bB(1-2\nu)}{3 - bB(1-2\nu)}, \quad B = \frac{3b(1-2\nu)M}{E + 3b^2(1-2\nu)M}, \quad (4.8)$$

This problem was solved numerically with the non-stabilized scheme using a rectangular grid comprised of 30 cells per horizontal extent h . Fig. 4.3 demonstrates the comparison of calculated results against the analytical solution from Eqs. (4.6) and (4.7). In the top left subfigure (Fig. 4.3a), pressure estimated at $x = 1.66$ m is shown over time. The top right subfigure (Fig. 4.3b) demonstrates pressure profiles over a horizontal line at three moments of time. The horizontal displacement u_x estimated at $x = 98.33$ m are plotted over time in the bottom left subfigure (Fig. 4.3c). The bottom right subfigure (Fig. 4.3d) shows the spatial profiles of vertical displacements at three moments of time.

Fig. 4.3 demonstrates a good match to the analytical solution obtained even with this coarse grid. The compression of the poroelastic domain causes an instant pressure build-up, uniform throughout the domain. As a result, thin boundary layer originates at the right side of the domain subjected to the constant initial pressure. Numerically it produces spurious oscillations that disappear over time. They can be observed in Fig. 4.3b. A more detailed discussion of this phenomenon is presented in one of the next sections.

4.4. Mandel's Problem

Consider the same domain as in the previous section with different boundary conditions illustrated in Fig. 4.4. Now roller boundary conditions are applied only to the left and bottom boundaries of the domain. The right boundary is free of both normal and tangential forces while a normal load is applied from the top. Note that

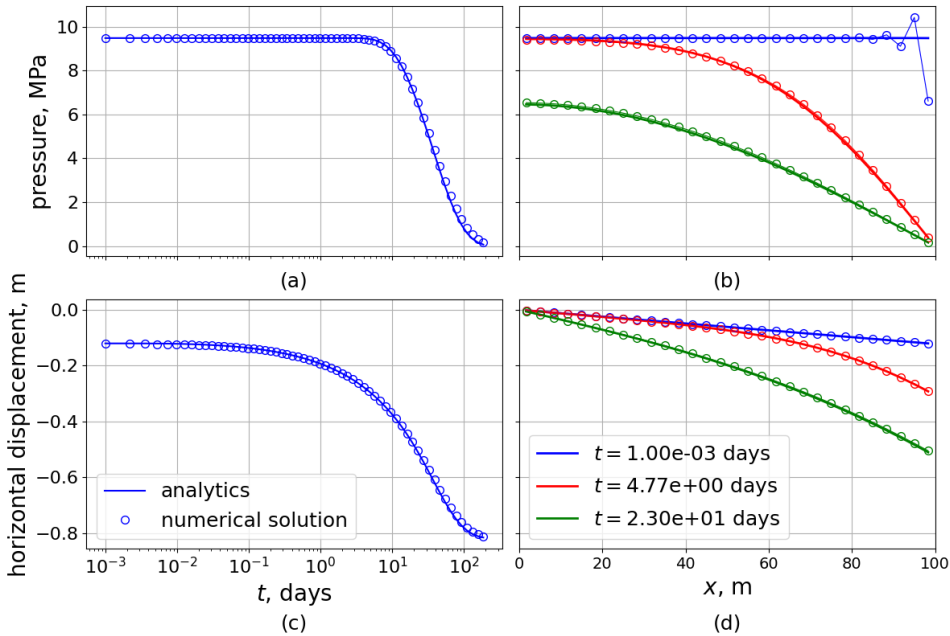


Figure 4.3.: Comparison of the analytical and numerical solutions for Terzaghi's problem. In the left column, pressure (a) and displacement (c) estimated at $x = 1.66$ m and $x = 98.33$ m respectively are shown over time. In the right column, pressure (b) and displacement (d) profiles over the whole domain are depicted at three moments of time.

this load is applied through the stiff bulk in a way that produces a uniform vertical displacement. Therefore, it could be more convenient to specify time-dependent normal displacement at the top estimated from analytical expressions. No-flow conditions are specified for all boundaries except for the right one subjected to the Dirichlet condition $p_0 = 0$ Pa. This setup is the so-called Mandel's problem which is often used as an example to demonstrate specific aspects of poroelasticity.

A porous homogeneous domain is characterized by Young's modulus $E = 1$ GPa, Poisson's ratio $\nu = 0.25$, a diagonal permeability tensor $\mathbf{K} = k\mathbf{I}$, $k = 1$ mD, saturated with a single-phase compressible fluid with compressibility $c_f = 10^{-5}\text{bar}^{-1}$, viscosity $\mu_f = 1$ cP, and with a Biot modulus $M = 10^{-5}\text{bar}^{-1}$ and a diagonal Biot tensor $\mathbf{B} = b\mathbf{I}$, $b = 0.9$.

The analytical solution of Mandel's problem reads as (Terekhov *et al.* 2022; Ver-

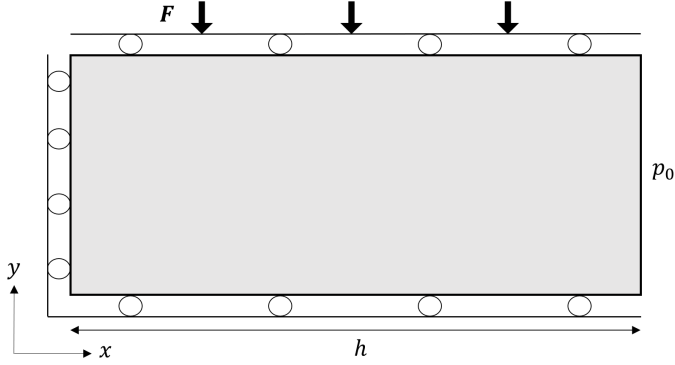


Figure 4.4.: Mandel setup.

4

ruijt 2016)

$$u_x(x, t) = \frac{F}{Gh} \left(\frac{v_x}{2} + \sum_{m=1}^{\infty} \frac{\left(h \sin \frac{\omega_m x}{h} - v_u x \sin \omega_m \right) \cos \omega_m}{\omega_m - \sin \omega_m \cos \omega_m} \exp \left(-\frac{\omega_m^2 ct}{h^2} \right) \right), \quad (4.9)$$

$$u_y(y, t) = \frac{F}{Gh} \left(\frac{(v-1)y}{2} - (v_u - 1)y \sum_{m=1}^{\infty} \frac{\sin \omega_m \cos \omega_m}{\omega_m - \sin \omega_m \cos \omega_m} \exp \left(-\frac{\omega_m^2 ct}{h^2} \right) \right), \quad (4.10)$$

$$p(x, t) = \frac{2FB(1+v_u)}{3h} \sum_{m=1}^{\infty} \frac{\left(\cos \frac{\omega_m x}{h} - \cos \omega_m \right) \sin \omega_m}{\omega_m - \sin \omega_m \cos \omega_m} \exp \left(-\frac{\omega_m^2 ct}{h^2} \right), \quad (4.11)$$

where ω_m are positive roots of the equation

$$\cos \omega_m - \frac{v_u - v}{1 - v} \frac{\sin \omega_m}{\omega_m} = 0,$$

and the consolidation coefficient c , the undrained Poisson's ratio v_u and Skempton's coefficient B are defined in Eq. (4.8). The initial values of displacements and pressure are assigned as

$$u_x(x, 0) = \frac{Fv_u x}{2Gh}, \quad u_y(y, 0) = \frac{F(v_u - 1)y}{2Gh}, \quad p(x, 0) = \frac{FB(1+v_u)}{3h}.$$

For the numerical solution, we use a 30×30 square mesh. Fig. 4.5 depicts a comparison between the numerical solution and analytics from Eqs. (4.9),(4.11). As in the previous section, the top left subfigure (Fig. 4.5a) shows the pressure dynamics evaluated at $x = 1.66$ m, the bottom left subfigure (Fig. 4.5c) shows the dynamics of horizontal displacement u_x at $x = 98.33$ m, the right top (Fig. 4.5b)

and the right bottom (Fig. 4.5d) subfigures illustrate the profiles of pressure and vertical displacement correspondingly over a horizontal centerline at three moments in time. The numerical solution matches analytics quite well. As in the previous example, spurious oscillations arise around the right side of the domain at the very beginning of simulation. They can be seen in the top right subfigure (Fig. 4.5b). A more detailed discussion of this instability is provided in Sec. 4.6.

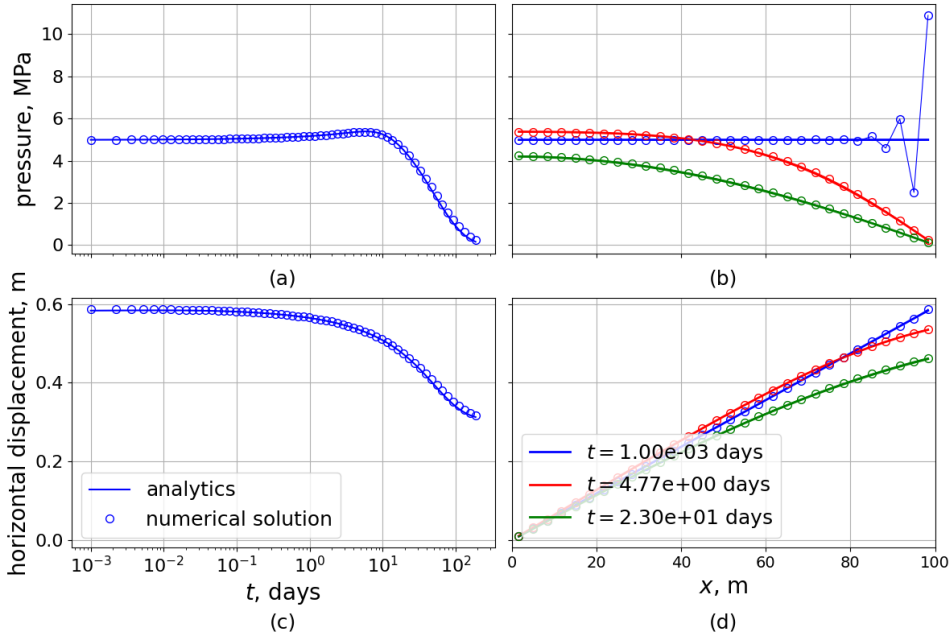


Figure 4.5.: Comparison of the analytical and numerical solutions for the Mandel's problem. In the left column, pressure (a) and displacement (c) at the center of the most left cell are shown over time. In the right column, pressure (b) and displacement (d) profiles over the whole domain are depicted at three moments in time.

4.5. Two-Layer Terzaghi's Problem

The analytical solution in the presence of the two heterogeneous layers in Terzaghi's problem remains feasible (Verruijt 2016). Thus, this test case represents a nice benchmark for the validation of the numerical solution in the presence of heterogeneity. As in the previous sections, we consider a poroelastic domain of vertical extent $h = 100$ m comprised of two layers of distinct properties with $h_1 = 25$ m and $h_2 = 75$ m respectively. The first layer is adjacent to the right boundary which is subjected to a constant normal load $F = 10$ MPa and a constant initial pressure $p_0 = 0$ Pa. As in the original Terzaghi's problem, the roller no-flow boundary conditions are applied to the other boundaries. The properties of the porous matrix and

the fluid are listed in Tab. 4.4.

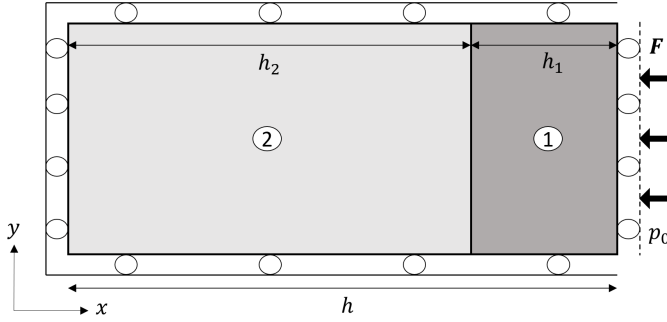


Figure 4.6.: Two-layer Terzaghi setup.

For simplicity, we assume that the Skempton's coefficient is equal in both layers: $B = B_1 = B_2$. In this case, the analytical solution follows as (Terekhov *et al.* 2022; Verruijt 2016)

$$g_m = \frac{2BF}{\omega_m} \frac{\exp(-\omega_m^2 c_2 t / h_2^2)}{(1 + \beta\theta) \cos(\theta\omega_m) \sin \omega_m + (\beta + \theta) \sin(\theta\omega_m) \cos \omega_m}, \quad (4.12)$$

$$p(\xi, t) = \sum_{m=0}^{\infty} g_m(t) \begin{cases} \cos \omega_m \cos(\theta\omega_m \xi / h_1) - \beta \sin \omega_m \sin(\theta\omega_m \xi / h_1), & \xi > 0, \\ \cos \omega_k \cos(\omega_m \xi / h_2) - \sin \omega_m \sin(\omega_m \xi / h_2), & \xi < 0, \end{cases} \quad (4.13)$$

$$u_x = F \begin{cases} m_1 \xi + m_2 h_2, & \xi > 0, \\ m_2 (\xi + h_2), & \xi < 0, \end{cases} - \sum_{m=0}^{\infty} \frac{g_m(t)}{\theta\omega_m} \begin{cases} \alpha_1 m_1 h_1 (\cos \omega_m \sin(\theta\omega_m \xi / h_1) + \beta \sin \omega_m \cos(\theta\omega_m \xi / h_1)) - \\ -\alpha_1 m_1 h_1 \beta \sin \omega_k + \alpha_2 m_2 h_2 \theta \sin \omega_m & \xi > 0, \\ \alpha_2 m_2 h_2 \theta (\cos \omega_m \sin(\omega_m \xi / h_2) + \sin \omega_m \cos(\omega_m \xi / h_2)), & \xi < 0. \end{cases} \quad (4.14)$$

where $\xi = x - h_2$, Skempton's coefficient B_i , the consolidation coefficient c_i , and the confined compressibility coefficient m_i are defined as

$$B_i = \frac{b_i m_i M_i}{1 + b_i^2 m_i M_i}, \quad c_i = \frac{k_i}{\mu_f} \frac{M_i}{1 + b_i^2 m_i M_i}, \quad m_i = \frac{(1 + \nu)(1 - 2\nu)}{E(1 - \nu)}, \quad (4.15)$$

Table 4.4.: The properties of two layers.

Layer	h , m	E , GPa	ν	b	k , mD	ϕ	μ_f , cP	c_f , bar ⁻¹
1	25	1	0.35	0.9	1	0.15	1	10^{-10}
2	75	5	0.15	0.01	0.001	0.00695	1	10^{-10}

while the following definitions are used

$$\beta = \frac{k_2 c_1}{k_1 c_2}, \quad \theta = \frac{h_1}{h_2} \sqrt{\frac{c_2}{c_1}}. \quad (4.16)$$

In this example, we do not specify the Biot modulus manually in each layer; we use the following relationship instead

$$M_i = \left[\frac{(b_i - \phi_{0,i})(1 - b_i)}{K_{s,i}} + \phi_{0,i} c_f \right]^{-1}, \quad K_{s,i} = \frac{E_i}{3(1 - 2\nu_i)}, \quad (4.17)$$

where $K_{s,i}$ is the drained bulk modulus in layer i , and $\phi_{0,i}$ is the initial porosity in layer i .

The assumption about identical values of Skempton's coefficients is satisfied by choosing the initial porosity ϕ_0 and Biot's modulus in the second layer as

$$M_2 = \frac{b_1 m_1}{b_2 m_2} \frac{M_1}{1 + b_1 m_1 (b_1 - b_2) M_1}, \quad \phi_{0,2} = \frac{K_{s,2} - b_2 M_2 (1 - b_2)}{M_2 (c_f K_{s,2} + b_2 - 1)}. \quad (4.18)$$

The comparison of results presented in Fig. 4.7 has the same format as in the previous two sections. We use a uniform mesh comprised of 40 cells, so that the top left subfigure (Fig. 4.7a) demonstrates pressure over time evaluated at $x = 1.25$ m and the bottom left subfigure (Fig. 4.7c) shows the dynamics of horizontal displacement u_x taken at $x = 98.75$ m. The top and bottom right subfigures (Fig. 4.7b, Fig. 4.7d) present pressure and horizontal displacement profiles over the domain respectively. Numerical results remain in good accordance with the analytical solution.

4.6. Inf-Sup Instability

The collocated arrangement of unknown pressure and displacements leads to the numerical schemes suffering from the violation of the inf-sup condition. The scheme presented in Sec. 3.3 is not an exception. In Sec. 3.4 we describe one of the possible stabilizations of the current scheme (Terekhov *et al.* 2022). In this section, we compare the behavior of both schemes with respect to inf-sup instability that emerges in the last three examples.

The instability appears in the behavior of pressure close to the drained boundary. The drainage creates a boundary layer in pressure in the case of sudden pressure change. Even though fluid fluxes tend to smoothen the boundary layer with time, the instability observed just after the sudden pressure change can have a significant effect that takes place at early times in Terzaghi's, Mandel's, and two-layer Terzaghi's problems discussed above. Close to the right boundary of the domain pressure starts oscillating with increasing magnitude towards the boundary. This can be seen in the top right subfigures, in Figs. 4.3b, 4.5b and 4.7b.

The magnitude of this instability depends on how accurately the numerical model resolves the boundary layer. Mathematically speaking, it is governed by the magnitude of the Biot's term in fluid mass balance relative to the magnitude of Darcy's

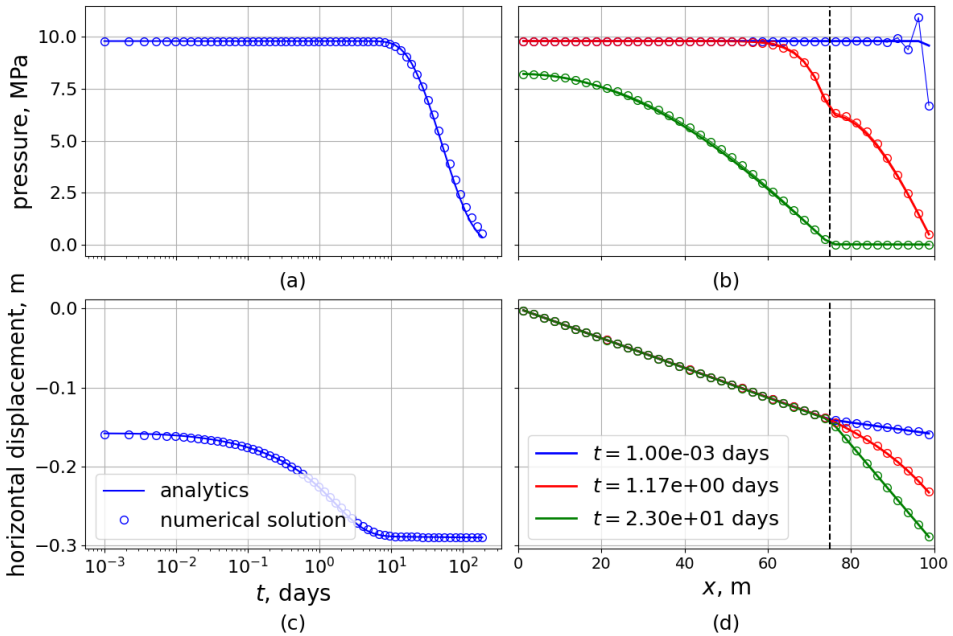


Figure 4.7.: Comparison of the analytical and numerical solutions for the two-layer Terzaghi's problem. In the left column, pressure (a) and displacement (c) at the center of the most left cell are shown over time. In the right column, pressure (b) and displacement (d) profiles over the whole domain are depicted at three moments of time.

fluxes. Therefore, not only physical properties like permeability and fluid viscosity affect the instability, but also numerical ones like time step and cell size. We can introduce the ratio $D = k\Delta t/(b\mu_f)$ where k is scalar permeability, Δt is time step, μ_f is fluid viscosity, b is scalar Biot's coefficient. The limit of $D \rightarrow 0$ implies the best resolution of the boundary layer which means that we can experience more pronounced oscillations whereas in the limit of $D \rightarrow \infty$ the boundary layer becomes smoothed and we observe no signs of instability.

Fig. 4.8 demonstrates a comparison of results produced with non-stabilized (NS) and stabilized (ST) schemes against analytical solutions. As in the previous sections, the top left subfigure (Fig. 4.8a) demonstrates pressure over time at $x = 1.66$ m, the bottom left subfigure (Fig. 4.8c) shows the dynamics of horizontal displacement u_x at $x = 98.33$ m and the top right (Fig. 4.8b) and top left subfigures (Fig. 4.8d) illustrate pressure and horizontal displacement profiles respectively plotted over the whole domain. As can be seen, the stabilized scheme does not experience spurious pressure oscillations close to the right boundary. Instead, it smoothens the boundary layer producing a large overshoot behind it.

Fig. 4.9 shows pressure profiles calculated with non-stabilized (NS) and stabilized (ST) schemes for three values of permeability (Fig. 4.9a) and in three grid

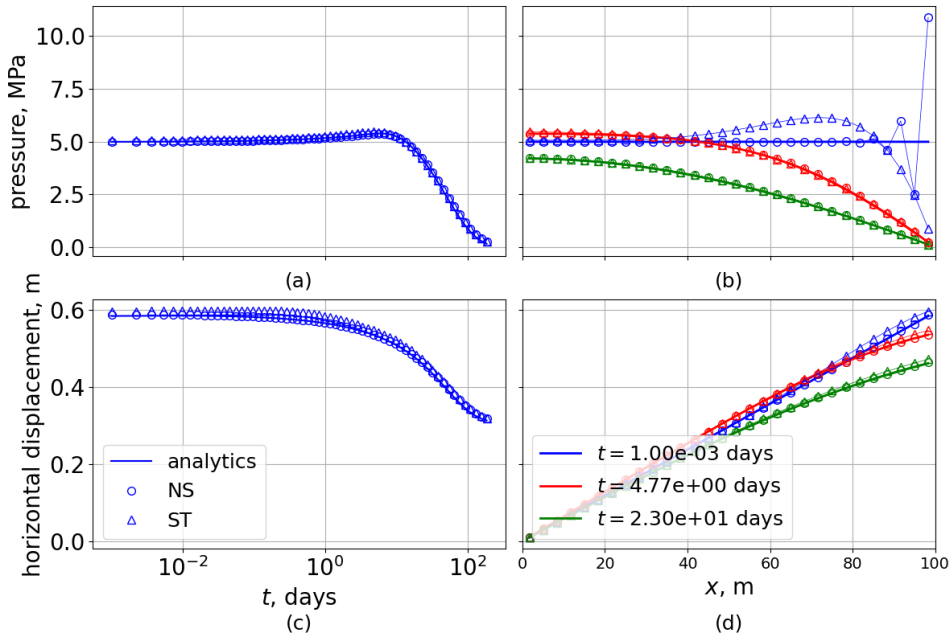


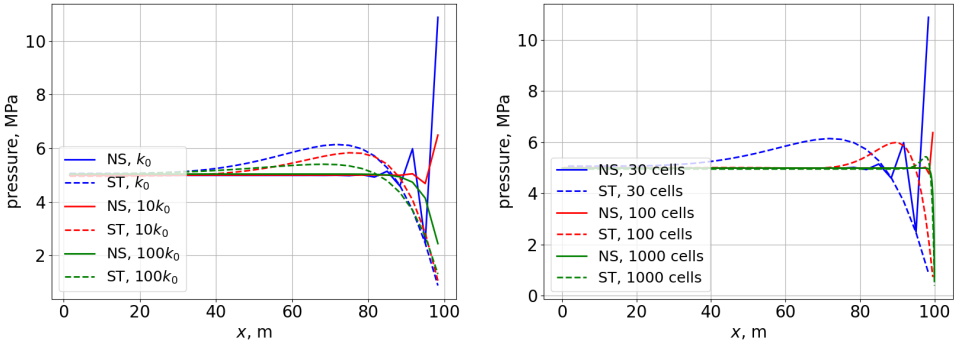
Figure 4.8.: Comparison of the analytical and two numerical solutions for Mandel’s problem. In the left column, pressure (a) and displacement (c) at the center of the most left cell are shown over time. In the right column, pressure (b) and displacement (d) profiles over the whole domain are depicted at three moments of time. NS - non-stabilized scheme, ST - stabilized scheme.

resolutions (Fig. 4.9b). Here we still can see that the stabilized scheme produces an overshoot behind the boundary layer. Nevertheless, the overshoot is decreasing with finer grids; in coarse grids this overshoot can span a big part of the domain introducing a significant deviation from the precise solution. At the same time, sub-figure (Fig. 4.9b) shows that the instability emerging in the non-stabilized scheme disappears with finer grid resolution.

Further analysis has revealed the sensitivity of the stabilized scheme to the aspect ratio of grid cells and to the choice of parameter α from Eq. (3.77) that is responsible for the magnitude of the stabilization term added to the scheme. Taking all these facts into account, we use the non-stabilized scheme for the numerical calculations presented below.

4.7. SPE10 with Mechanical Extension

In this field-scale test case, we use data from the SPE10 benchmark for flow supplemented by mechanical parameters, in particular a spatial distribution of Young’s modulus that depends linearly on the porosity (Garipov et al. 2018). The original



(a) multiple permeability values.

(b) multiple grid resolutions.

Figure 4.9.: Pressure profiles over the domain in Mandel's problem calculated for multiple values of permeability (a) and multiple grid resolutions (b) at the first time step $t = 10^{-3}$ days. NS means non-stabilized scheme, and ST stands for the stabilized scheme.

4

dataset represents a reservoir characterized by a channelized permeability and by a permeability field that has a Gaussian spatial covariance as shown in Fig. 4.10. The dataset was coarsened using a volume-averaging approach (Garipov *et al.* 2018). Although the original SPE10 benchmark was designed as a two-phase flow problem, here we consider single-phase flow. The reservoir is produced by a single doublet of an injector and producer. No-flow boundary conditions are prescribed for all the boundaries. Normal displacements and tangential tractions are set to zero at all boundaries except for the top boundary where a uniform distributed load of 900 bar is applied. Poisson's ratio is taken as constant $\nu = 0.2$, and Young's modulus and lateral permeability fields are depicted in Fig. 4.10.

The calculations are made using five rectangular grids of different resolutions: $20 \times 40 \times 20$, $20 \times 40 \times 40$, $40 \times 80 \times 20$, $40 \times 80 \times 40$, $40 \times 80 \times 80$. Constant bottom hole pressures are kept at the producer as $p_{prod} = p_0 - 100$ bar and the injector as $p_{inj} = p_0 + 100$ bar for $t_{max} = 2$ years. The results are summarized in Fig. 4.11. They demonstrate the applicability of block-partitioned preconditioning for the solution of a discrete system produced by a coupled FVM multi-point scheme.

In Fig. 4.11a it can be seen that the number of linear iterations (LI) increases as the problem size increases while the number of nonlinear iterations (NI) remains equal to 20. A similar behavior was observed in the nonlinear problem of two-phase flow in a deformable poroelastic medium (White *et al.* 2019) and was explained by the effect of upscaling. The upscaled grid tends to be more homogeneous, which may also improve the convergence of the linear solver. To distinguish the effect of upscaling, we also present calculations for a homogeneous reservoir in Fig. 4.11b). In the homogeneous case, the number of linear iterations flattens as the problem size grows which demonstrates the scalability of the solution strategy.

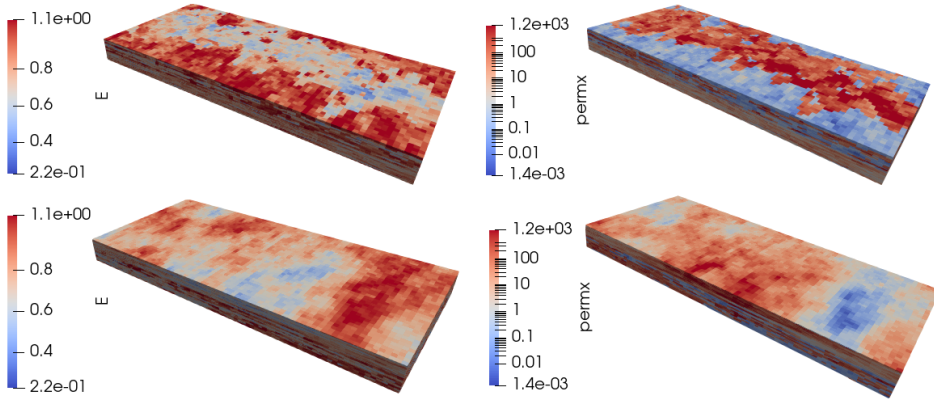


Figure 4.10.: Young modulus (in GPa) and lateral permeability (in mD) fields shown from the top (top row) and from the bottom (bottom row) of reservoir. Young’s modulus is calculated as a linear function of porosity. The top 24 layers represent a channelized structure whereas the bottom 16 layers correspond to a Gaussian distribution. Note that the colorbar of permeability is in logarithmic scale.

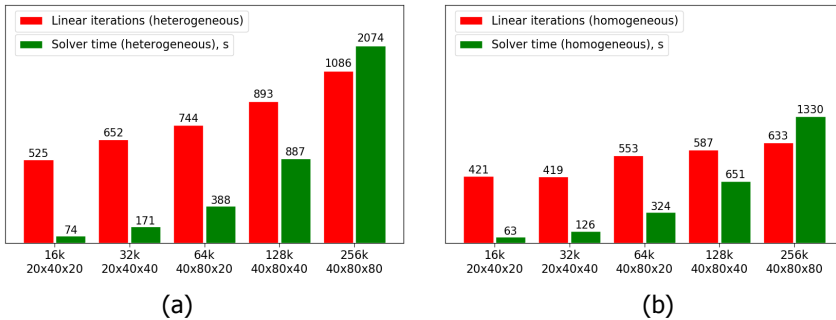


Figure 4.11.: Cumulative number of linear iterations and computational time taken by the linear solver to calculate 20 time steps and 20 nonlinear iterations for five different resolutions. For every resolution results are depicted for an upscaled heterogeneous reservoir (a) and for a homogeneous one (b). The rise in the number of linear iterations in the heterogeneous case can be explained by the effects of upscaling, while the flattening in the homogeneous case demonstrates the scalability of the solution strategy.

4.8. Comparison Against Other Simulators

4.8.1. GEOS

GEOS, an open-source exascale simulation framework for modeling coupled flow, transport, and geomechanics in the subsurface, has been developed to address the computational challenges introduced by geological CO₂ storage and geothermal energy applications (Settgast *et al.* 2022). It uses a combined cell-centered FVM and node-based FEM for the numerical integration of fluid mass and momentum balance laws respectively.

In this section, we compare the numerical solution obtained with the presented scheme of FVM against the numerical solution provided by GEOS. In particular, we investigate the behavior of the scheme at the contact between porous and non-porous rocks, which is of high practical relevance.

4

Two-Layer Terzaghi Problem

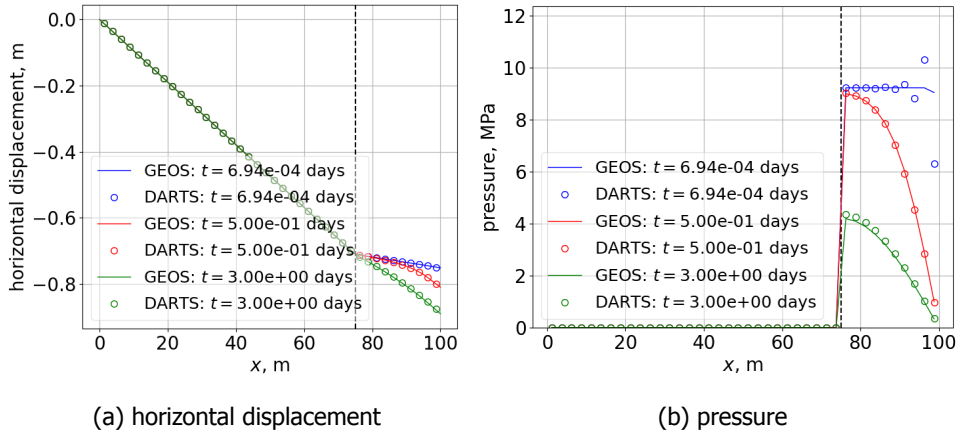


Figure 4.12.: The comparison of horizontal displacement (a) and pressure (b) against the solution obtained with GEOS for the Case #1.

Consider the two-layer Terzaghi problem presented in Sec 4.5. One of the two layers remains a porous permeable layer while the other is assigned a porosity, permeability and Biot's coefficient equal to zero. We consider two cases when the impermeable layer is either exposed or not to the right open boundary. The model

Table 4.5.: The parameters of two cases of the two-layer Terzaghi model.

Case	$E_{1,2}$, GPa	$\nu_{1,2}$	b_1	b_2	ϕ_1	ϕ_2	k_1 , mD	k_2 , mD
#1	1	0.15	0.9	0	0.15	0.0	1	0
#2			0	0.9	0.0	0.15	0	1

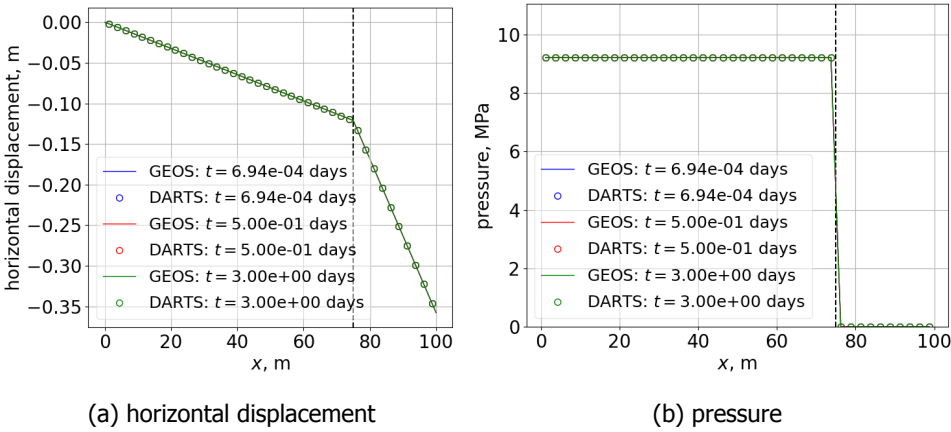


Figure 4.13.: The comparison of horizontal displacement (a) and pressure (b) against the solution obtained with GEOS for the Case #2.

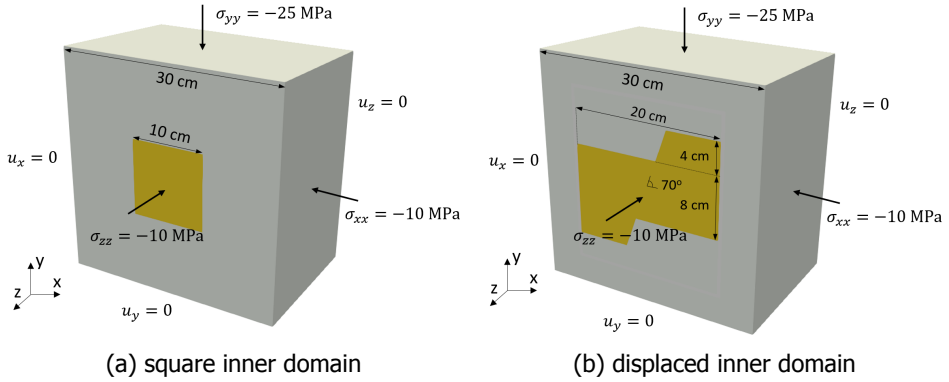
properties are listed in Tab. 4.5 while the remaining properties are taken from Tab. 4.4.

Fig. 4.12 and Fig. 4.13 demonstrate the comparison of displacement and pressure profiles across the domain at three moments of time for the two cases correspondingly. In case #1, when the right layer remains porous and permeable we observe a pressure build-up in this layer due to the poroelastic effect. The pressure in the left layer remains equal to zero as it is non-porous and impermeable. Both the proposed scheme (DARTS) and GEOS manage to resolve the pressure jump between two layers. Although both simulators may suffer from inf-sup instability, the proposed scheme demonstrates pressure oscillations of higher magnitude at the right boundary than the pressure obtained with GEOS. This jump decreases over time as fluid discharges from the right boundary. In case #2, the left layer remains porous and permeable whereas the right layer is non-porous and impermeable. Pressure rises in the left layer due to the poroelastic effect. However, as the impermeable right layer does allow fluid to discharge over the outlet at the right boundary, the pressure remains the same over time. It is worth to notice that a regular unidimensional grid is used in the calculations presented here.

A Porous Domain Inside Non-Porous Box

In this section, we demonstrate a comparison of numerical solutions for 2D poroelastic response in a porous domain placed inside a non-permeable box calculated with DARTS and GEOS. The contact of permeable and non-permeable materials is common in the geomechanical modeling of porous geological reservoirs surrounded by non-permeable formations.

We consider the triaxial compression of a box-shaped non-porous domain extracted from a square xy plane, see Fig. 4.14. In the center of xy plane we assign a porous and permeable inner region (yellow color) of two geometries, namely square



(a) square inner domain

(b) displaced inner domain

Figure 4.14.: Model setup.

4

and displaced-fault geometries shown in Fig. 4.14a and Fig. 4.14b respectively. Tri-axial forces $\sigma_{xx} = \sigma_{zz} = -10$ MPa, $\sigma_{yy} = -25$ MPa applied at the three positive sides compress the domain while the roller conditions assigned to three negative sides sustain compression. All boundaries are maintained impermeable. A uniform Young's modulus $E = 17$ GPa and Poisson's ratio $\nu = 0.3$ define an elastic response of both domains while Biot's coefficient $b = 0.9$ and initial porosity $\phi = 0.15$ define the poroelastic behavior of the inner region (yellow color). We assign permeability $k_0 = 1$ D to the inner permeable region and permeability $k = 10^{-8}k_0$ to the surrounding domain (grey color). Compression causes an instantaneous pressure build-up in the inner region. Fig. 4.14 illustrates the domain's geometry and boundary conditions.

Table 4.6.: The cases considered in the comparison.

Case	Geometry	Mesh	Number of cells
#1	square	60×60	3600
#2		240×240	57600
#3	displaced	62×60	3720
#4		244×240	58560

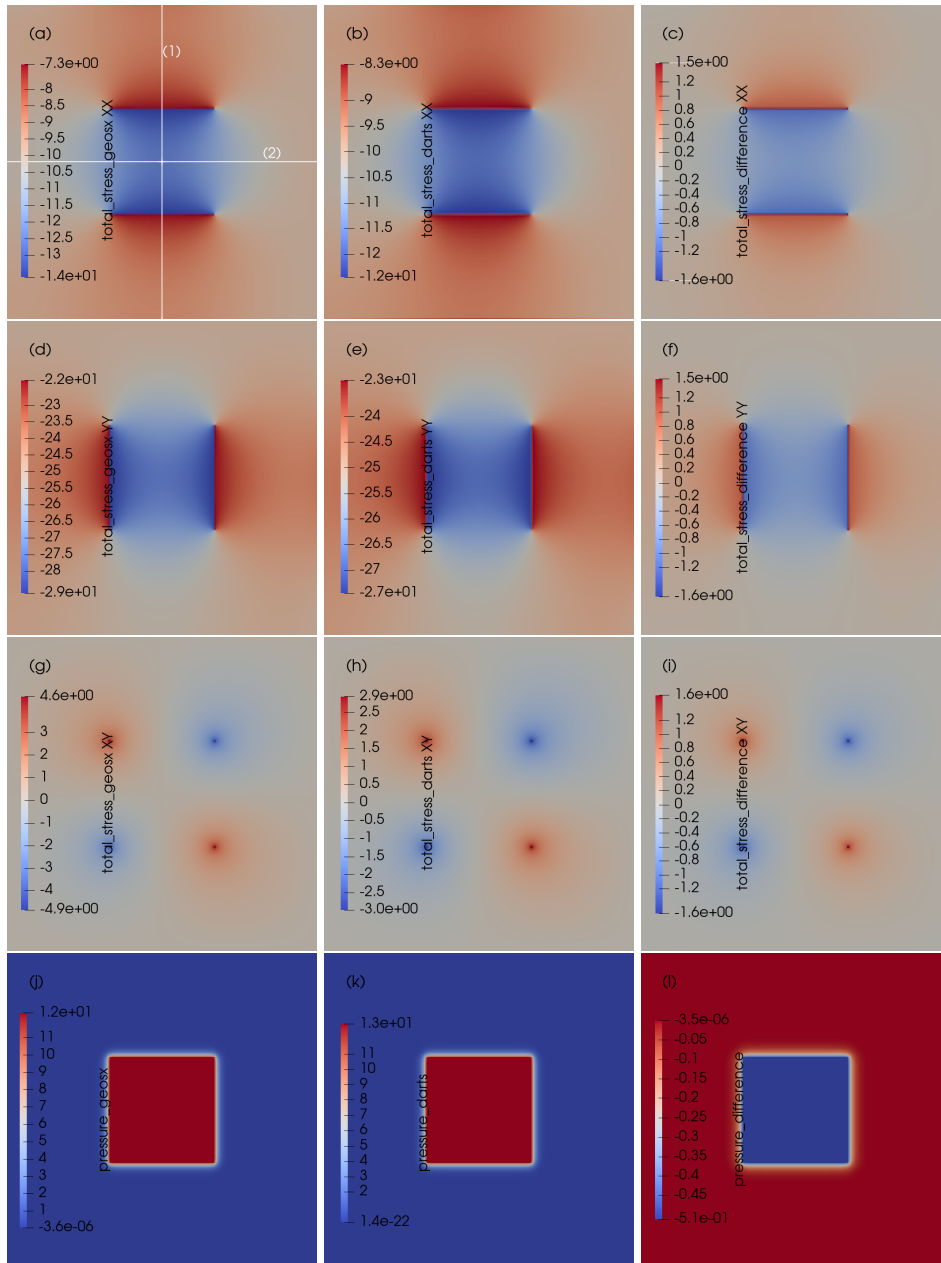


Figure 4.15.: The components of total stress tensor and pressure calculated with GEOS (left column), DARTS (middle column) and their difference (right column): σ_{xx} are shown in the first row (a)-(c), σ_{yy} are in the second row (d)-(f), σ_{xy} are demonstrated in the third row (g)-(i) and pressure are illustrated in the last row (j)-(l).

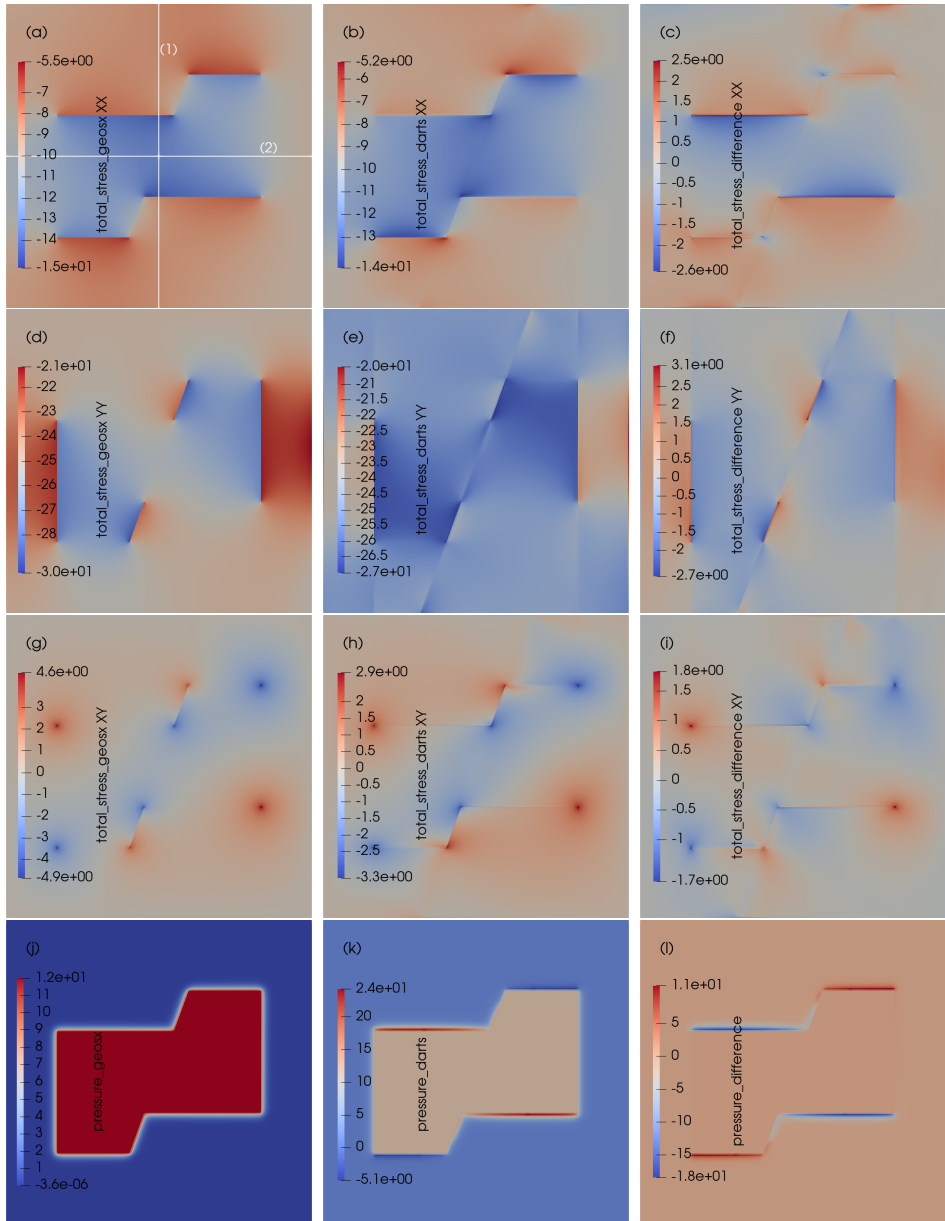


Figure 4.16.: The components of total stress tensor and pressure calculated with GEOS (left column), DARTS (middle column) and their difference (right column): σ_{xx} are shown in the first row (a)-(c), σ_{yy} are in the second row (d)-(f), σ_{xy} are demonstrated in the third row (g)-(i) and pressure are illustrated in the last row (j)-(l).

For the calculation of the numerical solution, we consider structured hexahedral meshes of coarse and fine resolutions for both geometries. In the case of the square geometry of the inner region we employ 60×60 , and 240×240 square grids. For the modeling of the displaced geometry, we utilize 62×60 and 244×240 quadrilateral grids. These grids are tagged and listed in Tab. 4.6.

The cell-centered arrangement of unknown pressures and post-processed stresses in both simulations enables their comparison within the same grid. We perform a comparison of results obtained after a single time step $\Delta t = 1$ h. Fig. 4.15 and Fig. 4.16 demonstrate the comparison of the components σ_{xx} (first row), σ_{yy} (second row), σ_{xy} (third row) of the total stress tensor and pressures (last row) calculated with GEOS (left columns) and DARTS (middle columns). The difference between the two numerical approaches is shown in the right column. The results presented in these two plots are obtained with the finer grids.

For convenient comparison, we also present 1D profiles of stresses and pressures over the vertical (1) and horizontal (2) centerlines of the domains. The centerlines are shown in Figs. 4.15a and 4.16a. Figs. 4.17 and 4.18 demonstrate the 1D profiles for the cases listed in Tab. 4.6.

The results of modeling for the displaced geometry shown in Fig. 4.16 exhibit an oscillating pressure at the boundary of the inner domain in the DARTS's solution (Fig. 4.16k) whereas the GEOS's results do not demonstrate similar oscillations (Fig. 4.16j). This difference can be clearly seen in 1D pressure profiles over the vertical centerline presented in Fig. 4.17e (Cases #3, #4). We attribute this behavior to the violation of the inf-sup condition discussed in the previous sections. Obviously, these pressure oscillations affect the whole comparison. Their effect on stresses is clearly seen in Figs. 4.16b, 4.16e and 4.16h.

Surprisingly, we observe the pressure oscillations only in the case of curved non-rectangular quadrilaterals. In the case of a rectangular cell geometry present at the left and right sides of the inner displaced region, the DARTS's pressure does not exhibit oscillations. This can be seen from both the 2D colormap in Fig. 4.16k and the 1D horizontal profiles in Fig. 4.18b. Furthermore, we observe no pressure oscillations in the case of the square geometry of the inner region. These observations may indicate that the non-rectangular grid geometry provokes the inf-sup instability for the current scheme of FVM.

At the same time, we observe that the magnitude of pressure build-up obtained with two simulators does not precisely match even in the absence of pressure oscillations in the square geometry, see Figs. 4.18a and 4.17a. The coarse and fine results from GEOS match each other while the DARTS's results approach them with finer grid resolution. Several other mismatches in stresses between the two solutions can be found in the square geometry (Cases #1, #2) in Figs. 4.17 and 4.18. Nevertheless, the results from both simulators seem converged, i.e. coarse and fine results match each other; the most significant discrepancy between the simulators is present in the σ_{xx} and σ_{yy} components. The source of this discrepancy requires further investigation.

It is important to note that the total stresses from both simulators maintain continuity over the boundary of the inner region. The vertical total stresses σ_{yy} remain

continuous over the vertical centerline shown in Fig. 4.17c and 4.17g while the horizontal total stress σ_{xx} is continuous over the horizontal centerline as presented in Figs. 4.18c and 4.18d. The non-smooth boundary of the inner region produces concentrations of the total shear stress σ_{xy} at corresponding locations. The difference in this stress component between two simulations is relatively high around those concentrations which can be seen in Figs. 4.15i and 4.16i. Besides, the 1D profiles of σ_{xy} calculated by both simulators on coarse grids with the square geometry demonstrate jumps (Figs. 4.17g and 4.18g) located far from the boundary of the inner region.

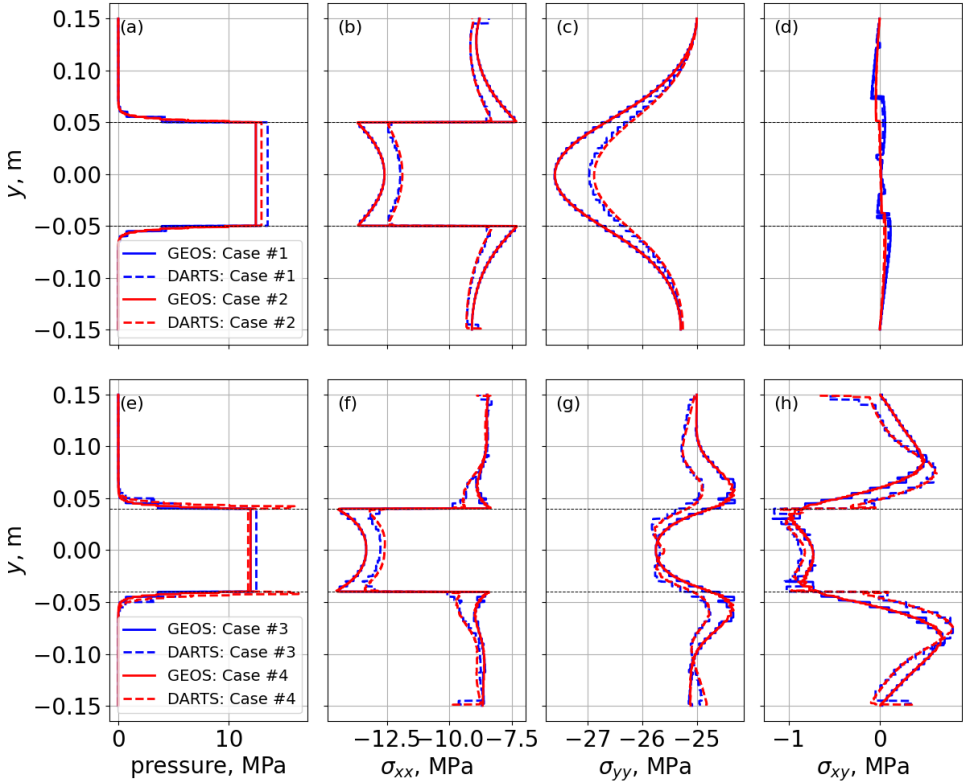


Figure 4.17.: Pressure and stress profiles over the vertical centerline.

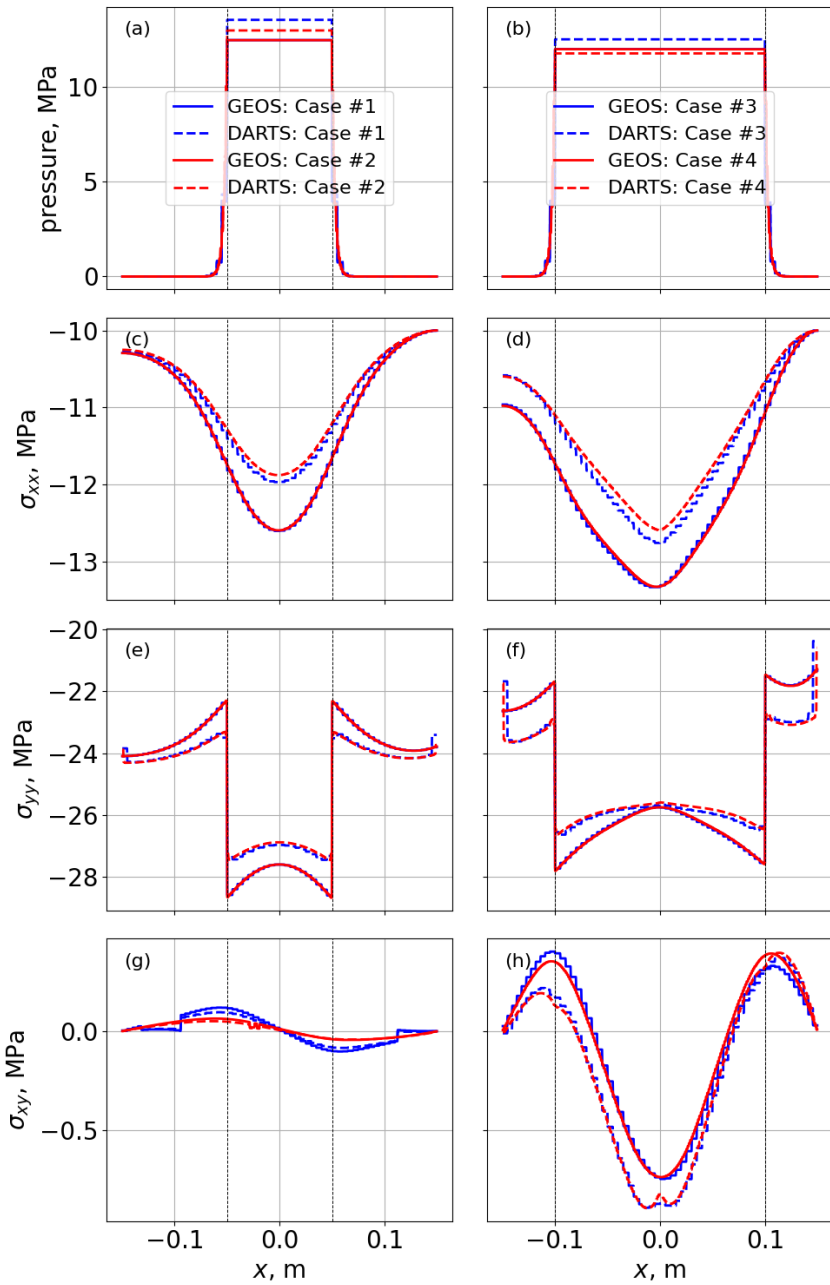


Figure 4.18.: Pressure and stress profiles over the horizontal centerline.

4.8.2. PorePy

The introduction of FVM for mechanics (Keilegavlen *et al.* 2017a; Martin 2014), coupled poroelasticity (Nordbotten 2016) and the recent development in the calculus of mixed-dimensional hydromechanical problems (Berge *et al.* 2020; Boon *et al.* 2023; Boon *et al.* 2021) inspired the development of the FVM reservoir simulation tool, called PorePy (Keilegavlen *et al.* 2021). In this section, we validate the proposed scheme against the numerical results calculated with PorePy.

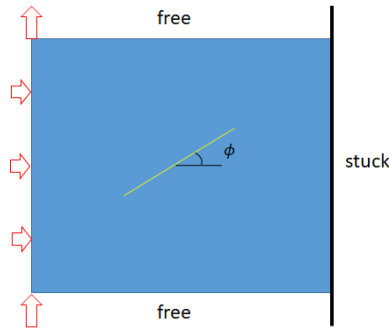


Figure 4.19.: The domain with an inclined fault and boundary conditions.

This case concerns a fault with Coulomb friction in the center of a square domain of size $a = 1$ m; see Fig. 4.19. The right boundary is fixed, the top and bottom boundaries are free of any forces, while displacements $\mathbf{u}_{left} = \{0.001, 0.01\}$ m are prescribed at the left. A plane strain setup is considered. The stiffness matrix is determined by Lamé coefficients $\lambda = G = 1$ Pa. A fault of length $L = 0.4a$ with friction coefficient $\mu = 0.85$ is allowed to slip once the sliding criterion is exceeded. A structured quadrilateral grid is used in the calculation. The resulting displacement and stress fields for a vertical fault are shown in Figs. 4.20 and 4.21. One can notice a small jump in horizontal displacements across the fault.

The results are compared with other ones, obtained by the PorePy simulation tool, for different orientations of the fault determined by a dip angle ϕ . The comparison is displayed in Fig. 4.22. Tangential tractions over the fault calculated by the proposed scheme (DARTS) and PorePy match quite well. For higher dip angles (nearly vertical orientation) the resulting slip also fits quite well. However, for lower dip angles the slip is decreasing and in the case of $\phi = 72^\circ$ it becomes located at the tips of the fault whereas the center of the fault displays higher normal tractions and smaller slip values. With decreasing dip angles, the slip magnitude decreases as well and a tiny mismatch in tangential traction results in a higher mismatch in slip (for $\phi = 72^\circ$). Below some threshold angle, no slip over the fault is observed.

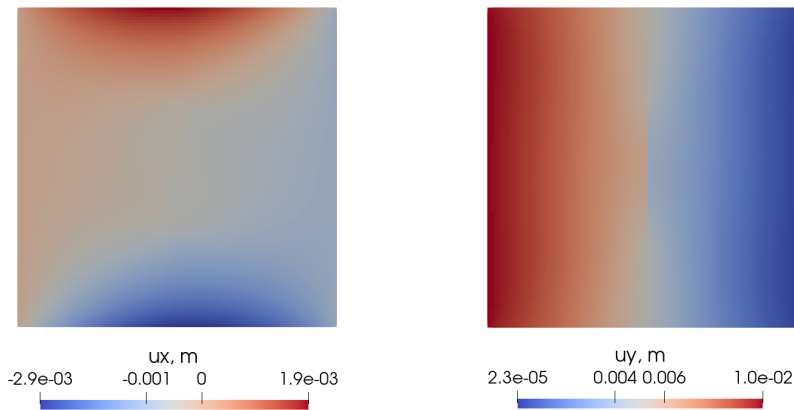


Figure 4.20.: Horizontal (left) and vertical (right) displacements for the case of a vertical fault ($\phi = 90^\circ$). Note the jump in vertical displacements at the fault.

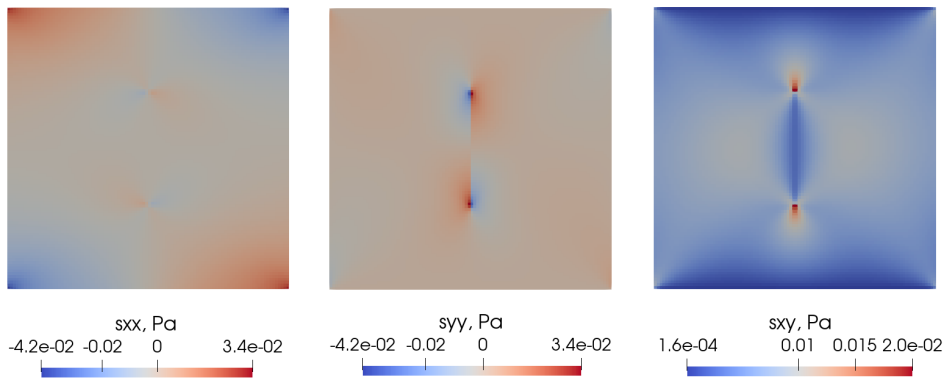


Figure 4.21.: Normal horizontal (left), vertical (middle) and shear stresses (right) for the case of a vertical fault ($\phi = 90^\circ$).

4.9. Displaced Fault Model

Reducing stress concentration is a challenging task, relevant to many applications in mechanical and civil engineering. From the mathematical point of view, the elasticity operator, unlike e.g. diffusion operator, can be severely influenced by

Parts of this section have been published in Novikov *et al.* 2023.

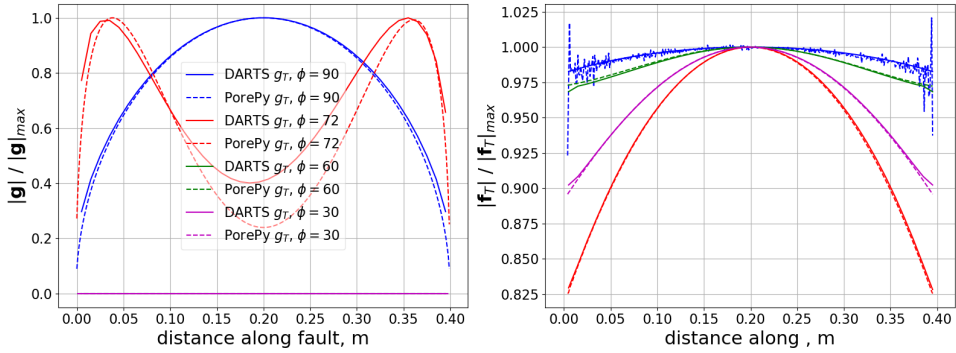


Figure 4.22.: Comparison of slip and tangential traction along the fault for different dip angles.

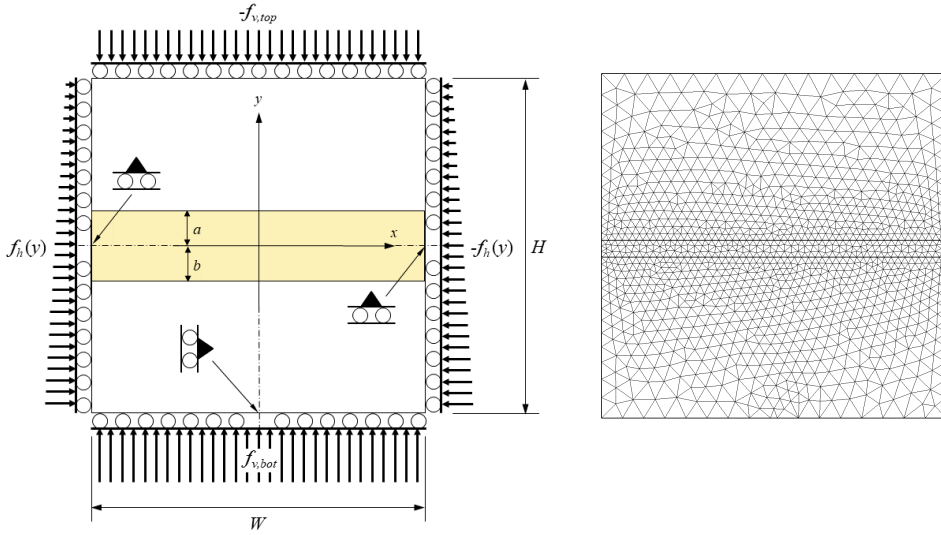
4

the smoothness of domain geometry. A non-smooth geometry in the domain's boundaries or in surfaces dividing homogeneous regions may introduce discontinuous stresses. Even though, in reality, those discontinuities are limited by non-linear material rheology, they still may introduce enormous stress concentration compared to the background stresses.

In reservoir engineering, the stress concentrations introduced by non-smooth geometry may appear on the faults and fractures dividing geological compartments, and may impair their stability. Real subsurface configurations often consist of multiple rock layers crossed by natural faults. Sometimes the parts of initially aligned formations can be displaced over these faults juxtaposing the rock layers with distinct properties against each other. This configuration increases the risk of fault reactivation during the extraction of geo-energy resources (Orlic *et al.* 2012; Van den Bogert 2018).

Fortunately, the analytical consideration is possible for the simple representation of this displaced fault configuration. The poroelastic stresses in a reservoir can be estimated analytically with the aid of inclusion theory (Eshelby 1957), or the closely-related nucleus of strain concept (Geertsma 1966; Geertsma 1973), based on potential theory (Goodier 1937). In particular, the analytical expressions for the stresses in a reservoir with a displaced fault induced by quasi-static pressure perturbations have been derived (Cornelissen *et al.* 2023; Jansen *et al.* 2019; Jansen *et al.* 2022).

In this section, we perform the validation of the developed FVM against the analytics existing for the displaced fault model in a number of cases. First, we validate the initial unperturbed stresses. Next, we check the stress and slip profiles over the fault in the case of vertical frictionless contact, and inclined contacts governed by constant and linear slip-weakening friction laws.



(a) Initial setup.

(b) Computational grid.

Figure 4.23.: Left: the initial setup to represent an infinitely wide reservoir without faults (not to scale). Load configuration and mechanical boundary conditions to simulate initial stresses. Right: computational grid used in the initial setup (cell size - not to scale).

4.9.1. Model Setup

The calculation of the displaced fault model implies the consideration of two setups. A square homogeneous poroelastic domain of equal height and width $H = W = 4500$ m is considered in both setups. Shear modulus $G = 6.5$ GPa, Poisson's ratio $\nu = 0.15$ and Biot coefficient $b = 0.9$ determine the mechanical response of the domain's material. Moreover, the specified pressure distribution is assigned in both setups due to an assumption about quasi-steady-state poroelasticity used in the analytical consideration. We apply the plain strain condition in the both setups. The origin of the coordinate system is placed in the center of the domain.

The first setup, shown in Fig. 4.23b, is designed to estimate the initial stresses as they behave in the subsurface. Therefore, initial horizontal stress $\sigma_{xx}^0(y)$, initial vertical stress $\sigma_{yy}^0(y)$, and initial pressure $p^0(y)$ depends on the depth aligned with the y -axis as follows

$$\sigma_{xx}^0(y) = K^0(\sigma_{yy}^0 + bp^0(y)) - bp^0(y), \quad (4.19)$$

$$\sigma_{yy}^0(y) = ((1 - \phi)\rho_s + \phi\rho_f)g(y - D_0), \quad (4.20)$$

$$p^0(y) = p^0(y = 0) - \rho_f gy, \quad (4.21)$$

where $K^0 = 0.5$ denotes the constant ratio of effective horizontal σ_{xx}'' to effective vertical σ_{yy}'' stresses, D_0 represents the depth assigned to the center of domain, ϕ is rock porosity, ρ_f, ρ_s are fluid and rock densities correspondingly, g is gravitational

Table 4.7.: Reservoir properties, fault geometry and simulation domain.

Symbol	Property	Value	Units
a	See Fig. 4.25	75	m
b	See Fig. 4.25	150	m
D_0	Depth at reservoir center ($y = 0$)	3500	m
g	Acceleration of gravity	9.81	m s^{-2}
G	Shear modulus	6500	MPa
H	Height of simulation domain	4500	m
K^0	Ratio of initial effective horizontal to vertical stresses	0.5	–
p_0^0	Initial reservoir pressure at reservoir center	35	MPa
W	Width of simulation domain	4500	m
b	Biot coefficient	0.9	–
θ	Dip angle	70	deg.
c	Cohesion	0	MPa
ν	Poisson's coefficient	0.15	–
ρ_f	Fluid density	1020	kg m^{-3}
ρ_s	Solid density	2650	kg m^{-3}
ϕ	Porosity	0.15	–

acceleration. The reservoir properties used in calculations are listed in Tab. 4.7.

The stress distributions defined in Eqs. (4.19)-(4.21) are satisfied with appropriate Neumann boundary conditions

$$f_h(y) = -\sigma_{xx}^0(y), \quad f_{v,top} = \sigma_{yy}^0(y = 2250), \quad f_{v,bot} = -\sigma_{yy}^0(y = -2250), \quad (4.22)$$

where f_h is a normal force applied to the left boundary at $x = -2250$ m and the opposite $-f_h$ normal force is applied to the right boundary at $x = 2250$ m, $-f_{v,top}, f_{v,bot}$ are normal forces applied to the top boundary at $y = 2250$ m and to the bottom boundary at $y = -2250$ m respectively. As we consider quasi-steady-state poroelasticity, the pressure distribution in Eq. (4.21) is provided as an input.

To regularize the purely Neumann problem and constrain rigid body motion we impose the following Dirichlet condition in tangential directions at three points

$$\begin{cases} u_y = 0, & \text{at } x = \pm 2500 \text{ m}, y = 0 \text{ m}, \\ u_x = 0, & \text{at } x = 0 \text{ m}, y = -2500 \text{ m}. \end{cases} \quad (4.23)$$

These specific locations of stick points allow stress concentrations around them to be avoided. The boundary displacements calculated from the modeling of the initial setup are shown in Fig. 4.24.

The second setup introduces a displaced fault geometry presented in Fig. 4.25 for two values of dip angle $\theta = 90^\circ$ and $\theta = 70^\circ$. In this setup, the reservoir, situated in the middle of the domain, becomes divided into two parts shifted with respect to each other. The boundary displacements calculated in the initial setup are taken as the left, right and bottom normal boundary conditions for the main

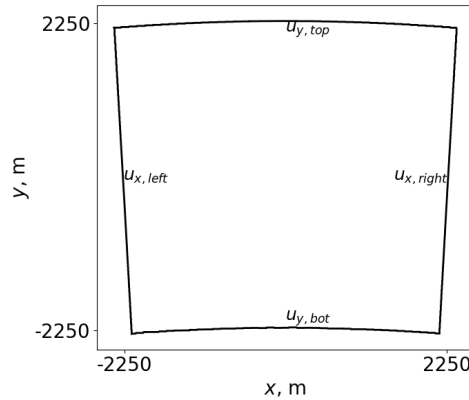


Figure 4.24.: The shape of the domain's boundary calculated in the initial setup (not to scale).

setup. The normal force $-f_v = -f_{v,top}$ is applied at the top boundary like in the initial setup. We impose a free condition in a tangential direction at all boundaries. The properties defining the domain's geometry are listed in Tab. 4.7.

In the main setup, we assign a uniform pressure depletion in the reservoir. Due to the displaced fault geometry, the discontinuous stresses appear over the fault at the inner ($y = \pm a$) and outer ($y = \pm b$) corners of reservoir which may cause fault reactivation. The resolving of these infinite stresses, albeit challenging, is inevitable for the quantification of seismicity risks in this setup.

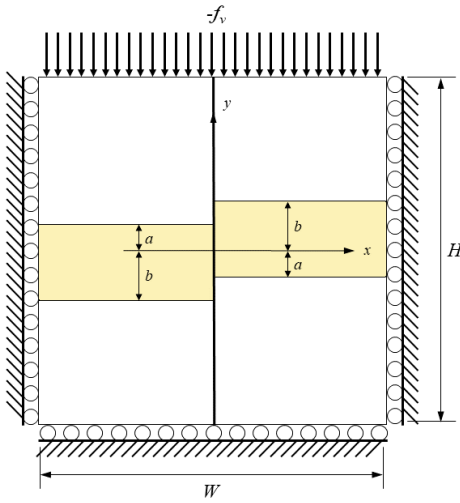
Having both weak (stress) discontinuities and strong (displacement) discontinuities over the fault imposes high requirements on the quality of the computational grid. We use an unstructured grid comprised of wedges and adaptively refined towards the fault. Figs. 4.25b, 4.25d illustrate the grids used for the modelling of the main setup with $\theta = 90^\circ$ and $\theta = 70^\circ$ respectively. For convenient representation, the cell size shown in the figures is much higher than used in simulation.

4.9.2. Initial State

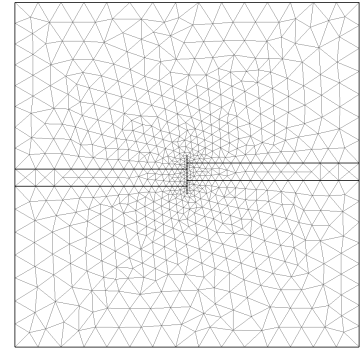
The initial setup described above is shown in Fig. 4.23b. The unstructured grid comprised of wedges and used in numerical simulation is demonstrated in Fig. 4.23a.

In order to check the consistency of the initial setup we check if the numerical solution satisfies the presumptions from Eqs. (4.19)-(4.21). Fig. 4.26 demonstrates the match of the numerical solution (DARTS) to the stresses presumed in Eqs. (4.19), (4.20) (Analytical) projected to the line crossing the center of the domain at an angle of 70° with horizontal.

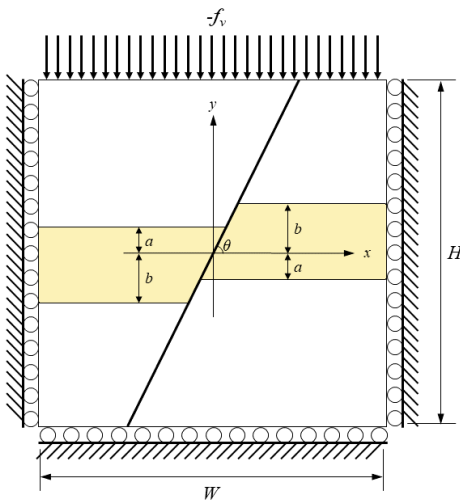
The main goal of the first setup is to calculate the initial state and to provide boundary conditions for the main setup. Fig. 4.27 presents the particular profiles of the displacements evaluated at the domain's boundaries normal to the boundary interface. Subfigures (a), (b) show the horizontal displacement u_x over the left and



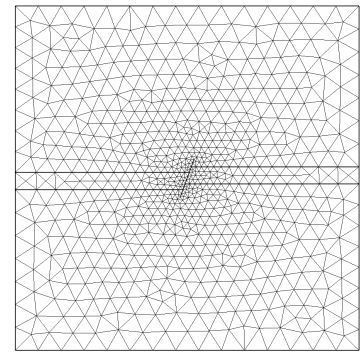
(a) Vertical fault: setup.



(b) Vertical fault: grid.



(c) Inclined fault: setup.



(d) Inclined fault: grid.

Figure 4.25.: The main setup with a displaced fault for the two values of dip angle: $\theta = 90^\circ$ (a) and $\theta = 70^\circ$ (c). Corresponding computational grids are shown in the right column.

right boundaries correspondingly whereas subfigures (c), (d) illustrate the profiles of vertical displacements u_y over the bottom and top boundaries respectively. In the main setup, these displacements will be applied as a Dirichlet boundary condition in the normal direction to the left, right and bottom boundaries.

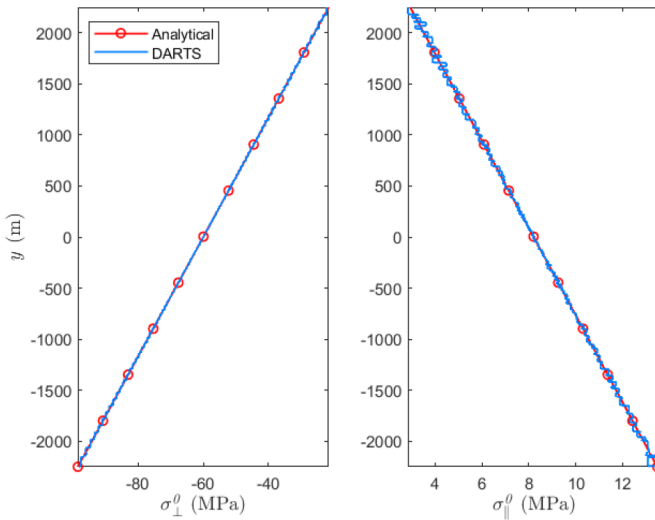


Figure 4.26.: Initial normal stresses σ_{\perp}^0 (left) and initial shear stresses σ_{\parallel}^0 (right) along a line through the center of the reservoir at an angle of 70° with horizontal.

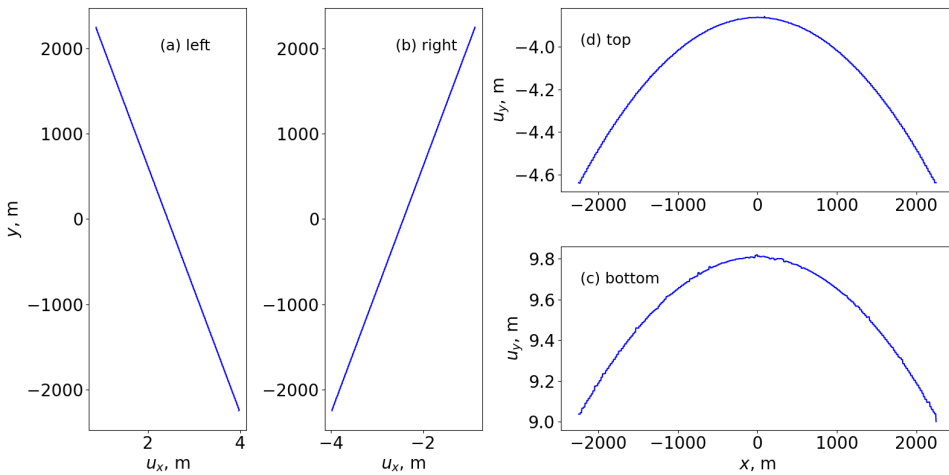


Figure 4.27.: Normal boundary displacements calculated from the initial setup. Subfigures (a), (b) show the horizontal displacements at the left and right boundaries respectively while subfigures (c), (d) present the vertical displacements evaluated at the bottom and top boundaries correspondingly.

4.9.3. Vertical Frictionless Fault

Consider the main setup described above with an introduced displaced vertical fault at the center of the reservoir by choosing $a = 75$ m and $b = 150$ m such that the reservoir contains a fault with throw $t_f = b - a = 75$ m, see Fig. 4.25a. As a first step, we don't allow for fault slip in the simulation and perform the same steps as in the previous example to generate the initial and incremental stress fields.

The combined pre-slip Coulomb stress Σ_C , i.e. the pre-slip Coulomb stress resulting from the sum of initial and incremental stresses is defined for an arbitrarily oriented fault with friction coefficient μ as

$$\Sigma_C = |\Sigma_{\parallel}| + \mu \Sigma_{\perp}. \quad (4.24)$$

For the particular case of positive shear stress in a vertical fault without friction, i.e. with $\theta = 90^\circ$ and $\mu = 0$, and an incremental pressure of $p = -25$ MPa this reduces to (Jansen *et al.* 2022)

$$\Sigma_C = \sigma_{xy} = \frac{C}{2} \ln \frac{(y-a)^2(y+a)^2}{(y-b)^2(y+b)^2}, \quad C = \frac{(1-2\nu)\alpha p}{2\pi(1-\nu)}. \quad (4.25)$$

Next, we allow for a slip in the fault over the entire simulation domain, i.e. from -2250 to 2250 m. The pressure in the fault is equal to the initial pressure $p^0(y)$ except for the reservoir section $-150 \text{ m} \geq y \geq 150 \text{ m}$ where it is equal to the combined pressure $p(y) = p^0(y) - 25 \text{ MPa}$. The analytical solution for the fault slip is given by (Jansen *et al.* 2022)

$$\delta(y) = \frac{C}{A} \times \begin{cases} 0 & \text{if } y \leq -b, \\ -(y+b) & \text{if } -b < y \leq -a, \\ (a-b) & \text{if } -a < y < a, \\ (y-b) & \text{if } a \leq y < b, \\ 0 & \text{if } b \leq y, \end{cases}, \quad A = \frac{G}{2\pi(1-\nu)}. \quad (4.26)$$

Fig. 4.28 (right) displays this slip distribution over the height of the reservoir, and Fig. 4.28 (left) displays the pre-slip Coulomb stress. The correspondence between the numerical results (DARTS) and the semi-analytical results (Analytical) is excellent.

4.9.4. Inclined Fault with Static Friction

Consider the same reservoir as in the previous section but now with a fault at $\theta = 70^\circ$ with respect to horizontal; see Fig. 4.25c. A sketch of corresponding computational grid is displayed in Fig. 4.25d. For convenient visualization, the cell size in the figure is much bigger compared to the one used in calculations. Fig. 4.29 (left) displays the pre-slip shear stresses Σ_{\parallel} and the slip threshold $\Sigma_{sl} = -\mu \Sigma'_{\perp}$ for an incremental pressure $p = -25$ MPa, and Fig. 4.29 (right) shows the corresponding pre-slip Coulomb stresses Σ_C . The numerical results (DARTS) closely match the semi-analytical ones (red curves).

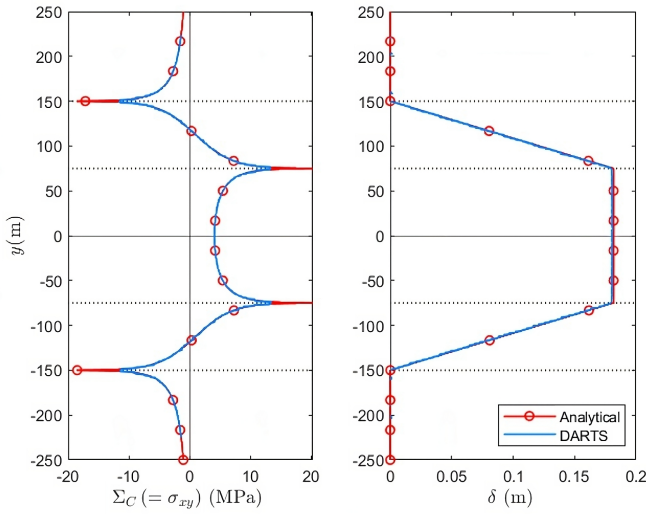


Figure 4.28.: Left: pre-slip Coulomb stresses Σ_C in a frictionless vertical fault with offset (which, for this particular case, just equals the incremental shear stress σ_{\parallel}). Right: the resulting slip δ .

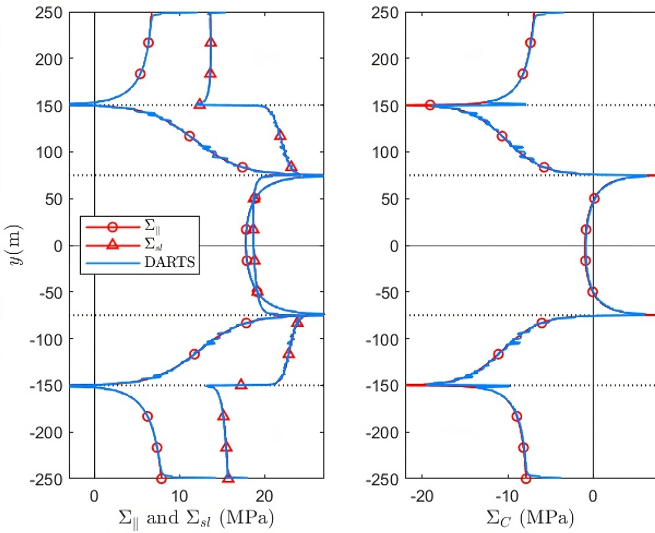


Figure 4.29.: Left: pre-slip shear stresses Σ_{\parallel} and slip threshold Σ_{sl} in an inclined fault with offset and constant friction. Right: the corresponding pre-slip Coulomb stresses Σ_C . Simulation domain width $W = 4500$ m.

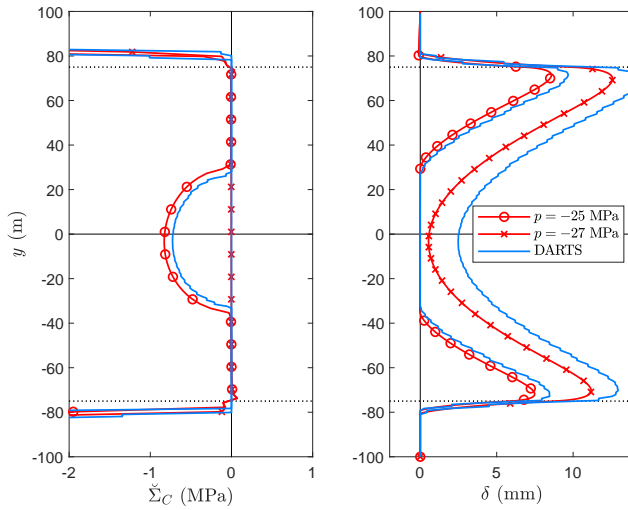


Figure 4.30.: Left: post-slip Coulomb stresses $\check{\Sigma}_C$. Right: the corresponding slip δ . Simulation domain width $W = 4500$ m.

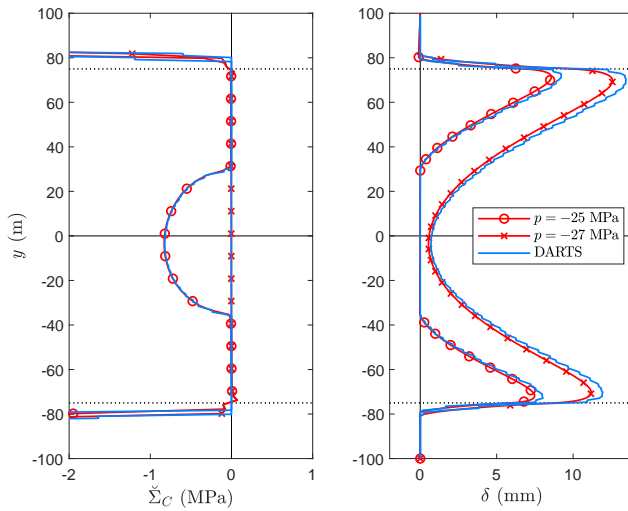


Figure 4.31.: Left: post-slip Coulomb stresses $\check{\Sigma}_C$. Right: the corresponding slip δ . Simulation domain width $W = 18$ km.

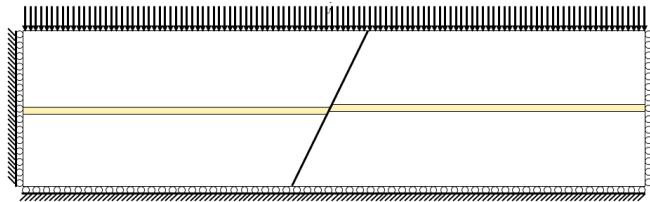


Figure 4.32.: Simulation set-up, with increased width $W = 18$ km, to scale.

Fig. 4.30 displays the post-slip Coulomb stresses (left) and fault slip (right) for $p = -25$ MPa. At this depletion level, the slip occurs in the form of two separate slip patches. For increasing depletion, the patches will merge as shown in the same figure with results for $p = -27$ MPa. Somewhat surprisingly the numerical results (DARTS) now show a discrepancy with the semi-analytical ones (red curves), especially for the merged slip patch. It can be explained by the fact that an analytical solution has been derived for an infinitely wide domain. Further comparisons revealed that this discrepancy disappears if the width W of the simulation domain is increased. Fig. 4.31 displays the same results but now for a simulation with $W = 18$ km, i.e. four times as wide as the original simulation domain. Apparently, the strongly nonlinear mechanics involved in fault slip leads to strong sensitivities of the slip patch size to the boundary conditions at the edges of the reservoir. This finding suggests that in reality there will also be a large sensitivity to the boundary conditions of the reservoir and probably also a significant interaction effect of neighboring faults. Fig. 4.32 displays the reservoir and the simulation domain, with increased width, to scale.

Fig. 4.33 displays the location of the four slip patch boundaries (two for each of the two patches) as a function of incremental pressure. Merging occurs when the pressure has dropped to $p = -26.9$ MPa and the numerical results (DARTS), computed with $W = 18$ km, match the semi-analytical ones (Analytical).

4.9.5. Inclined Fault with Linear Slip-Weakening friction

In the case of slip-weakening friction decreases as slip increases in absolute value. We use the linear slip-weakening friction law which implies a linear decrease of friction coefficient from a static value μ_s to a dynamic one μ_d over a critical slip distance δ_c . The friction remains equal to μ_d for the absolute values of slip larger than δ_c as shown in Fig. 4.34. Slip-weakening promotes fault reactivation and may cause unstable rupture propagation. Although simplistic, it is a representative model that describes seismicity observed in geological formations (Buijze *et al.* 2019; Buijze *et al.* 2017; Franceschini *et al.* 2023; Van den Bogert 2018).

Fig. 4.35 illustrates the comparison of analytical and numerical profiles of post-slip Coulomb stress and slip over an upper patch calculated in the square domain at a nucleation depletion pressure p^* . For the depletion pressures below p^* unstable rupture propagation is expected. With the parameters of $\mu_s = 0.52$, $\mu_d = 0.2$, $\delta_c = 0.02$ m analytics predicts $p^* = -17.44$ MPa while DARTS has $p^* = -17.3$ MPa. The small difference in slip profiles and nucleation depletion pressures can be explained by the finite domain width discussed above.

4.10. Benchmarking the Nonlinear Finite Volume Method

4.10.1. Convergence Study

In the first part, we prove the convergence of NTPSA and Average MPSA discretization techniques presented in Sec. 3.6. Let us consider the following reference solu-

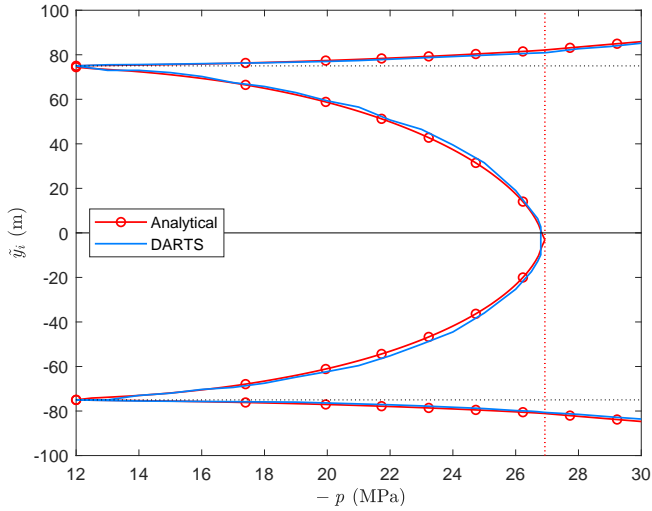


Figure 4.33.: Slip patch boundaries as a function of depletion pressure p . The vertical dotted line indicates the merging pressure. Simulation domain width $W = 18$ km.

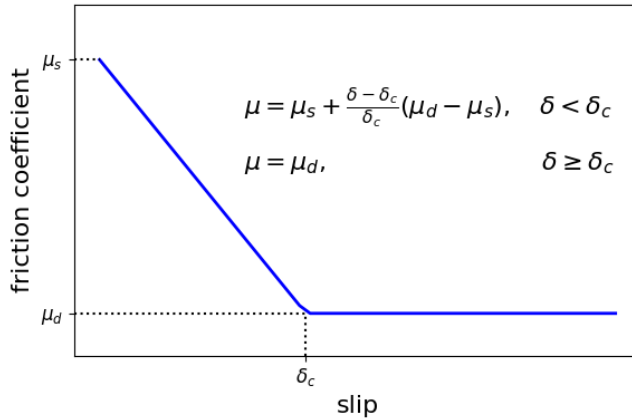


Figure 4.34.: Slip-weakening friction law.

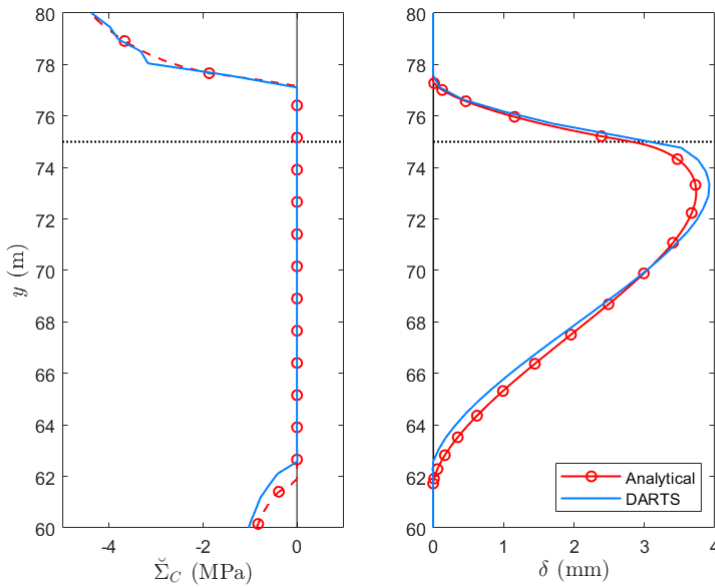


Figure 4.35.: Post-slip Coulomb stresses $\check{\Sigma}_C$ (left) and slip δ (right) profiles for an upper slip patch calculated with analytics (red curve) and DARTS (blue curve) at a nucleation depletion pressure p^* . Slip-weakening friction law is used with $\mu_s = 0.52$, $\mu_d = 0.2$, $\delta_c = 0.02$ m. The analytical estimate for the nucleation pressure is $p^* = -17.44$ MPa, the numerical one is $p^* = -17.3$ MPa.

tion of the elasticity problem (Terekhov *et al.* 2020) in the cubic domain $\Omega = [0, 1]^3$

$$u_x(x, y, z) = \left(x - \frac{1}{2}\right)^2 - y - z, \quad u_y(x, y, z) = \left(y - \frac{1}{2}\right)^2 - x - z, \quad u_z(x, y, z) = \left(z - \frac{1}{2}\right)^2 - x - y, \quad (4.27)$$

and the 6×6 stiffness matrix from Eq. (4.3).

We substitute the reference solution and the stiffness matrix to the left-hand side of the momentum balance equation and use the result of the calculation as the vector of volumetric forces in the right-hand side of the momentum balance equation. We also subject the domain to Dirichlet boundary conditions according to the reference solution. The solution of all three components of displacement can be seen in Fig. 4.36.

4

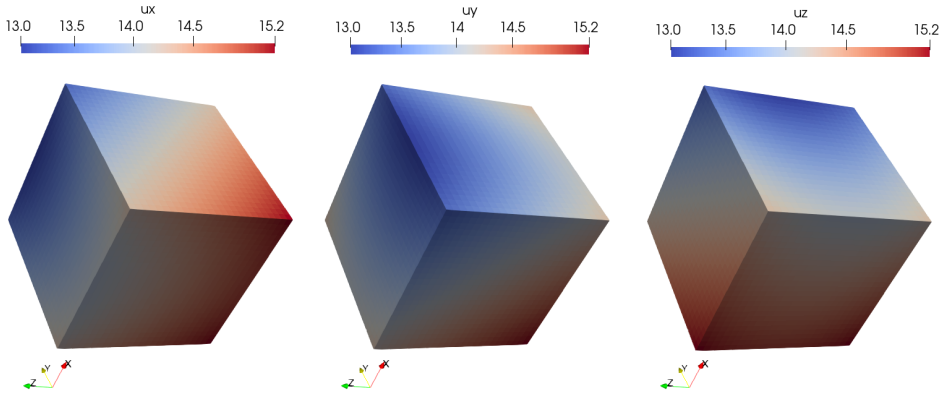


Figure 4.36.: Reference solution from Eq. (4.27) for displacement components u_x (left) u_y (center) u_z (right).

We reconstruct the stress tensor in the centers of the cells. This is done by the procedure described in (Terekhov *et al.* 2020). As we can see in Fig. 4.37, both NTPSA and AvgMPSA schemes converge with second order with respect to displacements and we observe superlinear convergence with respect to stresses. We use a cubic mesh in these calculations. In Fig. 4.37, m is the inverse of the cube root of a number of cells in the domain on a log scale.

The residual over NTPSA iterations is shown in Fig. 4.38 on a semi-log scale. The structured cubic and unstructured extruded wedge grids of various resolutions are considered. The residual drops more than by two orders of magnitude every iteration. Once a cut-off tolerance 10^{-10} (orange line) is reached nonlinear iterations are stopped. Fig. 4.37, Fig. 4.38 demonstrate good behavior of the scheme in a homogeneous domain.

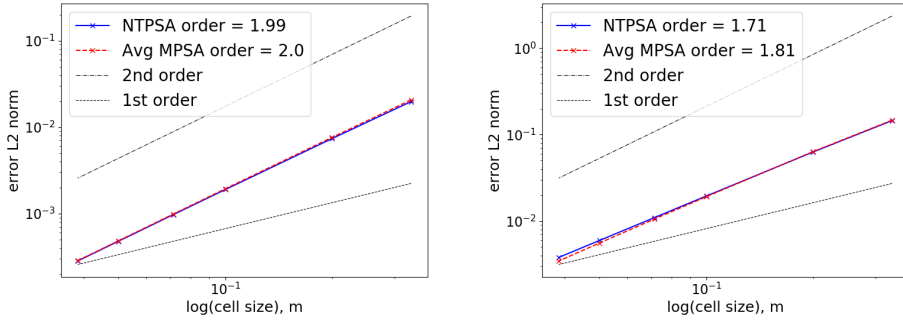


Figure 4.37.: The convergence of numerical solutions produced with nonlinear and linear schemes to the reference one. The second-order convergence for displacement vector (a) and superlinear convergence for stress tensor (b) is obtained.

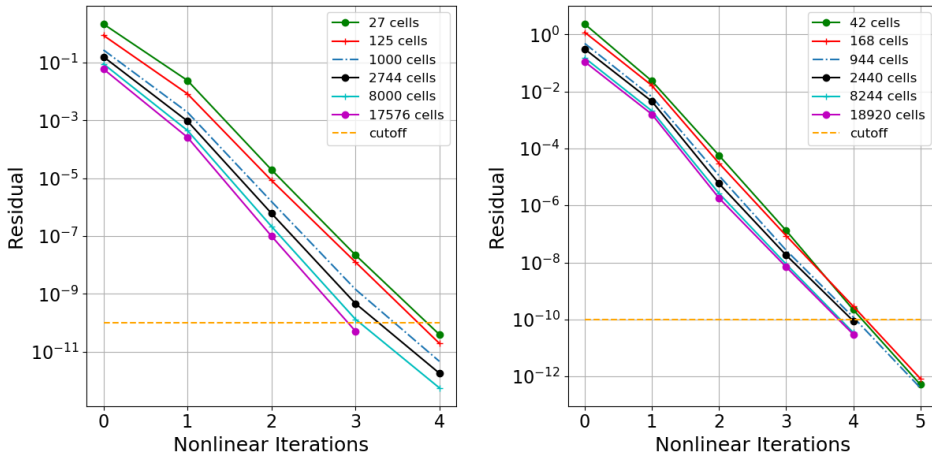


Figure 4.38.: Residual drop over nonlinear iterations for the setup calculated with a grid composed of structured hexahedrons (a) or unstructured wedges (b).

4.10.2. Compression and Shear

In this example, we consider the two-dimensional unit square domain ($\lambda = G = 1 \text{ Pa}$) shown in Fig. 4.19. The domain is subjected to shearing ($u_y = 0.01$) and smaller compressive ($u_x = 0.001$) displacements at the left boundary; the right boundary is kept fixed whereas the top and bottom sides are free. A plane strain setup is considered.

In contrast to the previous consideration of this setup, we do not allow the fault located in the center of the domain to slip. Instead, we analyze stress profiles over it while maintained stuck. In this test case, we consider a vertical fault with $\phi = 0^\circ$,

Table 4.8.: The properties of the meshes used in convergence study

Mesh type	L_c	$L_{c,frac}$	Cells	Least squares	Homogenization
Coarse square	0.025	0.025	1600	Smooth	Smooth
Coarse wedges	0.1	0.01	1274	Noisy	Noisy

see Fig. 4.19. Normal and tangential components of the traction vector over the line are presented in Fig. 4.39 for two types of mesh: an adaptive coarse wedge and a coarse square one. The details of the meshes are shown in Tab. 4.8. We compare the reference solution against the profiles obtained with three different schemes: Average MPSA with positivity-preserving gradient reconstruction, Average MPSA with least square gradient reconstruction and NTPSA. The magnitude of tangential traction is higher than the magnitude of the normal one which is consistent with displacements applied at the top boundary. Thus, the relative accuracy for tangential traction is noticeably higher than for normal traction. All considered schemes exhibit up to 3% deviation in tractions in this example. Although the regular square mesh produces much smoother traction profiles than the adaptive wedge mesh, it can not be used for more complex geometry.

In order to preserve a positive solution in the NTPSA scheme, we shift the reference state for displacements to $\{10, 10\}$ to make sure that they remain positive over nonlinear iterations. The NTPSA scheme takes 3 nonlinear iterations to converge to residual of 10^{-10} .

4.11. Conclusion

This chapter demonstrates the benchmarking of the numerical capabilities proposed in this thesis. To conclude, the following takeaways have been obtained

- The implemented scheme of FVM demonstrates linearity-preservation (Sec. 4.1) and convergence (Sec. 4.2, 4.10) in continuous anisotropic poroelastic media. It matches analytical solutions for poroelastic response in continuous homogeneous (Sec. 4.3, 4.4) and heterogeneous (Sec. 4.5) media.
- In conditions close to undrained, the implemented scheme of FVM exhibits unstable behavior caused by the violation of inf-sup conditions (Sec. 4.3-4.5). Although the considered stabilization (Sec. 3.4) reduces the oscillatory pattern appearing in these conditions, it introduces significant diffusion to the solution that, in some cases, leads to the worse solution accuracy compared to the non-stabilized scheme (Sec. 4.6).
- The scalability test of the implemented block-partitioned preconditioning strategy for continuous poroelastic media suggests about the weak scalability of the linear solver, although rigorous proof necessitates wider scalability analysis. (Sec. 4.7).

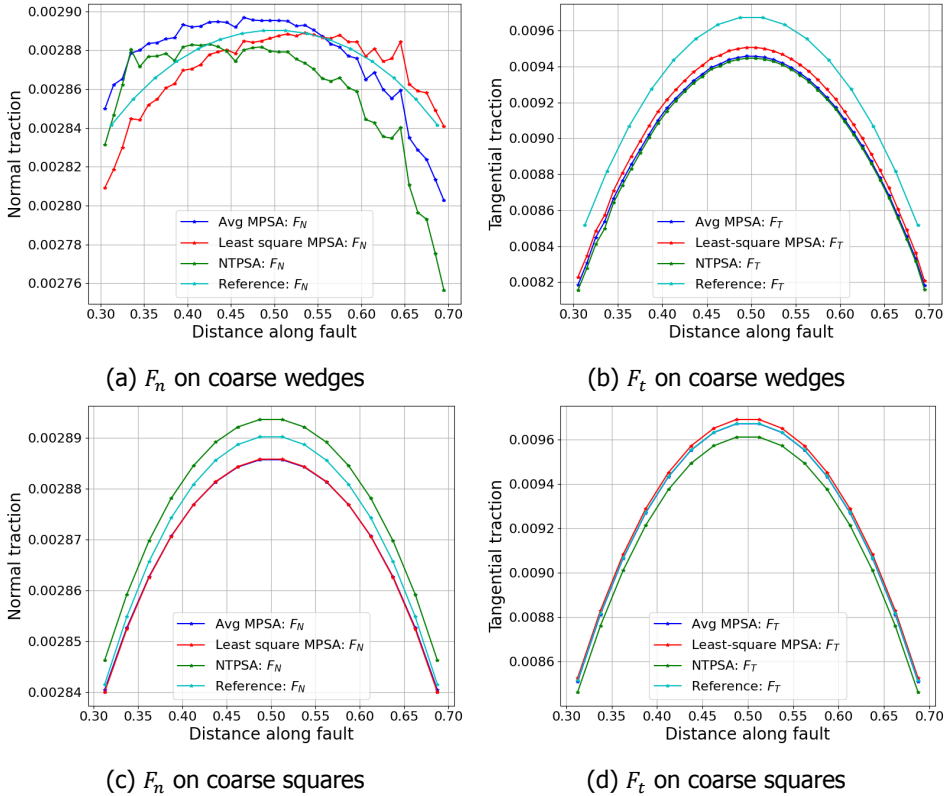


Figure 4.39.: Normal (a), (c) and tangential (b), (d) components of traction vector along the line in the center of the domain. (a), (b) and (c), (d) represent components calculated on the coarse wedge and coarse square grids respectively.

- The implemented scheme of FVM and the penalty method for contact mechanics provide solutions to the contact problems in a displaced fault configuration matching with the existing (semi-)analytical solutions (Sec. 4.9). The corresponding benchmarking has been conducted for the cases of frictionless, static and slip-weakening frictional contacts. This test case verifies the proposed numerical techniques for the modeling of contact problems in the presence of weak (stress) discontinuities.
- The comparison against an FEM simulator for the continuous heterogeneous proelastic setup (Sec. 4.8.1) and against a FVM simulator for the faulted homogeneous elastic setup (Sec. 4.8.2) further ensures the validity of the implemented scheme and the penalty method for contact constraints.
- The proposed nonlinear FVM demonstrates an accuracy in traction vector components over a straight line similar to the one obtained with linear FVM (Sec.

4.10). Thus, the supposed higher accuracy of the non-linear scheme have not been found.

5

Modeling of Experiments

Summary

This chapter considers the modeling of two experimental setups: injection-induced slip in core crosscut and the large-scale displaced fault setup. In the first setup, we demonstrate the validation of FVM numerical solutions against experimental results and the modeling of fault slip governed by rate-dependent friction law. The numerical investigation of the second case, performed with the other FE framework, focuses on the sensitivity study and the development of a possible loading path for the experiment.

5.1. Core Injection Experiments

The developed framework has been applied to model fluid-induced fault slip behavior observed in a core injection experiment (Wang *et al.* 2020a). The authors performed two fluid-induced slip experiments (SC1, SC2) conducted on permeable Bentheim sandstone crosscuts. Fault slip was triggered by fluid injection into the core at different rates. As a result, they measured slip, slip velocity, normal and shear stresses, and the apparent friction coefficient as a function of time.

In order to approximately simulate the experiment, the following setup is considered. A rectangular 2D domain (Fig. 5.1) of 50×100 mm size is loaded from the left and the right with confining normal stress $|\mathbf{f}| = 350$ bar and initially is loaded from the top by a constant displacement $u_y^{\text{top}} = -0.385$ mm in SC1 and $u_y^{\text{top}} = -0.36$ mm in SC2. A roller condition is specified for the tangential degree of freedom at the top boundary whereas the displacements at the bottom boundary are fixed. Following the post-processing of experimental results (Wang *et al.* 2020a) we apply plane strain conditions to the third dimension. Although, in the experimental setup the confining stress is applied to all domain's sides in xz plane, the combination of input parameters (σ_{xx}, p) and control parameter u_y^{top} used here allow the effect of missing confining stress along z -axis to be modeled with adjusting u_y^{top} while fitting measured fault stresses. Thus, the use of plane strain conditions is acceptable in this modeling. The domain has constant Young's modulus 26 GPa, Poisson's ratio $\nu = 0.17$, an isotropic Biot tensor $\mathbf{B} = b\mathbf{I}$, $b = 0.6$ an isotropic permeability tensor $\mathbf{K} = k_0\mathbf{I}$, $k_0 = 1$ D, porosity $\phi_0 = 0.23$ and constant compressibility $1.45 \cdot 10^{-10} \text{Pa}^{-1}$. The fault has the same permeability as the matrix.

The normal displacements applied from the top are chosen to match the initial vertical stress observed in the experiment. Using a Neumann condition for the top boundary directly is not possible because once the fault starts sliding, the problem becomes purely Neumann so that the displacements in the top piece become defined with respect to a constant.

Water of constant viscosity $\mu_f = 1$ cP and compressibility 10^{-9}Pa^{-1} is injected into the domain through the bottom boundary at a specified pressure $p = p(t)$ whereas the other boundaries are impermeable. The evolution of injection pressure and friction coefficient are taken precisely from the experimental data and are shown in Fig. 5.2. The injection pressure is increased step-wise in SC1 while in SC2 it is increased gradually while keeping the pressure constant during short periods of time.

Fig. 5.2 depicts the dynamics of experimental slip, slip velocity, normal and shear stresses compared to calculated values. Although we used a 2D approximation of a 3D setup, there is a good match in terms of slip, both stresses and slip velocity in both tests.

Above, we use the friction coefficient calculated from the experimental data. Now we employ the steady-state friction law defined as

$$\mu = \mu^* + (a - b) \ln \left(\frac{\dot{\mathbf{g}}_T}{\mathbf{v}^*} \right), \quad (5.1)$$

where μ^* is a reference friction coefficient measured at reference velocity \mathbf{v}^* , while

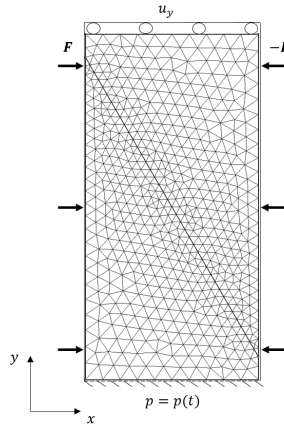


Figure 5.1.: Model setup.

a and b are the parameters of the rate-and-state friction law (Dieterich 1979; Ruina 1983).

A comparison of the friction coefficients obtained in modeling and measured in the experiment is shown in Fig. 5.3. The calculated friction coefficient manages to qualitatively represent the behavior observed in the experiment except during the final stage of SC2 where strong slip-weakening is exhibited.

The use of rate-dependent friction laws is complicated by the fact that friction goes to infinity in Eq. (5.1) when the slip velocity is equal to zero. One of the options is to use a regularized rate-and-state friction law (Lapusta *et al.* 2000). In this modeling, we impose a cut-off on the magnitude of the slip velocity $v_{co} = 0.01v^*$. Below this cut-off $|\dot{\mathbf{g}}_T| < v_{co}$ we assume the friction coefficient to remain equal to the reference value $\mu = \mu^*$. Another complication is that under the quasi-static assumption we may not observe the slip velocity to remain continuous over time. As a result, rate-dependent friction may exhibit noisy behavior. The results shown in Fig. 5.3 are calculated with a large time step $\Delta t = 20$ s. The use of smaller time steps leads to more frequent oscillations in slip velocity and in friction.

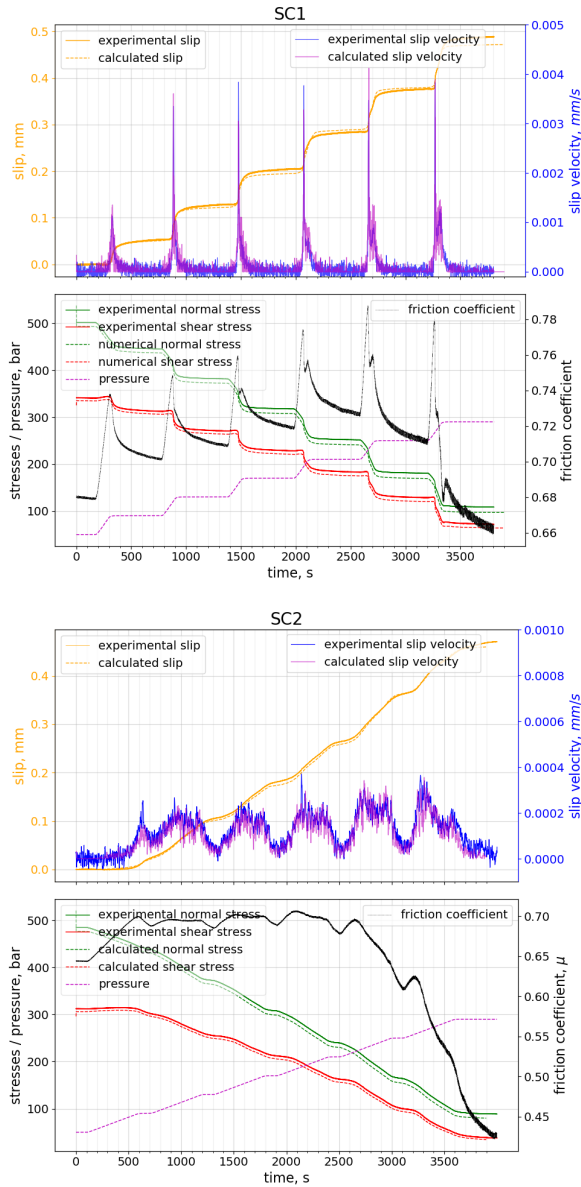


Figure 5.2.: Numerical simulation of core injection experiments from (Wang *et al.* 2020a). Two injection scenarios were considered: step-wise increase (SC1) and gradual increase (SC2) of injection pressure from 50 to 350 bar. The time-dependent friction coefficient was taken from the experiment.

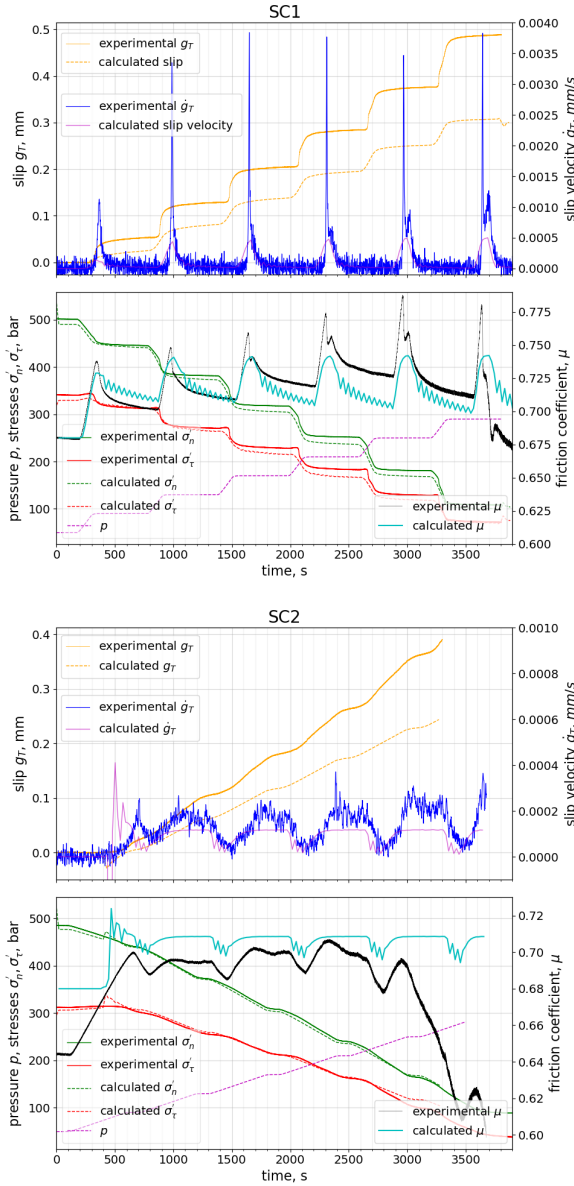
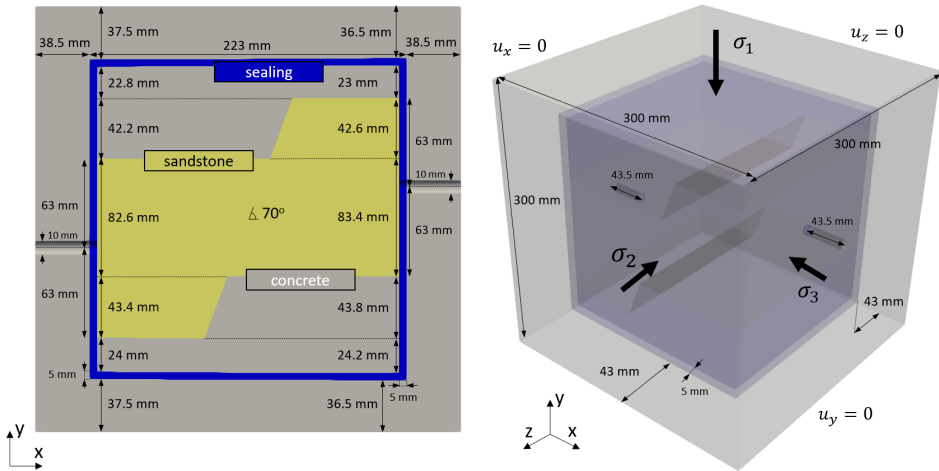


Figure 5.3.: Numerical simulation of core injection experiments from (Wang *et al.* 2020a). Two injection scenarios were considered: step-wise increase (SC1) and gradual increase (SC2) of injection pressure from 50 to 350 bar. Steady-state friction law defined in Eq. (5.1) is used, where $\mu^* = 0.68$, $a - b = 0.01$, $v^* = 1 \text{ nm s}^{-1}$ in experiment SC1, and $\mu^* = 0.68$, $a - b = 0.006$, $v^* = 1 \text{ nm s}^{-1}$ in experiment SC2.

5.2. Large-Scale Triaxial Loading Experiment

For the investigation of induced seismicity in a displaced fault configuration, a corresponding experimental setup has been designed and assembled in the GSE Laboratory of the Delft University of Technology. We prepared a numerical counterpart of this experimental setup in order to evaluate possible loading paths of the upcoming experiment. In this section, we present the numerical model of this setup, the results of simulation, and propose the loading path for the experiment.

5.2.1. Model Setup



(a) x-y midplane.

(b) 3D view and boundary conditions.

Figure 5.4.: Numerical model of the large-scale experimental setup.

We consider a cubic setup of $30 \times 30 \times 30$ cm dimensions constituted of three materials: purely elastic concrete, sealing material and poroelastic sandstone. The material properties are listed in Tab. 5.1 while Fig. 5.4 illustrates the domain geometry, materials and boundary conditions. The concrete frame covers the inner block of the cubic geometry. This block consists of concrete parts cemented to the sandstone. The block of sandstone was cut into two parts over an angle $\theta = 70^\circ$ to horizontal, and the parts were displaced over the cross-cut. The obtained displaced configuration was supplemented by concrete parts cemented to the sandstone in

Table 5.1.: Material properties.

Material	E , GPa	ν	b	ϕ_0	k , D
concrete	19.6	0.115	0	0	10^{-10}
sealing	5.2	0.34	0	0	10^{-10}
sandstone	17	0.3	0.9	0.15	1

order to achieve an almost cubic geometry. The 5 mm layer of sealing isolates the inner block and prevents fluid leakage. Two holes of 10 mm diameter were drilled from the outside towards the centers of the sides of the two sandstone blocks in order to be able to pump fluid to the sandstone.

The setup is subjected to triaxial compression with $\sigma_3, \sigma_1, \sigma_2$ uniform compressive forces applied at the positive sides (i.e. facing to the positive axis directions) of the domain respectively, see Fig. 5.4b. At the negative (opposite) sides, the zero normal displacement balances the applied forces. Tangential forces remain equal to zero at all boundaries. Besides, the injection of fluid into the displaced sandstone block is modeled by assigning a uniform pressure within the block.

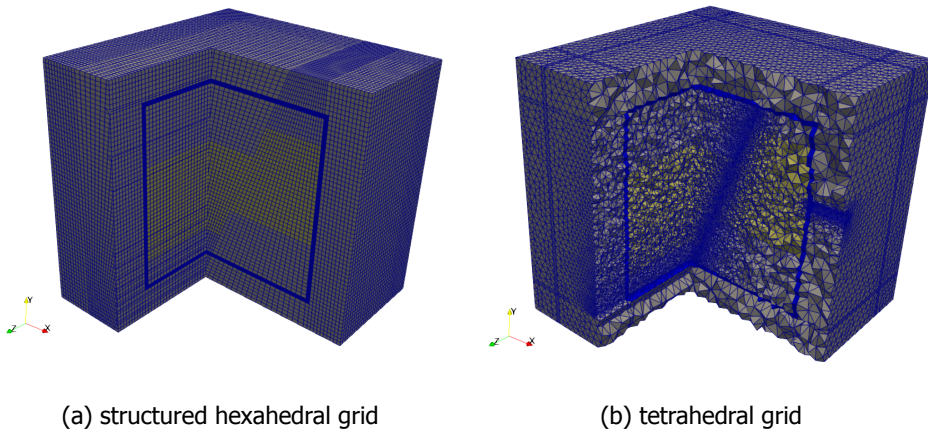


Figure 5.5.: Computational grids used in simulation. The structure hexahedral grid does not consider holes.

In Sec. 4.8.1, we presented a simplified 2D model of this setup. We conducted a comparison of the proposed FVM framework, implemented in DARTS, against the solution obtained with a simulation framework known as GEOS (Settgast *et al.* 2022). For modeling the full 3D experimental setup, we utilize GEOS, as it is more effectively optimized for handling large-scale models (exceeding 10^6 cells). GEOS employs a combined FEM-FVM numerical method for the fully implicit integration of momentum balance and fluid mass equations, respectively.

In simulations, we use structured hexahedral and tetrahedral grids of various resolutions. The grids are displayed in Fig. 5.5. Structured grids often provide a less noisy solution than tetrahedral grids. However, they are limited in terms of adaptivity. Therefore, the structured grid in our application does not consider holes introduced in the model geometry in Fig. 5.4. In contrast, the tetrahedral mesh enables adaptive grid refinement allowing holes and stress peaks to be accurately resolved. We set the origin of the coordinate system in the center of the domain.

In all calculations below, we consider the pre-slip state of the cross-cut plane mimicking the fault. However, we assess the fault stability by investigating the Coulomb stresses calculated under the assumption of the following distribution of

static friction coefficient

$$\mu = \begin{cases} 0.6, & \text{sandstone-sandstone contact,} \\ 0.62, & \text{sandstone-concrete contact,} \\ 0.67, & \text{concrete-concrete contact,} \end{cases} \quad (5.2)$$

which assigns different values of friction coefficient to the contacts between different materials. Coulomb stress utilizes the Terzaghi effective stress according to Eq. 2.38. Moreover, zero cohesion is assumed.

5.2.2. In-Plane Stress Distribution

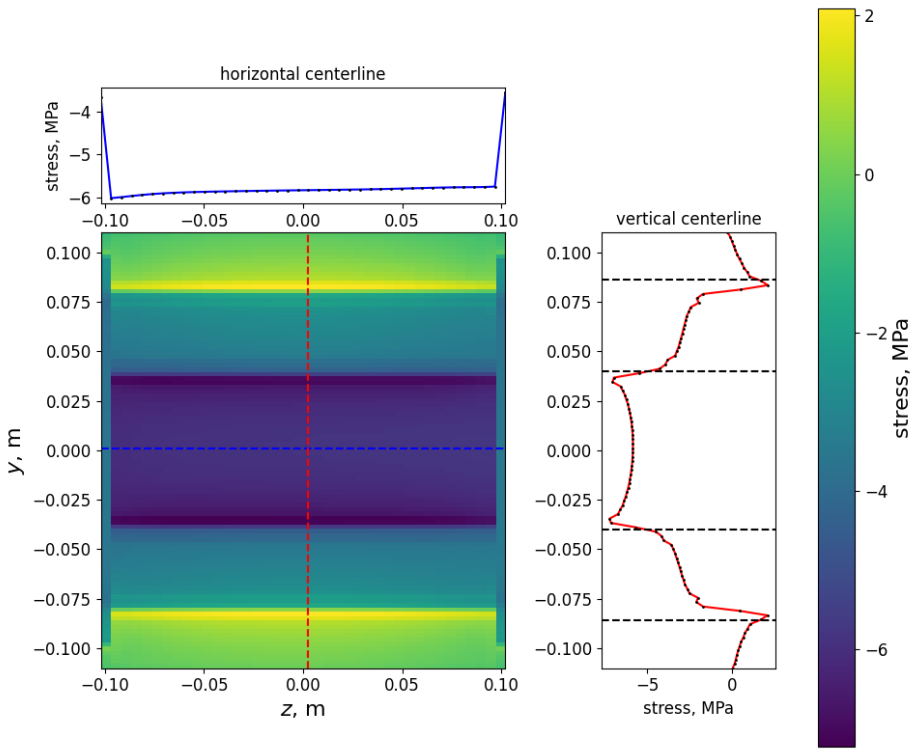


Figure 5.6.: The distribution of Coulomb stress over the cut plane with $\sigma_1 = -25$ MPa, $\sigma_2 = \sigma_3 = -10$ MPa, $p = 0.1$ MPa. Coulomb stress profiles over horizontal (blue) and vertical centerline (red) centerlines. The structured hexahedral grid of 231k cells is used.

First, we investigate the distribution of stresses in the cross-cut plane. Fig. 5.6 and Fig. 5.7 illustrate the results of simulation with the structured hexahedral and adaptive tetrahedral grids. They include 2D maps of Coulomb stress over

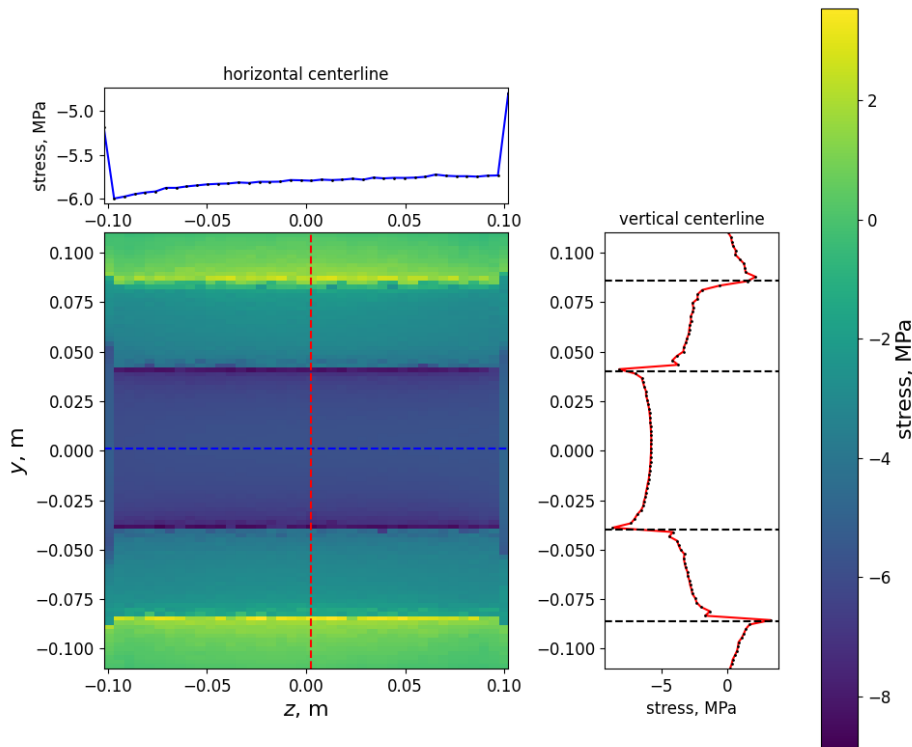


Figure 5.7.: The distribution of Coulomb stress over the cut plane with $\sigma_1 = -25$ MPa, $\sigma_2 = \sigma_3 = -10$ MPa, $p = 0.1$ MPa. Coulomb stress profiles over horizontal (blue) and vertical centerline (red) centerlines. The adaptive tetrahedral grid of 576k cells is used.

the plane with 1D profiles over horizontal and vertical centerlines for the stresses $\sigma_1 = -25$ MPa, $\sigma_2 = \sigma_3 = -10$ MPa and pressure $p = 0.1$ MPa. We see that a combined effect of pressure and heterogeneity introduces peaks in Coulomb stresses at the corners of sandstone blocks. As a result, the Coulomb stress exceeds zero at the outer corners of sandstone blocks which means that we expect the fault to slip at those locations. This fact is aligned with analytical expressions (Jansen *et al.* 2019) which presume having slip at the outer corners during fluid injection and at the inner corners during fluid extraction.

We may observe that the 2D map of Coulomb stress calculated with the structured hexahedral grid in Fig. 5.6 has less numerical noise than the one calculated with the tetrahedral grid in Fig. 5.7. However, the structured grid has a coarser resolution around the corners which can be seen in the vertical profile in Fig. 5.6. An other important observation is that the horizontal distribution (along the z-axis) of Coulomb stresses within the plane is almost uniform. This fact allows us to limit the investigation of stresses by the consideration of 1D stress profiles taken over

the vertical centerline of the fault plane, i.e. red line in Figs. 5.6 and 5.7.

5.2.3. Sensitivity Study

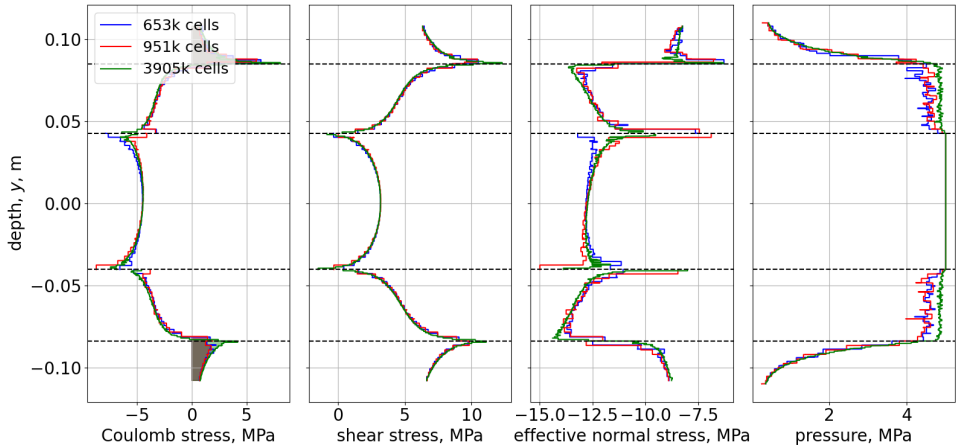


Figure 5.8.: The sensitivity of fault properties plotted over its centerline $z = 0$ to the resolution of the tetrahedral grid. The following stresses are applied at the boundary $\sigma_1 = -25$ MPa, $\sigma_2 = \sigma_3 = -10$ MPa while the pressure $p = 5$ MPa maintained in the sandstone block.

To facilitate a consistent modeling of the experimental setup we perform a set of sensitivity studies. We start with a resolution study of the adaptive tetrahedral grid shown in Fig. 5.5b. We prepared three grids comprised of 653k, 951k and 3905k cells adaptively refined towards the fault plane and holes.

Fig. 5.8 demonstrates the comparison of the fault properties obtained with these three grids for the uniform Neumann boundary conditions defined by $\sigma_1 = -25$ MPa, $\sigma_2 = \sigma_3 = -10$ MPa and uniform pressure $p = 5$ MPa assigned to the porous sandstone block. Coulomb stress, shear stress, Terzaghi effective normal stress and pressure are plotted over the centerline $z = 0$ of the fault plane.

We observe that the finer grid much better resolves stress peaks near both the inner and outer corners of the sandstone block. The Coulomb stress reveals the possibility of slip at the outer corners. The proper resolution of these stress peaks is important as they are responsible for generating positive Coulomb stress and, consequently, slip. This result suggests using finer grids in simulation.

Besides, we observe a strange noise in the fluid pressure over the contact between sandstone and concrete. This is a result of the interpolation of cell-centered pressure from the neighboring cells to the fault plane, where it exhibits a jump.

The experiment is supposed to be conducted with a large triaxial machine that applies uniform displacements at the boundaries of the experimental setup. However, it is more convenient to perform simulation with uniform Neumann boundary

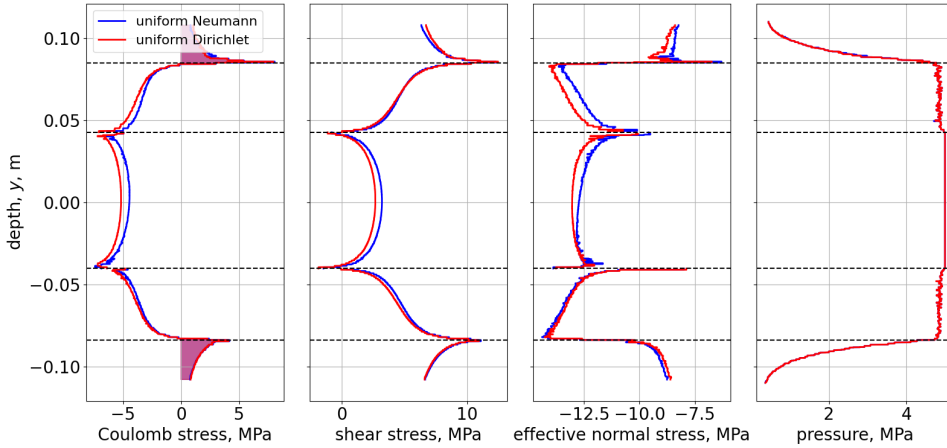


Figure 5.9.: The sensitivity of fault properties plotted over its centerline $z = 0$ to the kind of boundary condition. The uniform Neumann condition with $\sigma_1 = -25$ MPa, $\sigma_2 = \sigma_3 = -10$ MPa is compared against uniform Dirichlet conditions with $u_y = -0.349$ mm, $u_x = -0.062$ mm, $u_z = -0.063$ mm. Fluid pressure $p = 5$ MPa is maintained. Both conditions generate the same cumulative load at the boundaries. The tetrahedral adaptive grid with 3905k cells is used.

conditions because they allow the applied stresses to be directly controlled.

To ensure the similarity of uniform Neumann and uniform Dirichlet boundary conditions, we perform a comparison of the same setup calculated with the following two conditions. First, we model the experimental setup with uniform Neumann boundary conditions defined by $\sigma_1 = -25$ MPa, $\sigma_2 = \sigma_3 = -10$ MPa as we have done before. It implies that the constant normal load compresses every segment of the boundary planes, different for different boundary planes. Then, we perform a set of simulations with uniform Dirichlet boundary conditions of multiple magnitudes. The conditions imply having the normal displacements uniformly applied to every segment of the boundary surfaces. Three displacements applied to three surfaces define the boundary condition. As an initial guess for these displacements, we use the mean values of normal displacements we observed in the modeling with the Neumann boundary condition. Eventually, we find $u_y = -0.349$ mm, $u_x = -0.062$ mm, $u_z = -0.063$ mm produce cumulative loads at the boundaries close enough to what we specified for the Neumann boundary condition. In all calculations here we maintain a uniform fluid pressure $p = 5$ MPa inside the sandstone block.

Fig. 5.9 presents the comparison of fault properties obtained in simulations with these two boundary conditions. We observe insignificant difference between stresses inside the sandstone block whereas the stresses around the outer stress peaks match each other. This result justifies the use of the Neumann boundary

conditions for the modeling of the experimental setup.

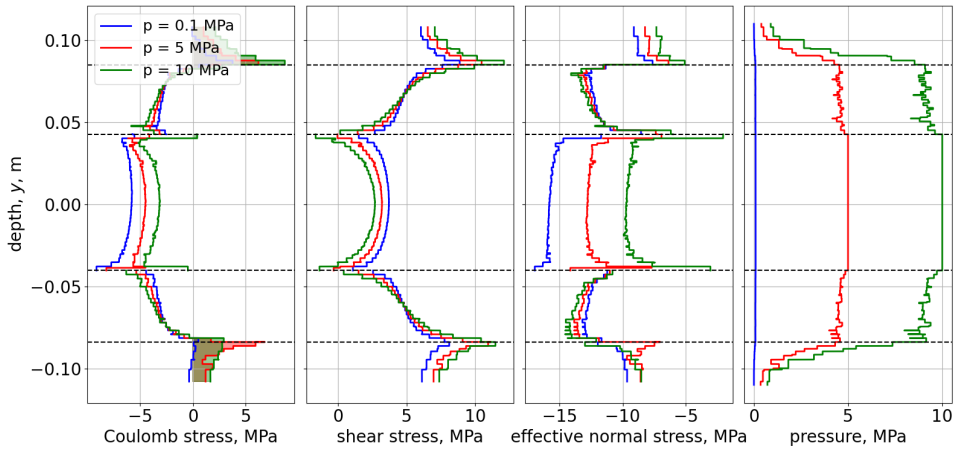


Figure 5.10.: The sensitivity of fault properties plotted over its centerline $z = 0$ to fluid pressure in sandstone. The compression stresses applied to the domain are $\sigma_1 = -25$ MPa, $\sigma_2 = \sigma_3 = -10$ MPa. The tetrahedral adaptive grid with 653k cells is used.

Next, we perform a sensitivity study to the variation of fluid pressure in the sandstone block. Fig. 5.10 illustrates the fault properties plotted over the centerline $z = 0$ of the fault plane. According to the figure, higher fluid pressure causes higher magnitudes of shear stress peaks at the corners. The profiles of shear and effective normal stress demonstrate a competition between corresponding contributions to Coulomb stress. Even though, in this particular case, the higher pressure tends to provoke higher Coulomb stress, and, consequently, slip at the upper corners and at the lower inner corner of the sandstone block; however, this result is not general and certainly changes for different values of input parameters. This, therefore, does not allow us to draw conclusive results about the effect of pressure on the Coulomb stress.

Fig. 5.11 illustrates the sensitivity of fault properties to the magnitudes of stresses applied at the boundary. We present results for three pairs of stresses: $\sigma_1 = 20$ MPa, $\sigma_2 = 5$ MPa, $\sigma_1 = 25$ MPa, $\sigma_2 = 10$ MPa and $\sigma_1 = 30$ MPa, $\sigma_2 = 15$ MPa maintaining $\sigma_3 = \sigma_2$ and $p = 0.1$ MPa. As can be observed from the figure, Coulomb stress is inversely proportional to the magnitudes of stresses. This can be explained by the higher compressive normal stresses obtained for the higher stress magnitude while shear stress, proportional to differential stress $\sigma_1 - \sigma_2$, remains almost unchanged. Therefore, the pair of stresses with the lowest magnitudes, namely $\sigma_1 = 20$ MPa, $\sigma_2 = 5$ MPa produces the higher profile of Coulomb stress, provoking much wider slip patches than the two other pairs of stresses. This result ensures the fact of slippage even in the case of low applied stresses. This information may be very useful for the experiment as the laboratory equipment has an

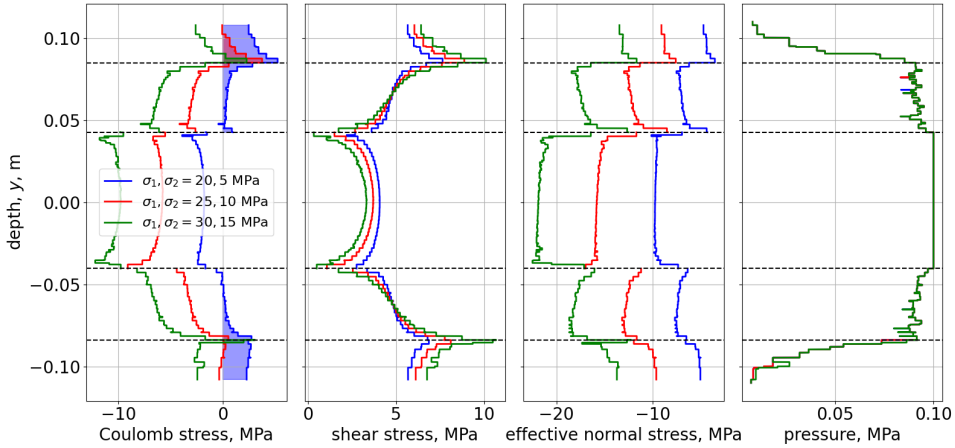


Figure 5.11.: The sensitivity of fault properties plotted over its centerline $z = 0$ to the magnitudes of applied stresses. Fluid pressure $p = 0.1$ MPa and x-axis stress $\sigma_3 = \sigma_2$ are maintained. The tetrahedral adaptive grid composed of 653k cells is used.

upper limit for the magnitude of compressive stresses.

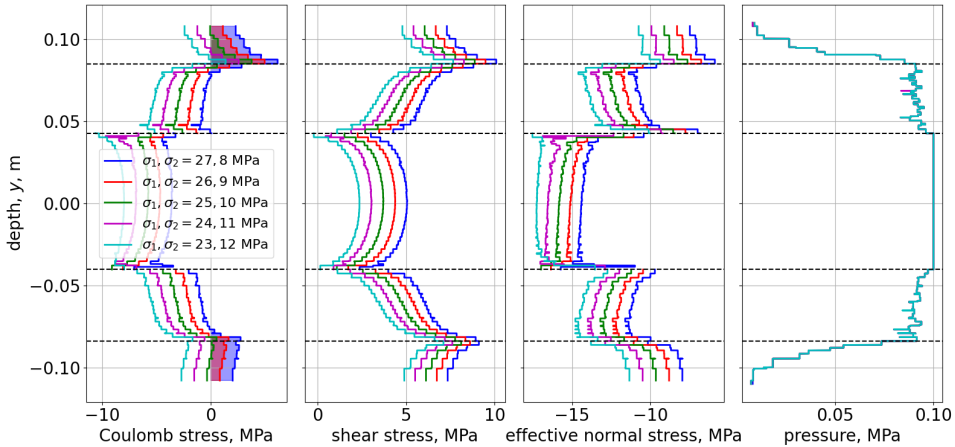


Figure 5.12.: The sensitivity of fault properties plotted over its centerline $z = 0$ to the applied differential stress. Fluid pressure $p = 0.1$ MPa and x-axis stress $\sigma_3 = \sigma_2$ are maintained. The tetrahedral adaptive grid composed of 653k cells is used.

In the last sensitivity study, we investigate the effect of differential stress on fault properties and, in particular, on Coulomb stress. We take $\sigma_1 = 25$ MPa, $\sigma_2 =$

10 MPa as a reference case keeping $\sigma_3 = \sigma_2$, $p = 0.1$ MPa and, then, we symmetrically change σ_1, σ_2 by 1 MPa a couple of times. As a result, Fig. 5.12 shows the fault properties calculated for 5 values of differential stress: starting from the lowest value $\sigma_1 - \sigma_2 = 23$ MPa - 12 MPa = 11 MPa up to the highest one $\sigma_1 - \sigma_2 = 27$ MPa - 8 MPa = 19 MPa. As expected, the highest differential stress generates the largest Coulomb stress over the fault as both shear and effective normal stresses promote slippage at the higher differential stress than for the lower ones considered. These results confirm the guess that the higher differential stress should provoke more slippage in the current displaced fault setup.

5.2.4. Loading Path

The goal of the laboratory experiment under the displaced fault setup is to investigate the acoustic emission generated during rupture initiation and propagation. This investigation can provide multiple insights into the induced seismicity observed in subsurface. To facilitate this investigation, the design of the experiment should be appropriately elaborated. In particular, the loading path, which involves the dynamics of boundary stresses $\sigma_1, \sigma_2, \sigma_3$ and fluid pressure p over the experiment's time, must satisfy multiple requirements.

First, the contact plane in the experimental setup must exhibit slippage. The sufficient condition of slippage is the satisfaction of slippage criterion which is assumed to be Coulomb stress in current consideration. Second, the laboratory equipment imposes certain limitations on the maximum compression stress achievable in the experiment ($\sigma_1 < 30$ MPa). Third, the materials and the assembly of the experimental setup impose restrictions on the maximum differential stress and the maximum fluid pressure ($p < 7$ MPa).

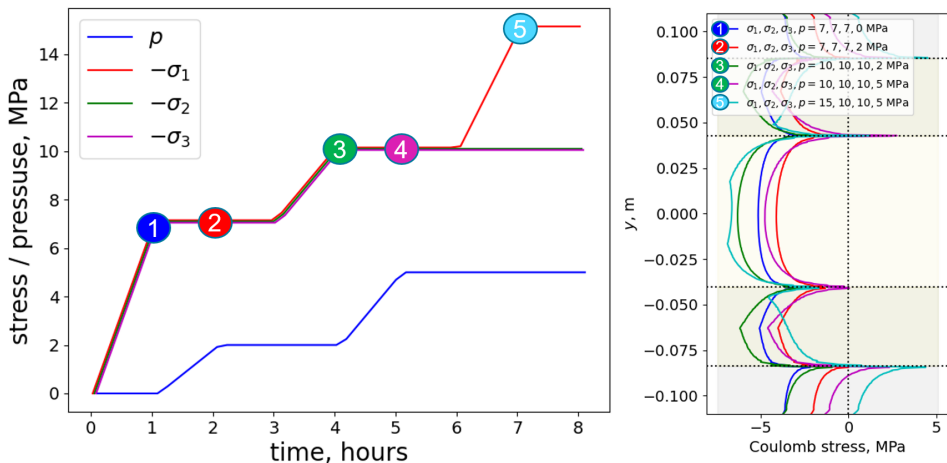


Figure 5.13.: The proposed loading path for the laboratory experiment. The applied boundary stresses and fluid pressure over time and Coulomb stress profiles over the $z = 0$ centerline of the fault plane.

Many simulation runs have been performed in the region of control parameters admissible for the mentioned constraints. As a result, Fig. 5.13 shows the proposed loading path and Coulomb stress profiles observed at several points over the loading. Coulomb stress suggests having slippage at the outer corners of the sandstone block starting from point #4. The unavoidable uncertainties in the material and contact properties motivate us to reach the estimated critical state slowly. That explains the multi-step behavior of the loading path preceding point #4.

5.3. Conclusion

This chapter is dedicated to the modeling of two experimental setups. The following presents concluding remarks regarding the modeling of injection-induced slip in core crosscuts (Sec. 5.1)

- The modeling with the predefined measured static friction coefficient demonstrates a good match of the measured slip (Fig. 5.2) and further validates the proposed numerical framework.
- The modeling with a rate-dependent friction coefficient qualitatively represents the measured behavior of the friction coefficient (Fig. 5.3). The significant deviation between estimated and measured slip can be explained by the disability of the quasi-static model to accurately resolve slip velocity. Furthermore, the modeling with rate-dependent friction involves nonlinear convergence issues, which are amplified with smaller time steps.

The second setup considers a large-scale block with displaced fault configuration (Sec. 5.2). The key takeaways obtained in the modeling of this setup are

- The distribution of Coulomb stresses within the fault plane is almost uniform along the z -axis (Figs. 5.6, 5.7). It enables to simplify the further consideration to 1D profiles over the vertical centerline of the fault plane.
- The conducted sensitivity study suggests using the tetrahedral grids adaptively refined towards the fault plane for a better resolution of stress peaks at the corners of the poroelastic reservoir (Fig. 5.8). While the type of boundary condition demonstrates a negligible effect on the distribution of Coulomb stress (Fig. 5.9), a lower stress magnitude and a higher differential stress are found to be more slip-provoking (Figs. 5.11, 5.12) whereas the effect of fluid pressure is ambiguous (Fig. 5.10).
- The proposed loading path for the experiment (Fig. 5.13) ensures the appearance of fault slippage, and it satisfies the limitations imposed by the materials and equipment used in the experiment.

6

Beyond the Quasi-Static Modeling of Induced Seismicity

Summary

In the previous sections, we have investigated the response of poroelastic media with frictional contact under quasi-static (QS) assumption. We demonstrated that the proposed Finite Volume scheme together with the penalty method has successfully resolved aseismic slip even in challenging examples. However, the contacts governed by non-static friction laws, which hold significant practical importance, present a profound nonlinearity that is challenging to address (Yastrebov et al. 2013) and usually leads to nonlinear convergence issues. Moreover, these issues naturally appear in the case of seismic events when slip may grow from aseismic values by up to a few magnitudes. In this case, the proposed method can successfully resolve only the onset of seismicity up to the nucleation point. The modeling of the subsequent or coseismic phase, which includes the propagation and arrest of contact rupture, requires additional treatment.

In order to resolve the rupture dynamics during the coseismic phase and to overcome convergence issues, quasi-dynamic (QD) and fully dynamic (FD) approaches have been utilized for decades. The QD approach augments the QS model with a radiation damping term. This term helps to avoid an unbounded slip speed appearing in QS simulation at rupture fronts (Rice 1993; Rice et al. 2001). At the same time, the QD approach does not account for inertia and avoids complicated integration of this term. In contrast, the FD approach does not consider radiation damping, but requires the integration of an inertia term. As a result, FD simulation allows not only rupture but also elastic wave propagation to be resolved, although at a much higher computational cost compared to the QD approach.

Below, we present the equations that govern both QD and FD approaches, the numerical strategies to incorporate them into the current framework, and the val-

idation of the FD strategy. In the end, we investigate the rupture dynamics in a displaced fault case study.

6.1. Quasi-Dynamic Approach

The QD approach considers a *radiation damping* term added to the sliding criterion in Eq. (2.38) as

$$\Phi = |\mathbf{f}_T| - \mu f'_N - c + \eta |\dot{\mathbf{g}}_T|, \quad (6.1)$$

where η is the radiation damping factor, and $\dot{\mathbf{g}}_T$ is slip velocity. The radiation damping term effectively introduces a velocity-dependent cohesion.

Taking into account the radiation damping term, the discrete equation in Eq. (3.101) reads

$$\mathbf{f}'_T{}^{n+1} - \tilde{\mathbf{f}}'_T + \langle \tilde{\Phi} \rangle \frac{\tilde{\mathbf{f}}'_T}{|\tilde{\mathbf{f}}'_T|} + \frac{\alpha \varepsilon_T}{\Delta t_n} |\mathbf{g}_T^{n+1} - \mathbf{g}_T^n| = \mathbf{0}, \quad (6.2)$$

where the backward Euler scheme approximates the slip velocity.

The penalization incorporated into $\tilde{\mathbf{f}}'_T$, $\tilde{\Phi}$ makes other terms in Eq. (6.2) insignificant in the presence of non-zero slip velocities. In this case, the radiation damping term should be correspondingly scaled. For this purpose, we introduce a penalty parameter ε_T in the radiation damping term $\eta = \alpha \varepsilon_T$, where α is an empirical coefficient.

6.2. Fully-Dynamic Approach

The FD approach introduces an inertia term in the QS momentum balance equation in Eq. (2.47) as

$$\alpha \rho \ddot{\mathbf{u}} - \nabla \cdot \boldsymbol{\Sigma} - \rho g \nabla z = 0, \quad (6.3)$$

where α is a control parameter, the total density ρ is defined in Eq. (2.53), and the total stress tensor $\boldsymbol{\Sigma}$ is defined in Eq. (2.48). The integration of Eq. (6.4) requires the knowledge of the initial velocity. The parameter α is used to turn off the inertia term controlling the (either QS or FD) mode of simulation.

The backward Euler scheme can be applied for the integration of inertia as

$$\ddot{\mathbf{u}}^{n+1} = (\Delta t_n + \Delta t_{n-1})^{-1} \left[\frac{\mathbf{u}^{n+1} - \mathbf{u}^n}{\Delta t_n} - \frac{\mathbf{u}^n - \mathbf{u}^{n-1}}{\Delta t_{n-1}} \right], \quad (6.4)$$

which provides a first-order approximation.

The following approximations of velocity and displacements

$$\dot{\mathbf{u}}^{n+1} = \dot{\mathbf{u}}^n + \Delta t ((1 - \gamma) \ddot{\mathbf{u}}^n + \gamma \ddot{\mathbf{u}}^{n+1}), \quad (6.5)$$

$$\mathbf{u}^{n+1} = \mathbf{u}^n + \Delta t \dot{\mathbf{u}}^n + \frac{\Delta t^2}{2} ((1 - 2\beta) \ddot{\mathbf{u}}^n + 2\beta \ddot{\mathbf{u}}^{n+1}). \quad (6.6)$$

lead us to the family of Newmark schemes with parameters γ, β (Newmark 1959). The choice of $\gamma = 0.5$ ensures second-order accuracy of the obtained scheme. Substitution of $\beta = 0$ provides an explicit scheme while $\beta = 0.25$ results in an implicit unconditionally stable scheme.

The incorporation of Eqs. (6.5), (6.6) into the Finite Volume scheme for the QS system in Eq. (3.13) provides system of equations with unknown acceleration $\ddot{\mathbf{u}}^{n+1}$ instead of displacement \mathbf{u}^{n+1} . It reads as follows

$$\mathbf{H}_{s,i}^{n+1} = \rho_i^{n+1} V_i (\ddot{\mathbf{u}}^{n+1} - g \nabla z) + \beta \Delta t_n^2 \sum_{j \in \partial V_i} \delta_j \mathbf{f}_j^{n+1}(\mathbf{u}^{n+1}), \quad (6.7)$$

where Eqs. (6.5) and (6.6) are used for the assembly of fluxes $\mathbf{f}_j^{n+1}(\mathbf{u}^{n+1})$.

6.3. Combined Quasi-Dynamic and Fully Dynamic Strategy

We use the combined QS and FD modeling to overcome the convergence issues appearing close to the nucleation point. The coefficient α in front of the inertia term in Eq. (6.3) determines a particular simulation mode. The QS mode implies having $\alpha = 0$ while the FD mode requires $\alpha = 1$. By default, the simulation runs in the QS mode. The loss of nonlinear convergence causes a reduction of time step. Whenever the time step is reduced to the magnitude of one second, the FD mode becomes activated. The backward transition to the quasi-static mode happens when arrest of the rupture is observed. We identify the rupture arrest by measuring the relative area of recently activated fault segments which left slip state and become stuck according to criterion in Eq. (2.25). Whenever the significant percentage of fault become stuck, we switch back to the QS mode.

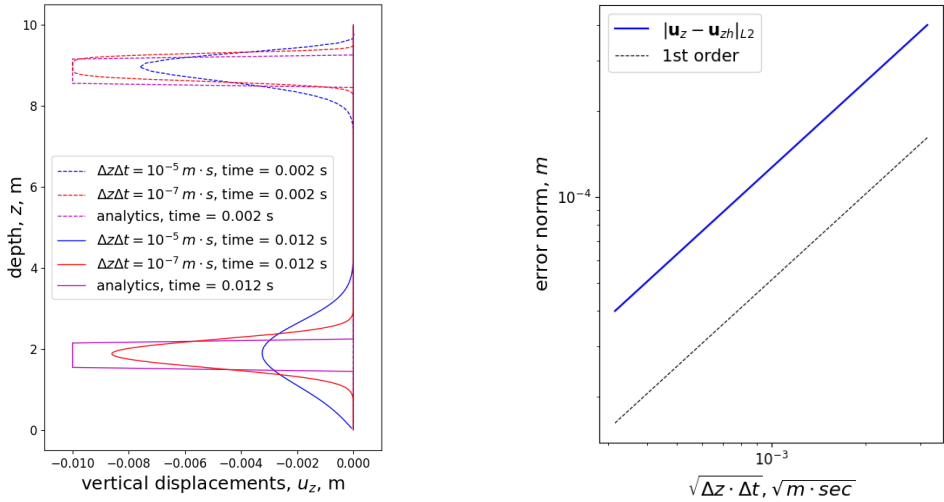
In this work we use the direct solver for the inversion of linear systems appeared in the QS mode. In the FD mode we find GMRES iterations quite efficient once used with ILU(0) preconditioner.

6.4. Validation

6.4.1. One-Dimensional Elastic Wave Propagation

The solution of the one-dimensional wave equation is perhaps the easiest way to validate the numerical schemes proposed for the FD approach. We consider a purely elastic one-dimensional column $[0, 1] \times [0, 1] \times [0, 10] \in \mathbb{R}^3$ with Young's modulus $E = 1$ GPa, Poisson's ratio $\nu = 0.25$ and total density $\rho = 2406$ kg m⁻³. All the boundaries are maintained under the roller condition, but, in addition to zero tangential traction, at the upper one $z = 10$ m, time-dependent normal displacements are specified as $u_z = u_z(t)$. The function $u_z(t)$ generates a rectangular compression wave of magnitude $u_z^0 = -0.01$ m that lasts $T = 0.001$ sec.

Fig. 6.1 demonstrates the calculated and analytical profiles of vertical displacements at two moments of time (Fig. 6.1a) and the obtained order of convergence



(a) Calculated and analytical displacements at $t = 0.002 \text{ s}$ and at $t = 0.012 \text{ s}$.

(b) Numerical convergence with respect to analytical solution

Figure 6.1.: Vertical displacements (a) and the convergence (b) for backward Euler time integration.

(Fig. 6.1b). We present a couple of results of different resolutions calculated with the same Courant–Friedrichs–Lewy number $\text{CFL} = 0.706$. As expected the backward Euler time integration significantly smoothens the initial profile even for a grid of finer resolution. It provides first order of convergence with respect to the square root of timestep and cell size.

The comparison of analytical and numerical displacement profiles obtained with the Newmark scheme is presented in Fig. 6.2. We use the implicit scheme with the trapezoidal integration rule ($\gamma = 0.5, \beta = 0.25$). Multiple spurious oscillations appear across the domain which is an essential feature of many higher-order schemes.

6.5. Case Study: Displaced Fault

The displaced fault setup is presented in detail in Sec. 4.9. Here we briefly remind the key features of the setup. It considers a square poroelastic domain of homogeneous material properties. A conductive fault with dip angle $\theta = 70^\circ$ passes throughout the domain. The reservoir situated in the middle of the domain is divided by the fault into two parts displaced with respect to each other over the fault. The domain is subjected to gravitational forces and to compressive boundary conditions mimicking real reservoir conditions. Fluid extraction from the reservoir causes a depletion of pore pressure within the reservoir which results in stress dis-

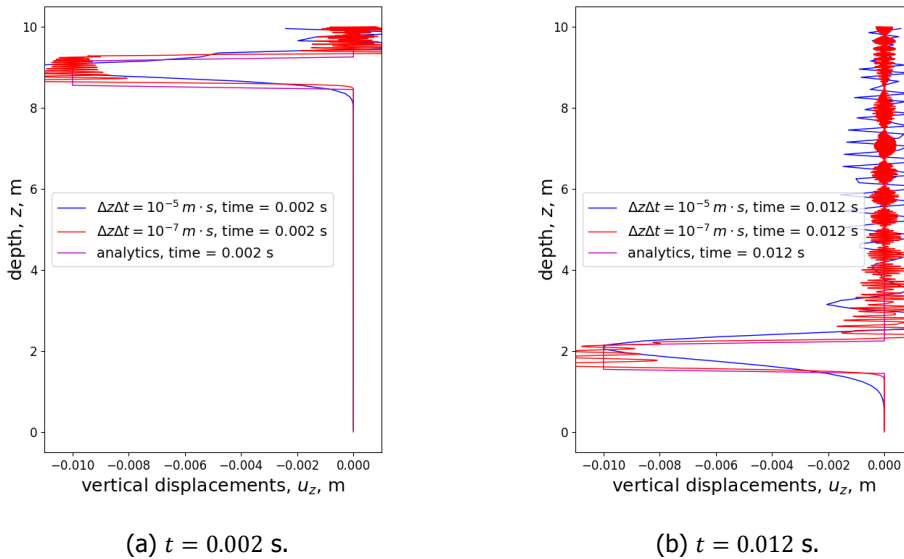


Figure 6.2.: Calculated and analytical vertical displacements at two moments of time for the Newmark scheme.

continuities at the non-smooth reservoir-fault corners appearing in the displaced configuration.

The QS modeling of the displaced fault setup was demonstrated in Sec. 4.9. The QS model faces nonlinear convergence issues when approaching the nucleation point. Here we employ QD and FD approaches to overcome convergence issues and to resolve the initiation, propagation and arrest of coseismic rupture.

6.5.1. Uniform Depletion

Nucleation Point

Tab. 6.1 summarizes the parameters of the considered test cases. It includes the parameters that specify the slip-weakening friction law and the characteristics of the nucleation point (nucleation pressure and nucleation length) obtained from both analytical and numerical considerations.

Note, that there are at least two reasons explaining the mismatch between the analytical and numerical nucleation pressure in Tab. 6.1. First, an infinite horizontal size of the domain is assumed by analytics (Jansen *et al.* 2022) while it remains finite in numerical calculations. Second, the smaller nucleation length requires a finer resolution for slip patches. However, all numerical calculations shown in Fig. 6.3 are performed using the same computational grid.

Table 6.1.: Parameters of the slip-weakening friction law: μ_s is static friction coefficient, μ_d is dynamic friction coefficient, D_c is critical slip distance, Δp_{an}^* is nucleation pressure determined analytically (Jansen *et al.* 2022), Δp_{num}^* is nucleation pressure determined from calculation, $L_{U\&R}^*$ is nucleation length calculated analytically (Uenishi *et al.* 2003) and L_{num}^* is nucleation length determined numerically (upper slip patch size).

Case	μ_s	μ_d	D_c , mm	Δp_{an}^* , MPa	Δp_{num}^* , MPa	$L_{U\&R}^*$, m	L_{num}^* , m
#1	0.52	0.2	20	-17.44	-17.3	15.92	15
#2	0.52	0.4	20	-21.38	-21.2	40.92	37.75
#3	0.6	0.45	5	–	-21.5	7.89	6.09

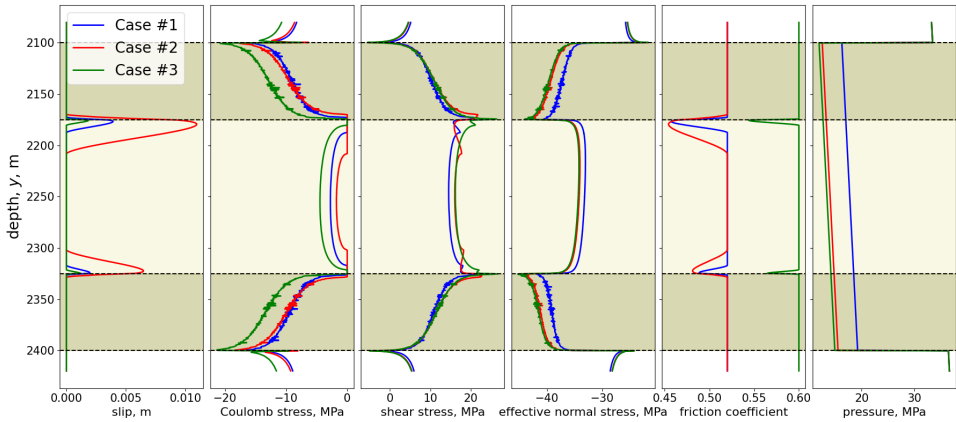


Figure 6.3.: Properties over the fault calculated for three sets of parameters from Tab. 6.1.

Nonlinear Convergence Issues

Numerical modeling of frictional contacts is a strongly nonlinear problem that may suffer from nonlinear convergence issues (Chouly *et al.* 2022; Dostál *et al.* 2016; Laursen 2010; Wriggers 2006; Yastrebov *et al.* 2013). The transition of contact from aseismic slip to coseismic slip furthermore amplifies these issues. As a result, at the nucleation point, the nonlinear iterations of the QS model exhibit divergent behavior. In this section, we investigate the appearance of this divergence.

Fig. 6.4 demonstrates the profiles of residuals, slip and Coulomb stress over Newton iterations for three grids of different spatial resolutions. The frictional slip-weakening contact (Case #1 from Tab. 6.1) perturbed by a depletion pressure $\Delta p = -17.2$ MPa is considered. For better representation, the profiles are shown only for the upper slip patch. The residual profiles are estimated by the calculation of the cell-wise norm of the residual vector corresponding to the three contact constraints Eqs. (3.99)-(3.101) in each cell. Note that we divide these equations by the corresponding penalty parameters after the assembly which results in units

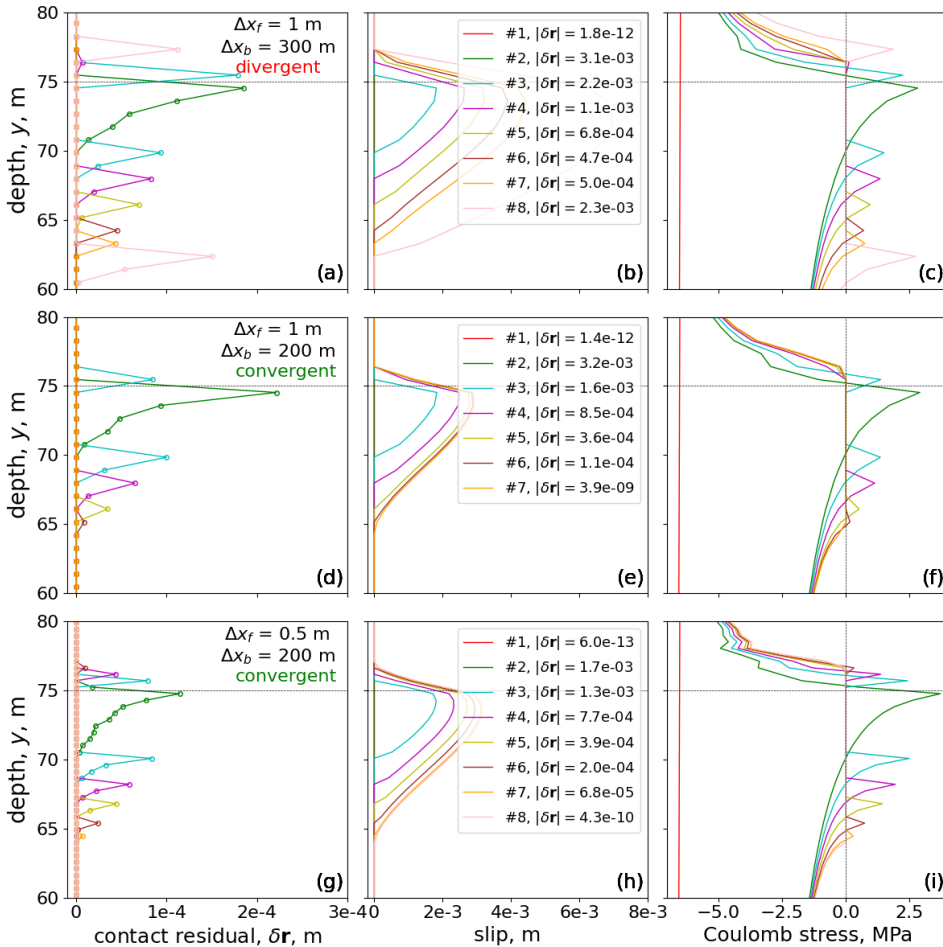


Figure 6.4.: The profiles of contact residual (left column), slip (middle column) and Coulomb stress (right column) over nonlinear iterations for the Case #1 from Tab. 6.1 at $\Delta p = -17.2$ MPa. The results are calculated for the three grid resolutions defined by Δx_f , the cell size at the fault and Δx_b , the cell size at the domain's boundary.

of residual measured in meters.

We use a cut-off equal to 10^{-7} as an absolute convergence tolerance for the Newton iterations. As a result, we observe that the coarsest grid characterized by a fault cell size $\Delta x_f = 1$ m and a boundary cell size $\Delta x_b = 300$ m does not allow the Newton iterations to converge. In contrast, two finer grids demonstrate that the solutions converged in 7-8 iterations. It is worth to note that the residuals in the matrix cells disappear after the first iteration and never exceed the cut-off later.

Let us inspect the behavior of the residual profiles over iterations depicted in

Figs. 6.4a, 6.4d, 6.4g. At the first iteration, the residuals are equal to zero as the Coulomb stresses stay below zero and the whole contact remains in stick mode. Starting from the second iteration, the residual profile follows the profile of the Coulomb stress. At the second iteration, Coulomb stresses resemble the pre-slip shear stress from Fig. 4.29, and they result in the appearance of a slip patch in the following iteration. After the second iteration, Coulomb stresses, and residuals, exceed zero at the boundaries of the slip patch promoting its spreading. As in this setup, the upper slip patch primarily propagates toward the deeper (negative y -axis) direction, and the upper peak in Coulomb stresses and residuals disappears in a few iterations while the magnitude of the lower peak decreases over iterations. As we can see, for the two finer grids this peak steadily disappears and the slip profile stabilizes near the converged solution. In contrast, in the case of a coarse grid, both (residual) peaks magnify starting from the 6th iteration. Thus, by the 8th iteration, the slip profile substantially exceeds the converged solutions obtained with the two other grids. The subsequent iterations generate a solution much further from the converged one, thus they are not shown in the plot. These observations hint that the divergence of nonlinear iterations may start from an overestimation of the slip profile which can be alleviated by chopping strategies.

An other important observation is about the relation between the smoothness of slip and convergence. As can be seen from Fig. 6.4, the converged slip profiles are smooth at the patch's tips while both non-converged and diverged slip profiles remain non-smooth at those points.

Fig. 6.5 demonstrates similar results calculated for a depletion pressure $\Delta p = -17.3$ MPa which defines the numerical nucleation pressure for Case #1 (see Tab. 6.1). As expected, we observed a poorer convergence for higher depletion that results in divergent iterations on the finest grid (Figs. 6.5g-6.5i). At the same time, the grid of medium resolution still provides a convergent solution (Figs. 6.5d-6.5f). The iterations with both the coarsest and finest grids before the divergence initiate a smaller separate patch in the direction of the main patch's propagation. The appearance of this smaller patch leads to a dramatic increase in the residual's profile that already never converges.

In order to have a detailed inspection of the transition from convergent to a divergent solution near the nucleation point, we demonstrate a comparison of the results obtained with a single grid ($\Delta x_f = 1$ m, $\Delta x_b = 200$ m) at three depletion pressures $\Delta p = -17.2, -17.3, -17.4$ MPa. Fig. 6.6 illustrates the profiles of residual, slip and Coulomb stress over several Newton iterations. The two smaller depletion pressures $\Delta p = -17.2, -17.3$ MPa allow the Newton iterations to converge and the converged slip profiles are shown by the marked bold lines. The highest depletion pressure $\Delta p = -17.4$ MPa lies beyond the estimated nucleation point at $\Delta p_{num}^* = -17.3$ MPa which results in divergent iterations. As we may observe from Fig. 6.6, the profiles for three depletion pressures stay close to each other over the few first iterations. Starting from the 4th iteration, the Coulomb stress and residuals at $\Delta p = -17.4$ MPa tend to outrun their counterparts at smaller depletion pressures which results in a noticeably higher slip profile. The iterations for $\Delta p = -17.2$ MPa converge by the 7th iteration whereas the convergence at

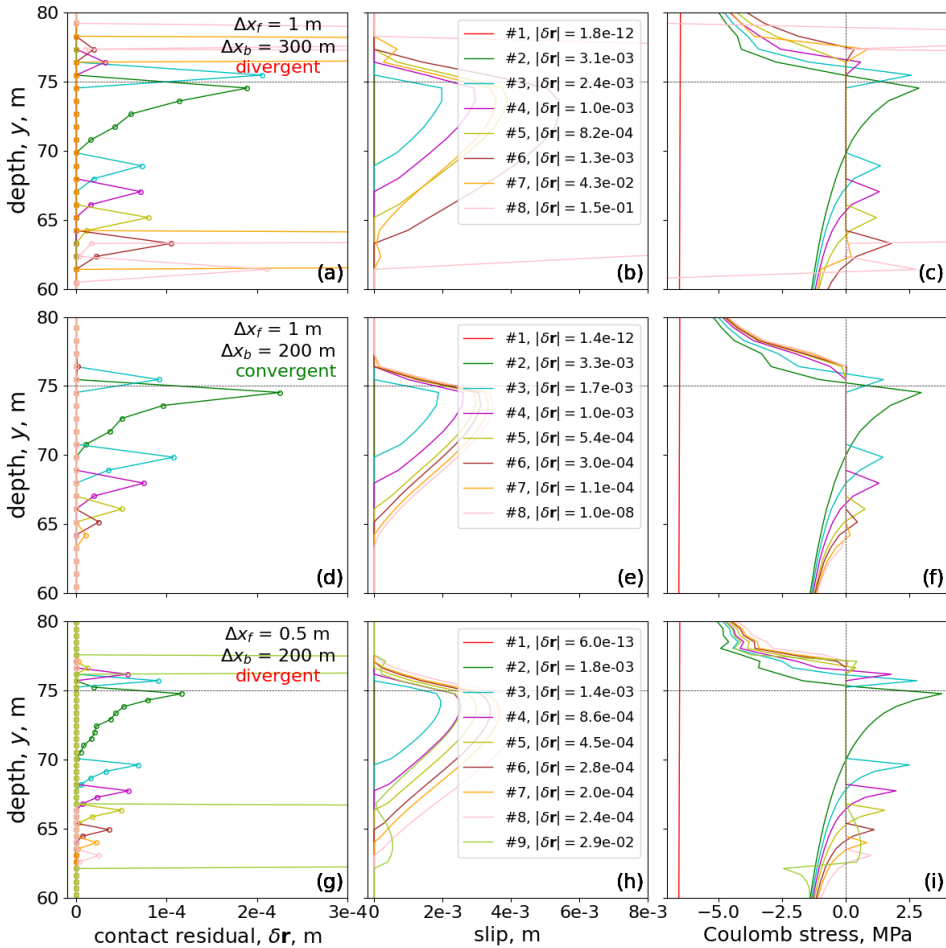


Figure 6.5.: The profiles of contact residual (left column), slip (middle column) and Coulomb stress (right column) over nonlinear iterations for the Case #1 from Tab. 6.1 at $\Delta p = -17.3$ MPa. The results are calculated for the three grid resolutions defined by Δx_f , the cell size at the fault and Δx_b , the cell size at the domain's boundary.

17.3 MPa spends one more iteration. In contrast, the residuals observed in the calculation at the highest depletion pressure dramatically increase at the 8th iteration and they never converge afterward.

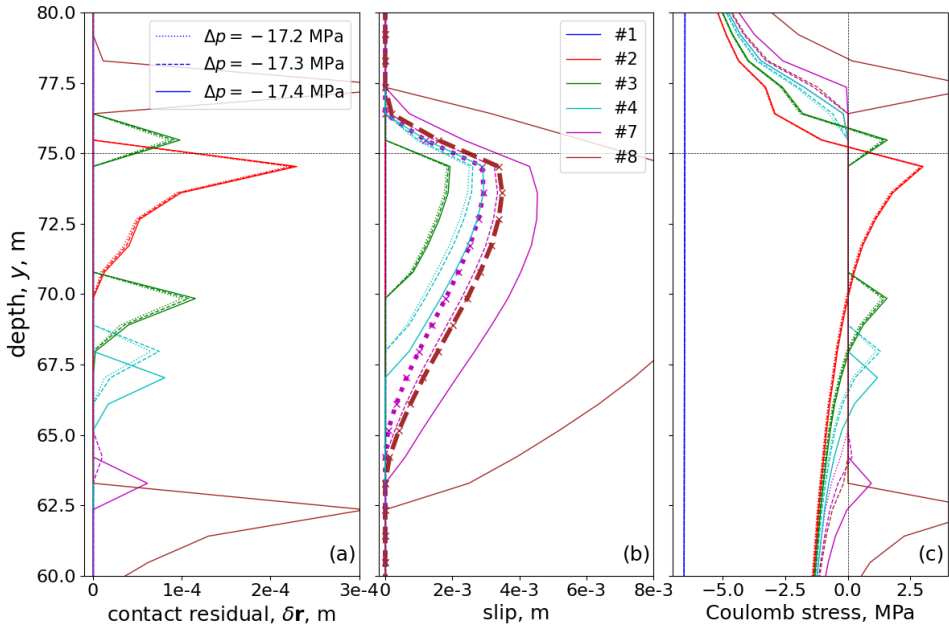


Figure 6.6.: The profiles of contact residual (left column), slip (middle column) and Coulomb stress (right column) over nonlinear iterations for the Case #1 from Tab. 6.1. The results are calculated for the grid defined by $\Delta x_f = 1$ m, the cell size at the fault and $\Delta x_b = 200$ m, the cell size at the domain's boundary.

6

6.5.2. Depletion from a Remote Production Well

Most of the induced seismicity in the subsurface, in one way or another, is caused by pore pressure perturbations imposed by wells. In this section, we investigate the seismicity induced by a remote well. Fig. 6.7 demonstrates a displaced fault configuration with a vertical well placed on the right side of the reservoir at $x = 2000$ m. The production well, controlled by a fixed wellbore depletion pressure $\Delta p = -25$ MPa, produces fluid defined by density $\rho_f = 1020$ kg m⁻³, viscosity $\mu_f = 1$ cP and compressibility $c_f = 10^{-5}$ MPa⁻¹ from the reservoir with permeability $k = 1$ D. The conductive fault crossing the reservoir has the same permeability as reservoir. We consider a slip-weakening fault defined by a static friction coefficient $\mu_s = 0.6$, a dynamic friction coefficient $\mu_d = 0.4$ and a critical slip distance $D_c = 5$ mm.

Fig. 6.8 demonstrates the evolution of fault rupture starting from nucleation. Initially, the production well imposes a pressure depletion propagating towards the fault. As a result, aseismic slip increases over time until the nucleation point. We model this phase in QS mode as we did before. At, approximately, $t_0 = 2$ d 13 h 22 min rupture nucleation is initiated and we switch simulation to the FD mode. During around 0.2 s the rupture propagates through the entire reservoir and

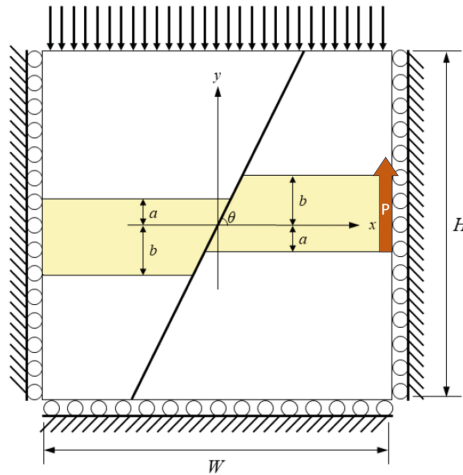


Figure 6.7.: Displaced fault setup in a square domain $W = H = 4500$ m with a vertical production well placed at $x = 2000$ m. Fault dip angle $\theta = 70^\circ$ and the parameters $a = 75$ m, $b = 150$ m.

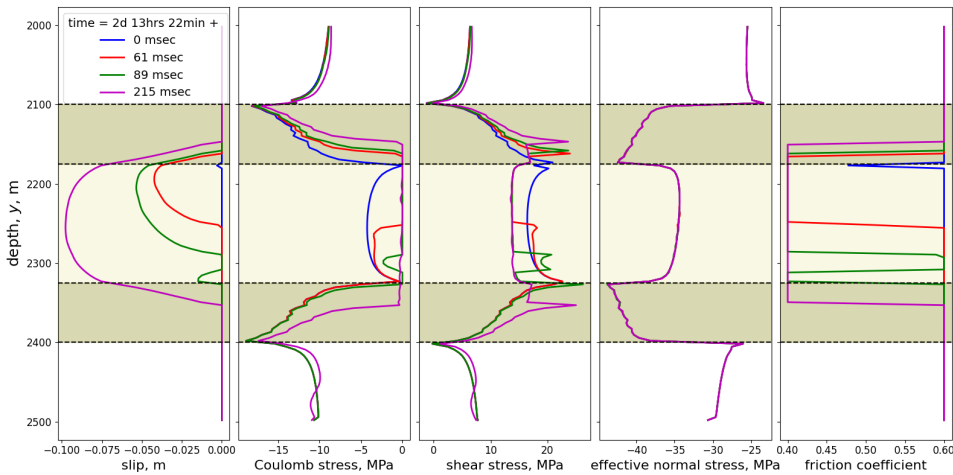


Figure 6.8.: The fault properties at the nucleation point (blue line), during rupture propagation and at the rupture arrest (magenta line) calculated with the grid of $\Delta x_f = 4$ m fault cell size.

parts of the overburden and underburden. We identify the arrest of the rupture at $t_a = t_0 + 215$ ms by the fact that we do not observe the rupture to propagate any further. Moreover, the friction coefficient at $t = t_a$ decreases to its minimal values indicating that the further rupture propagation is purely controlled by further depletion.

It is clear from the figure that the parts of the fault exposed to the contact

between reservoir and non-permeable formations are less prone to rupture propagation compared to the parts fault solely covered by reservoir. Note that we assume the same slip-weakening friction for both reservoir-reservoir and reservoir-over/under-burden contacts, which may be not a realistic assumption. The deviation of the shear stress below underburden at $t = t_a$ from its previous values is caused by induced elastic waves.

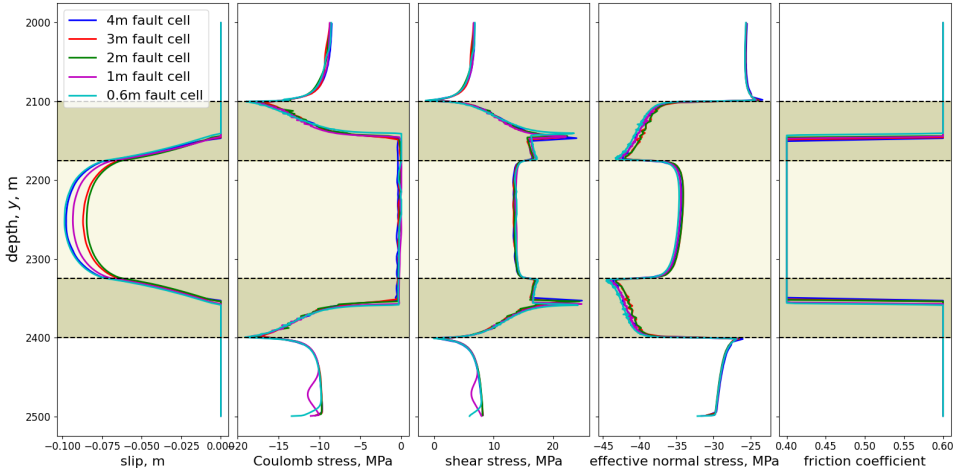


Figure 6.9.: Convergence study of the rupture arrest. The fault properties are calculated with the multiple grids listed in Tab. 6.2.

Fig. 6.9 demonstrates the convergence study. Grids of multiple fault cell sizes, starting from the coarsest $\Delta x_f = 4$ m up to the finest $\Delta x_f = 0.5$ m, are considered. In addition to the grid resolution, we decrease the maximum time step allowed in the FD mode. The parameters of the FD part of the simulation are listed in Tab. 6.2.

As we can see from the figure, even though the stresses do not exhibit significant differences among grids, a noticeable difference appears between slip profiles. A more remarkable difference can be observed between the values of the nucleation time t_{nuc} in Tab. 6.2. No sign of convergence with respect to this property indicates that the more sophisticated time-stepping strategy should be employed (Han *et al.* 2023).

One of the practically interesting questions regarding the mitigation of induced seismicity in depleted reservoirs is how subsequent reinjection may affect the fault stability. In order to investigate that, we perform the same simulation with an extra QS stage started after the rupture arrest. During this stage, we switch the production well into an injection mode by assigning wellbore pressure control of $\Delta p = 0$ MPa. It effectively means to inject fluid into reservoir up to its initial pressure.

Fig. 6.10 demonstrates the calculated fault properties at four key moments of the simulation run: 1) initial or unperturbed reservoir state, 2) nucleation point, 3)

Table 6.2.: The parameters of simulation runs for the convergence study. Δx_f and Δx_b are the characteristic fault and boundary cell sizes respectively, t_{nuc} is the time of nucleation, M is the seismic moment, Δt_{max} and Δt_{mean} are maximum and mean time steps in the FD mode.

$\Delta x_f, m$	$\Delta x_b, m$	N. of cells	t_{nuc}	$M, GN m^{-1}$	$\Delta t_{max}, ms$	$\Delta t_{mean}, ms$
4	300	7.8k	2 d 13 h 22 min	125.7	1	0.38
3	300	14k	2 d 7 h 34 min	112.2	0.5	0.379
2	200	30.6k	2 d 9 h 1 min	109.8	0.5	0.352
1	100	115.9k	3 d 7 h 46 min	121.6	0.5	0.346
0.6	60	308.5k	4 d 14 h 53 min	129.9	0.1	0.09

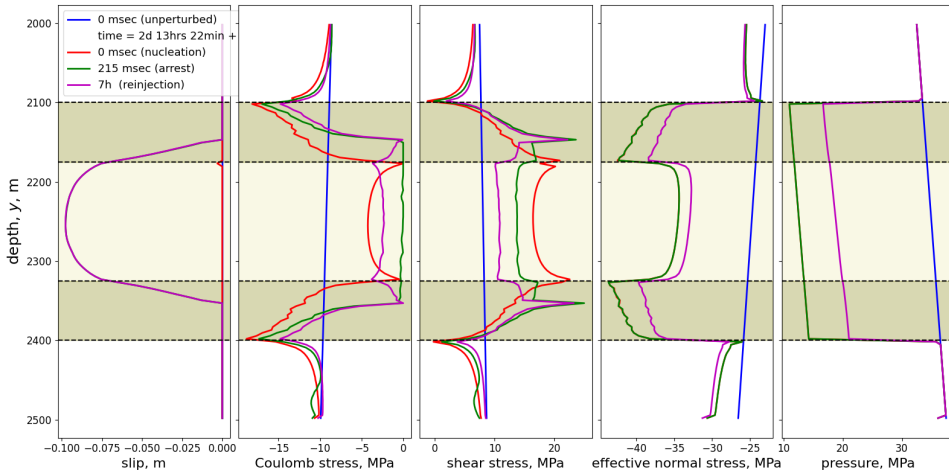


Figure 6.10.: The fault properties at the initial state (blue line), at nucleation point (red line), at the rupture arrest (green line) and some after reinjection (magenta line) calculated with the grid of $\Delta x_f = 4 m$ fault cell size.

rupture arrest and 4) at some point of time after the start of reinjection. As we can see from the figure, in this particular case of linear slip-weakening, the subsequent reinjection stabilizes the displaced fault. However, we observe opposite effects from shear and effective normal stresses: the relaxed shear stress stabilizes the fault while the less compressive normal stress destabilizes it. Therefore, we can not extend the conclusion about the stabilization effect of reinjection to a much wider parameter space.

Fig. 6.11 presents a sensitivity study with respect to the dynamic friction coefficient. The figure illustrates the fault properties at the moment of the rupture arrest. Generally, a lower friction coefficient provokes higher slip. The behavior of slip profiles in the area where the reservoir is juxtaposed to the non-permeable formations is close to linear. At the same time, we observe that rupture propagates noticeably further beyond reservoir depths. Again, it is worth to note that in this

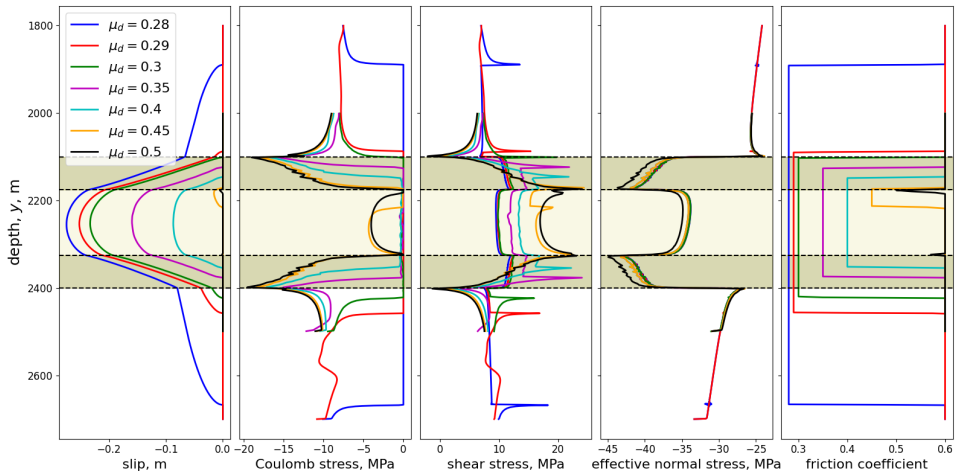


Figure 6.11.: The sensitivity study with respect to the dynamic friction coefficient μ_d performed with grid of $\Delta x_f = 4$ m fault cell size. The fault properties are shown at the time of rupture arrest.

6

case, we consider a homogeneous domain. The consideration of a more realistic heterogeneous configuration may qualitatively affect these results.

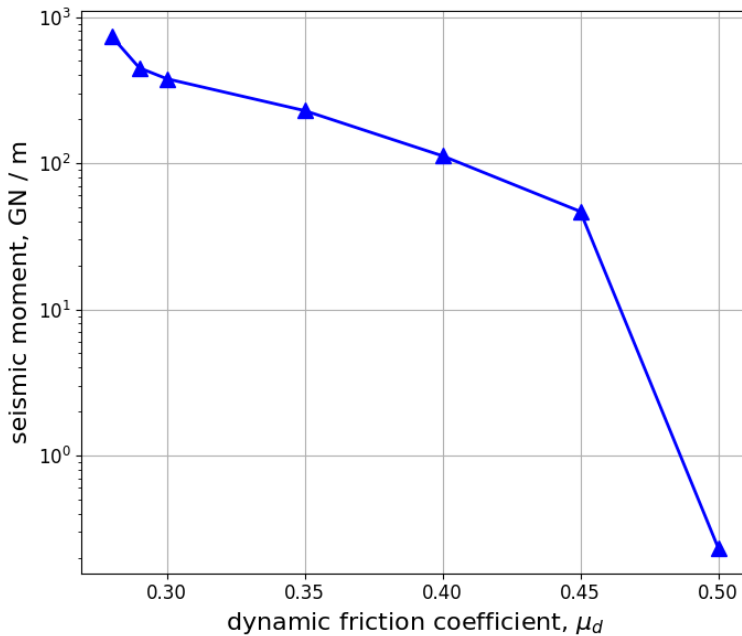


Figure 6.12.: The seismic moment against the dynamic friction coefficient.

The calculations with the dynamic friction coefficient below $\mu_d < 0.28$ require the extension of the fault throughout the whole domain and even further. This behavior when rupture propagates far beyond the reservoir depths is called a run-away rupture.

Fig. 6.12 illustrates how the seismic moment depends on the dynamic friction coefficient. According to the figure, the seismic moment exponentially increases with a falling dynamic friction coefficient. The observed slip profiles and the behavior of the seismic moment support the previous sensitivity studies conducted for a displaced fault configuration (Van den Bogert 2018). Note that in this particular setup, we do not observe the aseismic merging of two slip patches as the nucleation length is very small for the parameters of the slip-weakening law used here. Instead, the merging of slip patches happens during the coseismic phase.

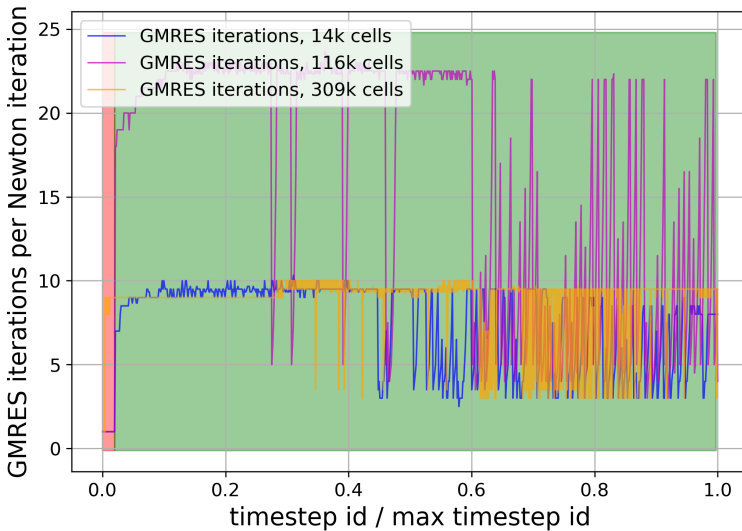


Figure 6.13.: Number of GMRES iterations over simulation timesteps for three grids characterized by fault cell sizes $\Delta x_f = 3, 1, 0.6$ m. The red background denotes the QS modeling with the direct solver used, and the green one – the FD modeling with the iterative GMRES+ILU(0) used.

Finally, Fig. 6.13 demonstrates the efficiency of the preconditioner based on the Incomplete LU factorization for solving linear systems appearing in the FD simulation mode. We present the number of GMRES iterations spent on a single Newton iteration in three simulation runs: with $\Delta x_f = 3, 1, 0.6$ m. In all cases, it takes less than 25 linear iterations to reduce residual by 10^{-12} from its initial values. As expected the number of iterations is proportional to the time step used in corresponding runs (see. Tab. 6.2 for time steps).

6.6. Conclusion

This chapter considers the fully dynamic (FD) modeling of rupture nucleation, propagation and arrest under slip-weakening friction law. The following key takeaways are obtained in this chapter

- The implemented second-order implicit Newmark scheme for the inertia term demonstrates strongly oscillating solution in a test case with unidimensional propagation of a rectangular wave (Fig. 6.2) while the first-order backward Euler scheme remains stable but exhibits high numerical dispersion (Fig. 6.1).
- The estimated nucleation length and nucleation depletion pressure in a displaced fault configuration with the slip-weakening frictional contact are found close enough to their analytically-derived counterparts (Tab. 6.1).
- The passing of the nucleation point with a quasi-static model introduces essential convergence issues to the numerical solvers. The analysis of nonlinear iterations indicates that the smoothness of slip profiles is improving over iterations (Fig. 6.4) and the finest grid is not always better from a convergence point of view (Fig. 6.5). The nonconverging behavior around the nucleation point is characterized by a sudden increase in slip (Fig. 6.6) which reflects the slip increase during the coseismic phase.
- The implemented FD modeling allows us to overcome the nonlinear convergence issues and to proceed with modeling beyond the nucleation point, resolving rupture propagation and arrest (Fig. 6.8). A resolution study indicates converged results with respect to stresses and poor convergence with respect to slip (Fig. 6.9). In the considered setup, reinjection leads to fault stabilization, indicating a stronger stabilizing effect caused by shear stress reduction in comparison to a destabilizing contribution from the effective normal stress (Fig. 6.10). The sensitivity of the seismic moment to the dynamic friction coefficient qualitatively supports the previous sensitivity study.
- In the proposed FD modeling framework, incomplete LU factorization demonstrates its efficiency as a preconditioner for the GMRES iterations (Fig. 6.13).

7

Conclusion

7.1. Recapitulation and Key Learning Points

In this thesis, a novel Finite Volume scheme for the fully implicit modeling of faulted poroelastic media has been developed. For this purpose, coupled multi-point flux and multi-stress approximations have been extended to contact interfaces. The penalty method with a return-mapping algorithm was utilized to enforce contact constraints. The proposed numerical techniques have been implemented in the open-source Delft Advanced Research Terra Simulator (DARTS). This implementation supports arbitrary boundary conditions, material heterogeneity, and anisotropy for the poroelastic media and multiple constitutive laws for the frictional contacts. The support of various fluid properties has been enabled by the use of Operator-Based Linearization as incorporated into DARTS. Finally, a nonlinear Finite Volume scheme for the pure elasticity problem has been proposed.

To accelerate the solution of linear systems appearing in the modeling, a block-partitioned preconditioning strategy based on a sparse approximation of Schur's complement with the fixed-stress split concept has been implemented. Moreover, the System Algebraic Multigrid solver and a preconditioner based on incomplete LU factorization have been incorporated into the simulation workflow.

The implemented modeling functionality has been validated in a number of benchmarks. First, we demonstrated the preservation of linearity and convergence of the scheme. Next, we examined the validity of the approximations by comparing the numerical solution to the analytical one for Terzaghi's, Mandel's and two-layer Terzaghi's cases, and to numerical solutions obtained with other modelling frameworks. Furthermore, we examined the capability of the scheme to handle highly heterogeneous media in a mechanical extension of the SPE10 model. Besides, we checked the acceleration and scalability provided by the block-partitioned preconditioner in this case. In the next part, we thoroughly investigated a displaced fault problem and validated the numerical solution against existing semi-analytics. Finally, we demonstrated the convergence of the nonlinear FV scheme and investigated the quality of numerical solutions obtained with different schemes.

We presented the modeling of two experimental setups: injection-induced slip

in a cross-cut core and a large-scale setup with a displaced fault configuration. The results of modeling the injection-induced slip in the core cross-cut, performed with measured friction coefficient, matched other experimental measurements, with steady-state rate-and-state friction – qualitatively represented the measured dynamics. In the modeling of the large-scale experimental setup the loading path for the experiment has been proposed.

Finally, we presented fully dynamic approaches to the modeling of rupture propagation based on the fully implicit Finite Volume scheme. We performed the modeling of rupture nucleation, propagation and arrest induced by a distant depletion well and subsequent re-injection.

The key takeaways from the thesis are

- The fully implicit fully coupled Finite Volume scheme proposed in Sec. 3.3 is capable of resolving fluid mass and momentum transfer in poroelastic media with frictional contacts, and has been validated in multiple benchmarks in Sec. 4.
- The scheme exhibits spurious oscillations due to violation of the inf-sup condition. Even though stabilization, considered in Sec. 3.4, reduces the oscillatory behavior, it does not completely eliminate it. Instead, the stabilization induces a significant pressure overshoot behind the boundary layer appearing in the region with undrained conditions. This overshoot does not allow the stabilized scheme to be utilized in many setups, and the original non-stabilized variant was found to be more robust, especially with finer grid resolution.
- The implemented block-partitioned preconditioner demonstrates a good performance for the modeling of poroelastic response in continuous media (Sec. 4.7). In the presence of discontinuities, even though in the current approach they introduce unknowns of the same type, the sparse approximation of Schur complement becomes not accurate which results in poor convergence of iterations of generalized minimal residual method (GMRES), or even in divergence. System algebraic multigrid (SAMG) demonstrates similar behavior in both continuous and faulted setups.
- The implemented mixed-dimensional fault representation provides a reasonable approximation of frictional contact and ensures accuracy of the solution without having to resolve displacement gradients in the narrow fault cells with a high aspect ratio.
- In a simple frictional fault with static friction coefficient, the penalty method with the return-mapping algorithm demonstrates a good-enough solution quality obtained in a reasonable number of nonlinear iterations (Sec. 4.8.2). However, either the presence of weak discontinuities (Sec. 4.9) or friction laws (Sec. 4.9.5, Sec. 5.1) requires very fine grid resolution. Moreover, even a very fine grid resolution does not guarantee the convergence of the nonlinear iterations.

- The dynamic simulation based on the proposed implicit FV scheme is capable of resolving the rupture dynamics at frictional contacts (Sec. 6). Incomplete LU factorization significantly accelerates the solution of linear systems appearing in the fully dynamic simulation.
- The nonlinear FV scheme for the pure elastic problem proposed in Sec. 3.6 provides a similar accuracy as the linear scheme (Sec. 4.10), and, in its current shape, does not bring any benefits for geomechanical modeling.

7.2. Future Perspectives

The main implications of this work for future developments can be formulated in the following list of points:

- Other stabilized FV schemes (Nordbotten 2016; Terekhov 2021a) or stabilization techniques (Aronson *et al.* 2023; Camargo *et al.* 2021) could be employed to avoid unstable behavior introduced by the violation of the inf-sup condition.
- The poor nonlinear convergence observed in the modeling of frictional contact exposed to weak discontinuities or complex frictional laws should be investigated in the simplest, perhaps 0D or 1D, numerical models. Furthermore, the same simplified models can be used for the modeling of slip in the experiments with core cross-cuts. The spatial simplicity of these models enables the incorporation of sophisticated friction laws and the identification of these laws from experimental data by solving corresponding inverse problems.
- A significant limitation of the geomechanical modeling in the presence of discontinuities is a robust and efficient iterative linear solution strategy. Further investigation should be performed for a better approximation of the Schur complement in regard to the fault's degrees of freedom (Ferronato *et al.* 2019; Franceschini *et al.* 2022a; Franceschini *et al.* 2022b).
- Dynamic modeling of induced seismicity can provide a much more comprehensive insight compared to quasi-static modeling. Being widely utilized in seismic studies, empowered by high-performance computing (HPC) infrastructure (Reinarz *et al.* 2020; Uphoff *et al.* n.d.; Walker *et al.* 2023), fully dynamic modeling has the potential to be conveniently integrated into the reservoir simulation and risk assessment workflows as it enables the direct evaluation of seismic moments in particular geological settings.

A

Finite Volume Method for Thermoporoelastic Media

A.1. Approximation of Fluxes at Interior Interfaces

The local problem between two neighboring cells written in Eqs. (3.16)-(3.18) can be easily extended to the case of thermoporoelastic media. It implies the continuity of unknown vector of unknowns $\mathbf{d} = [\mathbf{u}^T p \theta]$ including unknown temperature θ . Then the local balance of momentum, fluid and heat conduction fluxes can be written as follows

$$\begin{aligned} \mathbf{d}_{\beta_1} &= \mathbf{d}_1 + [\mathbf{I} \otimes (\mathbf{x}_\beta - \mathbf{x}_1)^T] (\nabla \otimes \mathbf{d}_1) = \mathbf{d}_2 + [\mathbf{I} \otimes (\mathbf{x}_\beta - \mathbf{x}_2)^T] (\nabla \otimes \mathbf{d}_2) = \mathbf{d}_{\beta_2}, & (A.1) \\ -[\mathbf{I} \otimes \mathbf{n}^T] \mathbf{S}_1 (\nabla \otimes \mathbf{u}_1) + p_{\beta_1} \mathbf{B}_1 \mathbf{n} + \theta_{\beta_1} \mathbf{A}_1 \mathbf{n} &= -[\mathbf{I} \otimes \mathbf{n}^T] \mathbf{S}_2 (\nabla \otimes \mathbf{u}_2) + p_{\beta_2} \mathbf{B}_2 \mathbf{n} + \theta_{\beta_2} \mathbf{A}_2 \mathbf{n}, & (A.2) \\ -(\nabla p_1 - \rho_f g \nabla z) \cdot \mathbf{K}_1 \mathbf{n} &= -(\nabla p_2 - \rho_f g \nabla z) \cdot \mathbf{K}_2 \mathbf{n}, & (A.3) \\ -\nabla \theta_1 \cdot \mathbf{\Lambda}_1 \mathbf{n} &= -\nabla \theta_2 \cdot \mathbf{\Lambda}_2 \mathbf{n}, & (A.4) \end{aligned}$$

where \mathbf{A} is the rank-two thermal dilation tensor, $\mathbf{\Lambda}$ is the rank-two heat conductivity tensor introduced in Sec. 2.4.2.

The following decomposition we use in heat flux

$$\mathbf{\Lambda}_i \mathbf{n} = \lambda_i \mathbf{n} + \boldsymbol{\lambda}_i, \quad \lambda_i = \mathbf{n}^T \mathbf{\Lambda}_i \mathbf{n}, \quad \boldsymbol{\lambda}_i = (\mathbf{I} - \mathbf{n} \mathbf{n}^T) \mathbf{\Lambda}_i \mathbf{n}, \quad (A.5)$$

where scalars λ_1 and λ_2 and vectors $\boldsymbol{\lambda}_1$ and $\boldsymbol{\lambda}_2$ provide co-normal decompositions of $\mathbf{\Lambda}_1$ and $\mathbf{\Lambda}_2$ respectively.

Fluid mass and heat fluxes in Eqs. (A.1)-(A.4) do not depend on neither displacements nor their gradients. Therefore the approximation of fluid mass and heat fluxes can be done independently of the approximation of momentum fluxes and Biot's terms. Following the same way we derived approximation in Eq. (3.28) we obtain the approximation for fluid mass q_f and heat fluxes q_θ at the interface β

as

$$[\mu_f q_f]_\beta = \kappa(p_1 - p_2) - \left(\kappa(\mathbf{y}_1 - \mathbf{y}_2)^T + \frac{d_1 \kappa_2 \boldsymbol{\kappa}_1^T + d_2 \kappa_1 \boldsymbol{\kappa}_2^T}{d_2 \kappa_1 + d_1 \kappa_2} \right) \boldsymbol{\xi}_\tau^p + \rho_f g \nabla z \cdot \frac{d_1 \kappa_2 \mathbf{K}_1 + d_2 \kappa_1 \mathbf{K}_2}{d_2 \kappa_1 + d_1 \kappa_2} \mathbf{n} \quad (\text{A.6})$$

$$[q_\theta]_\beta = \lambda(\theta_1 - \theta_2) - \left(\lambda(\mathbf{y}_1 - \mathbf{y}_2)^T + \frac{d_1 \lambda_2 \boldsymbol{\lambda}_1^T + d_2 \lambda_1 \boldsymbol{\lambda}_2^T}{d_2 \lambda_1 + d_1 \lambda_2} \right) \boldsymbol{\xi}_\tau^\theta, \quad (\text{A.7})$$

where $\kappa = \kappa_1 \kappa_2 (d_1 \kappa_2 + d_2 \kappa_1)^{-1}$, $\lambda = \lambda_1 \lambda_2 (d_1 \lambda_2 + d_2 \lambda_1)^{-1}$ are weighted harmonic mean permeability and heat conductivity respectively.

The following equations can be used for the reconstruction of pressure and temperature at the interface between matrix cells

$$(\kappa_2(\mathbf{x}_2 - \mathbf{x}_1) + d_2(\mathbf{K}_1 - \mathbf{K}_2)\mathbf{n})^T \nabla p_1 = \kappa_2(p_2 - p_1) + d_2 \rho_f g \nabla z^T (\mathbf{K}_2 - \mathbf{K}_1) \mathbf{n}, \quad (\text{A.8})$$

$$(\lambda_2(\mathbf{x}_2 - \mathbf{x}_1) + d_2(\boldsymbol{\Lambda}_1 - \boldsymbol{\Lambda}_2)\mathbf{n})^T \nabla \theta_1 = \lambda_2(\theta_2 - \theta_1). \quad (\text{A.9})$$

The pressure and temperature can be approximated at the center of the interface β as

$$p_\beta = (d_1 \kappa_2 + d_2 \kappa_1)^{-1} (d_2 \kappa_1 p_1 + d_1 \kappa_2 p_2) + (d_1 \kappa_2 + d_2 \kappa_1)^{-1} \left((d_1 d_2 (\boldsymbol{\kappa}_2 - \boldsymbol{\kappa}_1)^T + d_2 \kappa_1 (\mathbf{x}_\beta - \mathbf{y}_1)^T + d_1 \kappa_2 (\mathbf{x}_\beta - \mathbf{y}_2)^T \right) \boldsymbol{\xi}_\tau^p + d_1 d_2 \rho_f g \nabla z^T (\mathbf{K}_1 - \mathbf{K}_2) \mathbf{n}, \quad (\text{A.10})$$

$$\theta_\beta = (d_1 \lambda_2 + d_2 \lambda_1)^{-1} (d_2 \lambda_1 \theta_1 + d_1 \lambda_2 \theta_2) + (d_1 \lambda_2 + d_2 \lambda_1)^{-1} \left(d_1 d_2 (\boldsymbol{\lambda}_2 - \boldsymbol{\lambda}_1)^T + d_2 \lambda_1 (\mathbf{x}_\beta - \mathbf{y}_1)^T + d_1 \lambda_2 (\mathbf{x}_\beta - \mathbf{y}_2)^T \right) \boldsymbol{\xi}_\tau^\theta. \quad (\text{A.11})$$

Given the approximations for pressure, temperature, and their gradients presented above, we can rewrite the balance of momentum fluxes in Eq. (A.2) in the following form

$$-\mathbf{T}_1 \boldsymbol{\xi}_1^u - \Gamma_1 \boldsymbol{\xi}_\tau^u + (p_{\beta 1} \mathbf{B}_1 + \theta_{\beta 1} \mathbf{A}_1) \mathbf{n} = -\mathbf{T}_2 \boldsymbol{\xi}_2^u - \Gamma_2 \boldsymbol{\xi}_\tau^u + (p_{\beta 2} \mathbf{B}_2 + \theta_{\beta 2} \mathbf{A}_2) \mathbf{n}, \quad (\text{A.12})$$

where $p_{\beta 1}, \theta_{\beta 1}$ denote the left-side approximations

$$p_{\beta 1} = p_1 + (\mathbf{x}_\beta - \mathbf{x}_1)^T \nabla p_1, \quad \theta_{\beta 1} = \theta_1 + (\mathbf{x}_\beta - \mathbf{x}_1)^T \nabla \theta_1. \quad (\text{A.13})$$

The approximations of $\nabla p_2, \nabla \theta_2$ required in Eq. (A.13) significantly broaden the stencil of displacement gradients compared to the stencil of $\nabla p_2, \nabla \theta_2$. Below, we use the following approximations in the reconstruction of gradients which allow the supporting stencil between pressure and displacement gradients to be the same

$$p_{\beta 2} = p_2 + (\mathbf{x}_\beta - \mathbf{y}_2 - d_2 \kappa_2^{-1} (\mathbf{K}_1 \mathbf{n} - \boldsymbol{\kappa}_2))^T \nabla p_1 + d_2 \kappa_2^{-1} \rho_f g \nabla z^T (\mathbf{K}_1 - \mathbf{K}_2) \mathbf{n}, \quad (\text{A.14})$$

$$\theta_{\beta 2} = \theta_2 + (\mathbf{x}_\beta - \mathbf{y}_2 - d_2 \lambda_2^{-1} (\boldsymbol{\Lambda}_1 \mathbf{n} - \boldsymbol{\lambda}_2))^T \nabla \theta_1 \quad (\text{A.15})$$

According to Eq. (A.1) the tangential projections of the gradients are $\xi_{\tau 1}^u = \xi_{\tau 2}^u = \xi_{\tau}^u$. Deriving ξ_2 from Eq. (A.1) and substituting the result into Eq. (A.2) we obtain the following expression for ξ_1^u :

$$(d_1 \mathbf{T}_2 + d_2 \mathbf{T}_1) \xi_1^u = \mathbf{T}_2 (\mathbf{u}_2 - \mathbf{u}_1) + (\mathbf{T}_2 \otimes (\mathbf{y}_1 - \mathbf{y}_2)^T + d_2 (\Gamma_2 - \Gamma_1)) \xi_{\tau}^u + d_2 (p_{\beta 1} \mathbf{B}_1 + \theta_{\beta 1} \mathbf{A}_1 - p_{\beta 2} \mathbf{B}_2 - \theta_{\beta 2} \mathbf{A}_2) \mathbf{n}. \quad (\text{A.16})$$

Substitution of Eq. (A.16) in the left-hand side of Eq. (A.2) we obtain the approximation for the traction \mathbf{f} at the interface β as

$$\mathbf{f}_{\beta} = \mathbf{f}_{\beta}^{(d)} + \mathbf{f}_{\beta}^{(a)}, \quad (\text{A.17})$$

where

$$\begin{aligned} \mathbf{f}_{\beta}^{(d)} = & -\mathbf{T}_1 \xi_1^u - \Gamma_1 \xi_{\tau}^u = \mathbf{T} (\mathbf{u}_1 - \mathbf{u}_2) - \\ & - [(\mathbf{T} \otimes (\mathbf{y}_1 - \mathbf{y}_2)^T] + d_1 \mathbf{T}_2 (d_1 \mathbf{T}_2 + d_2 \mathbf{T}_1)^{-1} \Gamma_1 + d_2 \mathbf{T}_1 (d_1 \mathbf{T}_2 + d_2 \mathbf{T}_1)^{-1} \Gamma_2) \xi_{\tau}^u + \\ & + d_2 \mathbf{T}_1 (d_1 \mathbf{T}_2 + d_2 \mathbf{T}_1)^{-1} (p_{\beta} (\mathbf{B}_2 - \mathbf{B}_1) + \theta_{\beta} (\mathbf{A}_2 - \mathbf{A}_1)) \mathbf{n}, \end{aligned} \quad (\text{A.18})$$

$$\mathbf{f}_{\beta}^{(a)} = (p_{\beta} \mathbf{B}_1 + \theta_{\beta} \mathbf{A}_1) \mathbf{n}, \quad (\text{A.19})$$

where $\mathbf{T} = \mathbf{T}_1 (d_1 \mathbf{T}_2 + d_2 \mathbf{T}_1)^{-1} \mathbf{T}_2$ stands for 3×3 matrix and the approximations for $p_{\beta}, \theta_{\beta}$ are taken from Eqs. (A.10), (A.11).

The reconstruction of the gradients of displacements has to be performed before the assembly of momentum fluxes. The interface provides the following restrictions on it

$$(\mathbf{T}_2 \otimes (\mathbf{x}_2 - \mathbf{x}_1)^T + d_2 (\mathbf{T}_1 - \mathbf{T}_2) \otimes \mathbf{n}^T + d_2 (\Gamma_1 - \Gamma_2)) [\nabla \otimes \mathbf{u}_1] = \mathbf{T}_2 (\mathbf{u}_2 - \mathbf{u}_1) + d_2 (p_{\beta 1} \mathbf{B}_1 + \theta_{\beta 1} \mathbf{A}_1 - p_{\beta 2} \mathbf{B}_2 - \theta_{\beta 2} \mathbf{A}_2) \mathbf{n}. \quad (\text{A.20})$$

The advective term $\tilde{q}_{\beta} = (\mathbf{u}_{\beta} - \mathbf{u}_1) \cdot \mathbf{B}_1 \mathbf{n}$ depends on the approximation of displacements at the center of an interface \mathbf{u}_{β} that can be approximated as

$$\begin{aligned} \mathbf{u}_{\beta} = & (d_1 \mathbf{T}_2 + d_2 \mathbf{T}_1)^{-1} (d_2 \mathbf{T}_1 \mathbf{u}_1 + d_1 \mathbf{T}_2 \mathbf{u}_2) + \\ & + (d_1 \mathbf{T}_2 + d_2 \mathbf{T}_1)^{-1} ((d_1 d_2 (\Gamma_2 - \Gamma_1) + d_2 \mathbf{T}_1 \otimes (\mathbf{x}_{\beta} - \mathbf{y}_1)^T + d_1 \mathbf{T}_2 \otimes (\mathbf{x}_{\beta} - \mathbf{y}_2)^T) \xi_{\tau}^u + \\ & + d_1 d_2 (p_{\beta 1} \mathbf{B}_1 + \theta_{\beta 1} \mathbf{A}_1 - p_{\beta 2} \mathbf{B}_2 - \theta_{\beta 2} \mathbf{A}_2) \mathbf{n}). \end{aligned} \quad (\text{A.21})$$

A.2. Approximation of Fluxes at Boundary Interfaces

For the following system of boundary conditions enforced at the boundary of thermoelastic media

$$\begin{cases} \mathbf{n}^T (a_n \mathbf{u}_b - b_n \mathbf{f}_b) = r_n, \\ (\mathbf{I} - \mathbf{nn}^T) (a_t \mathbf{u}_b - b_t \mathbf{f}_b) = \mathbf{r}_t, \\ a_p p_b - b_p q_f = r_p, \\ a_\theta \theta_b - b_\theta q_\theta = r_\theta, \end{cases} \quad (\text{A.22})$$

we can derive the approximation of temperature θ_b and heat flux $\mathbf{n}^T q_{\theta,b}$ at the boundary in the same manner to the derivation of Eqs. (3.62), (3.63)

$$\theta_b = \left(a_\theta + \frac{b_\theta \lambda_1}{d_1} \right)^{-1} \left(r_\theta + \frac{b_\theta \lambda_1}{d_1} \theta_1 - b_\theta \left(\frac{\lambda_1}{d_1} (\mathbf{y}_1 - \mathbf{x}_b) + \lambda_1 \right) \cdot \boldsymbol{\xi}_\tau^\theta \right), \quad (\text{A.23})$$

$$q_{\theta,b} = - \left(a_\theta + \frac{b_\theta \lambda_1}{d_1} \right)^{-1} \left(\frac{\lambda_1}{d_1} r_\theta - a_\theta \frac{\lambda_1}{d_1} \theta_1 + a_\theta \left(\frac{\lambda_1}{d_1} (\mathbf{y}_1 - \mathbf{x}_b) + \lambda_1 \right) \cdot \boldsymbol{\xi}_\tau^\theta \right). \quad (\text{A.24})$$

The extension of Eqs. (3.64), (3.65), (3.67) to the thermoelastic stresses can be done with substitution of $\theta_b \mathbf{A}_1 \mathbf{n} + p_b \mathbf{B}_1 \mathbf{n}$ instead of $p_b \mathbf{B}_1 \mathbf{n}$.

A.3. Uniaxial thermoelastic consolidation

The semi-analytical solution for a coupled problem of fluid mass, energy, and momentum balance in the uniaxial consolidation test (Bai 2005) can be employed to benchmark the developed approximations. Thus, we consider the vertical column of 7 m height subjected to instant vertical loading with $F = 1$ Pa at the top boundary (Gao *et al.* 2020). The constant pressure $p = 0$ Pa and temperature $\theta = 50$ °C is maintained at the top boundary while the initial pressure and temperature are equal to $p_0 = 0$ Pa and $\theta_0 = 0$ °C, respectively. All other sides of the domain are impermeable to fluid and heat and subjected to the roller boundary condition. The domain is shown in Fig. A.1.

Furthermore, the stiffness tensor is defined by Young's modulus $E = 6$ kPa and Poisson's ratio $\nu = 0.4$. Isotropic permeability $\mathbf{K} = k\mathbf{I}$, Biot's $\mathbf{B} = b\mathbf{I}$, thermal dilation $\mathbf{A} = a\mathbf{I}$ and total heat conduction $\mathbf{\Lambda} = \lambda\mathbf{I}$ tensors are defined by the corresponding scalar values $k = 4 \times 10^{-9} \text{ m}^2$, $b = 1.0$, $a = 9 \times 10^{-7} \text{ }^\circ\text{C}^{-1}$ and $\lambda = 836 \text{ J m}^{-1} \text{ s}^{-1} \text{ }^\circ\text{C}^{-1}$, respectively. The total volumetric heat capacity is equal to $c = 167.2 \text{ kJ m}^{-3} \text{ }^\circ\text{C}^{-1}$. Fluid is maintained incompressible with fluid viscosity $\mu = 1$ cP.

Fig. A.2 illustrates the comparison of pressure, temperature, and vertical displacement to the analytical solution. Pressure, temperature, and vertical displacement evaluated at three points in space are plotted against time. The numerical solution obtained with the proposed approximations implemented in DARTS (Voskov *et al.* 2023) demonstrates a good match to the analytical solution (Analytics).

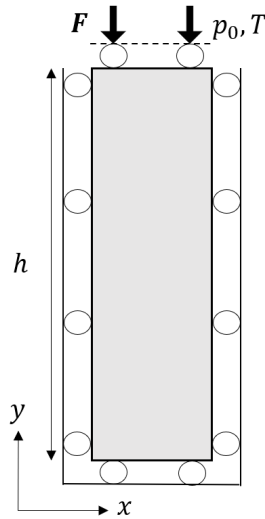


Figure A.1.: The setup for uniaxial thermoporoelastic consolidation test (Gao *et al.* 2020).

An instant loading causes an instant compression followed by further consolidation due to fluid discharge as in the uniaxial poroelastic consolidation test. However, heat conduction propagates energy from the top boundary, which is maintained under high temperature $T = 50^\circ\text{C}$, throughout the whole domain. Temperature increase causes thermal expansion, competing with consolidation.

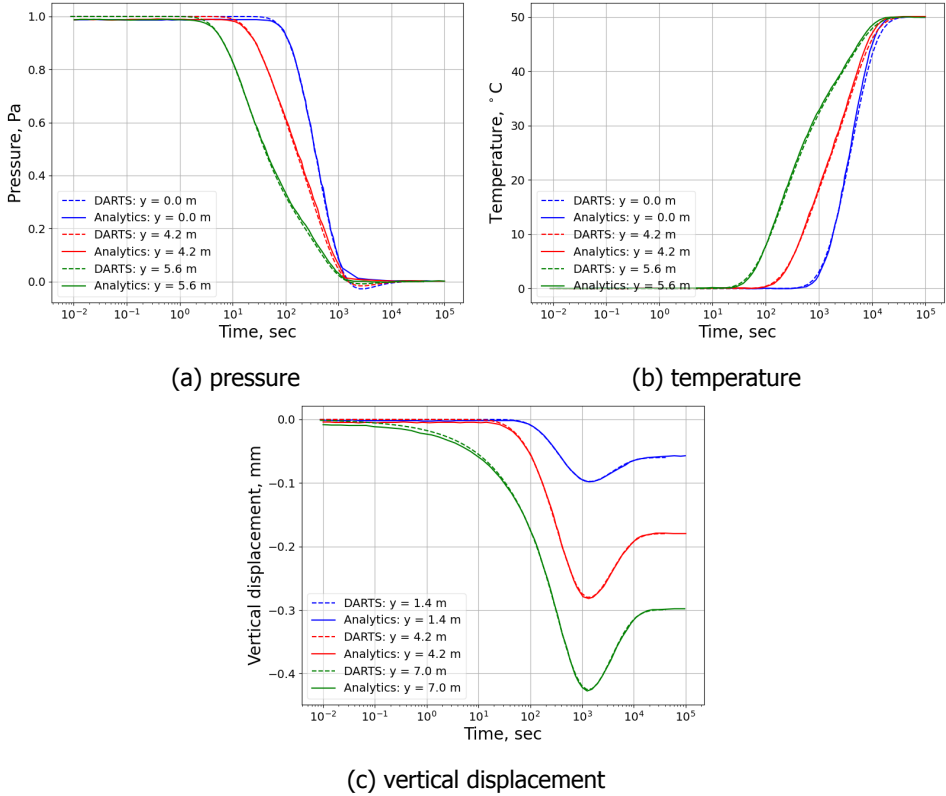


Figure A.2.: The dynamics of pressure (a), temperature (b) and vertical displacement (c) over time estimated in three points in space with semi-analytical method (solid curve) and numerical solution from DARTS (dashed curve).

Data availability statement

The simulation data for the cases considered in this dissertation is publicly available and can be accessed with the following link:

- Novikov, Aleksei (2024): Data underlying the PhD thesis: A Finite Volume Framework for Accurate Modeling of Fault Reactivation in Poroelastic Rocks. Version 1. 4TU.ResearchData. dataset. <https://doi.org/10.4121/8bda365e-888f-420b-9b16-f062fa2c5e4e.v1>

References

- Aagaard, B., M. Knepley and C. Williams (Oct. 2022). *geodynamics/pylith v3.0.3*. Version v3.0.3.
- Aagaard, B. T., R. W. Graves, A. Rodgers, T. M. Brocher, R. W. Simpson, D. Dreger, N. Anders Petersson, S. C. Larsen, S. Ma and R. C. Jachens (2010). 'Ground-motion modeling of hayward fault scenario earthquakes, part ii: Simulation of long-period and broadband ground motions'. In: *Bulletin of the Seismological Society of America* 100.6, pp. 2945–2977.
- Aavatsmark, I., T. Barkve, O. Boe and T. Mannseth (1996). 'Discretization on Non-Orthogonal, Quadrilateral Grids for Inhomogeneous, Anisotropic Media'. In: *Journal of Computational Physics* 127.1, pp. 2–14.
- Aavatsmark, I., G. Eigestad, B. Mallison and J. Nordbotten (2008). 'A compact multi-point flux approximation method with improved robustness'. In: *Numerical Methods for Partial Differential Equations* 24.5, pp. 1329–1360.
- Ambartsumyan, I., E. Khattatov, J. Nordbotten and I. Yotov (2020). 'A multipoint stress mixed finite element method for elasticity on simplicial grids'. In: *SIAM Journal on Numerical Analysis* 58.1, pp. 630–656.
- Arbogast, T., M. Wheeler and I. Yotov (1997). 'Mixed finite elements for elliptic problems with tensor coefficients as cell-centered finite differences'. In: *SIAM Journal on Numerical Analysis* 34.2, pp. 828–852.
- Arnold, D., R. Falk and R. Winther (2007). 'Mixed finite element methods for linear elasticity with weakly imposed symmetry'. In: *Mathematics of Computation* 76.260, pp. 1699–1723.
- Aronson, R., F. Hamon, N. Castelletto, J. White and H. Tchelepi (2023). 'Pressure Jump Stabilization for Compositional Poromechanics on Unstructured Meshes'. In.
- Atkinson, G. M., D. W. Eaton, H. Ghofrani, D. Walker, B. Cheadle, R. Schultz, R. Shcherbakov, K. Tiampo, J. Gu, R. M. Harrington, Y. Liu, M. Van Der Baan and H. Kao (2016). 'Hydraulic fracturing and seismicity in the western Canada sedimentary basin'. In: *Seismological Research Letters* 87.3, pp. 631–647.
- Bai, B. (Oct. 2005). 'One-dimensional thermal consolidation characteristics of geotechnical media under non-isothermal condition'. In: *Gongcheng Lixue/Engineering Mechanics* 22, pp. 186–191.
- Baker, A., T. V. Kolev and U. Yang (2010). 'Improving algebraic multigrid interpolation operators for linear elasticity problems'. In: *Numerical Linear Algebra with Applications* 17.2-3, pp. 495–517.
- Berge, R., I. Berre, E. Keilegavlen, J. Nordbotten and B. Wohlmuth (2020). 'Finite volume discretization for poroelastic media with fractures modeled by contact mechanics'. In: *International Journal for Numerical Methods in Engineering* 121.4, pp. 644–663.

- Berman, A. and R. J. Plemmons (1979). 'CHAPTER 6 - M-MATRICES'. In: *Nonnegative Matrices in the Mathematical Sciences*. Ed. by A. Berman and R. J. Plemmons. Academic Press, pp. 132–164.
- Berre, I., W. Boon, B. Flemisch, A. Fumagalli, D. Gläser, E. Keilegavlen, A. Scotti, I. Stefansson, A. Tatomir, K. Brenner, S. Burbulla, P. Devloo, O. Duran, M. Favino, J. Hennicker, I.-H. Lee, K. Lipnikov, R. Masson, K. Mosthaf, M. Nestola, C.-F. Ni, K. Nikitin, P. Schädle, D. Svyatskiy, R. Yanbarisov and P. Zulian (2021). 'Verification benchmarks for single-phase flow in three-dimensional fractured porous media'. In: *Advances in Water Resources* 147.
- Biot, M. (1977). 'Variational Lagrangian-thermodynamics of nonisothermal finite strain mechanics of porous solids and thermomolecular diffusion'. In: *International Journal of Solids and Structures* 13.6, pp. 579–597.
- Biot, M. A. (1941). 'General theory of three-dimensional consolidation'. In: *Journal of Applied Physics* 12.2, pp. 155–164.
- Bolton, D. C., S. Shreedharan, J. Rivière and C. Marone (2020). 'Acoustic Energy Release During the Laboratory Seismic Cycle: Insights on Laboratory Earthquake Precursors and Prediction'. In: *Journal of Geophysical Research: Solid Earth* 125.8.
- Boon, W. and J. Nordbotten (2023). 'Mixed-dimensional poromechanical models of fractured porous media'. In: *Acta Mechanica* 234.3, pp. 1121–1168.
- Boon, W. M., J. M. Nordbotten and J. E. Vatne (2021). 'Functional analysis and exterior calculus on mixed-dimensional geometries'. In: *Annali di Matematica Pura ed Applicata* 200.2, pp. 757–789.
- Brandt, A. (1986). 'Algebraic multigrid theory: The symmetric case'. In: *Applied Mathematics and Computation* 19.1-4, pp. 23–56.
- Brezzi, F. and J. Pitkäranta (1984). 'On the Stabilization of Finite Element Approximations of the Stokes Equations'. In: *Efficient Solutions of Elliptic Systems: Proceedings of a GAMM-Seminar Kiel, January 27 to 29, 1984*. Ed. by W. Hackbusch. Wiesbaden: Vieweg+Teubner Verlag, pp. 11–19.
- Buijze, A., P. Van den Bogert, B. Wassing and B. Orlic (2019). 'Nucleation and arrest of dynamic rupture induced by reservoir depletion'. In: *Journal of Geophysical Research: Solid Earth* 124, pp. 3620–3645.
- Buijze, A., P. Van den Bogert, B. Wassing, B. Orlic and J. Ten Veen (2017). 'Fault reactivation mechanisms and dynamic rupture modelling of production-induced seismic events in a Rotliegend gas reservoir'. In: *Netherlands Journal of Geosciences* 96, S131–S148.
- Buijze, L., L. Van Bijsterveldt, H. Cremer, B. Paap, H. Veldkamp, B. B. Wassing, J.-D. Van Wees, G. C. Van Yperen and J. H. Ter Heege (2020). 'Review of induced seismicity in geothermal systems worldwide and implications for geothermal systems in the Netherlands'. In: *Geologie en Mijnbouw/Netherlands Journal of Geosciences*.
- Camargo, J. T., J. A. White and R. I. Borja (2021). 'A macroelement stabilization for mixed finite element/finite volume discretizations of multiphase poromechanics'. In: *Computational Geosciences* 25.2, pp. 775–792.
- Cao, H., H. Tchelepi, J. Wallis and H. Yardumian (2005). 'Parallel scalable unstructured CPR-type linear solver for reservoir simulation'. In: pp. 3319–3326.

- Carder, D. S. (Oct. 1945). 'Seismic investigations in the Boulder Dam area, 1940-1944, and the influence of reservoir loading on local earthquake activity*'. In: *Bulletin of the Seismological Society of America* 35.4, pp. 175–192.
- Cardiff, P. and I. Demirdžić (2021). 'Thirty Years of the Finite Volume Method for Solid Mechanics'. In: *Archives of Computational Methods in Engineering* 28.5, pp. 3721–3780.
- Cardiff, P., Z. Tukovic, P. D. Jaeger, M. Clancy and A. Ivankovic (2017). 'A Lagrangian cell-centred finite volume method for metal forming simulation'. In: *International Journal for Numerical Methods in Engineering* 109.13, pp. 1777–1803.
- Chen, J., A. R. Niemeijer and C. J. Spiers (2022). 'Seismic Fault Slip Behavior Predicted From Internal Microphysical Processes'. In: *Journal of Geophysical Research: Solid Earth* 127.11.
- Chen, J. and C. J. Spiers (2016). 'Rate and state frictional and healing behavior of carbonate fault gouge explained using microphysical model'. In: *Journal of Geophysical Research: Solid Earth* 121.12, pp. 8642–8665.
- Chen, R., J. Zhu, S. Li, S. Zhang, X. Chen, Q. Li, P. Wang, J. Zhang, L. Dai and Y. Jia (2023). 'Characteristics and mechanisms of human-induced earthquakes in China from the QuakeQuake database'. In: *Geological Journal*.
- Chen, Z. (2007). 'Reservoir simulation mathematical techniques in oil recovery'. In: vol. 77, pp. 1–247.
- Cheng, A.-D. (1997). 'Material coefficients of anisotropic poroelasticity'. In: *International journal of rock mechanics and mining sciences & geomechanics abstracts* 34.2, pp. 199–205.
- Cheng, Y., W. Liu, T. Xu, Y. Zhang, X. Zhang, Y. Xing, B. Feng and Y. Xia (2023). 'Seismicity induced by geological CO₂ storage: A review'. In: *Earth-Science Reviews* 239.
- Chouly, F., P. Hild, V. Lleras and Y. Renard (2022). 'Nitsche method for contact with Coulomb friction: Existence results for the static and dynamic finite element formulations'. In: *Journal of Computational and Applied Mathematics* 416.
- Clees, T. (2005). 'AMG Strategies for PDE Systems with Applications in Industrial Semiconductor Simulation'. In.
- Cornelissen, P., B. Meulenbroek and J. Jansen (2023). *On the derivation of closed-form expressions for displacements, strains and stresses inside a poroelastic inclusion*. Tech. rep. Delft University of Technology.
- Coussy, O. (2004). *Poromechanics*. Wiley.
- Datta-Gupta, A. and M. J. King (2007). *Streamline Simulation: Theory and Practice*. Society of Petroleum Engineers.
- Davis, S. and W. Pennington (1989). 'Induced seismic deformation in the Cogdell oil field of west Texas'. In: *Bulletin - Seismological Society of America* 79.5, pp. 1477–1495.
- Day, S. M., L. A. Dalguer, N. Lapusta and Y. Liu (2005). 'Comparison of finite difference and boundary integral solutions to three-dimensional spontaneous rupture'. In: *Journal of Geophysical Research: Solid Earth* 110.12, pp. 1–23.

- Deb, R. and P. Jenny (2017a). 'Finite volume-based modeling of flow-induced shear failure along fracture manifolds'. In: *International Journal for Numerical and Analytical Methods in Geomechanics* 41.18, pp. 1922–1942.
- (2017b). 'Modeling of shear failure in fractured reservoirs with a porous matrix'. In: *Computational Geosciences* 21.5-6, pp. 1119–1134.
- De Boer, R. (2005). *Trends in continuum mechanics of porous media*. Theory and Applications of Transport in Porous Media. Springer.
- De Hoop, S., D. Voskov, G. Bertotti and A. Barnhoorn (2022). 'An Advanced Discrete Fracture Methodology for Fast, Robust, and Accurate Simulation of Energy Production From Complex Fracture Networks'. In: *Water Resources Research* 58.5.
- Demmel, J. W., S. C. Eisenstat, J. R. Gilbert, X. S. Li and J. W. H. Liu (1999). 'A supernodal approach to sparse partial pivoting'. In: *SIAM J. Matrix Analysis and Applications* 20.3, pp. 720–755.
- Dieterich, J. H. (1979). 'Modeling of rock friction 1. Experimental results and constitutive equations'. In: *Journal of Geophysical Research: Solid Earth* 84.B5, pp. 2161–2168.
- Dohrmann, C. R. and P. B. Bochev (2004). 'A stabilized finite elements method for the Stokes problem based on polynomial pressure projections'. In: *International Journal for Numerical Methods in Fluids* 46.2, pp. 183–201.
- Dost, B., F. Goutbeek, T. Eck and D. Kraaijpoel (Jan. 2012). 'Monitoring induced seismicity in the North of the Netherlands: Status report 2010'. In.
- Dost, B., E. Ruigrok and J. Spetzler (2017). 'Development of seismicity and probabilistic hazard assessment for the Groningen gas field'. In: *Geologie en Mijnbouw/Netherlands Journal of Geosciences* 96.5, s235–s245.
- Dostál, Z., T. Kozubek and V. Vondrák (2016). 'Contact Problems with Friction'. In: *Scalable Algorithms for Contact Problems*. New York, NY: Springer New York, pp. 211–229.
- Dumbser, M. and M. Käser (2006). 'An arbitrary high-order discontinuous Galerkin method for elastic waves on unstructured meshes - II. The three-dimensional isotropic case'. In: *Geophysical Journal International* 167.1, pp. 319–336.
- Edwards, M. G. and C. F. Rogers (1998). 'Finite volume discretization with imposed flux continuity for the general tensor pressure equation'. In: *Computational Geosciences* 2, pp. 259–290.
- Ellsworth, W. L. (2013). 'Injection-induced earthquakes'. In: *Science* 341.6142.
- Ellsworth, W. L., D. Giardini, J. Townend, S. Ge and T. Shimamoto (2019). 'Triggering of the Pohang, Korea, Earthquake (Mw 5.5) by enhanced geothermal system stimulation'. In: *Seismological Research Letters* 90.5, pp. 1844–1858.
- Erickson, B. A., J. Jiang, V. Lambert, S. D. Barbot, M. Abdelmeguid, M. Almquist, J.-P. Ampuero, R. Ando, C. Cattania, A. Chen, L. Dal Zilio, S. Deng, E. M. Dunham, A. E. Elbanna, A.-A. Gabriel, T. W. Harvey, Y. Huang, Y. Kaneko, J. E. Kozdon, N. Lapusta, D. Li, M. Li, C. Liang, Y. Liu, S. Ozawa, A. Perez-Silva, C. Pranger, P. Segall, Y. Sun, P. Thakur, C. Uphoff, Y. van Dinther and Y. Yang (2023). 'Incorporating Full Elastodynamic Effects and Dipping Fault Geometries in Community Code Verification Exercises for Simulations of Earthquake Sequences and Aseismic Slip (SEAS)'. In: *Bulletin of the Seismological Society of America* 113.2, pp. 499–523.

- Eshelby, J. D. (1957). 'The determination of the elastic field of an ellipsoidal inclusion and related problems'. In: *Proceedings of the Royal Society of London, Series A* 241, pp. 376–396.
- Ferronato, M., A. Franceschini, C. Janna, N. Castelletto and H. A. Tchelepi (2019). 'A general preconditioning framework for coupled multiphysics problems with application to contact- and poro-mechanics'. In: *Journal of Computational Physics* 398, p. 108887.
- Folch, A., C. Abril, M. Afanasiev, G. Amati, M. Bader, R. M. Badia, H. B. Bayraktar, S. Barsotti, R. Basili, F. Bernardi, C. Boehm, B. Brizuela, F. Brogi, E. Cabrera, E. Casarotti, M. J. Castro, M. Cerminara, A. Cirella, A. Cheptsov, J. Conejero, A. Costa, M. de la Asunción, J. de la Puente, M. Djuric, R. Dorozhinskii, G. Espinosa, T. Esposti-Ongaro, J. Farnós, N. Favretto-Cristini, A. Fichtner, A. Fournier, A.-A. Gabriel, J.-M. Gallard, S. J. Gibbons, S. Glimsdal, J. M. González-Vida, J. Gracia, R. Gregorio, N. Gutierrez, B. Halldorsson, O. Hamitou, G. Houzeaux, S. Jaure, M. Kessar, L. Krenz, L. Krischer, S. Laforet, P. Lanucara, B. Li, M. C. Lorenzino, S. Lorito, F. Løvholt, G. Macedonio, J. Macías, G. Marín, B. Martínez Montesinos, L. Mingari, G. Moguilny, V. Montellier, M. Monterrubio-Velasco, G. E. Moulard, M. Nagaso, M. Nazaria, C. Niethammer, F. Pardini, M. Pienkowska, L. Pizzimenti, N. Poiata, L. Rannabauer, O. Rojas, J. E. Rodriguez, F. Romano, O. Rudyy, V. Ruggiero, P. Samfass, C. Sánchez-Linares, S. Sanchez, L. Sandri, A. Scala, N. Schaeffer, J. Schuchart, J. Selva, A. Sergeant, A. Stallone, M. Taroni, S. Thrastarson, M. Titos, N. Tonello, R. Tonini, T. Ulrich, J.-P. Vilotte, M. Vöge, M. Volpe, S. Aniko Wirp and U. Wössner (2023). 'The EU Center of Excellence for Exascale in Solid Earth (ChEESE): Implementation, results, and roadmap for the second phase'. In: *Future Generation Computer Systems* 146, pp. 47–61.
- Forsyth Jr., P. and P. Sammon (1986). 'Practical considerations for adaptive implicit methods in reservoir simulation'. In: *Journal of Computational Physics* 62.2, pp. 265–281.
- Foulger, G. R., M. P. Wilson, J. G. Gluyas, B. R. Julian and R. J. Davies (2018). 'Global review of human-induced earthquakes'. In: *Earth-Science Reviews* 178, pp. 438–514.
- Franceschini, A., N. Castelletto, J. A. White and H. A. Tchelepi (2022a). 'Scalable preconditioning for the stabilized contact mechanics problem'. In: *Journal of Computational Physics* 459.
- Franceschini, A., L. Gazzola and M. Ferronato (2022b). 'A scalable preconditioning framework for stabilized contact mechanics with hydraulically active fractures'. In: *Journal of Computational Physics* 463.
- Franceschini, A., C. Zoccarato, S. Baldan, M. Frigo, M. Ferronato, C. Janna, G. Isotton and P. Teatini (2023). *Unexpected fault activation in underground gas storage. Part I: Mathematical model and mechanisms*. arXiv/2308.02198.
- Franco Brezzi, M. F. (1991). *Mixed and Hybrid Finite Element Methods*. 1st ed. Springer Series in Computational Mathematics. Springer.
- Gallyamov, E., T. Garipov, D. Voskov and P. Van den Hoek (2018). 'Discrete fracture model for simulating waterflooding processes under fracturing conditions'.

- In: *International Journal for Numerical and Analytical Methods in Geomechanics* 42.13, pp. 1445–1470.
- Gao, Q. and A. Ghassemi (Apr. 2020). 'Three-Dimensional Thermo-Poroelastic Modeling and Analysis of Flow, Heat Transport and Deformation in Fractured Rock with Applications to a Lab-Scale Geothermal System'. In: *Rock Mechanics and Rock Engineering* 53, pp. 1–22.
- Garipov, T. and M. Hui (2019). 'Discrete Fracture Modeling approach for simulating coupled thermo-hydro-mechanical effects in fractured reservoirs'. In: *International Journal of Rock Mechanics and Mining Sciences* 122.
- Garipov, T., M. Karimi-Fard and H. Tchelepi (2016). 'Discrete fracture model for coupled flow and geomechanics'. In: *Computational Geosciences* 20.1, pp. 149–160.
- Garipov, T., P. Tomin, R. Rin, D. Voskov and H. Tchelepi (2018). 'Unified thermo-compositional-mechanical framework for reservoir simulation'. In: *Computational Geosciences* 22.4, pp. 1039–1057.
- Gaspar, F., F. Lisbona and C. Oosterlee (2008). 'A stabilized difference scheme for deformable porous media and its numerical resolution by multigrid methods'. In: *Computing and Visualization in Science* 11.2, pp. 67–76.
- Gaspar, F., F. Lisbona and P. Vabishchevich (2003). 'A finite difference analysis of Biot's consolidation model'. In: *Applied Numerical Mathematics* 44.4, pp. 487–506.
- (2006). 'Staggered grid discretizations for the quasi-static Biot's consolidation problem'. In: *Applied Numerical Mathematics* 56.6, pp. 888–898.
- Geertsma, J. (1966). 'Problems of rock mechanics in petroleum production engineering'. In: *Proceedings of the 1st ISRM Congress*. 25 Sept.-1 Oct., Lisbon, Portugal.
- (1973). 'A basic theory of subsidence due to reservoir compaction: the homogeneous case'. In: *Verhandelingen Koninklijk Nederlandsch Geologisch Mijnbouwkundig Genootschap* 25, pp. 43–61.
- Germain, P. (1973). *Cours de mécanique des milieux continus . Tome I, Théorie générale*. fre. Paris: Masson.
- Goodier, J. (1937). 'On the integration of the thermo-elastic equations'. In: *The London, Edinburgh, and Dublin Philosophical Magazine and Journal of Sciences* 23, pp. 1017–1032.
- Griebel, M., D. Oeltz and M. A. Schweitzer (2003). 'An algebraic multigrid method for linear elasticity'. In: *SIAM Journal on Scientific Computing* 25.2, pp. 385–407.
- Gries, S., B. Metsch, K. M. Terekhov and P. Tomin (2019). 'System-AMG for fully coupled reservoir simulation with geomechanics'. In.
- Grigoli, F., S. Cesca, E. Priolo, A. P. Rinaldi, J. F. Clinton, T. A. Stabile, B. Dost, M. G. Fernandez, S. Wiemer and T. Dahm (2017). 'Current challenges in monitoring, discrimination, and management of induced seismicity related to underground industrial activities: A European perspective'. In: *Reviews of Geophysics* 55.2, pp. 310–340.

- Gupta, H. K. (2002). 'A review of recent studies of triggered earthquakes by artificial water reservoirs with special emphasis on earthquakes in Koyna, India'. In: *Earth-Science Reviews* 58.3-4, pp. 279–310.
- Han, Z., G. Ren and R. M. Younis (2023). 'Automatic Time Step Control to Resolve Hydromechanically Driven Fault Reactivation, Spontaneous Nucleation, and Seismic Arrest'. In: *Water Resources Research* 59.11, e2023WR035626.
- Harris, R., M. Barall, R. Archuleta, E. Dunham, B. Aagaard, J. Ampuero, H. Bhat, V. Cruz-Atienza, L. Dalguer, P. Dawson, S. Day, B. Duan, G. Ely, Y. Kaneko, Y. Kase, N. Lapusta, Y. Liu, S. Ma, D. Oglesby, K. Olsen, A. Pitarka, S. Song and E. Templeton (2009). 'The SCEC/USGS dynamic earthquake rupture code verification exercise'. In: *Seismological Research Letters* 80.1, pp. 119–126.
- Healy, J., W. Rubey, D. Griggs and C. Raleigh (1968). 'The Denver earthquakes'. In: *Science* 161.3848, pp. 1301–1310.
- Henson, V. E. and U. M. Yang (2002). 'BoomerAMG: A parallel algebraic multigrid solver and preconditioner'. In: *Applied Numerical Mathematics* 41.1, pp. 155–177.
- Honório, H. T., C. R. Maliska, M. Ferronato and C. Janna (2018). 'A stabilized element-based finite volume method for poroelastic problems'. In: *Journal of Computational Physics* 364, pp. 49–72.
- Hughes, T. J. and L. P. Franca (1987). 'A new finite element formulation for computational fluid dynamics: VII. The stokes problem with various well-posed boundary conditions: Symmetric formulations that converge for all velocity/pressure spaces'. In: *Computer Methods in Applied Mechanics and Engineering* 65.1, pp. 85–96.
- Hughes, T. J., L. P. Franca and M. Balestra (1986). 'A new finite element formulation for computational fluid dynamics: V. Circumventing the babuška-brezzi condition: a stable Petrov-Galerkin formulation of the stokes problem accommodating equal-order interpolations'. In: *Computer Methods in Applied Mechanics and Engineering* 59.1, pp. 85–99.
- Hunfeld, L., A. Niemeijer and C. Spiers (2017). 'Frictional Properties of Simulated Fault Gouges from the Seismogenic Groningen Gas Field Under In Situ P–T - Chemical Conditions'. In: *Journal of Geophysical Research: Solid Earth* 122.11, pp. 8969–8989.
- Hutka, G. A., M. Cacace, H. Hofmann, A. Zang, L. Wang and Y. Ji (2023). 'Numerical investigation of the effect of fluid pressurization rate on laboratory-scale injection-induced fault slip'. In: *Scientific Reports* 13.1.
- International Energy Agency (2022). *World Energy Outlook 2022*, p. 524.
- Jansen, J., S. Douma, D. Brouwer, P. Van den Hof, O. Bosgra and A. Heemink (Feb. 2009). 'Closed-Loop Reservoir Management'. In: SPE Reservoir Simulation Conference, SPE-119098-MS.
- Jansen, J., P. Singhal and F. Vossepoel (2019). 'Insights from closed-form expressions for injection- and production-induced stresses in displaced faults'. In: *Journal of Geophysical Research: Solid Earth* 124, pp. 7193–7212.
- Jansen, J.-D. and B. Meulenbroek (2022). 'Induced aseismic slip and the onset of seismicity in displaced faults'. In: *Geologie en Mijnbouw/Netherlands Journal of Geosciences* 101.

- Jha, B. and R. Juanes (2014). 'Coupled multiphase flow and poromechanics: A computational model of pore pressure effects on fault slip and earthquake triggering'. In: *Water Resources Research* 50.5, pp. 3776–3808.
- Ji, Y., H. Hofmann, K. Duan and A. Zang (2022). 'Laboratory experiments on fault behavior towards better understanding of injection-induced seismicity in geoenery systems'. In: *Earth-Science Reviews* 226.
- Jiang, J., B. A. Erickson, V. R. Lambert, J.-P. Ampuero, R. Ando, S. D. Barbot, C. Cattania, L. D. Zilio, B. Duan, E. M. Dunham, A.-A. Gabriel, N. Lapusta, D. Li, M. Li, D. Liu, Y. Liu, S. Ozawa, C. Pranger and Y. van Dinther (2022). 'Community-Driven Code Comparisons for Three-Dimensional Dynamic Modeling of Sequences of Earthquakes and Aseismic Slip'. In: *Journal of Geophysical Research: Solid Earth* 127.3.
- Jónsson, S., P. Segall, R. Pedersen and G. Björnsson (2003). 'Post-earthquake ground movements correlated to pore-pressure transients'. In: *Nature* 424.6945, pp. 179–183.
- K. Aziz, A. S. (1979). *Petroleum Reservoir Simulation*. Applied Science Publishers LTD.
- Kala, K. and D. Voskov (2020). 'Element balance formulation in reactive compositional flow and transport with parameterization technique'. In: *Computational Geosciences* 24.2, pp. 609–624.
- Karimi-Fard, M., L. Durlofsky and K. Aziz (2004). 'An efficient discrete-fracture model applicable for general-purpose reservoir simulators'. In: *SPE Journal* 9.2, pp. 227–236.
- Keilegavlen, E., R. Berge, A. Fumagalli, M. Starnoni, I. Stefansson, J. Varela and I. Berre (2021). 'PorePy: an open-source software for simulation of multiphysics processes in fractured porous media'. In: *Computational Geosciences* 25.1, pp. 243–265.
- Keilegavlen, E. and J. Nordbotten (2017a). 'Finite volume methods for elasticity with weak symmetry'. In: *International Journal for Numerical Methods in Engineering* 112.8, pp. 939–962.
- Keilegavlen, E. and J. M. Nordbotten (2017b). 'Finite volume methods for elasticity with weak symmetry'. In: *International Journal for Numerical Methods in Engineering* 112.8, pp. 939–962.
- Keranen, K. M. and M. Weingarten (2018). 'Induced Seismicity'. In: *Annual Review of Earth and Planetary Sciences* 46, pp. 149–174.
- Kershaw, D. S. (1981). 'Differencing of the diffusion equation in Lagrangian hydrodynamic codes'. In: *Journal of Computational Physics* 39.2, pp. 375–395.
- Khait, M. and D. Voskov (2018a). 'Adaptive parameterization for solving of thermal/compositional nonlinear flow and transport with buoyancy'. In: *SPE Journal* 23.2, pp. 522–534.
- (2018b). 'Operator-based linearization for efficient modeling of geothermal processes'. In: *Geothermics* 74, pp. 7–18.
- Kikuchi, N. and J. Oden (1995). *Contact Problems in Elasticity: A Study of Variational Inequalities and Finite Element Methods*. Studies in Applied and Numerical Mathematics. Society for Industrial Mathematics.

- Kim, J., H. Tchelepi and R. Juanes (2011). 'Stability and convergence of sequential methods for coupled flow and geomechanics: Fixed-stress and fixed-strain splits'. In: *Computer Methods in Applied Mechanics and Engineering* 200.13-16, pp. 1591–1606.
- Kim, W.-Y. (2013). 'Induced seismicity associated with fluid injection into a deep well in Youngstown, Ohio'. In: *Journal of Geophysical Research: Solid Earth* 118.7, pp. 3506–3518.
- Kloforn, R., E. Keilegavlen, A. F. Radu and J. Fuhrmann, eds. (2020). *Finite Volumes for Complex Applications - Methods, Theoretical Aspects, Examples: Fvca 9, Bergen, Norway, June 2020*. 1st ed. Springer Proceedings in Mathematics & Statistics. Springer-Nature New York Inc.
- Kondaurov, V. (2007). 'The thermodynamically consistent equations of a thermoelastic saturated porous medium'. In: *Journal of Applied Mathematics and Mechanics* 71.4, pp. 562–579.
- Labuz, J. F. and A. Zang (2012). 'Mohr-Coulomb failure criterion'. In: *Rock Mechanics and Rock Engineering* 45.6, pp. 975–979.
- Ladyzhenskaya, O. A. (1969). 'The mathematical theory of viscous incompressible flow'. In: *Gordon & Breach*.
- Lapusta, N., J. R. Rice, Y. Ben-Zion and G. Zheng (2000). 'Elastodynamic analysis for slow tectonic loading with spontaneous rupture episodes on faults with rate- and state-dependent friction'. In: *Journal of Geophysical Research: Solid Earth* 105.B10, pp. 23765–23789.
- Laursen, T. A. (2010). *Computational Contact and Impact Mechanics: Fundamentals of Modeling Interfacial Phenomena in Nonlinear Finite Element Analysis*. Springer Berlin, Heidelberg.
- LeVeque, R. J. (2002). *Finite Volume Methods for Hyperbolic Problems*. 1st ed. Cambridge texts in applied mathematics. Cambridge University Press.
- Li, L. and S. Lee (2008). 'Efficient field-scale simulation of black oil in a naturally fractured reservoir through discrete fracture networks and homogenized media'. In: *SPE Reservoir Evaluation and Engineering* 11.4, pp. 750–758.
- Li, X., J. Demmel, J. Gilbert, iL. Grigori, M. Shao and I. Yamazaki (1999). *SuperLU Users' Guide*. Tech. rep. LBNL-44289. <https://portal.nersc.gov/project/sparse/superlu/ug.pdf> Last update: June 2018. Lawrence Berkeley National Laboratory.
- Luenberger, D. G. and Y. Ye (2008). *Linear and nonlinear programming*. 3rd ed. International series in operations research and management science. Springer.
- Luo, L., J. Wu and Z. Gao (2017). 'A Family of Linearity-Preserving Schemes for Anisotropic Diffusion Problems on General Grids'. In: *Journal of Computational and Theoretical Transport* 46.2, pp. 77–99.
- Lyu, X., M. Khait and D. Voskov (2021a). 'Operator-based linearization approach for modeling of multiphase flow with buoyancy and capillarity'. In: *SPE Journal* 26.4, pp. 1858–1878.
- Lyu, X., D. Voskov and W. Rossen (2021b). 'Numerical investigations of foam-assisted CO₂ storage in saline aquifers'. In: *International Journal of Greenhouse Gas Control* 108.

- Majer, E. L., R. Baria, M. Stark, S. Oates, J. Bommer, B. Smith and H. Asanuma (2007). 'Induced seismicity associated with Enhanced Geothermal Systems'. In: *Geothermics* 36.3, pp. 185–222.
- Martin, N. J. (2014). 'Cell-centered finite volume discretizations for deformable porous media'. In: *International Journal for Numerical Methods in Engineering* 100.6, pp. 399–418.
- McCormick, S. F. (1987). *Multigrid Methods*. Ed. by S. F. McCormick. Society for Industrial and Applied Mathematics.
- McGarr, A. (1984). 'Some applications of seismic source mechanism studies to assessing underground hazard'. In: pp. 199–208.
- McGarr, A., D. Simpson and L. Seeber (2002). '40 Case histories of induced and triggered seismicity'. In: *International Geophysics* 81.PART A, pp. 647–661.
- Michael J. Pyrcz, C. V. D. (2014). *Geostatistical Reservoir Modeling*. 2nd ed. Oxford University Press.
- Morinishi, Y., T. S. Lund, O. V. Vasilyev and P. Moin (June 1998). 'Fully Conservative Higher Order Finite Difference Schemes for Incompressible Flow'. In: *Journal of Computational Physics* 143.1, pp. 90–124.
- Muntendam-Bos, A. G., G. Hoedeman, K. Polychronopoulou, D. Draganov, C. Weemstra, W. van der Zee, R. R. Bakker and H. Roest (2022). 'An overview of induced seismicity in the Netherlands'. In: *Geologie en Mijnbouw/Netherlands Journal of Geosciences* 101.2.
- Murad, M. A. and A. F. D. Loula (1994). 'On stability and convergence of finite element approximations of Biot's consolidation problem'. In: *International Journal for Numerical Methods in Engineering* 37.4, pp. 645–667.
- Naderloo, M., A. Veltmeijer, J. Jansen and A. Barnhoorn (2023). 'Laboratory study on the effect of stress cycling pattern and rate on seismicity evolution'. In: *Geomechanics and Geophysics for Geo-Energy and Geo-Resources* 9.1.
- Nardean, S., M. Ferronato and A. Abushaikha (2022). 'Linear Solvers for Reservoir Simulation Problems: An Overview and Recent Developments'. In: *Archives of Computational Methods in Engineering* 29.6, pp. 4341–4378.
- Newmark, N. M. (1959). 'A Method of Computation for Structural Dynamics'. In: *Journal of the Engineering Mechanics Division* 85.3, pp. 67–94.
- Niemeijer, A. and C. Spiers (2007). 'A microphysical model for strong velocity weakening in phyllosilicate-bearing fault gouges'. In: *Journal of Geophysical Research: Solid Earth* 112.10.
- Nigmatulin, R. I. (1978). *Fundamentals of the mechanics of heterogeneous media*. [In Russian]. Nauka.
- Nikitin, K., K. Terekhov and Y. Vassilevski (Aug. 2013). 'A monotone nonlinear finite volume method for diffusion equations and multiphase flows'. In: *Computational Geosciences* 18, pp. 311–324.
- Nikolaevskiy, V. N. (1996). *Geomechanics and Fluidodynamics: With Applications to Reservoir Engineering*. 1st ed. Theory and Applications of Transport in Porous Media 8. Springer Netherlands.

- Nordbotten, J. (2014). 'Cell-centered finite volume discretizations for deformable porous media'. In: *International Journal for Numerical Methods in Engineering* 100.6, pp. 399–418.
- Nordbotten, J., I. Aavatsmark and G. Eigestad (2007). 'Monotonicity of control volume methods'. In: *Numer. Math.* 106, pp. 255–288.
- Nordbotten, J. M. (2016). 'Stable cell-centered finite volume discretization for biot equations'. In: *SIAM Journal on Numerical Analysis* 54.2, pp. 942–968.
- Novikov, A., I. Saifullin, H. Hajibeygi, A. Pluymakers, J. Jansen and D. Voskov (2024a). 'A Finite Volume Framework for the Fully Implicit Thermal-Hydro-Mechanical-Compositional Modeling in Geo-Energy Applications'. In: *Accepted for 19th European Conference on the Mathematics of Geological Reservoirs*.
- Novikov, A., D. Voskov, H. Hajibeygi and J. Jansen (2022a). 'Collocated Finite Volume Scheme for Scalable Simulation of Induced Seismicity'. In: *18th European Conference on the Mathematics of Oil Recovery, ECMOR 2022 1*, pp. 1–18.
- Novikov, A., D. Voskov, M. Khait, H. Hajibeygi and J. Jansen (2022b). 'A scalable collocated finite volume scheme for simulation of induced fault slip'. In: *Journal of Computational Physics* 469.
- Novikov, A., D. Voskov, M. Khait, H. Hajibeygi and J. Jansen (2021). 'A collocated finite volume scheme for high-performance simulation of induced seismicity in geo-energy applications'. In: *Society of Petroleum Engineers - SPE Reservoir Simulation Conference 2021, RSC 2021*.
- Novikov, A. V., S. Shokrollahzadeh Behbahani, D. Voskov, H. Hajibeygi and J. D. Jansen (June 2023). 'Benchmarking Analytical and Numerical Simulation of Induced Fault Slip'. In: *U.S. Rock Mechanics/Geomechanics Symposium, ARMA-2023-0695*.
- Novikov, A., S. S. Behbahani, D. Voskov, H. Hajibeygi and J. D. Jansen (2024b). 'Benchmarking Analytical and Numerical Simulation of Induced Fault Slip'. In: *Under Review in Geomechanics and Geophysics for Geo-Energy and Geo-Resources*.
- Nur, A. and J. R. Booker (1972). 'Aftershocks caused by pore fluid flow?' In: *Science* 175.4024, pp. 885–887.
- Orlic, B. and B. Wassing (2012). 'Modeling stress development and fault slip in producing hydrocarbon reservoirs overlain by rock salt caprocks'. In: vol. 1, pp. 17–28.
- Pampillón, P., D. Santillán, J. C. Mosquera and L. Cueto-Felgueroso (2018). 'Dynamic and Quasi-Dynamic Modeling of Injection-Induced Earthquakes in Poroelastic Media'. In: *Journal of Geophysical Research: Solid Earth* 123.7, pp. 5730–5759.
- Perlaviciute, G., L. Steg, E. J. Hoekstra and L. Vrieling (2017). 'Perceived risks, emotions, and policy preferences: A longitudinal survey among the local population on gas quakes in the Netherlands'. In: *Energy Research and Social Science* 29, pp. 1–11.
- Perot, B. (2000). 'Conservation Properties of Unstructured Staggered Mesh Schemes'. In: *Journal of Computational Physics* 159.1, pp. 58–89.
- Phillips, P. and M. Wheeler (2007). 'A coupling of mixed and continuous Galerkin finite element methods for poroelasticity I: The continuous in time case'. In: *Computational Geosciences* 11.2, pp. 131–144.

- Pijnenburg, R., B. Verberne, S. Hangx and C. Spiers (2019). 'Inelastic Deformation of the Slochteren Sandstone: Stress-Strain Relations and Implications for Induced Seismicity in the Groningen Gas Field'. In: *Journal of Geophysical Research: Solid Earth* 124.5, pp. 5254–5282.
- Pranger, C. C. (2020). 'Unstable physical processes operating on self-governing fault systems, improved modeling methodology'. PhD thesis. ETH Zurich.
- Pratt, W. E. and D. W. Johnson (1926). 'Local Subsidence of the Goose Creek Oil Field'. In: *The Journal of Geology* 34.7, pp. 577–590.
- Preisig, M. and J. H. Prévost (2011). 'Stabilization procedures in coupled poromechanics problems: A critical assessment'. In: *International Journal for Numerical and Analytical Methods in Geomechanics* 35.11, pp. 1207–1225.
- Reinartz, A., D. E. Charrier, M. Bader, L. Bovard, M. Dumbser, K. Duru, F. Fambri, A.-A. Gabriel, J.-M. Gallard, S. Köppel, L. Krenz, L. Rannabauer, L. Rezzolla, P. Samfass, M. Tavelli and T. Weinzierl (2020). 'ExaHyPE: An engine for parallel dynamically adaptive simulations of wave problems'. In: *Computer Physics Communications* 254, p. 107251.
- Rice, J. (1993). 'Spatio-temporal complexity of slip on a fault'. In: *Journal of Geophysical Research* 98.B6, pp. 9885–9907.
- Rice, J. R., N. Lapusta and K. Ranjith (2001). 'Rate and state dependent friction and the stability of sliding between elastically deformable solids'. In: *Journal of the Mechanics and Physics of Solids* 49.9, pp. 1865–1898.
- Rice, J. R. and J. W. Rudnicki (1979). 'Earthquake precursory effects due to pore fluid stabilization of a weakening fault zone'. In: *Journal of Geophysical Research: Solid Earth* 84.B5, pp. 2177–2193.
- Riemer, K. and R. Durrheim (2012). 'Mining seismicity in the Witwatersrand Basin: monitoring, mechanisms and mitigation strategies in perspective'. In: *Journal of Rock Mechanics and Geotechnical Engineering* 4.3, pp. 228–249.
- Rivière, B. (2008). *Discontinuous Galerkin Methods for Solving Elliptic and Parabolic Equations*. Society for Industrial and Applied Mathematics.
- Ruan, J., R. Ghose and W. Mulder (2023). '3D geomechanical modelling of induced seismicity including intersecting faults and reservoir compartments'. English. In: 84th EAGE ANNUAL Conference and Exhibition 2023, EAGE 2023 ; Conference date: 05-06-2023 Through 08-06-2023.
- Rudnicki, J. (2001). 'Coupled deformation-diffusion effects in the mechanics of faulting and failure of geomaterials'. In: *Applied Mechanics Reviews* 54.6, pp. 483–502.
- Ruge, J. W. and K. Stüben (1987). '4. Algebraic Multigrid'. In: *Multigrid Methods*, pp. 73–130.
- Ruina, A. (1983). 'Slip instability and state variable friction laws'. In: *Journal of Geophysical Research* 88.B12, pp. 10359–10370.
- Schneider, M., B. Flemisch, R. Helmig, K. Terekhov and H. Tchelepi (Apr. 2018a). 'Monotone nonlinear finite-volume method for challenging grids'. In: *Computational Geosciences* 22.

- Schneider, M., D. Gläser, B. Flemisch and R. Helmig (2018b). 'Comparison of finite-volume schemes for diffusion problems'. In: *Oil and Gas Science and Technology* 73.1.
- Scholz, C. H. (2019). *The Mechanics of Earthquakes and Faulting*. 3rd. Cambridge University Press.
- Schultz, R., R. Wang, Y. J. Gu, K. Haug and G. Atkinson (2017). 'A seismological overview of the induced earthquakes in the Duvernay play near Fox Creek, Alberta'. In: *Journal of Geophysical Research: Solid Earth* 122.1, pp. 492–505.
- Sedov, L. I. (1997). *Mechanics of Continuous Media*. World Scientific.
- Segall, P. (1989). 'Earthquakes triggered by fluid extraction'. In: *Geology* 17.10, pp. 942–946.
- Segall, P. and J. Rice (1995). 'Dilatancy, compaction, and slip instability of a fluid-infiltrated fault'. In: *Journal of Geophysical Research* 100.B11, pp. 22, 155–22, 171.
- Seitz, A., W. A. Wall and A. Popp (2019). 'Nitsche's method for finite deformation thermomechanical contact problems'. In: *Computational Mechanics* 63.6, pp. 1091–1110.
- Settari, A. and F. Mourits (1998). 'A Coupled Reservoir and Geomechanical Simulation System'. In: *SPE Journal* 3.3, pp. 219–226.
- Settgast, R. R., B. C. Corbett, S. Klevtsov, F. Hamon, C. Sherman, M. Cusini, T. Gazzola, W. Tobin, J. White, N. Castelletto, A. Borio, A. Franceschini, J. Huang, B. Han, H. Gross, J. Franc, A. Mazuyer, J. Besset, A. Citrain, A. Vargas, M. Cremon, Y. Hao, M. Khait, X. Lacoste, S. Semnani, S. Frambati, M. N'diaye, S.-T. Nguyen and H. M. Morgan (Oct. 2022). *GEOSX*. Version 0.2.1.
- Shapiro, S. A. (2015). *Fluid-induced seismicity*, pp. 1–276.
- Shinohara, T., C. Spiers and S. Hangx (May 2022). 'Effect of loading rate on mechanical behavior and deformation mechanisms in clay-bearing sandstones'. In: *EGU General Assembly Conference Abstracts*. EGU General Assembly Conference Abstracts, EGU22-2425, EGU22–2425.
- Shokrollahzadeh Behbahani, S., H. Hajibeygi, D. Voskov and J. Jansen (2022a). 'Smoothed embedded finite-volume method (sEFVM) for modeling contact mechanics in deformable faulted and fractured porous media'. In: *Journal of Computational Physics* (111143).
- Shokrollahzadeh Behbahani, S., H. Hajibeygi, D. Voskov and J. D. Jansen (2022b). 'Smoothed embedded finite-volume method (sEFVM) for modeling contact mechanics in deformable faulted and fractured porous media'. In: *Journal of Computational Physics* 459, p. 111143.
- Silvester, D. and N. Kechkar (1990). 'Stabilised bilinear-constant velocity-pressure finite elements for the conjugate gradient solution of the stokes problem'. In: *Computer Methods in Applied Mechanics and Engineering* 79.1, pp. 71–86.
- Simo, J. and T. Laursen (1992). 'An augmented lagrangian treatment of contact problems involving friction'. In: *Computers and Structures* 42.1, pp. 97–116.
- Simpson, D. W. (1976). 'Seismicity changes associated with reservoir loading'. In: *Engineering Geology* 10.2-4, pp. 123–150.

- Sokolova, I., M. Bastisya and H. Hajibeygi (2019). 'Multiscale finite volume method for finite-volume-based simulation of poroelasticity'. In: *Journal of Computational Physics* 379, pp. 309–324.
- Tago, J., V. Cruz-Atienza, J. Virieux, V. Etienne and F. Sánchez-Sesma (2012). 'A 3D hp-adaptive discontinuous Galerkin method for modeling earthquake dynamics'. In: *Journal of Geophysical Research: Solid Earth* 117.9.
- Tene, M., S. Bosma, M. Al Kobaisi and H. Hajibeygi (2017). 'Projection-based Embedded Discrete Fracture Model (pEDFM)'. In: *Advances in Water Resources* 105, pp. 205–216.
- Terekhov, K. (2020a). 'Cell-centered finite-volume method for heterogeneous anisotropic poromechanics problem'. In: *Journal of Computational and Applied Mathematics* 365.
- (2020b). 'Multi-physics flux coupling for hydraulic fracturing modelling within INMOST platform'. In: *Russian Journal of Numerical Analysis and Mathematical Modelling* 35.4, pp. 223–237.
- (2021a). 'General finite-volume framework for saddle-point problems of various physics'. In: *Russian Journal of Numerical Analysis and Mathematical Modelling* 36.6, pp. 359–379.
- Terekhov, K., B. Mallison and H. Tchelepi (2017). 'Cell-centered nonlinear finite-volume methods for the heterogeneous anisotropic diffusion problem'. In: *Journal of Computational Physics* 330, pp. 245–267.
- Terekhov, K. and H. Tchelepi (2020). 'Cell-centered finite-volume method for elastic deformation of heterogeneous media with full-tensor properties'. In: *Journal of Computational and Applied Mathematics* 364.
- Terekhov, K. M. (2021b). 'Collocated finite-volume method for the incompressible navier-stokes problem'. In: *Journal of Numerical Mathematics* 29.1, pp. 63–79.
- Terekhov, K. M. and Y. V. Vassilevski (2019). 'Finite volume method for coupled subsurface flow problems, I: Darcy problem'. In: *Journal of Computational Physics* 395, pp. 298–306.
- (2022). 'Finite volume method for coupled subsurface flow problems, II: Poroelasticity'. In: *Journal of Computational Physics* 462.
- Toro, E. F. (2009). *Riemann solvers and numerical methods for fluid dynamics: A practical introduction*, pp. 1–724.
- Tripuraneni, S., A. Novikov and D. Voskov (2023). 'Nonlinear finite volume discretization of geomechanical problem'. In: *International Journal for Numerical and Analytical Methods in Geomechanics* 47.12, pp. 2283–2303.
- Truesdell, C. A. (1991). *A First Course in Rational Continuum Mechanics: General Concepts*. 2 Rev Sub. Vol. Vol 1. Pure and Applied Mathematics. Academic Press Inc.
- Tuković, Z., A. Ivanković and A. Karač (2013). 'Finite-volume stress analysis in multi-material linear elastic body'. In: *International Journal for Numerical Methods in Engineering* 93.4, pp. 400–419.
- Uenishi, K. and J. R. Rice (2003). 'Universal nucleation length for slip-weakening rupture instability under nonuniform fault loading'. In: *Journal of Geophysical Research: Solid Earth* 108.B1.

- Uphoff, C., L. Krenz, T. Ulrich, S. Wolf, A. Knoll, S. David, D. Li, R. Dorozhinskii, A. Heinecke, S. Wollherr, M. Bohn, N. Schliwa, G. Brietzke, T. Taufiqurrahman, S. Anger, S. Rettenberger, F. Simonis, A. Gabriel, V. Pauw, A. Breuer, F. Kutschera, K. Hendrawan Palgunadi, L. Rannabauer, L. van de Wiel, B. Li, C. Chamberlain, J. Yun, J. Rekoske, Y. G and M. Bader (n.d.). *SeisSol*.
- Uphoff, C., D. A. May and A.-A. Gabriel (2023). 'A discontinuous Galerkin method for sequences of earthquakes and aseismic slip on multiple faults using unstructured curvilinear grids'. In: *Geophysical Journal International* 233.1, pp. 586–626.
- Van den Bogert, P. (2018). 'Depletion-induced fault slip and seismic rupture: 2D geomechanical models for the Groningen field, the Netherlands'. In.
- Van der Voort, N. and F. Vanclay (2015). 'Social impacts of earthquakes caused by gas extraction in the Province of Groningen, The Netherlands'. In: *Environmental Impact Assessment Review* 50, pp. 1–15.
- Van Thienen-Visser, K. and J. Breunese (2015). 'Induced seismicity of the Groningen gas field: History and recent developments'. In: *Leading Edge* 34.6, pp. 664–671.
- Van Wees, J.-D., P. A. Fokker, K. Van Thienen-Visser, B. B. Wassing, S. Osinga, B. Orlic, S. A. Ghouri, L. Buijze and M. Pluymaekers (2017). 'Geomechanical models for induced seismicity in the Netherlands: Inferences from simplified analytical, finite element and rupture model approaches'. In: *Geologie en Mijnbouw/Netherlands Journal of Geosciences* 96.5, s183–s202.
- Van Wees, J.-D., M. Pluymaekers, S. Osinga, P. Fokker, K. Van Thienen-Visser, B. Orlic, B. Wassing, D. Hegen and T. Candela (2019). '3-D mechanical analysis of complex reservoirs: A novel mesh-free approach'. In: *Geophysical Journal International* 219.2, pp. 1118–1130.
- Vassilevski, Y., K. Terekhov, K. Nikitin and I. Kapyrin (Jan. 2020). *Parallel Finite Volume Computation on General Meshes*.
- Veltmeijer, A., M. Naderloo and A. Barnhoorn (May 2022). 'Acoustic Precursors to Laboratory Induced Fault Slip and Failure'. In: *EGU General Assembly Conference Abstracts*. EGU General Assembly Conference Abstracts, EGU22-4117, EGU22–4117.
- Verruijt, A. (2016). *Theory and problems of poroelasticity*. Delft University Press.
- Voskov, D., I. Saifullin, M. Wapperom, X. Tian, A. Palha, L. Orozco and A. Novikov (June 2023). *open Delft Advanced Research Terra Simulator (open-DARTS)*. Version 0.0.0.
- Voskov, D. V. (2017). 'Operator-based linearization approach for modeling of multiphase multi-component flow in porous media'. In: *Journal of Computational Physics* 337, pp. 275–288.
- Walker, R. L., M. G. Knepley, B. T. Aagaard and C. A. Williams (Sept. 2023). 'Multiphysics modelling in PyLith: poroelasticity'. In: *Geophysical Journal International* 235.3, pp. 2442–2475.
- Wallis, J., R. Kendall and T. Little (1985). 'CONSTRAINED RESIDUAL ACCELERATION OF CONJUGATE RESIDUAL METHODS.' In: pp. 415–428.
- Wang, H. (2017). *Theory of Linear Poroelasticity with Applications to Geomechanics and Hydrogeology*. Princeton Series in Geophysics. Princeton University Press.

- Wang, L., G. Kwiatek, E. Rybacki, A. Bonnelye, M. Bohnhoff and G. Dresen (2020a). 'Laboratory Study on Fluid-Induced Fault Slip Behavior: The Role of Fluid Pressurization Rate'. In: *Geophysical Research Letters* 47.6.
- Wang, Y., D. Voskov, M. Khait and D. Bruhn (2020b). 'An efficient numerical simulator for geothermal simulation: A benchmark study'. In: *Applied Energy* 264.
- Wapperom, M., X. Tian, A. Novikov and D. Voskov (2023). 'FluidFlower Benchmark: Lessons Learned from the Perspective of Subsurface Simulation'. In: *Transport in Porous Media*.
- Wheeler, M., G. Xue and I. Yotov (2014). 'Coupling multipoint flux mixed finite element methods with continuous Galerkin methods for poroelasticity'. In: *Computational Geosciences* 18.1, pp. 57–75.
- White, J., N. Castelletto and H. Tchelepi (2016). 'Block-partitioned solvers for coupled poromechanics: A unified framework'. In: *Computer Methods in Applied Mechanics and Engineering* 303, pp. 55–74.
- White, J. A., N. Castelletto, S. Klevtsov, Q. M. Bui, D. Osei-Kuffuor and H. A. Tchelepi (2019). 'A two-stage preconditioner for multiphase poromechanics in reservoir simulation'. In: *Computer Methods in Applied Mechanics and Engineering* 357.
- Wilson, M., G. Foulger, J. Gluyas, R. Davies and B. Julian (2017). 'HiQuake: The human-induced earthquake database'. In: *Seismological Research Letters* 88.6, pp. 1560–1565.
- Wolf, S., M. Galis, C. Uphoff, A.-A. Gabriel, P. Moczo, D. Gregor and M. Bader (2022). 'An efficient ADER-DG local time stepping scheme for 3D HPC simulation of seismic waves in poroelastic media'. In: *Journal of Computational Physics* 455.
- Wriggers, P. (2006). *Computational contact mechanics*, pp. 1–518.
- Wu, X. and R. Parashkevov (2009). 'Effect of grid deviation on flow solutions'. In: *SPE Journal* 14.1, pp. 67–77.
- Xu, F., H. Hajibeygi and L. Sluys (2021). 'Multiscale extended finite element method for deformable fractured porous media'. In: *Journal of Computational Physics* 436.
- Yastrebov, V. A. and P. Breitkopf (2013). *Numerical Methods in Contact Mechanics*.
- Zoback, M. D. (2007). *Reservoir Geomechanics*, pp. 1–452.

Acknowledgements

This work would not have been possible without my colleagues, people with whom I have had the pleasure of working together, sharing and discussing ideas over the past four years.

From the very beginning, I had the privilege of discussing my work with Denis Voskov, Hadi Hajibeygi, Jan Dirk Jansen and Sara Shokrollahzadeh Behbahani on our numerical sub-team weekly meetings. These four navigated my road through the dark corners of reservoir engineering, computational geomechanics and software development. Together we dived into the depths of Finite Volume Method, and, I believe, learned a lot along this road. I highly appreciate many fruitful discussions, sometimes sparring debates, constant encouragement, and all critical comments that helped me to stay aligned with the project's objectives.

I would like to express a special gratitude to **Denis** with whom we have been working closely throughout my PhD. We started studies in contact mechanics, which was a relatively new field for both of us. His constant support, responsiveness and wide experience helped me to grasp new material and, more importantly, to bring it to working code. I am deeply grateful to Denis for sharing and explaining many reservoir engineering concepts to me. His kindness, honesty, open-mindedness, and responsiveness are the qualities I would like to develop personally. I remain eternally grateful to him for this opportunity to work together and for the profound impact he has had on my academic and professional journey.

My sincere thanks are extended to **Hadi** for his invaluable contribution to my PhD work. His remarkable attention to detail and his exceptional ability to explain complex ideas in clear and comprehensible terms have impressed and encouraged me throughout my PhD. His dedication to exploring the depths of the Finite Volume Method, coupled with his willingness to both challenge and tolerate my ideas, has been instrumental in my academic growth. I am immensely grateful for his support and mentorship.

I am profoundly grateful to **Jan Dirk** for his exceptional contributions to my research. Juggling the immense responsibilities of managing a large faculty while conducting cutting-edge research, Jan Dirk has been a paragon of dedication and excellence. His deep knowledge and extensive experience in geomechanics and reservoir engineering have been invaluable to my work, offering not just solutions to numerous computational challenges but also helping me foresee and avoid potential issues. His unwavering commitment to the objectives of our project and his adherence to the highest research standards have been a constant source of inspiration and guidance.

I am deeply thankful to my colleague, **Sara**, for her invaluable support throughout our PhD journey. Together, we navigated the weekly challenges of reporting

to our supervisors, a task made easier and more enjoyable by her constant encouragement. Sara's remarkable ability to balance her PhD work and motherhood, all while facing significant challenges, has been a source of great admiration and inspiration to me. I am truly grateful for her friendship and the positive influence she has had on my work.

I am immensely grateful to my colleague, **Milad**, whose dedication to experimental excellence has become a cornerstone of our Science4Steer project. Milad's enthusiasm and persistence in doing high-quality tests have been a driving force behind our project's success, and I deeply appreciate the energy and excellence he brought to our team.

I would like to express my gratitude to **Pavan**, who joined Science4Steer in the last two years and brought fresh perspectives and invaluable insights. I have always been intrigued by his and Jan Dirk's work. I sincerely thank him for our conversations about the observability and controllability of geomechanics variables.

My great thanks to TUD DeepNL team who were the closest circle to me over my PhD track. They helped me an infinite number of times, brightened my daily routine and supported me in going through hardships. My deep gratitude to **Aukje**, who organized us and helped a lot with questions about life in the Netherlands, **Hamed**, who cheers us up, being a paragon of hardworking, **Jingming**, whose advances in the modeling of induced seismicity encouraged and motivated myself over the last years, **Samantha**, for her love to cycling that shortens distances, **Faezeh**, who explained me who stands behind Marchenko, **Iban**, who designed the best posters and presentations I have ever seen.

I extend my gratitude to DARTS team with whom we have working with on building a reservoir simulation framework. My thanks are to **Mark**, who became an example of a successful and professional computational engineer to me, **Stephan** who managed to combine the competencies in geology, advanced reservoir modeling and software development in our team, **Xiaoming** for his efforts of extending our forward models to practical inversion tools, **Michiel** for his invaluable contribution to usability of DARTS, **Ilshat** for his steering our research coding into a software development pipeline, **George**, for your dedication to the use of AI in reservoir modeling, **Luisa** and **Arthur** for their support in building a usable modeling framework out of DARTS. I highly appreciate the contribution of **Kiarash**, **Gabriel**, **Yang**, **Xiacong**, **Alex**, **Yuan**, **Guofeng**, and other members of DARTS team with whom I had less chances to work together. Additionally, I would like to thank **Teja** with whom we explored the depths of nonlinear FVM.

During these four years, I had a wonderful time spent with many people from our big department. My thanks are to **Andrea**, **Aydin**, **Eddy**, **David**, **Entela**, **Hermanio**, **Jasper**, **Jasper**, **Mahmoud**, **Marat**, **Maria**, **Menno**, **Parvin**, **Sepideh**, **Shihao**, **Thejas**, **Willelijn** and **Zhenja**.

Furthermore, I would like to express my gratitude to the support staff of our department. **Ingrid**, **Marlijn**, **Ralf**, **Barbara**, **Lydia**, **Rinda** took care of organizational problems that allowed me to focus on my research.

I would like to thank my outer colleagues who helped me with their advice and guidance throughout my PhD. My deepest gratitude to **Matteo**, **Jian**, **Herve**, **Eirik**,

Laura, Massimiliano, Timur, Kirill, Bert, Mathias, and to my previous advisors **Dmitrii, Regina** and **Leonid**.

My endless love and gratitude to **Julia**, whose support, patience and wisdom helped me to pass through four years of PhD. Even before PhD, she encouraged my interest in new things, and was, perhaps, the main motivation for starting a PhD abroad. Together we passed through corona time and started our joint living in the Netherlands. I am infinitely grateful to fate, through **Anton**, for the chance to meet you.

Finally, I express my sincere gratitude to my parents, **Lyudmila** and **Victor**, for their support and love.

Curriculum Vitæ

Aleksei Novikov

04-07-1993 Born in Saransk, Russia.

Education

- 2000–2010 Secondary School
School №36, Saransk, Russia
- 2010–2014 Bachelor in Applied Mathematics & Physics
Moscow Institute of Physics and Technology, Dolgoprudny, Russia
- 2014–2016 Master in Applied Mathematics & Physics
Moscow Institute of Physics and Technology, Dolgoprudny, Russia
Thesis: Numerical simulation of non-isothermal flows in porous media for the characterization of near-wellbore zone
Adviser: dr. L.A. Gaidukov
- 2020–2024 Doctor of Philosophy in Geoscience & Engineering
Delft University of Technology, Delft, The Netherlands
Thesis: A A Finite Volume Framework for Accurate Modeling of Fault Reactivation in Poroelastic Rocks
Promotor: dr. D.V. Voskov

Professional Experience

- 2014–2016 Research & Development Intern
Department of Technological Development and Innovations
PJSC Rosneft Oil Company, Moscow, Russia
- 2015 Research & Development Intern
Tyumen Oil Research Center
Tyumen, Russia
- 2015–2019 Junior Software Engineer
Department of Software Development, Roxar AS
Emerson Electric Co, Moscow, Russia
- 2019–2020 Software Engineer
Department of Software Development, Roxar & Paradigm
Emerson Electric Co, Moscow, Russia
- 2016–2020 PhD Candidate
Department of Applied Mathematics and Computer Modeling
Gubkin University, Moscow, Russia

List of Publications

Journal Articles

4. A. Novikov, S. S. Behbahani, D. Voskov, H. Hajibeygi and J. D. Jansen (2024b). 'Benchmarking Analytical and Numerical Simulation of Induced Fault Slip'. In: *Under Review in Geomechanics and Geophysics for Geo-Energy and Geo-Resources*
3. M. Wapperom, X. Tian, A. Novikov and D. Voskov (2023). 'FluidFlower Benchmark: Lessons Learned from the Perspective of Subsurface Simulation'. In: *Transport in Porous Media*
2. S. Tripuraneni, A. Novikov and D. Voskov (2023). 'Nonlinear finite volume discretization of geomechanical problem'. In: *International Journal for Numerical and Analytical Methods in Geomechanics* 47.12, pp. 2283–2303
1. A. Novikov, D. Voskov, M. Khait, H. Hajibeygi and J. Jansen (2022b). 'A scalable collocated finite volume scheme for simulation of induced fault slip'. In: *Journal of Computational Physics* 469

Conference Proceedings

4. A. Novikov, I. Saifullin, H. Hajibeygi, A. Pluymakers, J. Jansen and D. Voskov (2024a). 'A Finite Volume Framework for the Fully Implicit Thermal-Hydro-Mechanical-Compositional Modeling in Geo-Energy Applications'. In: *Accepted for 19th European Conference on the Mathematics of Geological Reservoirs*
3. A. V. Novikov, S. Shokrollahzadeh Behbahani, D. Voskov, H. Hajibeygi and J. D. Jansen (June 2023). 'Benchmarking Analytical and Numerical Simulation of Induced Fault Slip'. In: *U.S. Rock Mechanics/Geomechanics Symposium, ARMA-2023-0695*
2. A. Novikov, D. Voskov, H. Hajibeygi and J. Jansen (2022a). 'Collocated Finite Volume Scheme for Scalable Simulation of Induced Seismicity'. In: *18th European Conference on the Mathematics of Oil Recovery, ECMOR 2022* 1, pp. 1–18
1. A. Novikov, D. Voskov, M. Khait, H. Hajibeygi and J. Jansen (2021). 'A collocated finite volume scheme for high-performance simulation of induced seismicity in geo-energy applications'. In: *Society of Petroleum Engineers - SPE Reservoir Simulation Conference 2021, RSC 2021*